DEPARTMENT OF PHYSICS
UNIVERSITY OF JYVÄSKYLÄ
RESEARCH REPORT No. 3/2018

APPLICATIONS OF DNA SELF-ASSEMBLED STRUCTURES IN NANOELECTRONICS AND PLASMONICS

BY
BOXUAN SHEN

Academic Dissertation
for the Degree of
Doctor of Philosophy

To be presented, by permission of the
Faculty of Mathematics and Science
of the University of Jyväskylä,
for public examination in Auditorium FYS-1 of the
University of Jyväskylä on March 16, 2018
at 12 o'clock

Jyväskylä Finland
March 2018

Preface

The work reviewed in this thesis has been carried out during the years 2012-2017 at the Nanoscience Center, Department of Physics in the University of Jyväskylä.

First of all, I would like to thank my supervisor Adj. Professor Jussi Toppari for giving me an opportunity to work in his excellent group, and for his brilliant guidance and scientific insights throughout my M.Sc. and Ph.D. studies. I am especially grateful for his support and encouragement for freely pursuing the research I am interested in. I would also like to thank my co-supervisor Adj. Professor Veikko Linko for years of mentorship and collaboration. In addition, I would like to thank Prof. Mauri Kostiainen, Prof. Vesa Hytönen, Prof. Wolfgang Fritzsche, Asst. Prof. Sampo Tuukkanen, and all co-authors for fruitful collaborations.

It has been a great pleasure to work with Dr. Kosti Tapio, Dr. Siim Pikker, Dr. Tibebe Lemma, Dr. Janne Simonen, and Mr. Seppo-Tapio Paasonen from the research group. I could not have reached this far without their support. Special mention goes also to other members, Dr. Svitlana Baivea, Dr. Tommi Isoniemi, Dr. Andreas Johansson, and Dr. Eero Hulkko for pleasant and inspiring discussions. As an experimentalist, the technical support from Dr. Kimmo Kinnunen, Mr. Tarmo Suppula and Dr. Alli Liukkonen are indispensable and gratefully acknowledged. I would like to express my gratitude to the whole staff of Nanoscience Center and especially to the following persons for fascinating discussions, collegial support and wonderful atmosphere: Prof. Gerrit Groenhof, Prof. Janne Ihalainen, Prof. Ilari Maasilta, Dr. Matti Hokkanen, Dr. Peerapong Yotprayoonsak, Dr. Tero Isotalo, Dr. Saumyadip Chaudhuri, Dr. Juhani Julin, and Mrs. Leena Sovijärvi.

I have been privileged to share an office with Dr. Kosti Tapio and Mr. Andrii Torgovkin during my years as a PhD student. I enjoyed and missed the fun time we spent together a lot. It is difficult to find another office with a talkative Finn and a desk full of electronic components and 3D-printed gadgets. I am extremely grateful for the friendship and support in my life from Dr. Chuan Wang and Mr. Zhuoran Geng. I would also like to thank my Chinese friends and colleages: Ms. Tianbai Zhao, Dr. Xi Chen, Dr. Yaolan Tian, Mr. Dongkai Shao and Dr. Yan Zhu for creating a small Chinese community in which I can talk in my mother tongue and feel at home.

Finally, I wish to thank my grandmother Zunxiu Zhang, my parents Naimin

Shen and Jun Zhao, my aunt and uncles Fangtao Zhao, Shu Zhao, Zengxin Wei, and my cousin Wan Wei for their love, empathy and support during my studies in Finland. I truely regret that I could not spend more time with them.

Financial support from the Academy of Finland, Finnish Cultural Foundation, Finnish Academy of Science and Letters (Vilho, Yrjö and Kalle Väisälä Foundation) are gratefully acknowledged.

Espoo, March 2018

Boxuan Shen

Abstract

Shen, Boxuan
Applications of DNA self-assembled structures in nanoelectronics and plasmonics
Jyväskylä: University of Jyväskylä, 2018, 104 p.
(Research report/Department of Physics, University of Jyväskylä,
ISSN 0075-465X; 3/2018)
ISBN 978-951-39-7379-7 (paper copy)
ISBN 978-951-39-7380-3 (PDF)
diss.

In this thesis, the potential applications of DNA self-assembled structures were explored in both nanoelectronics and plasmonics. The works can be divided into two parts: electrical characterization of unmodified multilayered DNA origami and DNA-gold-nanoparticle conjugates after they were trapped between gold nanoelectrodes by dielectrophoresis, and the development of a novel fabrication method using DNA origami as a template for smooth, high resolution metallic nanostructures as well as optical characterization of them.

One of the biggest challenges in self-assembled nanoelectronic devices is to connect them to macroscopic circuits. Dielectrophoretic (DEP) trapping has been used extensively in manipulation of micro- and nanoscale objects in solution. We have demonstrated this technique by trapping four structurally distinct multilayered DNA origami between gold nanoelectrodes by DEP and electrically characterized some of the trapped structures at high relative humidity. Most of the samples showed insulating behavior in both DC I-V measurement and AC impedance spectroscopy. In the other experiment, an assembly of three gold nanoparticles (AuNPs) conjugated with a triple-cross-over-tile (TX-tile) structure were designed, synthesized, and trapped by DEP. At the beginning no current was observed, but after a few chemical gold growth steps, Coulomb blockade behavior was observed from the liquid helium temperature up to the room temperature. Although no gated measurement was carried out, the random switching at low temperature measurements highly resembled a similar behavior of single electron transistor (SET).

The second half of this thesis is focused on the development of a DNA-assisted lithography (DALI) method, in which DNA origami was used to mask the growth of SiO_2 on Si chips in order to generate a stencil mask with openings of the DNA origami shape. Then the stencil was used in conventional microfabrication processes

to deposit metallic nanostructures with almost the same shape as DNA origami on different substrates. Three different DNA origami were used to fabricate metallic structures with various optical properties on sapphire substrates. The localized surface plasmon resonance (LSPR) of Seeman tile and a bowtie antenna was characterized by a dark-field microscope. The surface enhanced Raman spectroscopy (SERS) of two different marker molecules on gold bowtie antennas was characterized too. Finally, the chiral double-L samples landed on a surface with different orientation combinations showed distinct circular dichroism (CD) spectra. In addition, a method to deposit DNA origami on unmodified surface with large area by spray coating technique was reported.

Keywords DNA, self-assembly, DNA origami, metallization, lithography, plasmonics, dielectrophoresis, SET, LSPR, SERS, CD.

Author's address Boxuan Shen
Department of Physics
University of Jyväskylä
Finland

Supervisor Adj. Professor J. Jussi Toppari
Department of Physics
University of Jyväskylä
Finland

Co-supervisor Adj. Professor Veikko Linko
Department of Bioproducts and Biosystems
Aalto University
Finland

Reviewers Asst. Professor Anton Kuzyk
Department of Neuroscience and Biomedical Engineering
Aalto University
Finland

Dr. Adrian Keller
Department of Chemistry
Paderborn University
Germany

Opponent Professor Tim Liedl
Department of Physics and Center for Nanoscience
Ludwig-Maximilians-Universität
Germany

List of Publications

The main results of this thesis have been reported in the following articles:

A.I B. SHEN, V. LINKO, H. DIETZ AND J. J. TOPPARI, *Dielectrophoretic trapping of multilayer DNA origami nanostructures and DNA origami-induced local destruction of silicon dioxide*. Electrophoresis **36** (2015) 255–262.

A.II K. TAPIO, J. LEPPINIEMI, B. SHEN, V. P. HYTÖNEN, W. FRITZSCHE AND J. J. TOPPARI, *Toward single electron nanoelectronics using self-assembled DNA structure*. Nano Letters **16** (2016) 6780–6786.

A.III B. SHEN, V. LINKO, K. TAPIO, M. A. KOSTIAINEN AND J. J. TOPPARI, *Custom-shaped metal nanostructures based on DNA origami silhouettes*. Nanoscale **7** (2015) 11267–11272.

A.IV B. SHEN, V. LINKO, K. TAPIO, S. PIIKER, T. LEMMA, A. GOPINATH, K. V. GOTHELF, M. A. KOSTIAINEN AND J. J. TOPPARI, *Plasmonic nanostructures through DNA-assisted lithography*. Science Advances **4** (2018) eaap8978 .

A.V V. LINKO, B. SHEN, K. TAPIO, J. J. TOPPARI, M. A. KOSTIAINEN AND S. TUUKKANEN, *One-step large-scale deposition of salt-free DNA origami nanostructures*. Scientific Reports **5** (2015) 15634.

Author's contribution

In **A.I** the author fabricated all the electrode samples, did all the trapping experiments, electrical measurements and data analysis, and participated in the writing process.

In **A.II** the author participated in sample fabrication, trapping experiments and the writing process.

In **A.III** the author conducted all the experiments except DNA origami fabrication and participated in the publication writing.

In **A.IV** the author participated in DNA origami design, fabricated all the samples and took all the SEM and AFM images, carried out the LSPR and CD measurements in collaboration with other authors, and also participated in SERS measurement, FEM simulation and data analysis. In addition, the author contributed to the writing process.

In **A.V** the author contributed to the spraying deposition experiment and AFM imaging as well as the manuscript preparation.

Other work to which the author has contributed:

B.I V. LINKO, J. LEPPINIEMI, B. SHEN, E. NISKANEN, V. P. HYTÖNEN AND J. J. TOPPARI, *Growth of immobilized DNA by polymerase: bridging nanoelectrodes with individual dsDNA molecules*. Nanoscale **3** (2011) 3788–3792.

B.II B. SHEN, K. TAPIO, V. LINKO M. A. KOSTIAINEN AND J. J. TOPPARI, *Metallic nanostructures based on DNA nanoshapes*. Nanomaterials **6** (2016) 146.

B.III F. HEIMBACH, A. ARNDT, H. NETTELBECK, F. LANGNER, U. GIESEN, H. RABUS, S. SELLNER, J. J. TOPPARI, B. SHEN AND W. Y. BAEK, *Measurement of changes in impedance of DNA nanowires due to radiation induced structural damage*. The European Physical Journal D **71** (2017) 211.

Contents

Introduction

Nanotechnology refers to the techniques which can manipulate matter in nanoscale. Within this range lie atoms, molecules and supramolecules. It is one of the frontiers of science and technology advances, not only because it is important to miniaturize existing devices, *i.e.*, integrated circuits (ICs) in order to achieve lower heating and higher operating frequency, but also to engineer new materials and devices at nanoscale to acquire unique properties which cannot be aquired naturally. By definition, nanotechnology and nanoscience study the matter with at least one dimension smaller than 100 nm. Two methodologically complimentary approaches are commonly used to build such materials, namely top-down and bottom-up. In the top-down approach, nanoscale objects are carved or sculpted from larger pieces, like in most of the conventional microfabrication processes. However, this route is intrinsically limited by the resolution of the instrument used for "carving". In the alternative bottom-up approach, devices are assembled from even smaller units, *e.g.*, molecules or supramolecules. The interactions between the components are commonly utilized to make them self-assemble, therefore the resolution of the methods are not limited by the instrumentation.

Among all the supramolecules, DNA is one of the most studied due to its important role in carrying the genetic information in all living organism. As a result, the DNA related biotechnology is well-established: DNA molecule can be easily synthesized, modified and manipulated by various methods. The foundation of emerging DNA nanotechnology, in which Watson-Crick base-pairing is used to direct the design and construction of DNA self-assembled structures, is laid on these methods. Although DNA is the genetic information carrier, the focus of DNA nanotechnology is not on genetic information but on the DNA self-assembled constructs which can be used as structural material for nano-devices. At the nanoscale the boundaries between physics, chemistry and biology become blurred. DNA nanostructures, especially the DNA origami [1] and its related design motifs [2–4], have spawned a plethora of applications in all these fields.

As a physicist, applications of these fascinating nano-objects in physics are of particular interest. There are two major physics subfields, namely nanoelectronics and plasmonics, in which DNA self-assemblies can play an important role to expand the boundaries set by traditional top-down methods. Despite numerous attempts to utilize DNA molecules directly in charge transportation (including **A.I**),

nowadays DNA constructs are mainly employed as scaffolds or templates for positioning, assembling or fabricating other nano-objects for physical applications. For example, in order to assemble new devices metallic nanoparticles (MNP), carbon nanotubes (CNT) or dye molecules can be easily conjugated to specific locations on DNA origami due to its sub-nanometer addressability and modularity. Subsequently, these devices can either be connected to macroscopic circuits *via*, e.g., dielectrophoresis (DEP) for electrical measurements (**A.II**) or be directly measured in optical applications. Moreover, the shape of DNA structures can also be transferred to other materials, like metal, with very high resolution by chemical or physical methods. This is particular exciting for plasmonic applications because localized surface plasmon resonances (LSPR) are very sensitive to the dielectric function, size and shape of the metal nanostructures. With the capability to fabricate under 100 nm metallic nanostructures with arbitrary shape with high resolution and in a parallel fashion, many applications including surface enhanced Raman spectroscopy (SERS), fluorescence enhancement (FE), chiral molecule detection or even metamaterials, can be achieved.

This thesis will be divided into 6 main chapters. In Chapter 1 an introduction about DNA nanotechnology with emphasis on the structural DNA nanotechnology and its applications, the electrical conductivity of DNA molecule and DNA construct, and DNA metallization methods will be given. In the following Chapter 2, important theory backgrounds including dielectrophoresis and localized surface plasmon resonances, as well as microfabrication methods repeatedly used in the works of this thesis, will be briefly introduced. From Chapter 3 to Chapter 5, the main scientific works of this thesis will be discussed. In Chapter 3, the DEP trapping and electrical measurement of various multilayered DNA origami structures (**A.I**) and a TX-tile-based gold nanoparticle chain which was assembled as a prototype single-electron-transistor (**A.II**), will be presented. The development of a metallization method, in which the shape of DNA origami can be transferred to metallic nanostructures on a substrate by evaporating metal through silicon oxide mask with origami-shaped openings, will be described in Chapter 4 (**A.III**-**A.V**). Three different optical measurements of the metal nanostructures fabricated by the method in Chapter 4, namely LSPR, SERS and circular dichroism (CD), and corresponding simulation results will be collected and presented in Chapter 5. Finally, in Chapter 6, all the major results in this thesis will be shortly summarized and some perspective for the future developments will also be discussed.

Chapter 1

DNA nanotechnology

1.1 DNA molecule

Deoxyribonucleic acid (DNA) is one of the most well-known biomolecules due to its important role as the genetic information carrier for all living organisms. Essentially, it is a biopolymer (polynucleotide) comprised of multiple monomers called nucleotides. Each nucleotide comprises of a phosphate group, a sugar called deoxyribose, and one of the four nitrogen-containing nucleobases, namely, cytosine (**C**), guanine (**G**), adenine (**A**), or thymine (**T**). The phosphate group and deoxyribose form the backbone of the DNA molecule, in which they are covalently binded through 3′, 5′ - phosphodiester bonds. Usually, a single string of such polynucleotides is called a single-stranded DNA (ssDNA).

Two ssDNAs can form the famous double-helix structure *via* Watson-Crick base pairing, in which the nucleobases on one strand bind to their complementary bases (A to T, C to G) on the other strand *via* hydrogen bonds [5], like shown in Fig. 1.1. The two complementary ssDNAs in a helix are situated in an anti-parallel configuration, meaning that the 3′, 5′ - phosphodiester bonds of them run in opposite directions. Such duplex is called a double-stranded DNA (dsDNA) molecule. Besides the hydrogen bonds, the base-stacking interactions, *i.e.*, dipole-dipole and van der Waals interactions between the adjacent bases, also contribute to the stability of the dsDNA molecule. [6]

Double-stranded DNA can form various helical structures, namely A-DNA, B-DNA and Z-DNA. In living organisms the most common form of dsDNA is B-DNA, which adopt the Watson-Crick base pairing and is a right-handed helix with 2 nm diameter, roughly 10.5 bases per helical turn and 0.34 nm distance between neighboring bases, as shown in Fig. 1.1b. Compared with B-DNA, A-DNA is a thicker right-handed duplex with a shorter distance between the base pairs. It occurs when a B-DNA is dehydrated as well as in RNA-DNA and RNA-RNA duplexes. Unlike the B-DNA, base pairs in A-DNA are not perpendicular to the helical axis. Z-DNA is another conformation dsDNA can take, but it is quite different from B-DNA. It is a

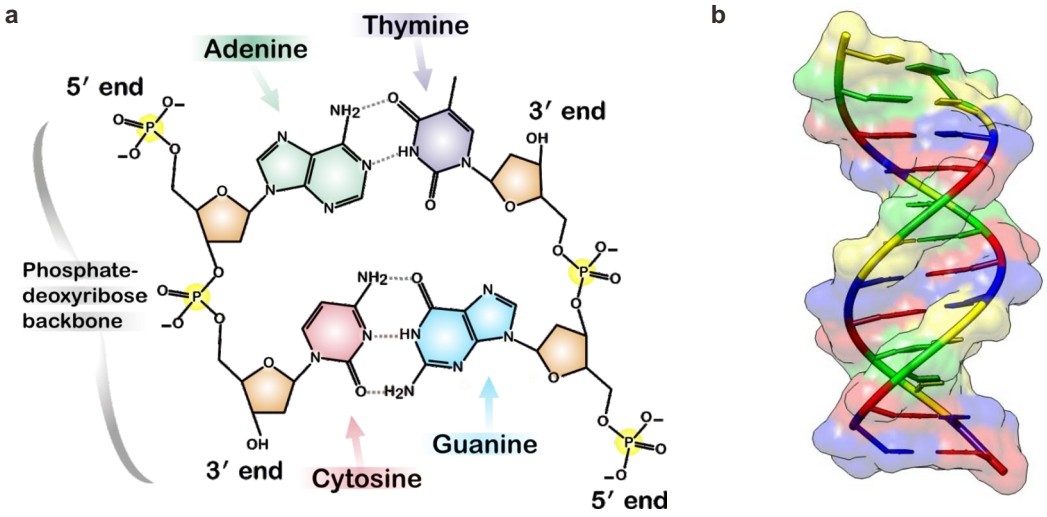

FIGURE 1.1 **a**, a schematic illustration of Watson-Crick base pairing in a dsDNA. Two ssDNA with nucleobases complementary to each other connected *via* different numbers of hydrogen bonds (two for A and T, three for C and G). **b**, a 3D model demonstrates a double-helix structure with a short 12 bp dsDNA in B-form.

left-handed helix which usually happens with dsDNA molecule with poly(dG-dC) sequences. In this thesis, unless stated otherwise, all dsDNA molecules are assumed to be in the B-conformation.

1.2 Structural DNA nanotechnology

Because of its robustness, nanometer diameter, and most importantly, the molecular recognition due to Watson-Crick base pairing, DNA molecule is one of the most promising candidate for bottom-up self-assembly. Enabled by the advancement of molecular biotechnology, *e.g.*, arbitrary sequence oligonucleotide synthesis, polymerase chain reaction (PCR) technique for amplification, and various enzymes for ligation, excising *etc.*, a whole field referred as DNA nanotechnology has been dedicated to using DNA molecules as building material for fabrication of nanoscale devices [7, 8]. Although there exist plenty of biological applications, the structural properties and programmable self-assembly of DNA rather than its genetic information are in the focus of the studies.

The beginning of the field is commonly attributed to Ned Seeman's proposal to use DNA molecules to form a rigid lattice in order to frame proteins which are hard to crystallize for crystallography [9]. After more than 30 years of development, there is a plethora of methods to program and build DNA nanostructures and the potential applications have been expanded to other fields in biology, plasmonics and molecular electronics.

In this section, the existing DNA self-assembled building motifs and the current trend of their applications will be briefly reviewed.

1.2.1 Construction motifs

The initial motivation to build DNA constructs was to apply them in crystallography. Therefore, the early construction motifs were targeted at periodical lattices. Most naturally occurring DNA molecules are linear, which are not sufficient for making two-dimensional (2D) or three-dimensional (3D) lattices. But branched structures do exist, *i.e.*, Holliday junction, which is a key feature during genetic recombination in cells. Instead of a linear double-helix dsDNA, a Holliday junction consist of 4 ssDNA, which are all partially complementary to each others, and thus result in a junction-like structure with 4 arms (Fig. 1.2a). It can also be thought as two dsDNA cross-linked at the junction. Based on the same idea, junctions with more arms have been designed by programming the oligonucleotides with corresponding sequences [10]. These junction building blocks can then join together and form a larger hierarchy by sticky-ends, a single-stranded overhang which can hybridize with its counterpart in another building block as shown in Fig. 1.2b. Both 2D and 3D lattices can be formed with similar ideas [11]. Besides lattices, objects with defined size have also been built, e.g. a cubic cage (Fig. 1.2c) [12].

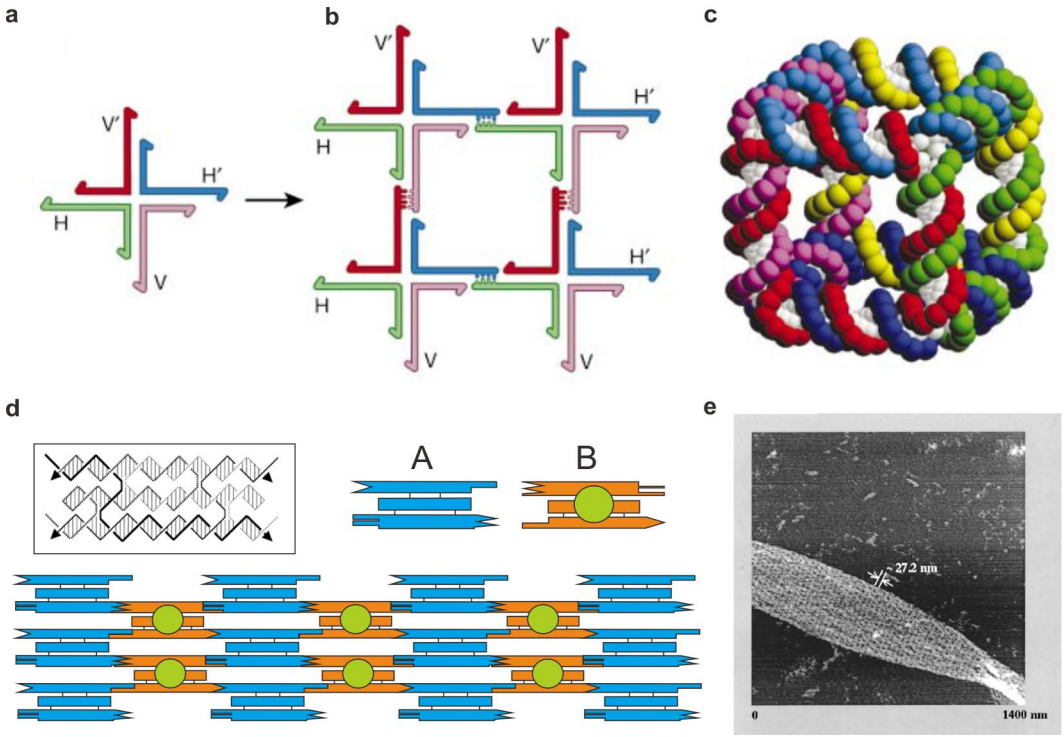

FIGURE 1.2 **a**, a Holliday junction with sticky-ends; or, **b**, a network made from connected building blocks in **a**, **c** a wireframe cube made from similar building blocks; or, **d**, two well-designed TX-tiles can assemble into a nanoribbon, inset: schematic view to show the crossovers; or, **e**, AFM micrograph of the nanoribbon on surface.Adapted with permission from Ref. [13](**a**-**c**) and [14] (**d** and **e**).

However, a single dsDNA strand is too floppy to form rigid enough structures

with a fixed lattice distance for crystallography. Consequently, tile-based motifs with multiple parallel helices were proposed. Among them, double crossover tiles (DX-tile) [15] and triple crossover tiles (TX-tile) [14] have been used in construction of 2D and 3D DNA nanostructures (Fig. 1.2d and e). Later, more diverse structures other than ribbons were also made from the tiles, *e.g.*, barcode [16], rigid trianglar lattice [17], grid with proteins [18], nanotube [19, 20] and tetrahedron [21, 22]. In Chapter 3 and article **A.II**, a define-sized TX-tile motif is used to construct a chain of gold nanoparticles in order to make a single-electron-transistor-like device.

In the aforementioned construction motifs, only synthesized oligonucleotides were employed in the designs. Because of the limited sequence length, the fabrication efficiency and yield are usually low. In addition, the self-assembly process is also very sensitive to stoichiometrical ratios of the strands. An alternative motif was later suggested, in which a 1.7 kb long ssDNA with the presence of five synthetic 40-mer oligonucleotides was folded into an octahedron by simple denaturation-renaturation procedure [23]. In this design, the long ssDNA mostly hybridized to itself. The five oligonucleotides only hold the shape in certain key locations. Therefore, the possible structures which can be made by this method is still limited and sequence specific.

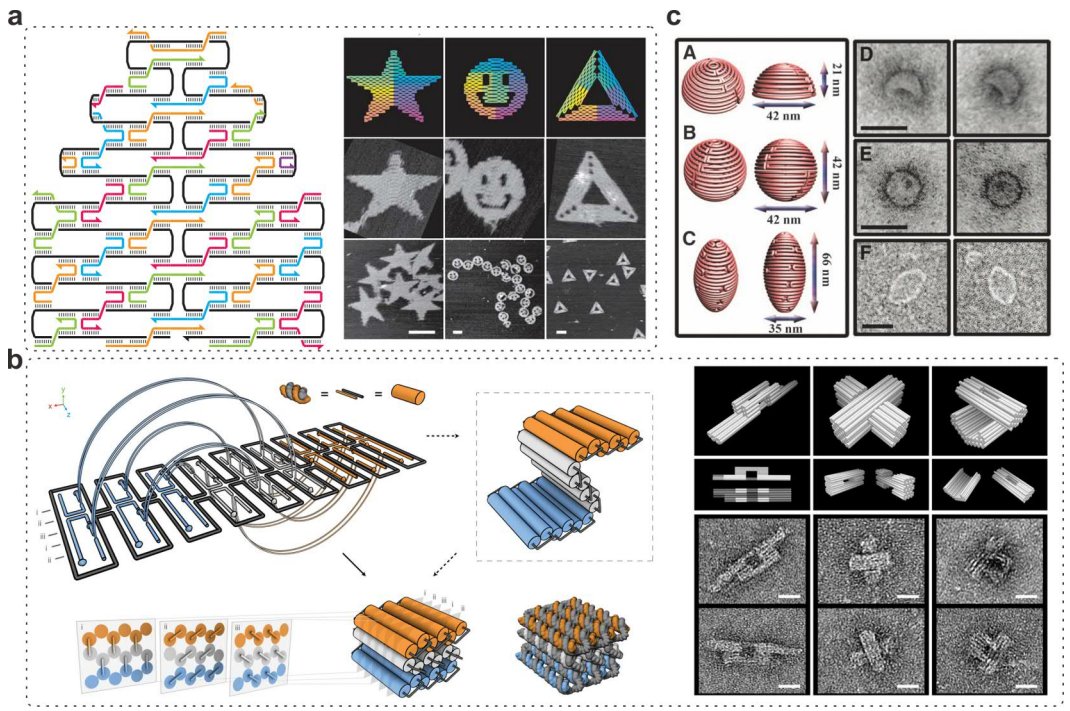

FIGURE 1.3 **a**, design concept and examples of 2D DNA origami on surface by AFM. **b**, design concept of 3D DNA origami in a honeycomb lattice and some examples under TEM. **c**, highly curved 3D origami shapes based on concentric rings and examples under TEM. Adapted with permission from Ref. [1](**a**), [2](**b**) and [4] (**c**).

In 2006, based on a similar idea, a more general method called "DNA origami" was introduced [1]. In this method, a viral strand DNA of more than 7 kb (scaffold)

was folded into a designed 2D shape with the help of over 200 short oligonucleotides (staple strands). All the scaffold strands were hybridized with staple strands, which made it possible to design completely different shapes by only altering the staple strand sequences. Moreover, every single staple strand in an origami design can be chemically modified, which makes it perfect template for hosting other nanoscale objects. The design concept and some examples of DNA origami is shown in Fig. 1.3a.

Later, the idea of DNA origami has been generalized to multilayer origami by folding a single layer of origami once more with staple strands [2] (Fig. 1.3b), and thus made fabrication of 3D objects possible. Other than regular constructs made from straight helices, curved structures [3] can also be made by skipping or inserting bases in the staple strands to artificially induce stress in the structure. In article **A.I** and Chapter 3, some of these multilayered structures were trapped by dielectrophoresis (DEP) and electrically characterized.

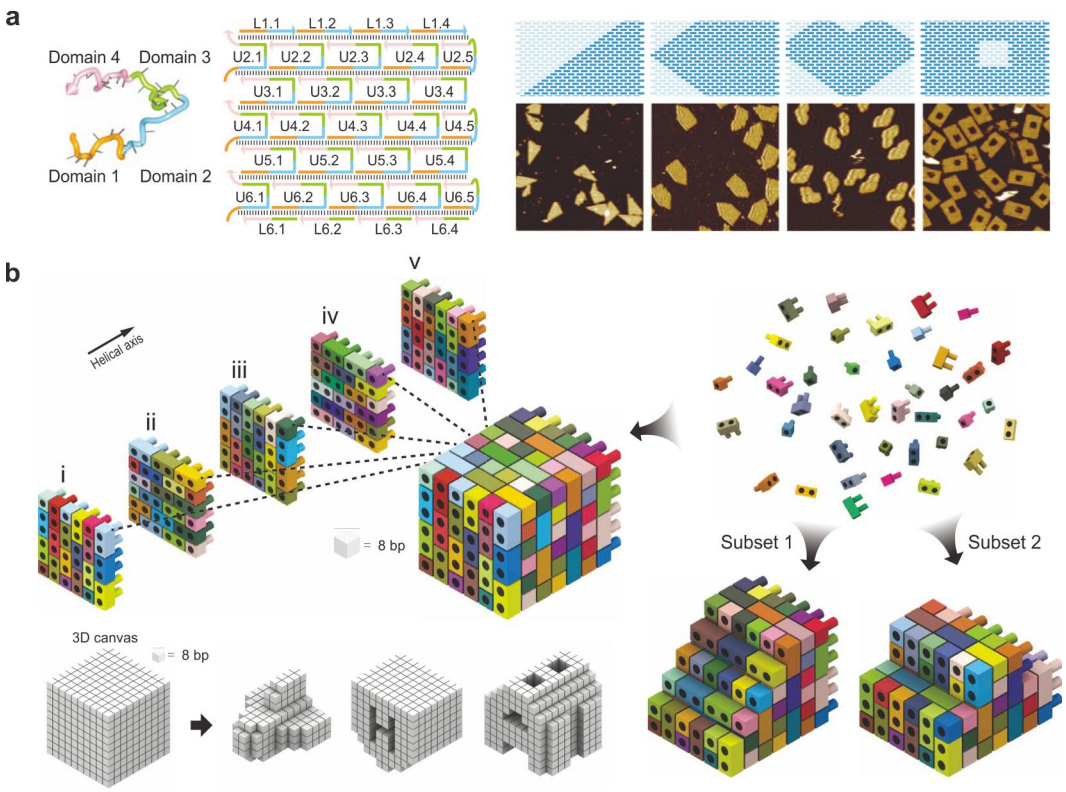

FIGURE 1.4 **a**, design concept of 2D DNA tiles and examples under AFM. **b**, design concept of 3D DNA bricks. Adapted with permission from Ref. [24] (**a**) and [25] (**b**).

Because the shape of an origami structure is determined by a whole set of staple strands, any change in the shape requires a complete replacement of all the staple strands, which makes the cost of fabrication a new DNA origami nontrivial. Another DNA-origami-like motif, but without the scaffold strand, can produce almost arbitrary shapes without modifying the entire staple set [24]. In such a 2D

DNA tile and its later 3D brick version [25], oligonucleotides, which connect to its neighbors by sticky-ends, acted as pixels in a 2D canvas or voxels in 3D bricks, as shown in Fig. 1.4a and b. Specific shapes can be made by removing certain set of pixels or voxels in the canvas or brick. Therefore, numerous shapes can be made based on the same collection of oligonucleotides without additional purchase.

Analog to the coordinate systems in a mathematical representation, both DNA origami and DNA bricks are intrinsically Cartesian, which makes it cumbersome to form fully curved structures. Yan *et al.* [4,26] fabricated highly curved structures, *e.g.* a nano-vase, with a series of concentric circles, which can be considered as a design motif in cylindrical coordinates. Some designs and TEM micrographs of such highly curved structures are shown in Fig. 1.3.

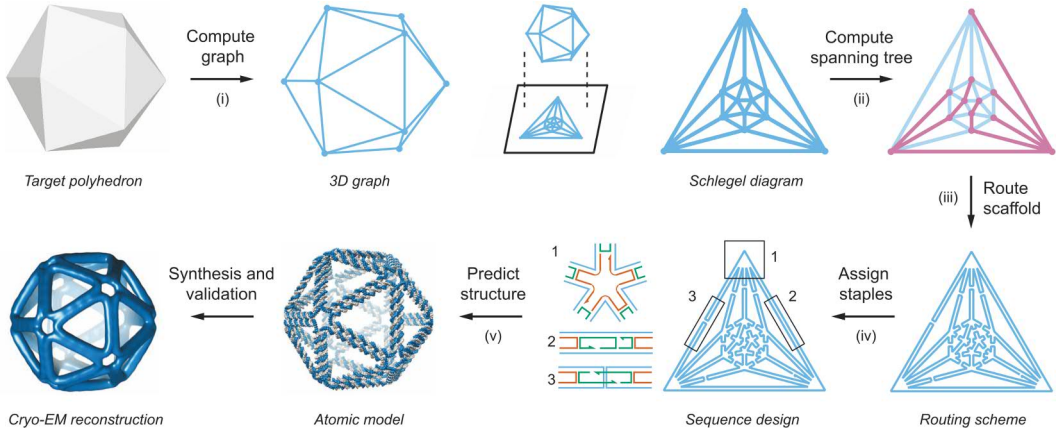

FIGURE 1.5 Top-down sequence design procedure for scaffolded DNA origami nanoparticles of arbitrary shape. Adapted with permission from Ref. [27].

Recently, inspired by the algorithms in computer science for modeling 3D objects, polyhedron-based designs with corresponding automated software have also been proposed. A routing algorithm based on the graph theory was used to automatically design DNA architectures constructed by polyhedrons with one helix at each edge [28]. Arbitrary shapes, *e.g.* spheres, bottles, or even bunnies, can be designed and fabricated by the software without manual adjustment. The single-helix edge made the structures less densely packed as DNA origami, and therefore stable under ionic conditions in biologial assays, but more squishy. A similar design route, but with more rigid DX-structures at each edge, was published not long after [27], as shown in Fig. 1.5. In this work, an asymmetric PCR was used to produce scaffold strands with custom lengths, and thus increased the level of automation even more.

1.2.2 Applications of DNA constructs

Along with the rapid development of various DNA construction motifs, DNA self-assembly became a promising tool for construction and study of nanoscale objects in

other fields of natural science. They either were used as inert templates or scaffolds to host the components of interest or acted as important structural materials to build devices or vehicles. After three decades, the researches in this field slowly shifted from fundamental studies towards real applications.

Template

As mentioned earlier, the oligonucleotides used in DNA constructs can be easily modified with various chemical groups, which enables the use of DNA constructs as templates for other nanoscale components, *e.g.* proteins (enzymes) [29–31], metallic nanoparticles [32–34], carbon nanotubes [35, 36], fluorescence dyes [37] and polymers [38].

DNA constructs, especially DNA origami, can be characterized and recognized by atomic force microscope (AFM) and transmission electron microscope (TEM) due to their sizes. Combined with the fact that every individual oligonucleotide can be addressed and chemically modified, it provides an excellent platform for studying reactions of individual molecules. The cleavage reactions of various linker molecules were studied by placing streptavidin *via* a linker to a rectangular DNA origami, and comparing the AFM images before and after the reactions [29]. The enzymatic reactions of glucose oxidase (GOx) and horseradish peroxidase (HRP) can be facilitated if they are placed in hexagonal DNA tubes in a cascade fashion [30].

DNA origami were also used to position multiple objects, *e.g.* metallic nanoparticles (MNP), quantum dots (QD) or carbon nanotubes (CNT) in a specific arrangement to build plasmonic or electronic devices with intriguing properties. A good example is chiral plasmonic material. By conjugating a series of gold nanoparticles (AuNPs) to a cylindrical DNA origami in a spiral form, circular dichroism (CD) effect has been observed. The CD effect can be tailored by altering the arrangement of the AuNPs [32]. Gold nanorods (AuNRs) positioned in different angles have also been utilized to achieve chiral effect [33]. Hierarchical assemblies of combinations of AuNPs, QDs, and organic dyes offer a new architecture for building plasmonic devices [39]. Moreover, chiral plasmonic devices made from AuNRs, which can be later reconfigured after fabrication, have proven that DNA origami is not only useful in static but also in dynamic devices [40]. Several review articles about building plasmonic devices with DNA nanotechnology are available as in Ref. [41, 42]

Nanoelectronic devices can also benefit from the DNA templates. CNTs functionalized by either DNA molecule [35] or biotin [36] have been arranged to a cross pattern on rectangular DNA origami to form a field effect transistor (FET). Single electron transistor (SET) is a highly demanded nanoelectronic device, and therefore DNA self-assembly-based SETs have also been developed. A structure resembling a SET was made by self-assembling one AuNP and three AuNRs on a rectangular DNA origami [34]. In article **A.II** included in this thesis and Chapter 3, a chain of three AuNPs conjugated with a TX-tile structure were trapped by dielectrophore-

sis between gold electrodes and chemically grown on-site to achieve a very small distance between the particles for tunneling. Afterwards a Coulomb blockade behavior, which is essential for SET, was measured at both low temperature and the room temperature.

It is well known that electromagnetic field can be greatly enhanced when two metallic particles are very close to each other. The physical phenomena which depend on electric intensity can therefore be enhanced at such locations. Fluorescence and Raman scattering are two important examples in sensing applications. By attaching metallic NPs on DNA origami, both fluorescence enhancement (FE) [43] and surface enhanced Raman scattering (SERS) [44, 45] have been observed. The addressability of DNA origami has enabled positioning not only the NPs close together, but also planting the fluorophore exactly in the hotspot. In some cases, when the distance between particles are not small enough, chemical growth method can help to increase the particle size and create narrower gaps [46].

In many applications, the key challenge is the precise positioning of nanoscale objects in a large scale substrate. DNA origami can work as a nano-adapter to bridge the gap between nanometer precision and micrometer precision. With the lithographically fabricated hydrophilic patterns, which fit to the shape of DNA origami, *e.g.* triangles, AuNP or fluorophore on a DNA origami can be precisely positioned on a substrate within a large ordered array [47] or in specific locations on a photonic crystal [37].

As a mechanical structure

Besides serving as an inert template or substrate, DNA constructs can also be used as cargo-carrier to protect and deliver substances into cells or used in building nanomachines. As early as 2009, a DNA origami box with a lid, which can be controlled by strand displacement, was designed and fabricated [48]. Later, DNA nanotubes were also designed to selectively release drugs [49]. Recently, enzymes loaded in a hexagonal DNA origami tube were delivered into cells and proved to be still intact [50]. This aspect of DNA nanotechnology has attracted a lot of attention. Multiple groups are actively developing techniques for DNA-based drug delivery at the moment.

The mechanical properties of DNA constructs were also employed to study the interactions of proteins, *e.g.* nucleosome-nucleosome [51]. Two rigid DNA beams connected with a hinge were used as a force spectrometer to characterize the force between two nucleosomes arranged in different relative positions by monitoring the opening angles of the beams. Moreover, the possibility to build a nanoscale rotary apparatus has also been explored [52].

1.3 Electrical properties of DNA

Due to its excellent programmability and self-recognition, DNA molecule is a very promising candidate for molecular electronics, which is an emerging branch of nanoelectronics. The focus of molecular electronics is to use molecular building blocks to fabricate electronic components, *e.g.* conducting wires, rectifiers, switches, transitors, and memories. [53] No matter whether DNA will be used as wires, active components or as a breadboard, characterizing its electrical properties and understanding the charge transfer mechanisms are crucial. Moreover, molecular electronics is not the only reason why the conductivity of DNA molecule is of great interest. Other motivations like alternative readout scheme for biochips [54] and study of genetic damage and mutation by radiation (**B.III**) have also contributed to the demand of electrical measurements of DNA molecule.

In fact, not long after the double-helix model was discovered, the possibility of using dsDNA as a conducting/semiconducting wire has already been discussed [55]. It was suggested that the delocalised π orbitals in the aromatic rings of the adjacent bases can couple with each other (π-stacking) in the direction of the helical axis, and thus lower the energy gap to facilitate charge transport along DNA. However, it has also been pointed out that this coupling is very sensitive to the conformation and sequence of DNA. The distance and angle between the adjacent base pairs, as well as the highest occupied molecular orbital (HOMO) and lowest unoccupied molecular orbital (LUMO) of the adjacent base pairs can greatly affect the energy gap. Therefore, in principle, a homogeneous sequence should provide the best configuration for π-stacking. In addition, the backbone flexibility and the water molecules with counter-ions surrounding the negatively charged DNA affect the electrical structure of the π-stacking.

The charge transfer through a DNA molecule with heterogeneous sequence was experimentally observed in physiological conditions. Double-stranded DNA molecules functionalized with electron donors and acceptors on each end were prepared, and the electron transfer was measured through a fluorescence quenching as a function of distance [56–59]. Evidences showed that DNA charge transport can even proceed over long molecular distances (~ 200 Å) [60, 61].

Two theories were proposed for the charge transport through DNA duplexes in long distances: tunneling (superexchange) through the DNA bridge between the bound donor and acceptor, and thermal hopping between discrete base orbitals. The tunneling theory predicts that the charge transport rate will decrease exponentially when the distance increase, while the thermal hopping theory has a much more shallow distance dependence. A research on charge transfer induced guanine oxidation showed that when the guanines in dsDNA were separated by less than three TA bases, the oxidation decreased steeply vs. distance. However, when there were more base pairs in between, the oxidation rate exhibited a more shallow distance dependence [62]. This rate change suggested a mechanism shift from tunneling at

short distance to thermal hopping at long distance.

Although numerous investigations have been carried out in a biochemical way, and the charge transfer in DNA molecules was evident, the use of DNA molecule in nanoelectronics still requires direct dry state electrical measurement. Because of the DNA nanotechnology, significant efforts have been invested in direct electrical measurement of DNA in the recent 20 years. However, the published experimental results were very contradicting. The conductivity of DNA has been reported as conductor [63], insulator [64], semiconductor [65] or even proximity-induced superconductor [66]. More comprehensive reviews can be found in Refs. [67–69].

The contradicting DNA conductivity results were possibly influenced by many factors, *e.g.*, contacts, DNA molecule structure, and the environment. First of all, the contacts between DNA molecules and macroscopic metallic electrodes are very critical for accurate measurement. Ideally, these contacts should be ohmic and low in resistance to ensure that the properties measured are those of the molecule and not those of the molecule-electrode interface. Moreover, the medium surrounding and supporting the DNA molecule must be several orders of magnitude more insulating than the molecule itself because the contact area of the support is often much greater than that of the molecule [70]. A simple mechanical contact does not necessarily ensure an electrical contact between a molecule and an electrode, and usually, a chemical bond is preferred. For gold or silver electrode, a thiol group is commonly used to form a covalent bond with the metal. As demonstrated by the biochemical methods, base pair stacking is crucial for charge transfer, therefore B-DNA provides the most suitable conditions for conductivity. However, in solid state measurement, the DNA molecule are usually dehydrated, and thus cannot maintain the B conformation [71]. In addition, the sequence of DNA in question can also affect the conductivity. The environment [72], including salt concentration, counterion charge, pH and temperature, also plays a role in the results.

Most of the dry state experiments used simple dsDNA or bundles of DNA as subjects. DNA self-assembled constructs were rarely measured. Due to the their excellent self-assembly and molecular recognition properties, the DNA origami and tile-based structures are very promising as templates for nanoelectronics. The electrical properties of these constructs need to be understood for such applications. Previously in our research group, single layered DNA origami and define-sized TX-tiles were trapped and immobilized between gold electrodes and characterized by both DC method and AC impedance spectroscopy (AC-IS). [73,74] Characterization of multilayered DNA origami structures will be presented in Chapter 3 and **A.I**.

Although there are still controversies about the conductivity of DNA, most results agree that unmodified long DNA molecules or structures in dry condition are good insulators, and thus are appropriate for template.

1.4 DNA metallization

The insulating or low conductive nature of DNA has limited its applications in nanoelectronics and plasmonics. Instead of investigating the conditions or methods to enable pure DNA molecule to conduct electrical current, transferring the spatial information of DNA nanostructures into metallic materials have attracted more and more attention. By doing so, it not only enabled fabrication of conductive components for nanoelectronics with nanoscale precision, but also provided essential material for plasmonics, since the application of plasmonics largely rely on the complex permittivity and precise shape of the metallic structures.

To date, various methods have been developed to utilize the DNA constructs in arrangement or fabrication of metallic nanostructures, which were commonly referred as DNA metallization. Four metallization routes will be discussed in this section, namely conjugation of metal nanoparticles with DNA self-assemblies, chemical reduction of metal ions to DNA molecules, using DNA origami as a mold to cast nanoparticles with specific geometries and using DNA as a lithography mask. **B.II** is a more comprehensive review about fabrication of metallic nanoshapes *via* self-assembled DNA structures.

1.4.1 Conjugation of metallic nanoparticles

Metallic nanoparticles (MNP) can be easily incorporated onto self-assembled DNA nanostructures thanks to their addressability and modularity. Some of the examples have already been discussed in Section 1.2.2.

MNPs, especially the ones made from noble metal, are of great interest among nanoscientists, which is attributed to its fascinating properties and robust synthesis procedures. MNPs are usually chemically synthesized: the metal ions in solution are first reduced to zerovalent metal by various reducing agents, and the metal atoms will grow into nucleing center when they collide with each other. Then the nucleing center can function as a seed for further growth process. For stability, the MNPs are usually protected by capping agents, which prevent the MNPs from agglomeration by either electrostatic repulsion or steric stabilization. By using different surfactants, the growth direction can also be controlled. As a result, nanoparticles with diverse morphologies have been produced, including, *e.g.*, spheres [75–77], triangles [78], rods [79], rectangles [80] and stars [81].

The synthesized MNPs can be modified with various functional groups, which allow them to be conjugated to other nanoscale objects. For gold nanoparticle (AuNP) and silver nanoparticle (AgNP), the thiol group is most commonly used to form a covalent bond between the gold/silver and sulfur atom [82]. Gold-sulfur bond is actually one of the strongest covalent bonds found in nature [83], therefore a thiol group can easily substitute any ligand or ions on the surface of the AuNPs. Other available linkers include, *e.g.*, disulfides [84], phosphine [85] and amines [86].

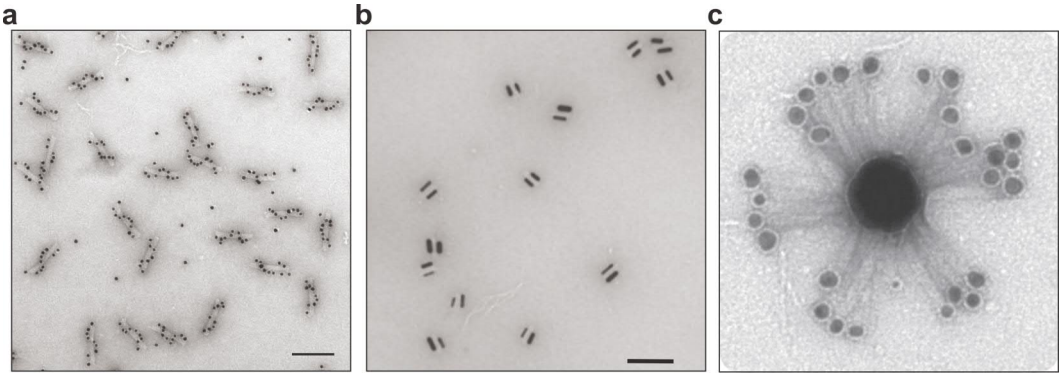

FIGURE 1.6 Conjugation of DNA origami with AuNPs, AuNRs, and AgNPs. Adapted with permission from Ref. [32] (**a**), [40] (**b**) and [39] (**c**).

For conjugation of nanoparticles with DNA constructs, oligonucleotides modified with thiol groups are mostly used for functionalization of the MNPs. Then the modified MNPs can attach to the designed location by complementary strands hybridization. Overabundant works [32–34, 39] have been carried out to incorporate MNPs to DNA origami and other constructs (also in **A.II**). Some of the conjugated structures are demonstrated in Fig. 1.6. The MNP-DNA assemblies can be directly used as plasmonic devices or they can be utilized as seeds for the growth of metallic structures which are either continuous or with nanoscale gap for field enhancement or electron tunneling, as will be discussed in the next subsection.

1.4.2 Direct chemical reduction

Driven by the demand of making narrower conductive wires from poorly conducting DNA molecules, chemical reduction methods, in which DNA molecules are chemically plated with various metals, have been extensively investigated. The methods falling in this category usually comprise three steps: (1) initial binding of seed ions or complexes onto DNA; (2) the chemical reduction of the seeds into nucleation clusters; and (3) the growth of these nucleation clusters into a metallic structure by further reduction reactions.

Simple dsDNA and ssDNA

Early DNA metallization research focused on linear DNA or networks of DNA. Double-stranded DNA have been metallized into nanowires with diverse metals, *e.g.*, silver [87–89], palladium [90, 91] (Fig. 1.7a), platinum [92, 93], nickel [94], gold [95–97] and copper [98]. Single-stranded DNA has also been metallized with similar methods [99–101], but it usually forms nano-ring structures. Besides the reducing agents, UV light can equivalently employed in DNA metallization to convert ions to metal atoms [102–104]. The thickness of metallic nanowires produced by linear DNA molecules ranges from 1.5 nm to ∼100 nm depending on both the metal

species and the type of the reaction. In some of the works, the resistance of the metallic nanowires were also measured, resulting in the range of kΩ [91].

It is worth pointing out that even for simple dsDNA molecules, sequence-specific metallization has been achieved by blocking a segment of dsDNA by a nucleoprotein filament (ssDNA polymerized with RecA) [97]. The filament can tightly bind with a duplex with the same sequence as the ssDNA within, and thus prevent the metal reduction in the specific region. A carbon nanotube (CNT) field-effect transistor has been fabricated based on this technique by first connecting a single-wall carbon nanotube (SWNT) at the blocked site before subsequent metallization. [105]

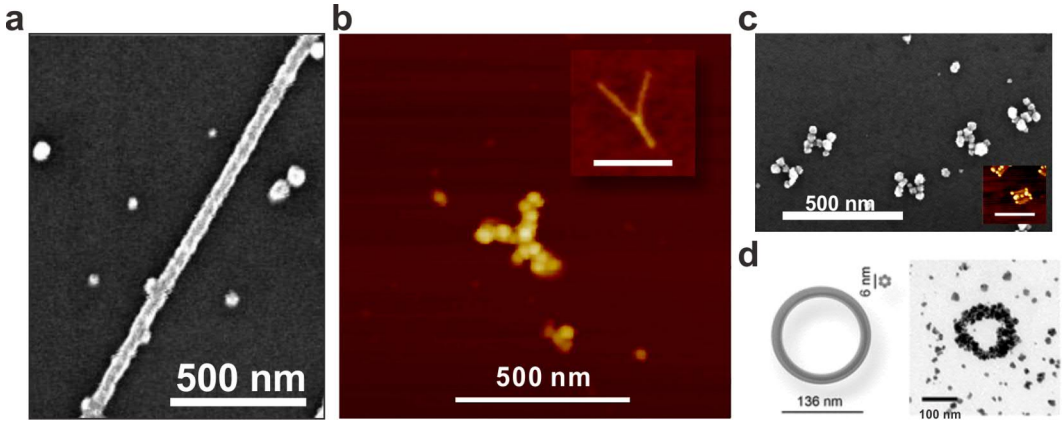

FIGURE 1.7 Metallized **a**, dsDNA and **b**, Y-shaped DNA origami. **c**, AuNP conjugated origami followed by metal ion reduction. **d**, metallization of AuNPs electrostatcially attached to a DNA origami. Adapted with permission from Ref. [91] (**a**), [106] (**b**), [107] (**c**) and [108] (**d**).

DNA constructs

Since the chemical reduction methods only rely on the interaction between metal-ions and DNA molecules, it is intuitive to extend the treatment from a linear structure to more complex DNA nanostructures. For both nanoelectronics and plasmonics, the capability to make metallic components with desired topology and composition is extremely valuable.

An attempt to metallize DNA constructs already started while the tile-based designs were still dominant. Silver nanoribbons comprised of 4×4 DNA tiles [18] showed a resistivity of $2.4 \times 10^{-6} \Omega \cdot m$. Nanotubes assembled from TX- or DX-tiles were also treated with silver [20] and palladium [109], respectively. However, these assemblies did not have a defined size and were still linear, therefore they could not be used for any other than wire-like purposes.

After the invention of DNA origami, its robustness and capability to form arbitrary define-sized shape were very appreciated by the scientific community. However, it would provide even more possibilities for nanotechnology if they could be

fully metallized. Nevertheless, there have been a few challenges in the metallization of DNA origami, *e.g.*, the stability of the origami during the metallization process, the poor adhesion of DNA origami to a surface, the increased selectivity and precision requirements due to its miniaturized size and the presence of free staple strands. In 2011, the first successful DNA origami metallization attempt was reported [106]. A Y-shaped DNA origami was first seeded with Ag and then chemically plated with Au, as shown in Fig. 1.7b. The selectivity was increased by a couple of dialysis processes to remove the excess reactants from the solution, and a lower staple to scaffold ratio was also employed for the same purpose. The stability of the origami during the procedure and the adhesion to surface were maintained by addition of Mg^{2+} to every steps including seeding, dialysis and rinsing. Later, origami structures that were chemically plated with palladium and copper were also demonstrated [110, 111].

Besides chemically induced seed ions on the DNA molecule, pre-synthesized MNPs, especially AuNPs, can also act as seeds for metal growth. Oligonucleotide functionalized AuNPs can be arranged into certain patterns *via* conjugation to specific sites on a DNA origami. By growing these particles bigger, a continuous metallic structure can take shape [107], as demonstrated in Fig. 1.7c. If the growth was controlled to the point that particles are barely touching, a great field enhancement in, *e.g.*, SERS can be achieved within the gap [46]. In **A.II**, a similar method was used to grow AuNPs closer to each other in order to enable electron tunneling. Moreover, partial metallization [112] and multiple metal plating [113] have also been reported by taking advantage of the recognition property of a DNA origami. Last but not least, if one want to transform the whole origami into metallic structure, very small AuNPs can also be electrostatically attached to 3D DNA origami and grow into a continuous nano-object [108], as the gold ring shown in Fig. 1.7d.

Although the shapes of the metallized origami *via* the method mentioned above were still recognizable, they usually suffered from the granular features due to the nucleation growth. Because of the isotropic growth in all directions from the nuclei, in order to ensure a continuous structure, either the seed density or the growth time need to be increased. It could be tricky to apply these structures in plasmonic applications which require very smooth and defined shapes.

1.4.3 Mold casting

Beyond functioning as a scaffold or template for metal nanostructures, DNA origami can also be exploited as a mold to confine the growth of nanoparticles within the cavity inside the origami. As a result the particle will adopt the shape of the mold. In this method, a AuNP seed is attached inside a hollow 3D origami cavity, then the seed is chemically grown by reducing metal ions until it fully fills the chamber and take the shape prescribed by the origami mold. Because the whole nanostructure is

originated from one seed, the end shape does not have the same granular feature as the ones based on multiple seeds.

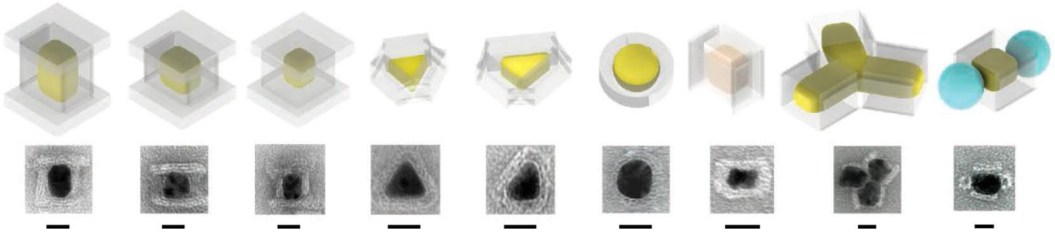

FIGURE 1.8 Metallic nanoparticles fabricated *via* mold-casting method. Scale bars are 20 nm. Adapted with permission from Ref. [114].

Two research groups have independently published their approaches following similar ideas [114, 115]. In these approaches, both gold [115] and silver [114] has been grown into various shapes, *e.g.*, round disc, cuboid and triangle, as shown in Fig. 1.8. Since the origami mold are not covered by metal, they still retain their addressability and recognition properties. Because of this, complex assemblies and further functionalizations can be easily implemented. Therefore, mold-casting has excellent compatibility with both nanoelectronics and plasmonics, owing to the variety of possible devices that can be directly assembled with this method.

1.4.4 DNA nanolithography

The metallization methods based on "wet chemistry" and biological approaches have their advantages. For example, they do not need very sophisticated instruments, and further functionalization or assembly is possible if the DNA constructs are still intact in liquid. However, the conventional surface-based lithography methods have a much better control over the dimensions than these methods, and the compatibility with microfabrication processes (used in industry) can facilitate more applications of DNA nanotechnology. Naturally, the efforts to combine DNA nanotechnology with lithography have been made.

Early activities were concentrated on using dsDNA molecule or DNA constructs directly in the lithography. For example, the spatial information of DNA nanogrid can be directly transfered to a gold film by evaporating gold to a surface with pre-deposited nanogrid [116]. λ-DNA has also been used as a mask in angled metal evaporation [117] to pattern etched lines with $\sim$7 nm linewidth. These pioneer studies explored new ways to utilize DNA constructs for nanofabrication, however, the dimensions and pattern quality were limited by the fact that DNA molecule is a soft material. Although there has been an attempt to use metallized DNA origami to pattern graphene *via* etching [118], the spatial information of chemically metallized nanostructures is degraded after several steps.

One possible improvement is to first transfer DNA patterns to materials like silicon oxide, which are more durable and widely used in microfabrication processes [119–121], and then use the SiO_2 as mask for metal deposition. The pattern can be transferred *via* either etching [120,121] or chemical vapor deposition (CVD) [119]. In most of these reactions, water molecules play an important role. Since DNA structures and the SiO_2 surface have different water affinities, the reaction rates are different, and thus the pattern can be imprinted on the SiO_2 surface. In Chapter 4 and **A.III**-**A.V**, similar SiO_2 mask-based DNA-assisted lithography method for fabrication of high resolution metallic nanostructures will be presented.

Chapter 2

Theory and methods

2.1 Dielectrophoresis

The word *dielectrophoresis* (DEP) was first used by H.A. Pohl in 1958 [122] for describing a translational motion of particles caused by polarization effect in a nonuniform electric field. To distinguish from electrophoresis, which is caused by Coulomb force on charged particles, dielectrophoresis can happen to any polarizable particle even without a net charge. When a particle suspended in medium is exposed to an external electric field, positive and negative charges will be induced on opposite sides of the particle surface. When the external field is uniform like in Fig. 2.1a, the Coulomb force exerted on both sides of the particle will cancel each other out, resulting in a zero net force. However, if the external field is nonuniform as in Fig. 2.1b, a total force (DEP force) will act on the particle and cause the translational motion. The DEP force is parallel to the gradient of the square of the electric field, but the sign of its direction depends on the polarizability of the particle compared to the surrounding medium. In the case when the particle is attracted towards the electric field maximum, it is called positive DEP. Oppositely, when the particle is pushed away from the electric field maximum, it is called negative DEP.

2.1.1 DEP force

Before deriving the DEP force for a polarizable particle, let us first consider an infinitesimal electric dipole in an electric field, as shown in Fig. 2.2. The total force exerted on the dipole $\vec{d}$ can be written as the summation of Coulomb forces on both the positive charge and the negative charge:

$$\vec{F} = q\vec{E}(\vec{r} + \vec{d}) - q\vec{E}(\vec{r}) \tag{2.1}$$

where $\vec{r}$ is the position vector of $-q$. When the dimension of the dipole d is much smaller than the nonuniformity of the electric field, the electric field at the positive

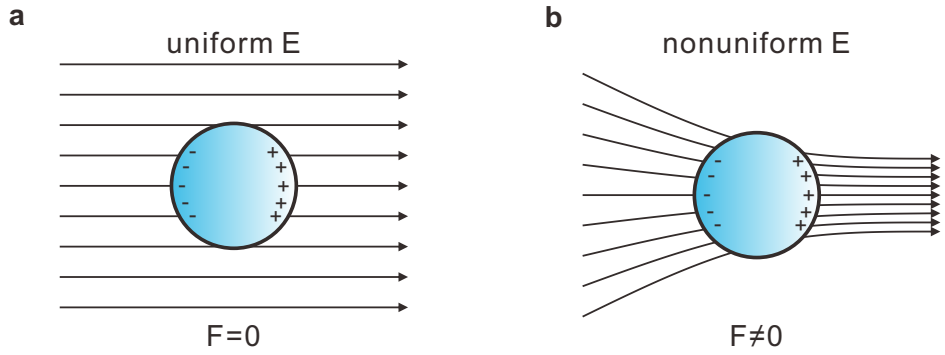

FIGURE 2.1 Schematic illustration of dielectrophoresis. **a**, the total force exerted on a spherical particle in a uniform electric field is zero. **b**, the total force exerted on a spherical particle in a nonuniform electric field has a finite value.

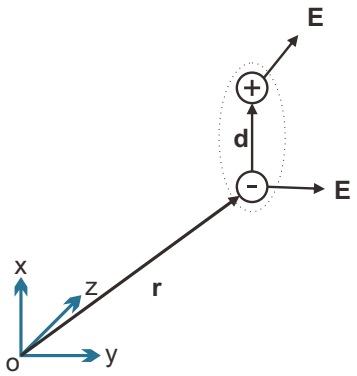

FIGURE 2.2 Dipole in an electric field.

charge can be expanded by vector Taylor series into a form:

$$\vec{E}(\vec{r}+\vec{d}) = \vec{E}(\vec{r}) + \vec{d}\cdot\nabla\vec{E}(\vec{r}) + \cdots \tag{2.2}$$

where all the terms with higher order of $\vec{d}$ have been neglected. By inserting Eq.2.2 back into Eq.2.1, the force on the dipole can be simplified as

$$\vec{F} = q\vec{d}\cdot\nabla\vec{E} + \cdots \tag{2.3}$$

if the dipole moment $\vec{p} \equiv q\vec{d}$ is finite, then the dipole force can be approximated as

$$\vec{F}_{dipole} = (\vec{p}\cdot\nabla)\vec{E}. \tag{2.4}$$

The gradient of electric field here indicates that there will be a force only when the electric field is not uniform. This approximation is quite adequate for the dipole which is smaller than the non-uniformity of the electric field, but when the dimension of the dipole is comparable with the nonuniformity, the higher order terms should not be neglected.

Now, let us consider a homogeneous spherical dielectric particle. Unlike the

electric dipole, whose charges are intrinsic, the surface charges of the dielectric particle are induced by the external electric field, therefore the dipole moment of the particle can be written as a function of electric field,

$$\vec{p} = \alpha \vec{E}. \tag{2.5}$$

where α is the effective polarizability of the particle. By substituting the dipole moment $\vec{p}$ in Eq.2.4 with Eq.2.5, the DEP force exerted on a dielectric particle can be written as,

$$\vec{F}_{\mathrm{DEP}} = \frac{\alpha}{2} \nabla E^2. \tag{2.6}$$

From this rather general form of DEP force, it is obvious to see that the DEP force is proportional to the gradient of the square of the electric field and the polarizability of the particle. The direction of the force is parallel to the gradient, but also depends on the sign of the polarizability.

In order to calculate the dipole moment for a particle of interest, effective dipole method [123] is commonly used. In this approach, the solution of Laplace's equation of the dielectric particle in homogeneous electric field is compared with the potential induced by an infinitesimal dipole to get the effective dipole moment for the particle. For a spherical dielectric particle, its effective dipole moment is [123]

$$\vec{p}_{\mathrm{eff}} = 4\pi\epsilon_m a^3 \frac{\epsilon_p - \epsilon_m}{\epsilon_p + 2\epsilon_m} \vec{E} \tag{2.7}$$

where a is the radius of the particle, ϵ_p and ϵ_m are the permittivities of the particle and the surrounding medium, respectively. The term, $\frac{\epsilon_p - \epsilon_m}{\epsilon_p + 2\epsilon_m}$, is actually the Clausius-Mossotti factor [124] of a spherical dielectric particle. Therefore the effective polarizability is written as

$$\alpha = 4\pi\epsilon_m a^3 K(\epsilon_p, \epsilon_m), \tag{2.8}$$

where K is the Clausius-Mossotti factor. It can be generalized for particle in AC electric field by replacing the permittivity with its complex counterpart, which in a simple Drude model has the form of

$$\epsilon^* = \epsilon - j\frac{\sigma}{\omega}, \tag{2.9}$$

where j is the imaginary unit, σ is conductivity, ω is angular frequency. The polarizability becomes

$$\alpha = 4\pi\epsilon_m a^3 \mathrm{Re}[K(\epsilon_p^*, \epsilon_m^*)], \tag{2.10}$$

where $\mathrm{Re}[K]$ denotes the real part of the Clausius-Mossotti factor. Then we can obtain the most well-known equation for the time-averaged DEP force for a spherical

particle in AC field

$$\left\langle \vec{F}_{\mathrm{DEP}} \right\rangle = 2\pi\epsilon_m a^3 \mathrm{Re}\left[\frac{\epsilon_p^* - \epsilon_m^*}{\epsilon_p^* + 2\epsilon_m^*}\right] \nabla E_{\mathrm{RMS}}^2 \tag{2.11}$$

where $\left\langle \vec{F}_{\mathrm{DEP}} \right\rangle$ is the time-averaged DEP force, and E_{RMS} is the root-mean-square value of the electric field.

From this equation, one can conclude that the DEP force is size-dependent and it favors bigger particles. In AC electric field, the force is also frequency-dependent due to the complex permittivity. The direction of the force remains same for a given frequency, even though the electric field changes direction in an AC electric field. However, the direction can be reversed for the same system, if a different frequency is used. When the K factor is positive, in other words when $\epsilon_p > \epsilon_m$, it results in a positive DEP. In contrast, when $\epsilon_p < \epsilon_m$, the K factor is negative, and thus the DEP is negative.

For a spherical particle, analytical solution like in Eq.2.11 can be derived. However, for objects like dsDNA or DNA origami which may have very different aspect ratio, the spherical model is unsuitable. A more general form of the Clausius-Mossotti factor,

$$K = \frac{1}{3}\frac{\epsilon_p^* - \epsilon_m^*}{\epsilon_m^* + A(\epsilon_p^* - \epsilon_m^*)}, \tag{2.12}$$

can be used for ellipsoidal particles. Here, A is a geometrical factor that varies from zero to one: $A = 1/3$ for a sphere, $A = 1$ for a short rod. For even more complicated geometries and inhomogeneous objects, numerical approximation has to be employed.

2.1.2 DEP trapping

The DEP force derived previously can be used to manipulate particles suspended in medium. Especially, if there exist locations where electric field has its extreme values, the particles may be trapped in such locations. However, the DEP force is not the only force experienced by the particles. In order to trap with DEP, other forces need to be overcome. One of the fundamental phenomena need to be considered is Brownian motion, which is a representation of the randomized thermal force on a particle. The maximum value of this thermal force can be roughly given by [125]

$$F_{\mathrm{thermal}} \approx \frac{k_B T}{\sqrt[3]{V}} \tag{2.13}$$

where k_B is the Boltzmann constant, T is the temperature, and V is the volume of the particle. Clearly, this thermal force is inversely proportional to the size of the particle. Combining with the fact that the DEP force is also size dependent, it makes

DEP trapping of nanoscale particles particularly difficult. The smaller the particle, the higher is the required field gradient to overcome the thermal forces. The DEP force can be increased either by increasing the amplitude of the electric field, or by inducing greater electric field changes in a confined space. Since increase of the electric field may cause it to exceed the breakdown field strength of the medium, electrodes with sharp features made by microfabrication techniques are more often used to trap nanoscale objects.

Besides the Brownian motion, other forces also exist when a high electric field is applied to the liquid medium where the DEP is usually carried out, *e.g.*, a high frequency AC electric field may induce Joule heating in the liquid and thus create fluid flow and electrothermal forces or electro-osmosis at the diffuse double layer on top of the electrodes [126]. These forces may also limit the ability to manipulate the nanoparticle by DEP.

Dielectrophoresis has already been widely used in manipulation, separation and trapping of various micro- and nanometer scale objects. Because the DEP force originates from the gradient of the electric field, and thus no mechanical contact is needed to move the particle. As a result, DEP can be used as a nondestructive way to manipulate and separate sensitive biological particles, *e.g.* cells [127, 128], proteins [124], virus particles [129] and DNA molecules [130]. By carefully tuning the trapping parameters, clusters or even an individual nanometer object can be isolated from the media and make contact with the electrodes used for DEP. This enables the electrical characterization and application of various bottom-up synthesized or self-assembled nanostructures, *e.g.* carbon nanotubes [131, 132], quantum dots [133] and DNA self-assembled structures [73, 74, 134] (also **A.I**, **A.II** and **B.I**).

In Chapter 3, based on previous work of trapping and characterization of 2D DNA origami [73] and TX-tiles [74], and as a natural continuation, experiments for trapping and measuring various 3D DNA origami (article **A.I**) and a TX-tile-based SET-like assembly (article **A.II**) will be presented.

2.2 Basics of LSPR

The concept of plasmon is used to describe the collective oscillation of conduction electrons in metal or semiconductor. It can be considered as a quasi-particle, which quantize the classical plasma oscillation. Therefore, most of its properties can be understood by Maxwell's theory. Surface plasmon (SP) can be excited by light or electrons at the interface between materials with negative real permittivity (usually metal) and positive permittivity (dielectric). As a hybrid mode of electron density oscillation and the electromagnetic field associated with it, SPs can propagate along the interface, and its intensity decays exponentially in the direction perpendicular to the interface.

When surface plasmon is confined in a metallic nanoparticle whose size is

comparable or smaller than the wavelength of the light used to excite the plasmon, it is called a localized surface plasmon (LSP). The LSP can induce two important phenomena: the electromagnetic field near the surface of the nanoparticle can be greatly enhanced; and the optical absorption and scattering has a resonance at the plasmon resonant frequency, *i.e.*, at localized surface plasmon resonance (LSPR). The field enhancement effect can be used in amplification of electric field in many detection methods, *e.g.*, surface enhanced Raman spectroscopy (SERS) and fluorescence enhancement (FE). LSPR is very sensitive to the dielectric constant of surrounding materials, and thus can be used in sensing applications.

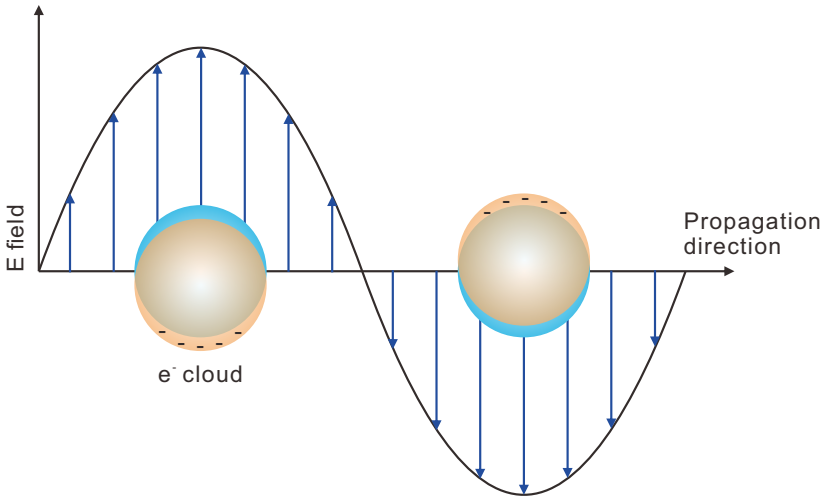

FIGURE 2.3 Schematic of a localized surface plasmon resonance (LSPR) where the free conduction electrons in the metal nanoparticle are oscillating due to the external electromagnetic wave.

2.2.1 Quasi-static approximation

As previously mentioned, the properties of plasmon can be interpreted by classical Maxwell's equations. A simple starting point to understand the LSP is the so-called quasi-static approximation, in which the behavior of a homogeneous sphere in electrostatic field is studied by Maxwell's equations and boundary conditions. For the nanoparticles much smaller than the wavelength of the electromagnetic field, the electrostatic approximation is valid. Actually, this physical scenario is almost the same as in derivation of the DEP force in the last section. By considering the sphere as an effective dipole, its polarizability is

$$\alpha = 4\pi a^3 \frac{\epsilon_p - \epsilon_m}{\epsilon_p + 2\epsilon_m}, \tag{2.14}$$

where ϵ_p and ϵ_m are the complex dielectric function of the particle and media around it, respectively, and a is the radius of sphere. Apparently, the polarizability experi-

ences a resonant enhancement when $|\epsilon_p + 2\epsilon_m|$ is at its minimum, which in the case of small $\mathrm{Im}[\epsilon_p]$, can be simplified as

$$\mathrm{Re}[\epsilon_p(\omega)] = -2\epsilon_m. \tag{2.15}$$

This is the so-called Fröhlich condition. With the definition of $\vec{p} = \epsilon_0\epsilon_m\alpha\vec{E}_0$, the electric field inside and outside the sphere can be written as

$$\vec{E}_{\mathrm{in}} = \frac{3\epsilon_m}{\epsilon_p + 2\epsilon_m}\vec{E}_0, \tag{2.16}$$

$$\vec{E}_{\mathrm{out}} = \vec{E}_0 + \frac{3\vec{n}(\vec{n}\cdot\vec{p}) - \vec{p}}{4\pi\epsilon_0\epsilon_m}\frac{1}{r^3}, \tag{2.17}$$

where $\vec{n}$ is a normal vector. From this approximation, it is obvious that both the electric field inside the particle and outside the particle experience a resonance due to the polarizability. The electric field enhancement due to the LSPR is one of the most important properties for sensing applications.

Next, let us consider the electrodynamic properties of the sphere. For small sphere with $a \ll \lambda$, when it is illuminated by a plane electromagnetic wave

$$\vec{E}(\vec{r}, t) = \vec{E}_0 e^{-i\omega t}, \tag{2.18}$$

the dipole moment will oscillate following the field

$$\vec{p}(t) = \epsilon_0\epsilon_m\alpha\vec{E}_0 e^{-i\omega t}, \tag{2.19}$$

where the polarizability α from the quasi-static approximation is valid for a vanishingly small particle. The radiation of the oscillating dipole moment will scatter the incident electromagnetic wave. In classical electrodynamics, the electromagnetic field of an oscillating dipole can be written as [135]

$$\vec{H} = \frac{ck^2}{4\pi}(\vec{n}\times\vec{p})\frac{e^{ikr}}{r}\left(1 - \frac{1}{ikr}\right), \tag{2.20}$$

$$\vec{E} = \frac{1}{4\pi\epsilon_0\epsilon_m}\left\{k^2(\vec{n}\times\vec{p})\times\vec{n}\frac{e^{ikr}}{r} + [3\vec{n}(\vec{n}\cdot\vec{p}) - \vec{p}]\left(\frac{1}{r^3} - \frac{ik}{r^2}e^{ikr}\right)\right\}, \tag{2.21}$$

where $k = 2\pi/\lambda$ and $\vec{n}$ is the normal vector as in Eq.2.17. The scattering cross section and absorption cross section can be evaluated from Poynting vector calculated from Eq.2.20 [136]

$$C_{\mathrm{sca}} = \frac{k^4}{6\pi}|\alpha|^2 = \frac{8\pi}{3}k^4a^6\left|\frac{\epsilon_p - \epsilon_m}{\epsilon_p + 2\epsilon_m}\right|^2, \tag{2.22}$$

$$C_{\mathrm{abs}} = k\mathrm{Im}[\alpha] = 4\pi ka^3\mathrm{Im}\left[\frac{\epsilon_p - \epsilon_m}{\epsilon_p + 2\epsilon_m}\right], \tag{2.23}$$

where a is the radius of the sphere particle.

According to the equations above, both the scattering and absorption have also resonance when the Fröhlich condition is met. It can also be noticed that the scattering cross section scales with a^6 while the absorption cross section scales only with a^3, which means for $a \ll \lambda$, the absorption dominates. But when the particle becomes bigger, the scattering increases much faster and can surpass the absorption.

The quasi-static approximation is a very simplified derivation of LSPR related properties, and it has limited valid work regime. However, it can can give a general qualitative idea about the field enhancement effect and the cross section dependence on size and permittivity. A more rigorous and widely accepted theory about the scattering and absorption of metallic nanoparticles was given by Mie in 1908. This theory is also valid for particles whose sizes are comparable with the wavelength of the excitation electromagnetic field.

2.2.2 Mie theory

In Mie theory, the internal and scattered fields were expanded into a set of normal modes described by vector harmonics. The derivation is rather lengthy and has been treated in many different sources including Ref. [136], so only the most important conclusions will be listed here. The scattering and extinction cross sections are given as

$$C_{\text{sca}} = \frac{2\pi}{k^2}\sum_{n=1}^{\infty}(2n+1)(|a_n|^2 + |b_n|^2), \tag{2.24}$$

$$C_{\text{ext}} = \frac{2\pi}{k^2}\sum_{n=1}^{\infty}(2n+1)\text{Re}[a_n + b_n]. \tag{2.25}$$

where a_n and b_n are scattering coefficients. When the permeabilities of the particle and the media are the same, they are defined as

$$a_n = \frac{m^2 j_n(mx)[xj_n(x)]' - j_n(x)[mxj_n(mx)]'}{m^2 j_n(mx)[xh_n(x)]' - h_n(x)[mxj_n(mx)]'} \tag{2.26}$$

$$b_n = \frac{j_n(mx)[xj_n(x)]' - j_n(x)[mxj_n(mx)]'}{j_n(mx)[xh_n(x)]' - h_n(x)[mxj_n(mx)]'} \tag{2.27}$$

j_n and h_n are spherical Bessel functions and first order spherical Hankel functions, respectively. x and m are size parameter and relative refractive index, respectively, which are defined as:

$$x = ka = \frac{2\pi na}{\lambda}, m = \frac{k_1}{k} = \frac{n_1}{n}. \tag{2.28}$$

where n and n_1 are the refractive index of the media and particle respectively.

In the quasi-static approximation, only the magnitudes of scattering and absorption cross section have a dependency on particle size. However, in practice, the

spectral position of the resonance peak also depends on the particle size as clearly visible from Eqs. 2.27 and 2.28 . This shift of the resonance peak can be calculated by Mie theory, and it can be understood as that the restoring force in the particle becomes smaller when the distance between the opposite charges becomes larger due to the increased particle size. This lowering of restoring force causes a lower resonant frequency and thus makes the spectrum red-shift.

Both the quasi-static approximation and Mie theory are formulated based on the simplest geometry, a sphere, or in some cases they can be extended to ellipsoids. For more complicated geometries, it is very difficult to arrive in any analytical solution, therefore, numerical simulation methods are usually employed, *e.g.*, Finite-Element Methods (FEM) or Finite-Difference Time-Domain method (FDTD). In Chapter 5 and **A.IV**, the LSPR of metallic nanostructures fabricated by DNA origami template will be measured by dark-field microscopy and compared with simulation results by FEM.

2.3 Microfabrication processes

Various microfabrication techniques were used in the works included in this thesis. For the DEP related studies, nanoelectrodes were fabricated with an electron-beam lithography (EBL), reactive ion etching (RIE) and physical vapor deposition (PVD). In DNA-assisted lithography, chemical vapor deposition (CVD), RIE and PVD were heavily used, because the main goal of the research was to integrate the DNA origami into microfabrication process. Therefore, it is beneficial to briefly introduce the basics of these techniques.

2.3.1 Electron-beam lithography (EBL)

Electron-beam lithography (EBL) is widely used in research and industry for patterning structures on microchips with micrometer to nanometer resolution. It is a maskless lithography method, in which pattern can be directly drawn by electron beam in a raster scanning fashion without the need of a physical mask.

EBL systems are usually combined with scanning electron microscope (SEM) since they share the same electron source and lens systems. The electrons emitted from the source travel through several electromagnetic condenser and objective lenses and then can be focused on the sample surface. To enable the scanning, an electrostatic or magnetic deflector is implemented before the objective lens. The high energy electrons can interact with the sample surface, the secondary electrons caused by the interaction are detected for imaging purpose.

For lithography, electron beam sensitive polymers, so-called resists, are deposited on the sample surface. Depending on the resist choice, the polymers at the

area exposed to e-beam can either be broken into shorter chains (scission) or cross-linked into stronger networks (crosslinking). The shorter chains (positive resist) or the cross-linked networks (negative resist) can be distinguished from the unexposed area *via* different solubility in specific solvent (developer). The process in which the unwanted polymers are dissolved is called development. After the development, the pattern written by e-beam is revealed, and materials can be deposited by PVD or CVD into the formed pattern, or the exposed thin film under the resist can be etched.

The resolution of EBL is limited by both the e-beam instrument and the resist. The energy of the e-beam, the focusing capability of the system and the sensitivity of the resist can all affect the resolution. In practice, the smallest feature that can be patterned by EBL is around 20 nm. In addition, EBL shares the low speed as other raster-based method. Drawing a pattern with square millimeter areas can easily take hours.

2.3.2 Physical Vapor Deposition (PVD)

Physical vapor deposition (PVD) is a category of deposition methods, in which the material is first detached from a target in condensed phase, then travel through vacuum in gas phase, and finally condensed on the substrate again. Usually, there is no chemical reaction happening in the process, hence the name. The most commonly used PVD methods are sputtering and evaporation. In this thesis, only the evaporation is used, therefore the introduction is limited to this subject.

To start the evaporation, the temperature of the target is increased by either resistive heating or electron-beam heating. Usually, the evaporation chamber is in a high vacuum (HV 10^{-3} - 10^{-7} mbar) or ultra high vacuum (UHV, $< 10^{-7}$ mbar) and thus the mean free path of the evaporated atoms/molecules is much longer than the distance between the target and the substrate. As a result, most of the particles arrive from the target to the substrate ballistically. The high temperature difference between the target and the substrate also makes the arrived particles stick on the position immediately without much surface diffusion. The ballistic transportation results in a line-in-sight coverage of the deposited thin film, which means that the material evaporated through a mask will take almost the same shape of the mask. By taking the advantage of the line-in-sight coverage, angled evaporation can produce shadows, where the evaporated material is absent. In **A.I**, a series of titanium resistors were fabricated *via* blocking certain part of the pattern from gold deposition by angled evaporation.

The evaporation rate can be monitored by quartz crystal microbalance (QCM). The resonant frequency of a single quartz crystal is very sensitive to its mass. By electrically measuring the resonant frequency changes, the deposition rate can be determined almost with a precision of a single atomic layer. Therefore the thickness

of the thin film deposited by evaporation can be controlled with sub-nanometer accuracy.

2.3.3 Chemical Vapor Deposition (CVD)

Chemical vapor deposition (CVD) refers to the formation of a thin film on a substrate from a reaction of one or more volatile precursors. CVD is very versatile and compatible with elements and compounds in different forms, *e.g.*, monocrystalline, polycrystalline, and amorphous. The crystalline structure of the deposited film can be affected by the type and parameters of the reaction.

In CVD reactions, the precursors are commonly in gas phase. But unlike the PVD methods, the transportation of precursors to the surface of the substrate largely depends on diffusion. In addition, the removal of the by-product from the reaction also rely on diffusion. In many cases, higher energy are required for the reaction to happen, this is usually provided by increasing the chamber temperature. As a result, the deposition rate of the CVD processes can be either transport limited or reaction limited.

There are three major CVD methods which are commonly used in microfabrication industry, namely, atmospheric pressure CVD (APCVD), low-pressure CVD (LPCVD) and plasma-enhanced CVD (PECVD). The main difference between an APCVD and an LPCVD is the pressure, hence the diffusion rate, in the reaction chamber. The pressure in LPCVD is about 1 mbar, which increases the diffusion by factor 10^3 over APCVD. Therefore the wafers in LPCVD chamber can be packed much more densely, but LPCVD is more temperature sensitive because the process is reaction limited. On the other hand, APCVD has higher deposition rate but is usually transport limited and not as sensitive to temperature as LPCVD. In addition, the step coverage of APCVD is usually poor due to the diffusion limit. In **A.III** and **A.IV**, APCVD was used to selectively grow SiO_2 mask with holes of DNA origami shape.

In PECVD, radio frequency (RF) electric field is used to ionize the precursors to form plasma (RF-plasma) and thus facilitate the reaction. Ion bombardment is also provided by the plasma, which provides the energy necessary to form a stable end product. Therefore, much lower temperature can be used. Normally, PECVD is a reaction limited process. In **A.IV**, PECVD was used to deposit amorphous Si sacrificial layer on Si_3N_4 or Al_2O_3 substrate.

2.3.4 Reactive Ion Etching (RIE)

The RF-plasma can also be used to ionize volatile gas molecules to ease the etching of solid substrate, which is called reactive ion etching (RIE). In RIE, both the ionized and excited molecule species are formed in a vacuum chamber by RF-plasma. These molecules are very reactive, and thus can chemically etch the substrate in a selective

way. Thanks to the enhancement of plasma, the etching can be performed at room temperature or even low temperature.

Because of the ionization and acceleration due to the RF-plasma, ion bombardment can also happen in the vacuum chamber. The ion bombardment can be increased by increasing the RF-power, lowering the pressure, increasing stabilization gas (Ar, N_2, *etc.*) or biasing the substrate. By tuning the power of ion bombardment, the etching process can vary between chemical etching and sputter etching. When there is less ion bombardment, chemical etching is dominant. The etching profile tend to be isotropic and highly selective. However, when the ion bombardment increases, the sputtering of the substrate become significant, the physical etching tend to be more anisotropic but unselective.

In **A.III** and **A.IV**, as well as in Chapter 4, RIE was used to etch thin SiO_2 and Si layers after APCVD. An isotropic Si etching process is used to achieve high selectivity.

Chapter 3

Dielectrophoresis of DNA-based objects

One of the most promising fields where DNA nanotechnology can be applied is nanoelectronics or molecular electronics. Driven by the never-ending demand of smaller and cheaper integrated circuit (IC), microfabrication techniques have been constantly pushing the limit of miniaturization and at the same time lowering the costs. However, the development of the top-down silicon-based fabrication has already shown a sign of deceleration. Various alternative techniques are being pursued including bottom-up self-assembled approaches. DNA nanostructures are excellent candidates due to their accessibility and molecular addressability. Despite the promises DNA nanotechnology provides, multiple challenges are also present. One of them, specific to DNA nanostructures, is that their electrical properties are not well understood. No matter whether they would be used as functional components or as templates (nano-breadboards), systematic characterization is needed for reliable device fabrication. The other challenge which is common for all self-assembled approaches is how to integrate the spontaneously formed individual nano-objects (usually in solution) into the ICs for macroscopic access.

Dielectrophoresis (DEP) has been widely used as a tool to manipulate nano- or micro-objects, and its basic principles have already been introduced in Section 2.1. Our group previously succeeded in trapping and characterizing dsDNA, single-layered DNA origami and TX-tile by lithographically fabricated nanoelectrodes. In this chapter, the efforts will be expanded to multi-layered DNA origami (**A.I**) as well as to conjugates of TX-tile and gold nanoparticle (**A.II**). DEP is a rather straightforward method, therefore the nanoelectrode sample fabrication and characterization setup were more or less the same for these works. To avoid repetition, the common experimental setup for the articles **A.I** and **A.II** will be introduced in Section 3.1 in advance. The variance related to specific projects and the experimental results will be described in Section 3.2 and Section 3.3, respectively.

3.1 Experimental setup

3.1.1 Dielectrophoretic trapping

The setup of DEP trapping can be divided into two parts: (1) a microchip with lithographically fabricated nanoelectrodes and contact pads which can be accessed by external macroscopic probes, (2) a sample stage with metal wire probes which is connected to a function generator.

Nanoelectrode fabrication

The nanoelectrodes were fabricated on a *p*-doped Si chip with a thermally grown SiO_2 layer of thickness $\sim$300 nm on top. The Si wafer was first cut with diamond cutter into desired-size chips ranging from 3 mm$\times$7 mm to 8 mm$\times$8 mm. Then the chips were cleaned with hot acetone and isopropanol (IPA) and dried by N_2 gas flow. A 100-nm layer of poly(methyl methacrylate) (PMMA) resist was spin-coated on the chip and baked for 5 mins at 160°C to evaporate the solvent. After the resist was ready, the chip was exposed by a Raith e-line e-beam lithography system. The exposed sample was then developed in MIBK[1]:IPA (1:3 v/v) solution for 30 sec and the development was stopped by rinsing the chip with pure IPA. Prior to metal PVD, the developed sample was treated with a gentle and short O_2 plasma process to remove the possible PMMA residue at the bottom of the open pattern in order to make sure the finest lines in the pattern are properly connected. The PVD was carried out in a homemade ultra-high vacuum ($\sim 10^{-8}$ mbar) chamber with e-beam evaporation. A 2-nm layer of titanium was deposited before the 18-nm gold layer to improve the adhesion of gold. Finally, the PMMA layer and metal on top of it were removed in hot acetone solution. Bear in mind that the sample was treated with O_2 plasma again before it was used for trapping, to make the surface hydrophilic and so that the DNA nanostructures will not be confused with PMMA residues on the sample surface while they were imaged by AFM.

The pattern drawn to the sample by e-beam lithography usually consists of 3 layers[2]: (1) a finest layer with single pixel lines for the nanoelectrodes, (2) a coarse layer containing the millimeter pads and (3) an intermediate layer that connects the previous two parts. The most important parts are single pixel lines which define both the gap size and the line width of the nanoelectrodes. Before exposing this layer, the focus of the electron beam has to be adjusted carefully until a roughly 20-nm spot size can be achieved. Because of the single pixel line, the electrode width will be a bit wider than 20 nm taking the proximity effect into consideration. The gap size can be adjusted in the pattern design for different projects. To make sure

[1]Methyl isobutyl ketone

[2]The layer here is merely a way for the software to organize the design, there is no physical layer separation after sequentially exposing the layers in design to the resist.

the DNA-based nano-objects can contact both of the electrodes, the gap size were usually set to the same or shorter than the length of the nano-object. The layer with pads has very little accuracy requirement, so it can be drawn using high current and large aperture settings in a shorter time. The distance between the two pads was fixed to 2 mm to match the distance between the probes on the sample stage.

Trapping setup

The DEP was performed in a humid chamber to keep the sample from drying out during the trapping. The aforementioned microchip was positioned on a sample stage inside the humid chamber, while the pads on the chip were connected with the metallic probes by mechanical pressing. Before the trapping started, 5-10 μl of DNA solution was dropped on the microchip by a micropipette, covering the gap region. The buffer, in which the DNA self-assemblies were suspended, need to be changed to a low conductivity one (6 mM HEPES, 2 mM NaOH, and 3 mM MgAc, conductivity 275 μScm^{-1}) by spin-filtering in advance. The DEP was initiated by applying AC voltage from an Agilent 33220A function generator in sinusoidal waveform. For DNA origami, frequencies ranged from 8 MHz to 13 MHz and the voltage from 0.6 to 1.5 V_{pp} (peak-to-peak value). The DEP usually lasted for 1-5 min. After the trapping, the microchip was detached from the stage and gently washed by deionized water and blown dry by N_2 gas. The trapping results were confirmed by AFM afterwards.

3.1.2 Electrical measurement

Both articles **A.I** and **A.II** involve DC I-V characterization. However, in **A.I** the DC measurements were performed in different relative humidity (RH) conditions at room temperature while in **A.II** the measurements were performed at different temperatures in dry condition. In article **A.I**, AC Impedance Spectroscopy (AC-IS) was used to study the contributions of various components to the charge transfer.

All the electrical measurement instruments except the control computer were situated in an electromagnetically shielded (EMS) room which has its own grounding separated from the electrical power system of the building. The signals were transferred into and out from the EMS room either through an optical cable or a powerful low-pass filter. Only the microchips with an individual DNA nanostructure bridging the lithographically fabricated nanoelectrodes after the DEP trapping were chosen for measurement, and the microchip was connected with measurement system *via* the same sample stage as used in trapping.

DC characterization

In the case of DC I-V characterization, a setup as depicted in Fig. 3.1a was used. The I-V curve was obtained by sweeping the voltage generated by a computer con-

trolled digital-to-analog converter (DAC) which was powered by two lead-acid batteries. The voltage and current measured from the sample were first amplified by voltage pre-amplifier (DL-Instruments Model 1211) and current pre-amplifier (DL-Instruments Model 1201), respectively, then collected by a Data acquisition (DAQ) card (National Instruments PXI-6251), and finally outputted to a computer with homemade LabVIEW software for analyzing.

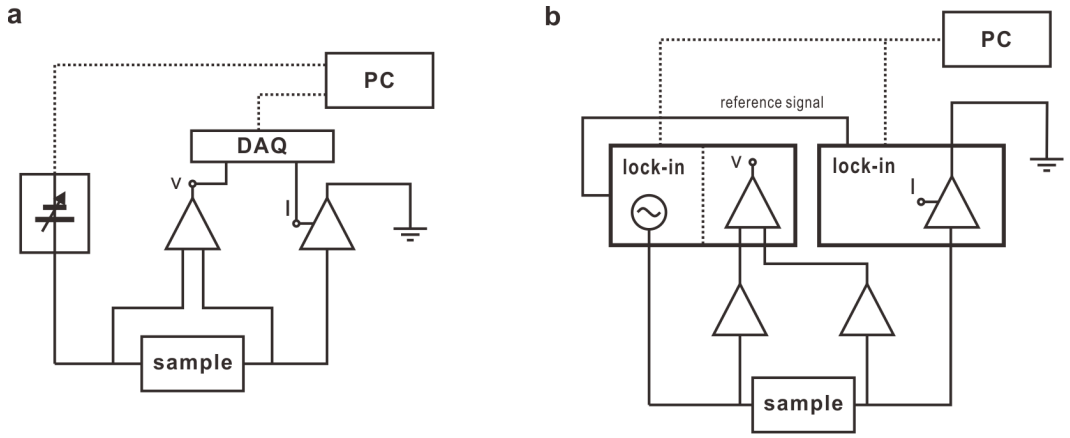

FIGURE 3.1 Electrical measurement setups: **a**, DC I-V characterization setup. **b**, AC-IS setup.

AC-IS

For AC-IS, the frequency dependence of complex impedance of the sample was investigated. The complex impedance can be written in a generalized form of Ohm's law:

$$Z(j\omega) = V(j\omega)/I(j\omega) \tag{3.1}$$

where j is the imaginary unit, ω is the angular frequency, Z is the complex impedance, V is the complex voltage and I is the complex current. To obtain the complex voltage and current, two lock-in amplifier (Stanford Research Instruments SR830) controlled with general-purpose interface bus (GPIB) were used. The circuit diagram of AC-IS setup is demonstrated in Fig. 3.1b. Excitation voltage of 50 $\mathrm{mV_{RMS}}$ with a frequency of 0.01 Hz to 100 kHz was generated by the lock-in amplifier used for voltage measurement and was fed to the sample. Its reference signal was connected to the lock-in amplifier that was also used to measure the current. Therefore, the voltage and current response can be compared against the same reference signal to determine both the amplitude and phase at the same frequency. Additional voltage pre-amplifiers (HMS Electronics, Model 568) were used between the sample and lock-in amplifier. The input impedances of these pre-amplifers were much higher than the sample to avoid excessive current division. For every measured frequency, a software-based feedback system was used to adjust the voltage at the sample always to 50 $\mathrm{mV_{RMS}}$

before the measurement started. By dividing the readings from both lock-in amplifiers as Eq. 3.1, the complex impedance of the sample as a function of frequency can be obtained.

3.2 3D DNA origami DEP and conductivity

The motivation for doing 3D DNA origami DEP trapping was two-fold. Firstly, the questions whether the 3D DNA origami can be manipulated by DEP and how they behave under the high electric field gradient can provide valuable information for the applications of the multilayer DNA origami structures. Second, based on the results and implications from 2D origami [73] and TX-tile structure measurements [74], the capability to adsorb water molecules has a significant effect on the conductivity of DNA nanostructures at high relative humidity (RH) conditions. The 3D DNA structures, which is more densely packed than the 2D and TX-tile structures, should contain more water molecules. In addition, the inner helices are able to remain intact even in dry conditions. Therefore the 3D DNA structure should show better conductivity than the 2D and TX-tile ones.

3.2.1 DEP trapping

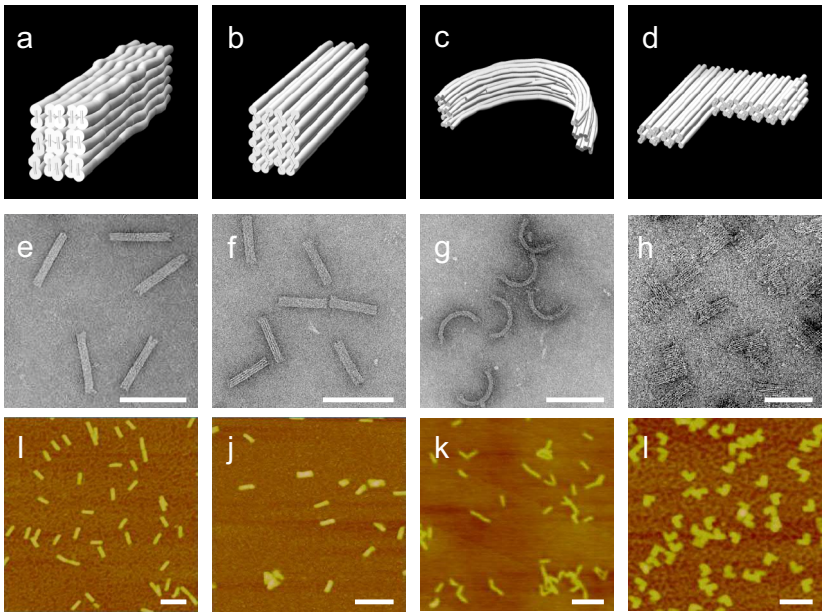

FIGURE 3.2 The four multi-layered DNA origami trapped by DEP. **a**-**d**, computer simulated models of 30-helix brick, 32-helix brick, "C"-shape and "L"-shape. **e**-**h** and **i**-**l** TEM and AFM images of the DNA origami, respectively.

Four structurally distinct multi-layered DNA origami structures with different traits were used in this experiment. A 30-helix bundle brick in square lattice (SQL),

a 32-helix bundle in honeycomb lattice (HCL), a curved "C" shape in HCL and an angular "L" shape in HCL. Their designs and how they look like in TEM and AFM are shown in Fig. 3.2. The SQL brick and the HCL brick had almost the same size and shape, but the packing density and internal stress of the SQL one is higher than the other. The curvature of "C"-shaped piece was induced by base skipping in the origami design, while the "L"-shaped origami had a unique attribute that the two perpendicular arms were not connected by any continuous helices of dsDNA from end to end.

Besides the nanoelectrode fabrication protocol described in the Section 3.1, a special design with built-in Ti resistors were used for some of the origami samples in order to protect the electrodes and/or DNA structures from overheating due to possible high current. In such a design, instead of straight electrodes, several meanders were designed near the gap. After the exposure and development, 10 nm of titanium was evaporated to the chip perpendicularly, then 10 nm of gold was deposited with a $\pm 70^\circ$ angle in the direction of the gap from each side. The part of the electrode which was perpendicular to the gap direction will not get gold deposited due to the shadowing effect, leaving several Ti resistors in series with total resistance of $\sim 70\ \mathrm{k}\Omega$.

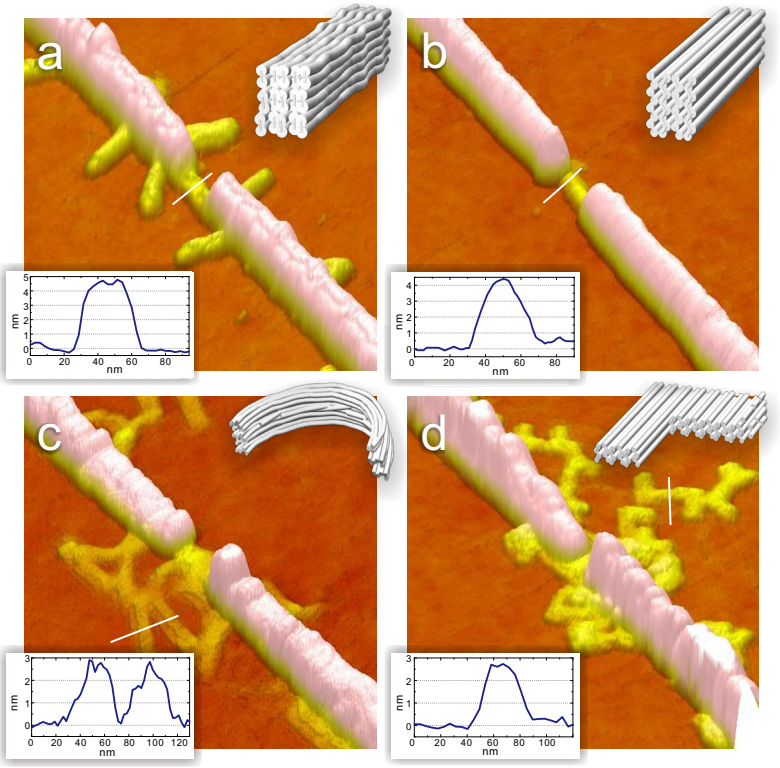

FIGURE 3.3 AFM images of the trapped 3D DNA origamis. **a**, 30-helix brick. **b**, 32-helix brick. **c**,"C"-shape. **d**, "L"-shape. The insets are the height profiles along the white line in the AFM images.

All four types of multi-layered DNA origami shown in Fig. 3.2 were successfully trapped and immobilized by DEP. Some of the selected results are demonstrated in Fig. 3.3. Individual brick-like structures, no matter whether constructed in SQL or HCL, could be trapped and aligned along the electrodes precisely across the gap as shown in Fig. 3.3a,b. Compared with the SQL brick structure, which maintained its shape after trapping, the structures in HCL were mostly flattened and deformed on the substrate. The "C"- and "L"- shaped origami could be trapped individually, but their shapes can hardly be distinguished between the gap. Especially, the curvature of "C" was very unstable under the effect of electric field and the interaction with the substrate.

Based on the experiments, the parameters for trapping single structures or small bundles were obtained. While the DEP frequency was set to 12.5 MHz, a voltage from 0.8-1.5 V_{pp}, a trapping time from 3 to 5 min and a 20 to 50 times dilution of the origami solution after buffer exchange were optimal for the origami used. The yields for successfully trapping varied from 40% to 63% for different designs, and were calculated based on a total 121 samples. Specific parameters for different origami can be found in article **A.I** Table 1. The yields can be easily increased to higher value by increasing the origami concentration in the trapping solution, but the probability of trapping individual structure will be significantly dropped.

3.2.2 Conductivity characterization

Similarly to previous works in Refs. [73] and [74], the conductivity of several single brick-like structures trapped by DEP were measured at room temperature and 90% RH conditions. The sample on a stage was placed in a small chamber with high humidity air flowing through all the time in order to keep the RH constant as well as prevent condensation. The measurement setup in Fig. 3.1a was used for DC I-V characterization.

For comparison purposes, control samples were prepared in the same way as the samples with DNA origami trapped except with only trapping buffer without DNA origami in the solution. At dry condition (room RH), the resistances of the samples and controls were all very high (over tens of TΩs) which was the same as reported in Ref. [73] and [74]. But at 90% RH, the measured resistances for 3D brick samples were ranged from 30 GΩ to over 200 GΩ, which was much higher than in Ref. [73] and [74], and indicates an insulating behavior of a plain multilayer DNA origami. Some of the I-V characterizations are shown in Fig. 3.4a.

Furthermore, AC complex impedance of a brick-like DNA origami in SQL is shown in Fig. 3.4b by a Cole-Cole plot. Within the whole frequency range, both the real and imaginary components of impedance were much higher than the ones reported for 2D origami [73] or TX-tile structures [74], and the Cole-Cole plot resembled the ones of control samples. The AC-IS measurement results also indicated an insulating behavior for the multilayered DNA origami.

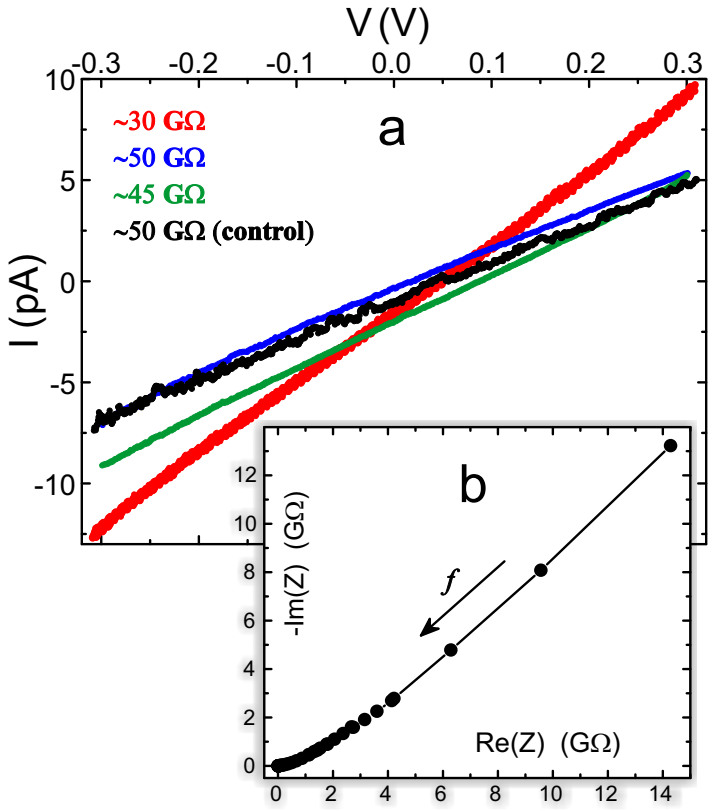

FIGURE 3.4 **a**, IV characteristics of several trapped 30-helix brick origami and a control sample without origami. **b**, a typical AC-IS plot of the 30-helix brick sample, the frequency decreases along the arrow line.

3.2.3 Nanocanyon formation

Because of the disagreement between the conductivity of 3D DNA origami and the 2D structures measured previously, insufficient contacts were suspected. To enhance the contact between the DNA origami structure with the gold electrodes similarly as what had been conducted in previous 2D origami measurements [73], 18 thiolated staples were incorporated into the SQL brick at each ends. Unexpectedly, in the first attempts to trap the thiolated origamis, multiple simple straight nanoelectrodes were completely destroyed after the trappings. A few of the intact samples with origami trapped were measured electrically, but yielded the similar results as the unmodified structures.

The sudden destruction of the electrodes could be due to a high shortcut current after trapping of a conducting origami. To lower the current, the meandered Ti resistor was involved as mentioned in the last subsection (also as shown in Fig. 3.5a). Interestingly, instead of complete destruction of the electrodes, nanocanyons were formed exactly between the electrodes in the gap region after DEP. An AFM image of a typical nanocanyon is shown in Fig. 3.5b. Some hypotheses have been described in article **A.I**. But the exact mechanism of this nanocanyon formation was unclear.

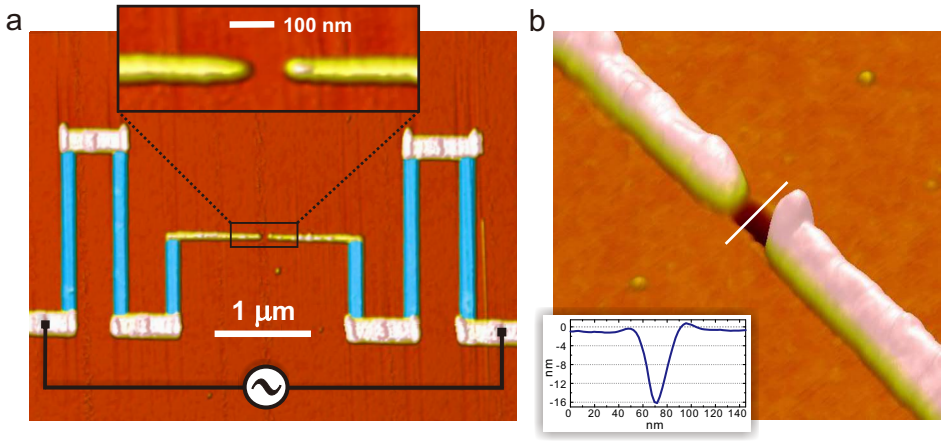

FIGURE 3.5 **a**, an AFM image of a typical nanoelectrode sample with meandered Ti resistors (blue). **b**, the AFM image of a nanocanyon formed after DEP, inset is the height profile along the white line in the AFM image.

To fully understand it, larger sample number and more comprehensive experiments would be needed.

3.3 DNA Single Electron Transistor (SET)

In order to use DNA self-assembled nanostructures in nanoelectronics, they have to be modified due to their insulating behavior at dry condition confirmed by Section 3.2 and Ref. [73,74]. One of the most extensively studied approaches to incorporate electrical or optical active components to DNA structures is to functionalize chemically synthesized metallic nanoparticles by DNA strands modified with various chemical groups, *e.g.*, thiol and biotin. Many such conjugates were fabricated and characterized (see Chapter 1) but they were mostly intended to plasmonic applications [32]. Among all the possible self-assembled electronic nano-devices, a single electron transistor (SET) [137] is one of the most studied and demanded. It can be employed, *e.g.*, as an extremely sensitive electrometer [138], single electron pump for quantum current standard [139], or Coulomb blockade (CB) thermometer [140]. Recently, a SET-like structure has been fabricated by DNA origami, gold nanoparticle and nanorod conjugate [34], but no electrical characterization has been performed. In addition, although the gap size between the metal particles within such structures are under 10 nm, it is still too big for tunneling of electrons.

In article **A.II**, our approach to fabricate a SET by DNA self-assembly and gold nanoparticle conjugation, as well as electrical characterization has been demonstrated. In this work, an individual self-assembled SET component was trapped and connected to prefabricated nanoelectrodes by DEP, and thus enabled the electrical measurement. A first-generation DNA self-assembled structure, namely TX-tile, was used due to its simplicity and continuity of the previous work [74]. Com-

bined with a few chemical gold growth steps after the conjugate was trapped, a clear Coulomb blockade was observed from 4.2 K up to room temperature.

3.3.1 BAB-AuNP assembly

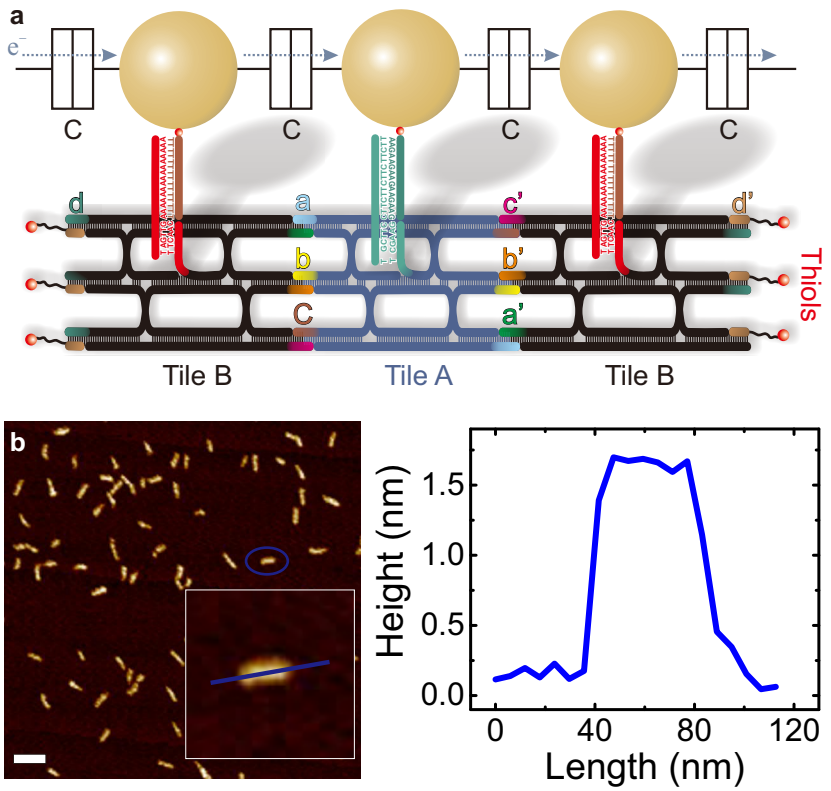

FIGURE 3.6 **a**, schematic illustration of BAB complex with gold nanoparticle conjugated by complementary DNA strand. The figure is not in scale. **b**, AFM image of BAB complexes deposited on a mica surface. The inset shows the circled single BAB complex, from which the height cross-section on the right is taken along the blue line. The scale bar is 100 nm.

Unlike earlier designs of TX-tile, which were usually assembled into a lattice structure with undefined size, the design we employed forms a complex with defined size of 55 nm. In order to do so, two TX-tiles (A and B) were designed to assemble into a BAB complex in a palindromic fashion as shown in Fig. 3.6a. Three thiol-linkers were incorporated at one end of tile B, so they will point outwards after a BAB complex were formed and anchor it to the nanoelectrodes after DEP. On each tile, one of the ssDNA in the middle was extended to hybridize with a AuNP functionalized with its complementary strand. These AuNPs have a size distribution around 10 to 15 nm according to the UV-vis absorption. The BAB-AuNP assembly was conjugated by mixing AuNP solution with the BAB solution and annealed from 45°C to 21 °C with a ramping rate of 0.025 °C/s. The annealing resulted in a reasonable yield (19-45%) of BAB-AuNP assemblies with three nanoparticles

(trimers). Unfortunately, only a fraction of the trimers were linear, but mostly they were bent (Fig. 3 in **A.II**), which could be caused by the steric or Coulomb repulsion between the particles.

3.3.2 DEP and chemical growth

Microchips with nanoelectrode pair about 60 nm apart were fabricated using the method explained in Section 3.1. Before DEP trapping, the BAB-AuNP solution was spin-filtered to change the folding buffer to a trapping buffer with low conductivity. Since the Brownian motion, which competes with DEP force, scales inversely with the particle dimension $\propto V^{-1/3}$, assemblies with all three AuNPs conjugated were preferably trapped by DEP. The AFM image of one of such samples is shown in Fig. 3.7a. The AC DEP was carried out at 12.5 MHz, 1 V_{pp} for 10 mins.

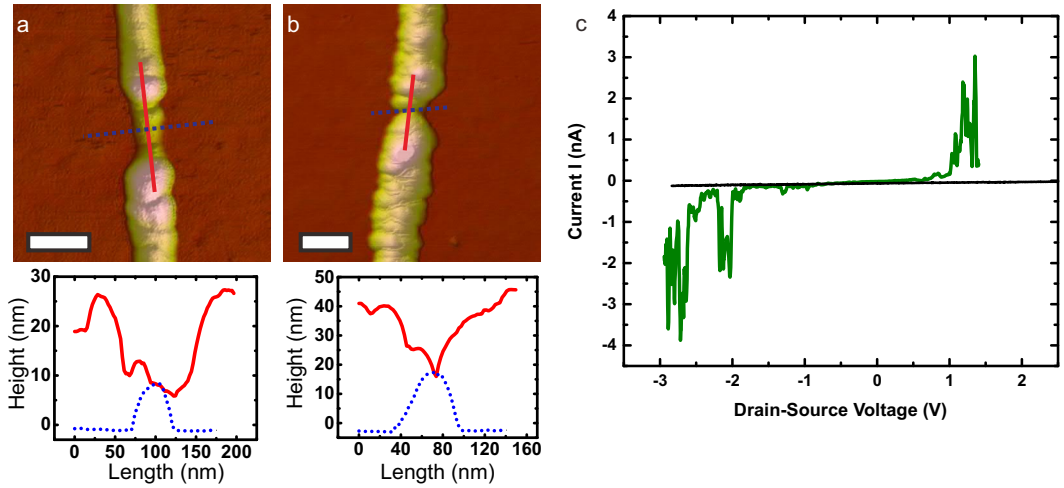

FIGURE 3.7 **a**, AFM image with cross section of a trapped BAB-AuNP trimer assembly between gold nanoelectrodes. **b**, the same sample after five steps of gold enhancement. **c**, the I-V characteristics of the sample initially (black line) and after the gold enhancement processes (green) at room temperature. The scale bars are 100 nm.

The I-V characteristics of individual trapped BAB-AuNP assembly were measured with the DC setup in Section 3.1. The current versus drain-source voltage of them showed a linear, TΩ-range, nonconducting behavior as shown in Fig. 3.7c (the black line). It was most probably due to the fact that the AuNPs were not close enough for electrons to tunnel through the insulating barrier. The distance between the sticky ends on the BAB complex is 14 nm, and the AuNPs were of the size 10-15 nm. According to the design, the AuNPs should be very close to each other. But because the dsDNA which connects the AuNP and the TX-tile itself are both quite flexible, the negatively charged AuNPs will repulse each other, and the actual distance could be longer than required.

In order to shorten the particle-to-particle as well as particle-to-electrode distances, chemical gold growth processes were involved. A commercial gold enhancer

kit was used to reduce gold ions to metallic gold on the existing gold nucleation sites. To precisely control the growth, the gold enhancer was heavily diluted and the growth was carried out in several sequential short steps. After each growth step, the sample was cleaned and its I-V characteristics was measured until a CB appeared, as shown in Fig. 3.7c (the green curve). Usually, 3-5 steps were required and it resulted in a grainy structure as shown in Fig. 3.7b.

3.3.3 I-V characterization at low T

The drain-source I-V curve in Fig. 3.7c was full of fluctuation and sudden jumps. In order to eliminate the thermal effects such as thermal hopping, low temperature measurements were conducted. The sample was first cooled down to 77 K by dipping into liquid nitrogen and then to 4.2 K by liquid helium. The I-V curves were measured at these two temperatures as well as various temperatures in between, as shown in Fig. 3.8. The fluctuations were indeed significantly quenched, but sudden jumps still persisted. However, the jumps at low temperature were more like switchings between different I-V characteristics as circulated by red marks in Fig. 3.8. It is possible that the switching was due to the random fluctuations in the background charge, which essentially have the same effect as quick manipulations of the gate voltage of SET. In addition, this effect was implicated by the random changes of threshold voltage at 77 K (orange, violet, and cyan curves in Fig. 3.8).

Control samples were also prepared by using chemical growth process on trapped plain BAB complex. Most of the control samples ended up in merged electrodes with varying resistances (kΩ to TΩ). However, in a single isolated case, the control sample showed CB. Compared with the control sample, the BAB-AuNP assembly still offers higher probability to form isolated islands for CB to be observed even at room temperature by providing a ready-made template for chemical growth.

3.4 Conclusion

On one hand, the DEP trapping results, especially the possibility of trapping individual origami, were unambiguously positive for the multilayered DNA origami structures. It offers a valuable method for manipulation of these nano-objects after they are formed in solution. In addition, the behavior of 3D DNA origami with different shapes and lattice structures under high electric field gradient provided useful information for designing and applying such structures in nanoelectronics. On the other hand, although the conductivity measurement results at high RH disagree with the previous reports, the multi-layered DNA origami can be safely concluded as an insulator in dry conditions. They can be used as appropriate template and substrate in nanoelectronic applications. Nevertheless, the inconsistency of the measurement results pinpointed the drawback of the DEP method in nanoelectronic

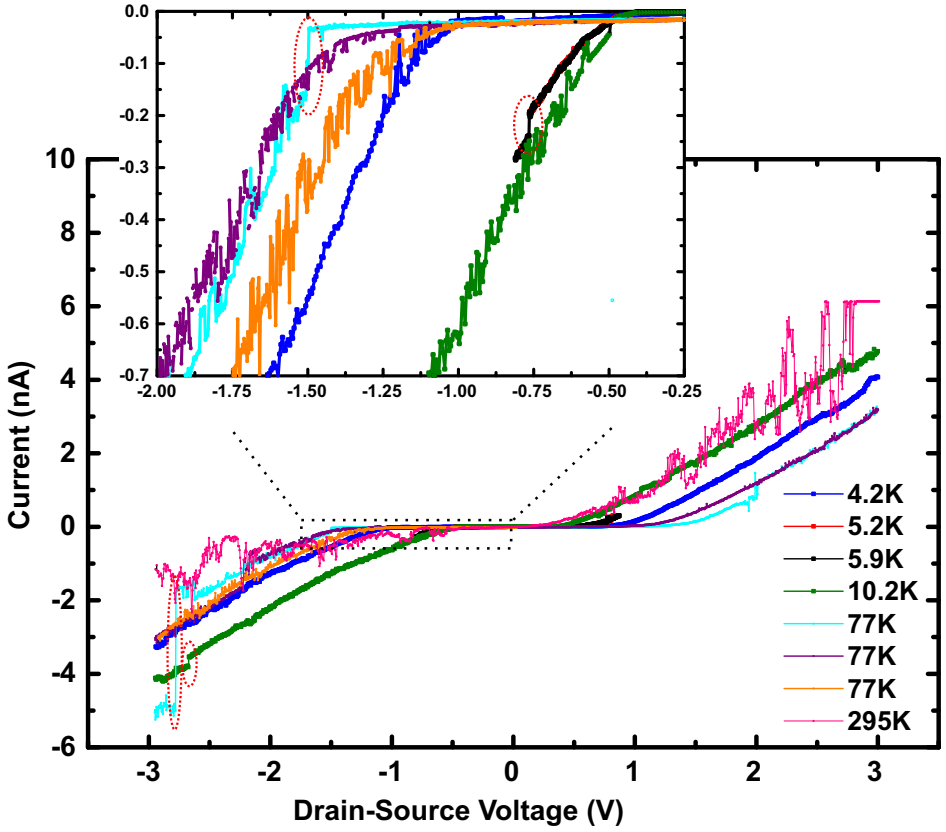

FIGURE 3.8 I-V characteristics of a sample measured from 4.2 K to room temperature. The inset shows details of the current curves at 77 K and below. The random current fluctuations, i.e., thermal noise, quench as the temperature goes down, but rapid switching and jumps between different I-V curves (red circulated places) due to sudden changes in background charges are still observed.

applications. Special cautions should be taken when investigating the connectivity between the pre-fabricated nanoelectrodes and the trapped objects.

The BAB-AuNP assembly presented in this section is technically not a full SET, since the gate electrode is missing. However, it is the only self-assembled SET-like structure by DNA nanotechnology to date which has been characterized electrically and shown CB up to room temperature. Due to the absence of gate electrode, no gated I-V characteristics has been measured, but the switching effect and changes of threshold voltage in low temperature measurement suggested the possibility to implement a fully functional SET by addition of a proper gate electrode.

Unfortunately, the chemical growth process had to be involved to make the CB to appear. The DNA TX-tile cannot bring the AuNPs sufficiently close by this design because of the flexibility of the single DNA linker and the repulsion between the negatively charged AuNPs. More rigid scaffold and optimized annealing condition should be investigated in the future to shorten the distance between the particles. Although one of the control sample showed CB effect, the probability of islands for-

mation based on the trimer should still be much higher and much more controllable.

In summary, the combination of DNA self-assembled structures and DEP has provided a novel fabrication path in which nanoscale electronic devices can be first self-assembled in a controllable fashion in solution and subsequently be incorporated into macroscopic circuits.

Chapter 4

DNA-assisted lithography (DALI)

In the field of plasmonics, there is no need to physically and precisely connect the nano-objects of interest to the macroscopic circuits for excitation or characterization like in the case of nanoelectronics. Therefore, the parallel self-assembly nature of structural DNA nanotechnology can be more readily exploited. Numerous investigations have been conducted using DNA self-assembled structures, especially DNA origami, as a scaffold or template to construct metallic nanostructures for plasmonic uses. Two of the most commonly employed methods are attaching of synthesized metallic nanoparticles and direct chemical reduction of metal, as briefly discussed in Section 1.4. However, the former limits to highly symmetric synthesized nanoparticles, while the latter suffers from a granular structure due to the chemical nucleation growth method used. To produce metallic nanostructures with smooth surface and fully utilize the versatile DNA origami shapes as templates, an alternative approach has been developed in this thesis work. In this approach, the self-assembled DNA origami is only used for producing a negative silicon oxide stencil for subsequent material deposition. It is a surface based method like UV and e-beam lithography, but does not need any sophisticated instrumentation for the pattern generation. Even better, the molecular level precision of DNA origami can easily result in sub-10-nm feature size, and the self-assembly process is intrinsically parallel which is compatible with the large-scale production.

In this chapter, the work in **A.III**, **A.V** and the fabrication part of **A.IV** will be discussed since they are closely related. I will introduce the basic principles of the DNA-assisted lithography (DALI) and how it has evolved from a proof of principle fairly limited method, to a much more applicable stage which is suitable for fabricating plasmonic nanostructures on any flat transparent substrate. To demonstrate the advantages of DALI, different nanostructures with unique optical properties and applications were fabricated and optically characterized, including a cross-shaped structure (Seeman Tile, ST [141]), a bowtie origami (BO) and two mirrored chiral double-L (CDL) structures. The measurement results and theoretical simulations can be found in Chapter 5. In an attempt to cover large area substrates with DNA

origami, a spray-based deposition method will be presented in Section 4.5.

4.1 Principles of DALI

The starting point of this method is that DNA origami on a Si surface can modulate the growth of SiO_2 in such a way that the SiO_2 layer will either deposit faster on the bare native oxide surface or on DNA origami in a controlled environment [119]. In the negative-tone case, where the SiO_2 layer grows on native oxide surface, a hard mask of SiO_2 with openings of the shape of the silhouettes of DNA origami will form. This mask can then be used in the subsequent nanofabrication processes for metallic nanostructure production.

4.1.1 Controllable growth of SiO_2 mask

In 2013, Surwade *et al.* [119] first proposed a method, in which the difference in water affinity between DNA molecule and native silicon oxide was utilized to create inorganic nanoscale patterns based on the shape of DNA origami. The chemical reaction in this process is:

$$Si(OC_2H_5)_4 + 2\,H_2O \xrightarrow{NH_3} SiO_2 + 4\,C_2H_5OH$$

In this reaction, tetraethyl orthosilicate (TEOS) and water are reactants, and ammonia is a catalyst which can facilitate the reaction at room temperature. The differences in water affinity between DNA molecule and native oxide layer can be summarized as in the following way: at low humidity, native oxide will always adsorb at least a monolayer of water molecules, which makes its affinity higher than for DNA molecules; but at higher humidity, DNA molecule can absorb more water than silicon oxide [119]. By tuning the humidity in the reaction chamber, the SiO_2 growth can be either positive-tone or negative-tone, *i.e.*, grow preferably on top of the DNA or SiO_2, respectively.

In order to produce SiO_2 with DNA origami silhouette-shaped openings as a mask for lithography, there are two major technical details to be taken care of. First, the SiO_2 layer can only grow on existing native oxide, therefore the DNA origami must be deposited on Si substrate. Secondly, the growth process must be controllable in both selectivity and rate.

Unlike naturally negatively charged mica, which is most commonly used for studying DNA origami, native SiO_2 or thermally grown SiO_2 are neutral. To immobilize the DNA origami on Si substrate (with native oxide), the sample surface must be treated with either piranha solution or O_2 plasma to generate $-OH$ group at the topmost layer, so it will be slightly negatively charged in water. In Ref. [119], piranha solution was used. In our case, since piranha solution is a hazardous method and O_2 plasma is a standard RIE process in lithography, O_2 plasma is selected instead.

Moreover, a side effect of O_2 RIE is benefical for fabrication on Si_3N_4 and Al_2O_3 . This effect will be discussed in Section 4.3. The Mg^{2+} ions in origami buffer can then facilitate the attachment of negatively charged DNA structures with negatively charged surfaces. The 12.5 mM Mg^{2+} in folding buffer is sufficient for immobilization on mica. But the charging of a SiO_2 surface is relatively weaker. Thus in order to achieve a reasonable density of DNA origami on the surface, the concentration of Mg^{2+} needs to be increased up to 100 mM. In addition, the weak bonding also requires more gentle washing techniques.

In Surwade's original paper, some of the parameters of the reaction are not clearly stated, or they are highly device (chamber) dependent. Thus, to reproduce the results, and obtain smooth SiO_2 film, humidity was systematically varied to find the optimal recipe. To be more specific, the amount of TEOS and NH_4OH was fixed and silica gels treated in humidity chamber was introduced into the CVD chamber to maintain a more controlled environment. It was noticed that the high humidity can provide faster deposition rate, but too high humidity results in either poor selectivity or bigger grains on the surface which can be problematic in the later steps. So, to realize a reproducible process with reasonable deposition rate, a humidity buffer (here silica gel incubated in a humidity chamber) is necessary.

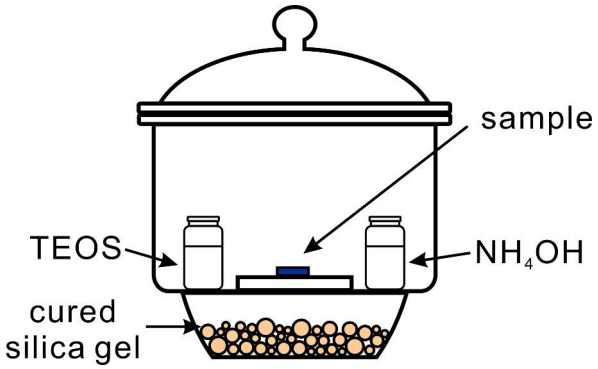

FIGURE 4.1 An illustration of the reaction chamber setup. The sample with DNA origami immobilized is placed on a small stage in the center of the desiccator between the glass vials with TEOS and NH_4OH. Silica gel incubated in a humidity chamber is placed at the bottom of the desiccator.

In the established experiment setup, a desiccator of 1.5 l volume was chosen to accommodate the reaction as shown in Fig. 4.1. Vials of 10 ml of TEOS and NH_4OH was placed on either side of the sample, 100 gram of treated silica gel was situated beneath the sample and vials. It has been observed that without the silica gel, the film quality and selectivity of the growth were not very well controllable. After adding fresh (dry) silica gel, the deposited film became very smooth, but the deposition rate went down significantly. The film quality comparison of with and without silica gel can be seen from Fig. 4.2. As a result, silica gel incubated in humidity chamber at 80% relative humidity (RH) for 20 hours were used to achieve

acceptable growth rate and good reproducibility.

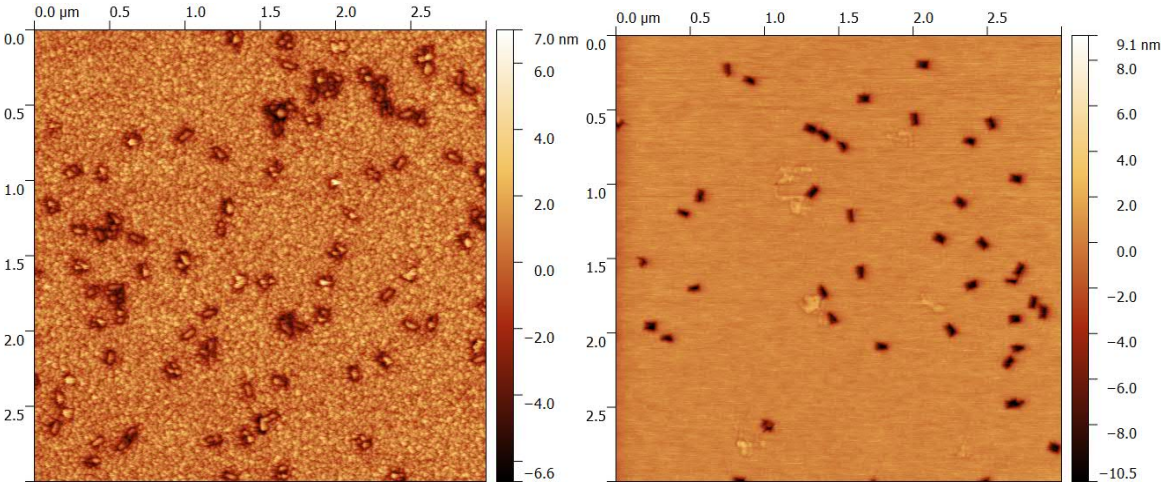

FIGURE 4.2 An example of different outcomes of SiO_2 growth. left) without silica gel right) with silica gel incubated in humidity chamber at 80% RH.

The other factor which affect the growth is the freshness of the TEOS, the deposition rate of the SiO_2 film decreases slowly after a container of TEOS has been opened. The reason for this is that atmospheric pressure chemical vapor deposition (APCVD) of SiO_2 is a mass transportation limited process, *i.e.*,the film growth is very sensitive to the concentration of reactant and the diffusion rate. Even on the same sample, the thickness of the SiO_2 film may have minor differences between the side near the TEOS vial and the opposite side. As a result, the fabrication steps following the SiO_2 deposition need to be adjusted slightly to get the best results.

4.2 Fabrication on Si wafer

To test the feasibility of using the grown SiO_2 layer as a hard mask for evaporation, the most intuitive way is to slightly etch the thin SiO_2 layer on top of the DNA and DNA so the metal can be deposited on the exposed Si substrate by PVD. Then remove the rest of the SiO_2 by hydrofluoric acid (HF) lift-off. However, because of the imperfect conformation of the SiO_2 deposition, only a limited thickness of the mask can be grown with high pattern resolution. To achieve a proper lift-off process, the metal layer should be much thinner than the mask. With a SiO_2 thickness of 10 nm to 20 nm, which is common in this process, the reasonable amount of metal that can be deposited would be even thinner than 10 nm. The integrity of such thin metal layer is hard to preserve in the following fabrication processes, not to mention the very limited application of it.

Before considering the possible applications, the ability of the SiO_2 mask to transfer the DNA origami shape into metal by PVD has to be investigated. A proof of principle experiment was design as shown in Fig. 4.3. In this experiment, instead

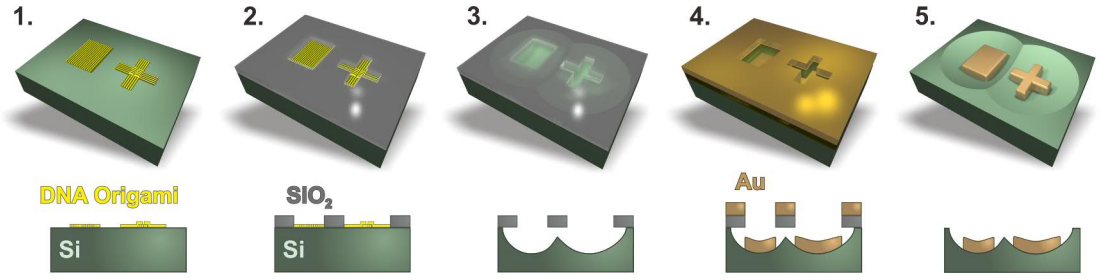

FIGURE 4.3 Schematic and cross-section of the fabrication protocol on Si. *Step 1*: DNA origami was deposited on O_2 plasma treated Si surface. *Step 2*: a thin layer of SiO_2 is grown selectively. *Step 3*: isotropic RIE etching of Si under the SiO_2 layer. *Step 4*: physical vapor deposition of gold. *Step 5*: removing of the SiO_2 layer together with gold film by HF lift-off.

of etching only the thin oxide on top of DNA origami and expose the silicon surface, an Si etching RIE process is carried out after the oxide etching. Because of the RIE Si etching is isotrophic at room temperature, there will be an semi-spherical cavity forming under each origami-shaped opening. Certain area near the opening is suspended. This cavity creates extra space for subsequent physical vapor deposition (PVD). After the metal evaporation, the oxide mask and the metal on top of it can be easily removed in HF solution. The details of the fabrication protocol can be found in **A.III** and its supplementary information and is illustrated in Fig. 4.3.

The primary goal of this study is to test how the SiO_2 mask behaves in the lithography processes. One of the important criteria is whether the mask can preserve the high resolution of DNA origami. The other is the durability of the mask in both the RIE etching and metal deposition procedures. It determines whether the mask is suitable for conventional lithography. In principle, the thickness of the fabricated metal pattern is not limited by the mask thickness. But in reality, there are a few factors which will limit the structure thickness, *e.g.* the silhouette-openings can be slowly blocked by the evaporated metal or the suspended mask can only support a certain weight before collapsing.

It turned out that the overall results were encouraging. Metallic nanostructures with two different DNA origami shapes (AFM images shown in Fig. 4.4) were successfully fabricated with high resolution, namely Seeman tile (ST) and Rothemund rectangles (RR) [1] as shown in Fig. 4.5 and Fig. 4.6. The mask was not blocked or collapsed during the evaporation of $\sim$ 20 nm of metals. The metallic ST and RR structure have shapes roughly the same as the DNA origami, but slightly smaller. It is due to the fact that the SiO_2 not only grows perpendicularly to the sample surface, but also attaches to the freshly formed SiO_2 on all possible directions including on the walls inside the openings. The silhouettes will become smaller and smaller as the thickness of total oxide thickness increases. It provides an extra degree of freedom for manipulation, which can be taken as an advantage in producing nanoparticle pairs (see Section 4.3). On the other hand, the thickness of the SiO_2 mask is lim-

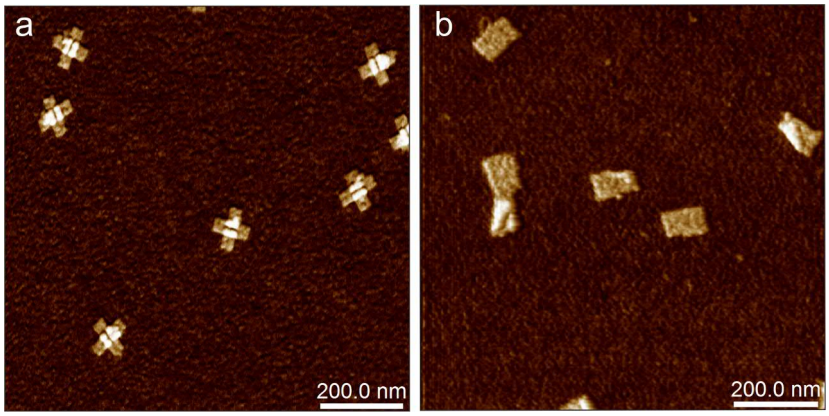

FIGURE 4.4 AFM images of ST (**a**) and RR (**b**) origami immobilized on a O_2 plasma treated silicon surface.

ited due to the isotropic growth. However, the good mechanical properties of SiO_2 makes it sufficient for deposition of at least tens of nanometer of metal, which is suitable for many applications.

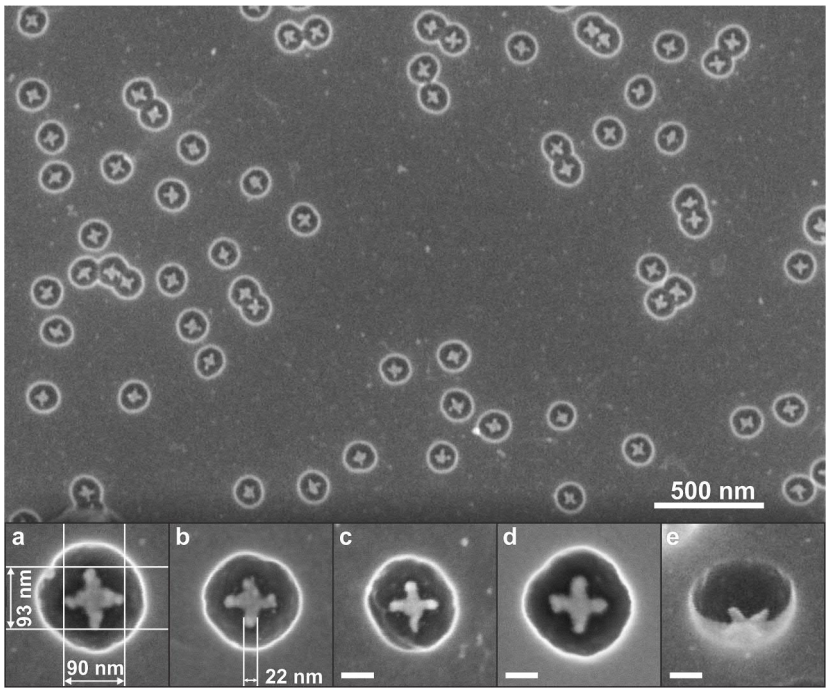

FIGURE 4.5 SEM images of gold ST structures in silicon cavities. **a**-**e** high magnification images of individual structures. **e** was taken with a tilted SEM sample stage. Inset scale bar: 50 nm.

In addition, the physical deposition method does not restrict the deposited materials as chemical methods. Theoretically, any material including metals, dielectric or semiconductor, can be evaporated through the mask made from DNA origami and form corresponding nanostructures. Three different metals (namely gold, silver and copper) have been tested, since they are most relevant in plasmonic field. They

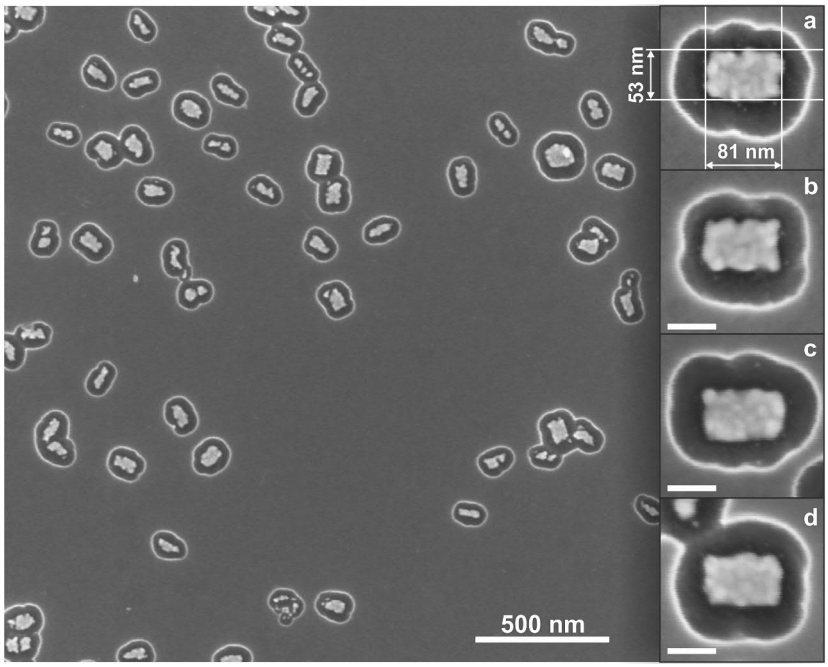

FIGURE 4.6 SEM images of gold RR structures [1] in silicon cavities. **a-d** high magnification image of individual structures. Inset scale bar: 50 nm.

can follow the stencil shape similarly. But compared with gold, silver and copper are less stable, which makes the corners become rounder to different extents, as shown in Fig. 4.7.

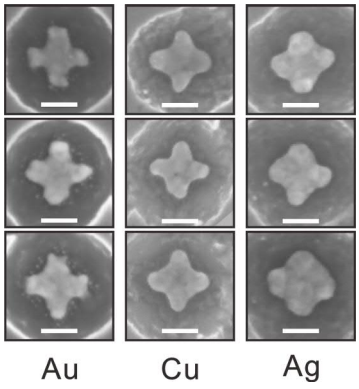

FIGURE 4.7 SEM images of nanoparticles with ST shape made from gold, copper and silver. Scale bars are 50 nm.

Another fact which can be learned from this experiment is that because the spatial information of the DNA origami can be accurately transferred to metallic structures, the defects happened in folding or deposition will significantly affect the final shapes of the metallic nanoparticles. Especially the deposition of DNA origami on a silicon substrate can result in partially overlapped structures, as the RR origami shown in Fig. 4.4. This phenomenon usually happens when the Mg^{2+} concentration in deposition buffer is elevated and the DNA origami has intrinsic twist, which is

most obvious in the case of RR origami. In the AFM image after the deposition, most of the RR origami already have one corner or even half of the area folded back. The silhouette of such origami will be snapshotted into an incomplete rectangular shape. Metal evaporated through these imperfect stencils are usually much narrower than the full shape or missing a corner as in Fig. 4.6. Reducing the concentration of Mg^{2+} can help to lower the percentage of folded origami on the surface, but unfortunately due to the weak bonding, the overall number of DNA origami immobilized on the Si surface will also decrease. The most effective way to avoid this situation is taking the twist and the flexibility into consideration while designing the DNA origami. The basic idea is to iterate on skipping certain amount of bases and simulating the stresses in the DNA origami by CanDo-program until the DNA origami has minimal curvature in the structure.

4.3 Fabrication on Si_3N_4 and sapphire chips

The successful fabrication of high resolution ST and RR metallic structures on Si has proven that the SiO_2 stencil can precisely transfer the 2D DNA origami shape to metallic pattern, and it is compatible with standard microfabrication processes. However, the situation that all the metallic structures sit in a semispherical Si well makes it impossible to characterize their optical properties, and to be used in any applications.

To enable optical measurements and potential applications, flat and transparent substrates are essential, especially for single particle measurement. Because the lift-off step in previous method involves HF which can etch SiO_2 and glass, materials which can resist the etching of HF has to be selected without further major modification of the protocol. Si_3N_4 and sapphire (Al_2O_3) are the most accessible materials which satisfy these conditions. Si_3N_4 is a common substrate material in silicon industry, and it is compatible with most of the microfabrication processes. However, the optical properties of Si_3N_4 are not optimal for many applications, since it has high refractive index (over 2) and non-flat transmittance spectrum in the visible range. In addition, the Si_3N_4 usually is in a form of thin film on a Si substrate which will act like a mirror and induce optical interference pattern if not removed. Sapphire (Al_2O_3), on the other hand, has very good transmittance for wavelengths from 150 nm (UV) to 5500 nm (IR). It has been frequently used in optic and electronic applications. Single crystal sapphire ingot can be grown by Czochralski process [142], which enabled cutting the wafer in the lattice directions which minimize the birefringence for optic uses.

In order to deposit the metal nanostructures on a flat substrate with a mask with limited thickness, certain spacer or sacrificial layer has to be placed between the substrate and the mask. Naturally the sacrificial layer cannot be of the same material as either substrate or the mask to avoid damaging either one during the etching

processes. In addition, since the SiO_2 growth process has only been tested on native SiO_2 , it would be most straightforward to have a silicon layer as the spacer. Therefore a layer of Si was deposited on the substrate and then used for DNA origami immobilization. Plasma enhanced chemical vapor deposition (PECVD) was used to deposit the silicon layer since it is a relatively fast process and requires lower temperature. After roughly 50 nm thick amorphous silicon layer was deposited on the Si_3N_4 or sapphire (here the Si_3N_4 was used for process development since it was readily available), the rest of the processes are similar to the case of fabricating on Si substrate except an extra RIE Si etching needs to be performed after the HF lift-off to remove the sacrificial layer. A 3D rendered schematic of the processes and corresponding cross-section view of each step is shown in Fig. 4.8.

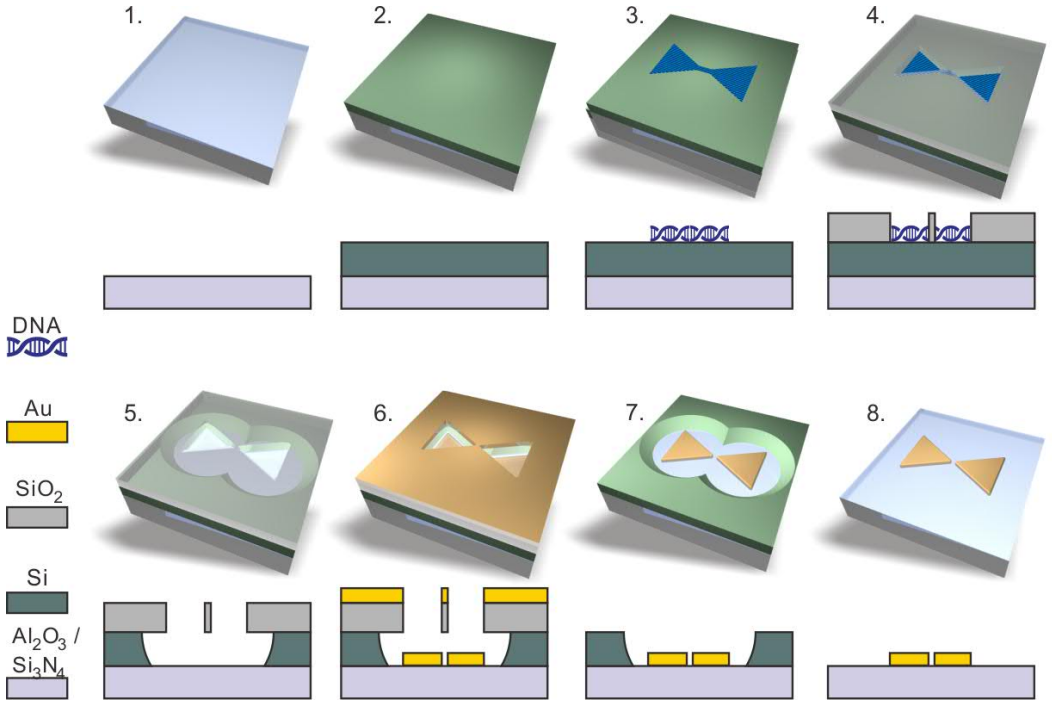

FIGURE 4.8 Schematic illustration of the DALI fabrication processe on flat substrates using bowtie origami as an example. *Step 1*: plain substrate. *Step 2*: deposition of a layer of amorphous silicon by PECVD. *Step 3*: immobilization of DNA origami on the O_2 plasma treated sample. *Step 4*: a thin layer of SiO_2 is grown at room temperature. *Step 5*: RIE etching of thin oxide layer on top of DNA and the Si sacrificial layer. *Step 6*: PVD of gold. *Step 7*: HF lift-off. *Step 8*: post-RIE etching of the remaining Si.

The new protocol was first tested with ST origami on Si_3N_4 substrate, and the obtained resolution of the fabricated nanostructures was comparable with the previous method in silicon cavity. However, unlike the cavity, flat surface cannot hold the nanostructures during the lift-off process. Combined with the poor adhesion of gold to other surfaces, many of the nanostructures were flushed away after the lift-off and cleaning. Even when the metal was changed from pure gold to gold-palladium (AuPd) alloy, which should have better adhesion properties, some of the structures

were still disappeared or moved after the lift-off process, as shown in Fig. 4.9. Gently handling of the sample in HF lift-off can reduce the detaching of nanostructures, but the results are less reproducible due to human error. Conventionally, the adhesion of gold is improved by an additional thin layer of titanium or chromium which works as a glue between the gold layer and substrate. Since hydrofluoric acid can etch titanium, chromium becomes the only option. By evaporating a 1-2 nm layer of Cr before the Au, most of the nanostructures can be kept on the surface after all the processes.

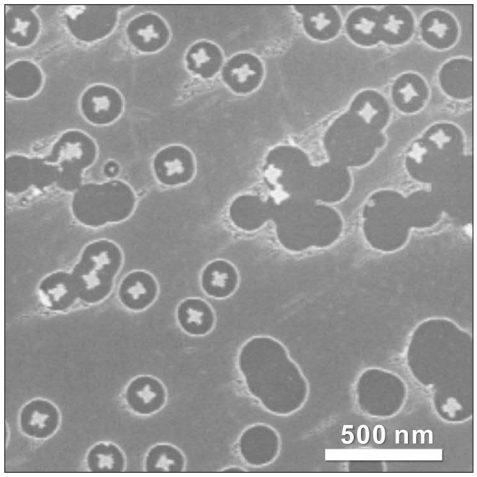

FIGURE 4.9 SEM image of ST-shaped AuPd nanostructures on Si_3N_4 with the sacrificial Si layer unremoved, so the empty spots and drifted structures can be seen.

With the protocol established, all the later samples were fabricated with sapphire chips to enable optical characterization. In particular, two shapes with intriguing plasmonic properties were emphasized, namely bowtie origami (BO) and chiral double-L (CDL). The bowtie shape with a nanometer scale gap between two triangles has been widely studied for its electric field enhancement which can be used in sensing applications, *e.g.*, surface enhanced Raman spectroscopy (SERS) and fluorescence enhancement (FE). The CDL is one implementation of planar chiral plasmonic nanostructures[1] which absorbs right-handed circularly polarized light and left-handed circularly polarized light differently. These two origami design and previously fabricated ST are demonstrated side by side in Fig. 4.10. The AFM images and the CanDo simulation are almost identical in dimensions, on the other hand, the metallic structures in SEM images are a slightly smaller for the reason stated in last section.

Both the BO and CDL fabrication have their specific challenges due to their different application purposes. For BO structure, the formation of the narrow gap be-

[1] A planar or 2D chiral structure usually refers to a pattern which cannot overlap with its mirror image unless it is lifted from the plane. The structures are not chiral themselves by definition, because the chirality is a 3D concept. The optical chirality is raised by the combination of the 2D structure and the substrate. [143]

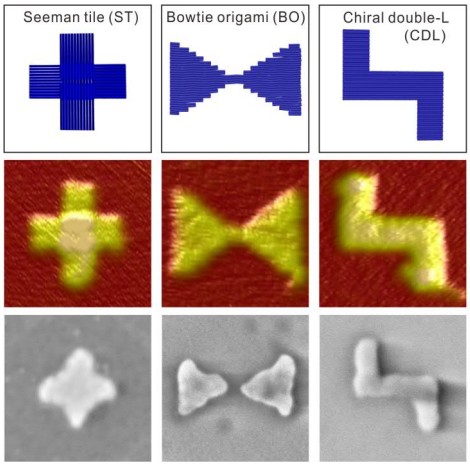

FIGURE 4.10 CanDo simulation, AFM images and SEM images of three different shapes which have been fabricated by DALI. Top panel: CanDo simulation, Middle panel: AFM images of origami deposited on mica, Bottom panel: SEM images. Each frame is 150 nm $\times$ 150 nm.

tween the triangles, for the plasmonic hotspot requires employment of the isotropic growth of the SiO_2 mask. And for the CDL structure, the circular dichroism can only be observed when most of the structures landed with same handedness. For this intention, the DNA origami needs to be modified and the immobilization process needs adjustment. The challenges and solution will be discussed separately in more detail below.

4.3.1 Bowtie antenna fabrication

By design, the BO is a single origami with two triangles connected with a narrow bridge of four helices. It was intended so to maintain the relative position of the two triangles constant after they are immobilized on surface. However, the bowtie antenna is only relevant when there is a gap between the triangles, since the electric field can be greatly enhanced there and form a hotspot. The isotropic growth of SiO_2 during the deposition reaction had already been notice earlier, so the connection was made as narrow as possible to facilitate the convergence later.

To obtain the real growth profile of the SiO_2 around a DNA origami is rather problematic due to the miniature size and characterization limitation. However, considering all the AFM data, SEM data and etching parameters comprehensively, an estimated growth scenario can be deduced. First, the deposition is not only in the direction perpendicular to the surface, since the silhouettes did get smaller after growth. This effect is especially obvious when the humidity is slightly higher and the deposition time is elongated, as shown in Fig. 4.11, the arms of the STs have become much narrower. The isotropic growth can also be noticed by the bumpy surface profile.

Secondly, the sizes of the origami stencil are not uniform at different depths.

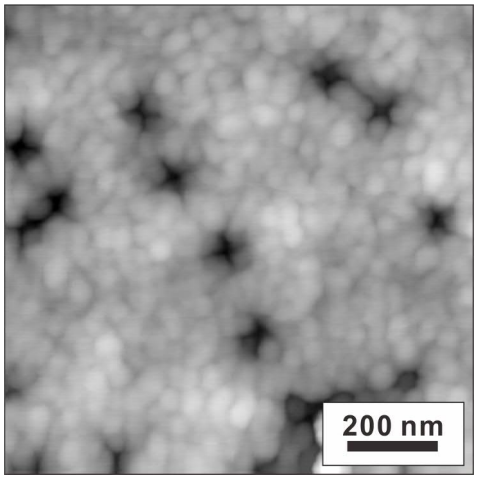

FIGURE 4.11 AFM micrograph of a sample with STs after an elongated SiO_2 growth in higher humidity.

More specifically, if viewed from the top surface of the mask, the opening on top of a DNA origami is the smaller the deeper. This effect can already be seen in the AFM images, but due to the tip convolution, it is difficult to draw a conclusion. By etching different thicknesses of the SiO_2 mask and evaporating metal, the size and shape differences can be clearly compared, as shown in Fig. 4.12. On the sample which was etched less, most of the bowtie antennas have a gap and the overall sizes are smaller. In comparison, the bowties on the sample, whose SiO_2 layer was etched more, are bigger in size and do not possess gaps.

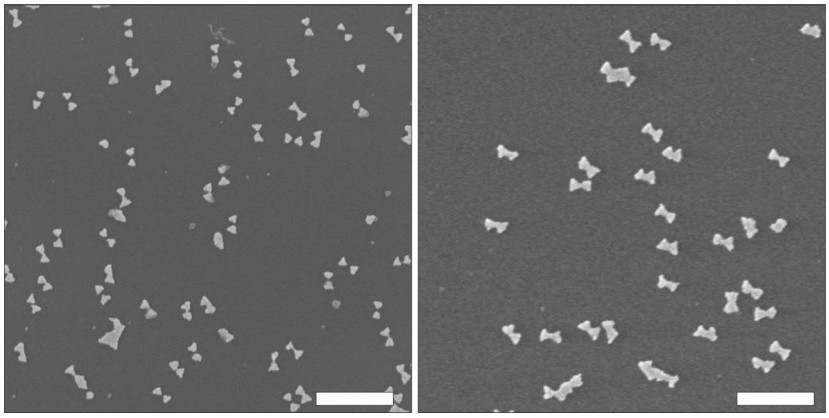

FIGURE 4.12 Two BO samples on Si_3N_4 with the same growth parameters, but the SiO_2 was etched by RIE with different time. The etching time was 18 s for the left sample and 22 s for the right sample. Scale bars: 500 nm.

By combining these two findings, the SiO_2 growth profile can be concluded. The new SiO_2 product from the reaction will attach to all existing SiO_2 surfaces including the inner wall of the opening on top of DNA origami. The part of the wall deeper in the hole will have more SiO_2 deposited on them since they are formed ear-

lier. The cross-section of the mask has a shape of a trapezoidal trench as illustrated in Fig. 4.13. Moreover, at the very narrow locations, like the connection between the two triangles in BO design, the inner walls on both sides of the trench will start to touch and eventually merge together. This merging will lift the bottom of the trench a few nanometers higher compared with other area which is more open. The thickness difference between the open and narrow areas is essential for gap formation in metallic BO structures. As long as the RIE etching of SiO_2 can be controlled to only etch the open areas through, but leave the thicker narrow connection still blocked with SiO_2 , a hotspot will form between the two metallic triangles.

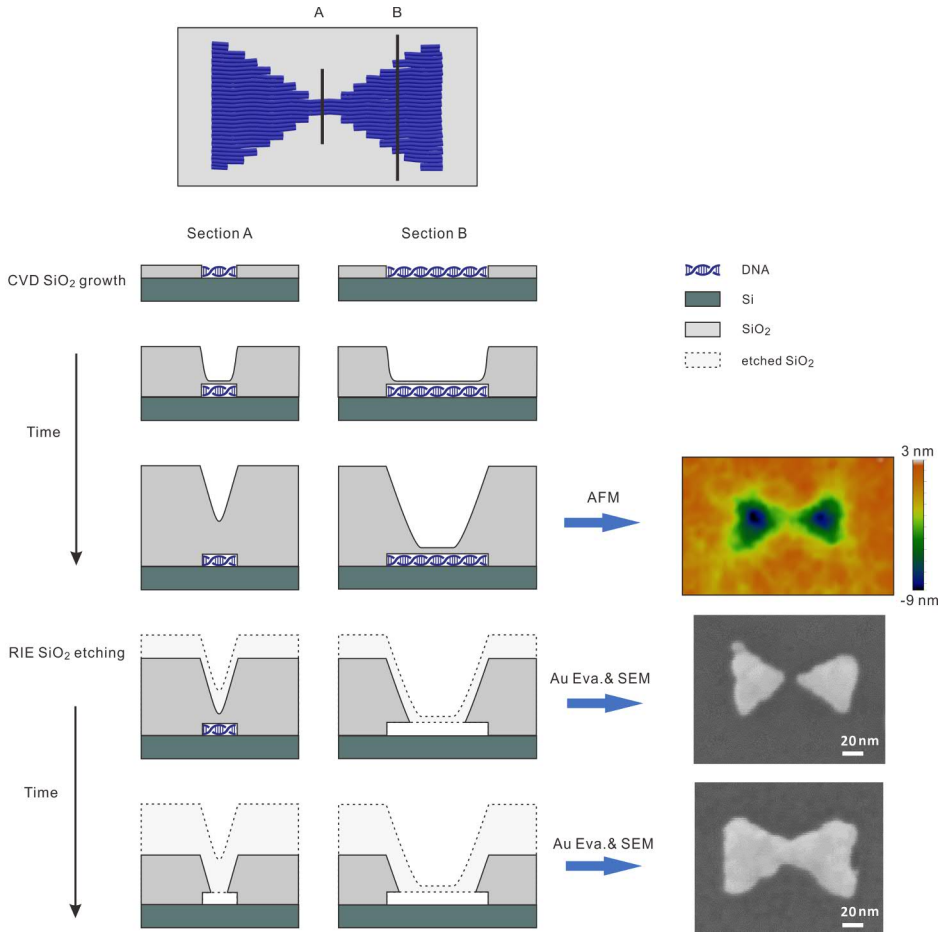

FIGURE 4.13 Schematic illustration of the SiO_2 growth process and the effect of RIE etching on different thicknesses.

In principle, once the SiO_2 growth profile is known, it is possible to control the hotspot size quantitatively by etching a specific thickness of mask. But at the current stage, the precision of the SiO_2 growth control is not sufficient. There are still few reaction parameters which are not well controlled, namely the diffusion rate and the concentration of reactant. Especially, the local rate of these parameters are difficult to control due to the crude desiccator setup. If a chamber with sophisticated flow control can be implemented, quantitative control is possible. With the simplified

setup, the gap formation can be qualitatively controlled by varying the RIE etching time of SiO_2 . A typical sample of gold BO structures with smaller gaps on sapphire substrate is shown in Fig. 4.14. The yield of correctly formed bowtie antenna in such samples is usually between 45% to 65% (see article **A.IV** supplementary info).

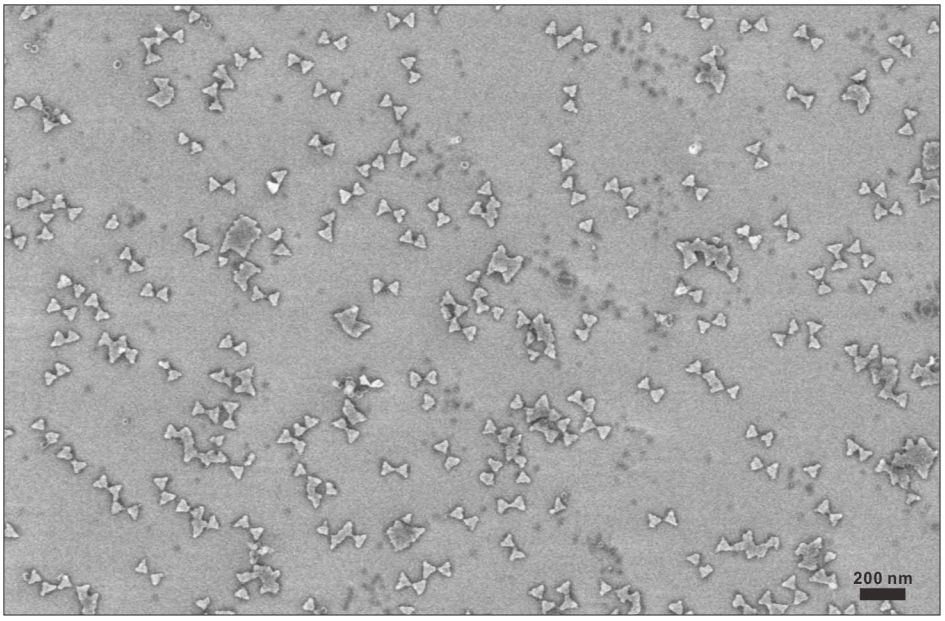

FIGURE 4.14 SEM image of gold BO structures on a sapphire substrate.

4.3.2 Chiral double-L structures fabrication

Unlike the BO structures, the CDL structure can and preferably should be the same as the origami design. Yet the challenge lays in controlling the face on which origamis are immobilized on the substrate. The symmetry of the DNA origami has to be broken so that they will preferably land on the substrate in one chirality, *i.e.*, certain face down. An individual origami will either resemble a letter "S" or a letter "Z" once it lands on the substrate. The S-CDLs and Z-CDLs have opposite chirality. One of the proposed methods making them predominantly adapt one chirality is to decorate one side of the CDL origami with multiple oligonucleotide extensions (entropy brushes). During the immobilization, if the origami is landed on the side with oligonucleotide brushes, the binding force should be weaker due to the dynamics of the free ssDNA, hence there will be a higher probability for it to be desorbed and re-adsorbed on the other side.

The original idea was to design only one CDL origami which can be modified to land on either faces so the handedness can be controlled by simply modifying the corresponding face. To avoid the intrinsic stress in the origami which may cause twisting, honeycomb lattice was used since it satisfies the B-DNA structure better than the square lattice. The CanDo simulation [144, 145] of the origami deformation

and the root-mean-square fluctuations (RMSF) is shown in Fig. 4.15. Assuming the helicity of 10.5 bp/turn for B-DNA, the simulated design appears without bending or twisting. The RMSF map shows that the ends of the two arms have more fluctuations than the rest of the origami.

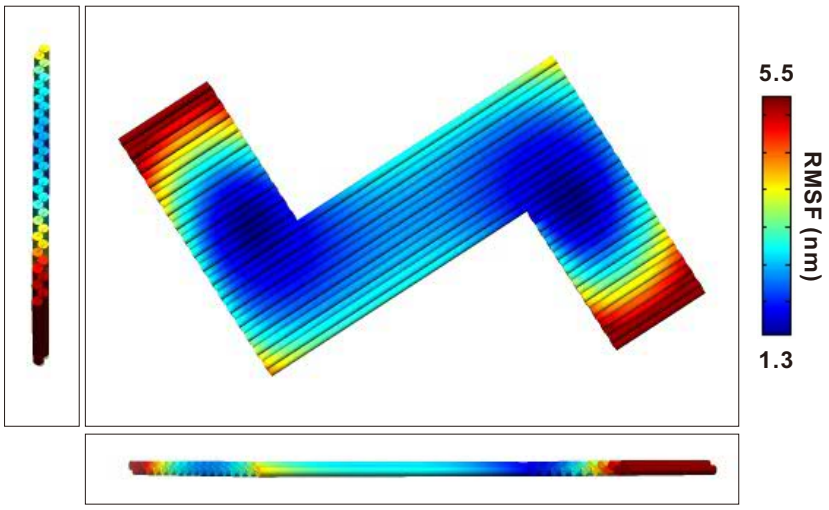

FIGURE 4.15 CanDo simulated deformation model of the CDL origami with local root-mean-square fluctuations (RMSF) heat map as color.

The CDL origami without modification in the folding buffer can be immobilized on mica with either handedness as shown in AFM image in Fig. 4.16a. However, there are slightly more S-shaped CDLs (SCDL) than Z-shaped CDLs (ZCDL) which indicates that the origami is not perfectly symmetric. Once the CDLs were modified with multiple poly-T extensions on either face, they showed very selective immobilization on the S side and Z side (Fig. 4.16b and 4.16c). It proved that the entropy brush modification indeed can control the immobilization orientation of CDLs on mica.

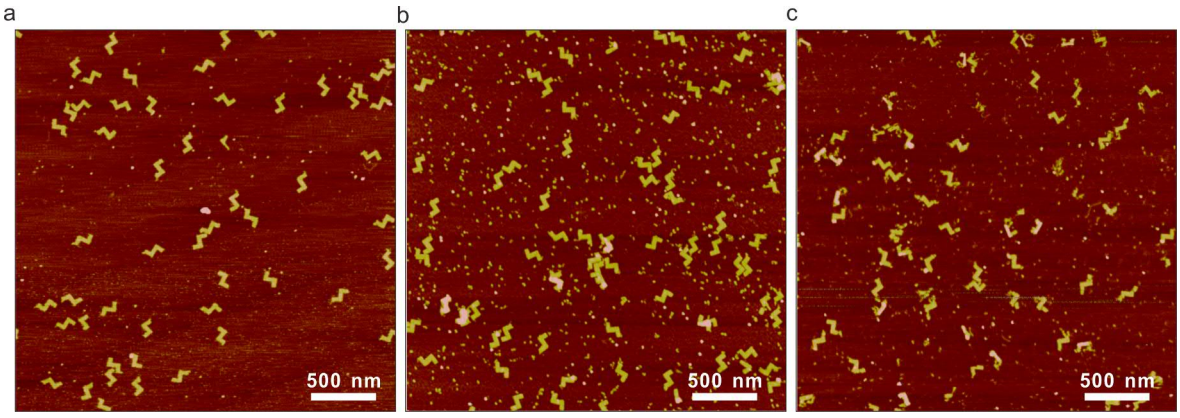

FIGURE 4.16 AFM image of different versions of CDL origami on mica. **a**: unmodified CDLs, **b**: S-shaped CDLs, **c**: Z-shaped CDLs.

However, the immobilization selectivity on Si surface was not the same as on mica. First of all, although the CDL origami was designed to be stress-free, the ends of the two arms tend to roll back to the main body of the origami when the Mg^{2+} concentration is elevated for deposition on a Si surface. The rolling makes the CDL become a bar and lose the handedness. Thus, the concentration of Mg^{2+} had to be lowered to ease the rolling condition.

Secondly, the selectivity of the handedness is affected not only by the modification, but also the Mg^{2+} concentration. Take the unmodified CDL as an example: when the Mg^{2+} concentration is 37.5 mM, around 80% of the CDLs adapt the S conformation. But when the Mg^{2+} concentration raises to between 65 and 100 mM, the S and Z conformations have a roughly 50:50 ratio. The CDLs modified to prefer S conformation can reach a 99% selectivity at 37.5 mM of Mg^{2+}, but the ones modified on opposite face behave unlike any other versions. To be more specific, the amount of the Z CDLs adsorbed on the Si surface is always much less than the unmodified and S-modified versions. In addition, the selectivity seems random from experiment to experiment. Thus, only samples with most S-shaped nanostructures and almost equal amount of either S or Z are fabricated and characterized, as shown in Fig. 4.17. In order to achieve the half-half sample, Mg^{2+} concentration needed to be higher, therefore the sample suffers more from the rolling of origami, which can be seen from the gold structures with shorter arms.

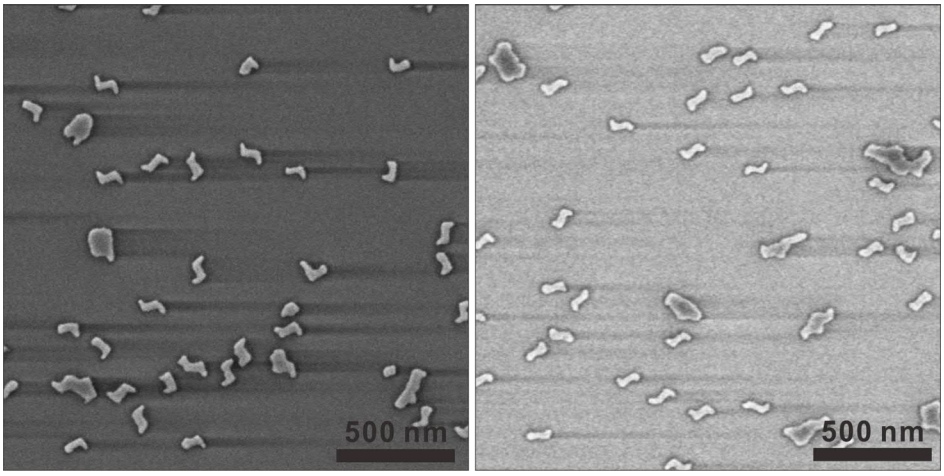

FIGURE 4.17 SEM images of gold samples with S conformation CDLs on the left and equal amount of S and Z on the right.

Taking all the information into consideration, it appears that the CDL origami design prefers the S conformation on Si substrate even without any modification. This preference most probably is caused by the curvature of the origami, which should not be the case if the CanDo simulation is precise enough. According to cryo-EM result of a 3D DNA origami [146], a helicity of B-DNA might not be exactly 10.5 bp/turn, which can explain the invisible twist from the simulation. When the preferred side is passivated with the entropy brushes, the origami starts to be adsorbed

on the other side on mica, but become unlikely to be adsorbed on Si surface at all. It suggests that the selectivity on the Si surface is achieved not because the origami can be desorbed and then be re-adsorbed but rather because all the origami which are weakly adsorbed on the surface are washed away during the cleaning process. In other words, the washing is the selective process. When the relative stronger binding side was passivated by entropy brushes, neither side can bind strongly to the Si surface, so after washing, only very little amount of origami can stay on the surface.

If the aforementioned hypothesis was true, the key to control handedness of origami on Si surface would be design a truly flat DNA origami, whose both faces can strongly bind to the Si surface. Then no matter which side is passivated, the origami landed on that side can be washed away later and leave only the preferred conformation on the surface. Unfortunately, the amount of work and time required to prove this hypothesis is not allowed for the time span of this thesis work, but would be an interesting project later.

In summary, the fabrication of custom-shaped plasmonic nanostructures on flat Si_3N_4 and sapphire surface has pushed the method one step closer to real applications. A series of optical characterization results will be described in Chapter 5 to further prove this promise.

4.4 Preliminary fabrication on glass substrate

As mentioned in the previous section, the substrate material of the DALI method was so far limited to sapphire for HF etching resistance and good optical properties. With a refractive index of more than 1.7, it is problematic to match the index with common optical systems designed for glass, not to mention the much higher cost of optical grade sapphire wafers. Furthermore, the HF etching is a limiting factor not only to the substrate but also to the nanostructures, *e.g.*, to adhere the gold to substrate only chromium can be used, and the quality of silver and copper nanostructures are worse than gold due to their higher reactivity. To widen the scope of applications for which DALI can be used, fabrication on glass substrate and getting rid of HF etching would be a significant leap forward.

With the current Si sacrificial layer setup, the only option to avoid using HF etching would be lift-off with the Si layer. Unfortunately, the common etchant for Si, *e.g.*, sodium hydroxide (NaOH) or potassium hydroxide (KOH) can also etch glass and several important metals, therefore not too much can be gained by switching from HF to them. If the current setup can be changed, for example, to add another spacer layer which can be etched or dissolved in a less aggressive etchant/solvent, then glass can be used as substrate and HF can be abandoned.

The new configuration which was chosen uses common glass slide as a substrate and a 100 nm poly(methyl methacrylate) (PMMA) layer was deposited on the glass as an additional sacrificial layer, as shown in Fig. 4.18. PMMA is one of

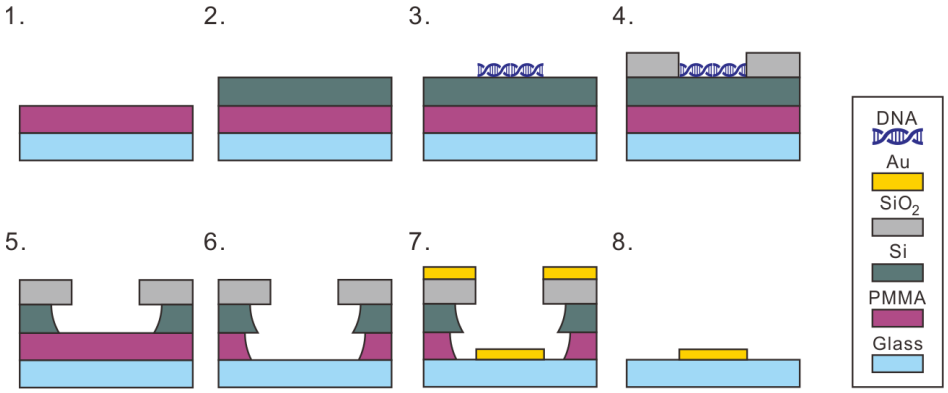

FIGURE 4.18 Schematic illustration of a DALI method with glass-PMMA-Si configuration.*Step 1*: glass substrate with PMMA layer. *Step 2*: PECVD of amorphous Si. *Step 3*: immobilize DNA origami on the O_2 plasma treated sample. *Step 4*: a thin layer of SiO_2 is grown at room temperature. *Step 5*: RIE etching of thin oxide layer on top of DNA and the Si sacrificial layer. *Step 6*: RIE etching of PMMA with O_2 plasma . *Step 7*: metal deposition with PVD. *Step 8*: Lift-off with acetone.

the most widely used resist in microfabrication processes. It can be easily dissolved in acetone which is harmless for most materials. The PMMA layer is usually very smooth, but it cannot withstand too high temperature, otherwise the polymer will be hardened and will be no longer removable by acetone. The key challenge of using PMMA in this setup is to deposit the Si layer on PMMA resist at a temperature lower than its hardening temperature. In addition, PMMA is not as rigid as silicon or sapphire, and thus its ability to preserve the high resolution of the mask has to be tested.

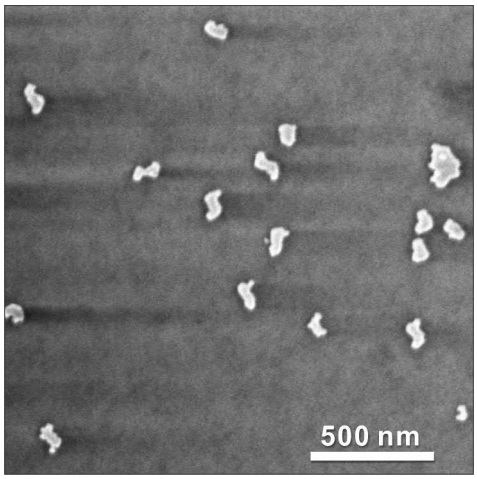

FIGURE 4.19 SEM image of gold CDL structures on glass substrate with titanium as an adhesion layer.

The procedures of the amorphous Si deposition and O_2 plasma has been adjusted to avoid hardening of the PMMA layer. The chamber temperature was reduced from 250°C to 100°C in the PECVD receipe. And for the O_2 plasma treatment,

the time has been reduced from 20 mins to 3 mins. Besides the adjustment for the existing protocol, one more step of RIE O_2 etching has been added after the Si RIE process to etch through the PMMA layer and reveal the glass substrate. After the metal deposition, only hot acetone was needed to remove the PMMA, Si and gold layer all together. A test sample of CDL nanostructures is shown in Fig. 4.19. To note, titanium was used in this sample because the HF etching was no more needed. The resolution of metallic nanostructures in this preliminary sample was not as good as on the sapphire substrate. Whether it can be improved by parameter optimization is yet to be tested. The glass-PMMA-Si configuration can potentially open new avenue for wider material choices for both the substrate and the nanostructures. In plasmonic applications, the optical properties can be tuned more flexibly by enabling versatile metals.

4.5 Large-scale deposition of DNA origami on surface

The development of HF-free DALI in the last section is only one direction to expand its possible applications. Another possible direction would be to incorporate DALI in a large-scale production and lower its cost. As mentioned in Section 4.1, the Si surface need to be treated with either O_2 plasma or piranha solution to adsorb DNA origami in buffer with high Mg^{2+} concentration. This process limits the surface area and DNA origami choices to some extent. In addition, a large amount of DNA origami were always washed away, hence wasted, after the surface was incubated with origami solution. This unavoidably increased the overall cost of the technique. To avoid this step, deposition of "salt-free" DNA origami on an arbitrary large surface by spray-coating has been developed in article **A.V**.

In the past, print-coating technology has been proven to be very cost-effective and suitable for large-scale production of solution processable materials [147]. But it has not been expanded to the field of structural DNA nanotechnology yet. The basic idea was to homogeneously cover the substrate by using as little DNA origami as possible, while maintaining a preferred final density of DNA origami on the substrate. Instead of dropping a overabundant amount of origami and washing the excess away, the spray-coating method allows deposition of small amount of origami over a large area. Moreover, to achieve the highest cost-effectiveness, the origami solution was left to dry on the surface without any washing in which case every origami was stuck to the surface. In order to eliminate the salt residue, origami solution was spin-filtered right before the deposition to exchange the buffer to pure water.

In this study, four different DNA origami designs were deposited on either silicon wafer or glass slides. The two 2D origami were used already in the DALI method, namely ST and DT (double triangle, one version of the bowtie origami). The other two were 3D origami with the shapes of a hexagonal tube (HT) [30] and

a 60-helix bundle (HB). The 2D origami were used for examination of the results by atomic force microscope, while the 3D origami decorated with fluorescent dye were used for deposition with a polydimethylsiloxane (PDMS) mask and later characterized by fluorescent microscopy.

Buffer exchange and stability

To remove the excess amount of stable strands and/or fluorescent dye from the origami solution and replace the buffer with pure water, the origami solution was purified by a non-destructive spin-filtering process. Fifty μl of DNA solution was diluted to 500 μl with Milli-Q water in a filter column of 100 kDa molecular weight cut-off (MWCO). The column was placed in a 2 ml eppendorf tube and spun at 14,000 rcf for 3 minutes in a centrifuge. The flowthrough was discarded and 450 μl water was added to the filter and centrifuged again. The process was usually repeated 3 times, after which the concentration of Mg^{2+} in the origami solution would be reduced from 12.5-20 mM to 1-4 μM. The stability of DNA origami in water (with

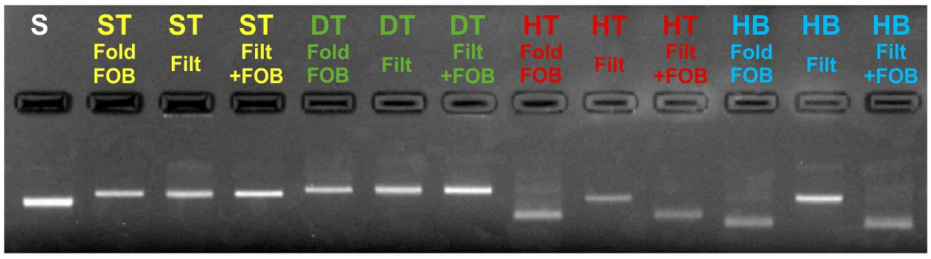

FIGURE 4.20 Agarose gel electrophoresis for all four types of DNA origami structures. Fold = DNA structures after folding in the folding buffer (FOB) (for ST and DT FOB is 1× TAE + 12.5 mM Mg++ and for HT and HB 1× TAE + 20 mM Mg++). Filt = DNA structures filtered with pure water. Filt+FOB = Filtered DNA structures stored in water for 1 day, after which the buffer conditions have been adjusted to the same as for folding. S is a scaffold strand (M13mp18), which is used as a reference sample.

very low Mg^{2+} concentration) was studied by gel electrophoresis. The 2D origami survived very well in water, while 3D DNA origami seemed to undergo some distortion. But it is very surprising that the distortion was reversible as shown in the gel electrophoresis in Fig. 4.20. The longest time tested for the stability in water was 14 weeks. This unexpected robustness of DNA origami in water can simplify many applications in which the salt residues in buffer is undesirable.

Spray-coating

Spray-coating of DNA origami nanostructures was performed with a manual airbrush (nozzle size 300 μm) using compressed air (pressure $\sim$3 bar) as a carrier gas.

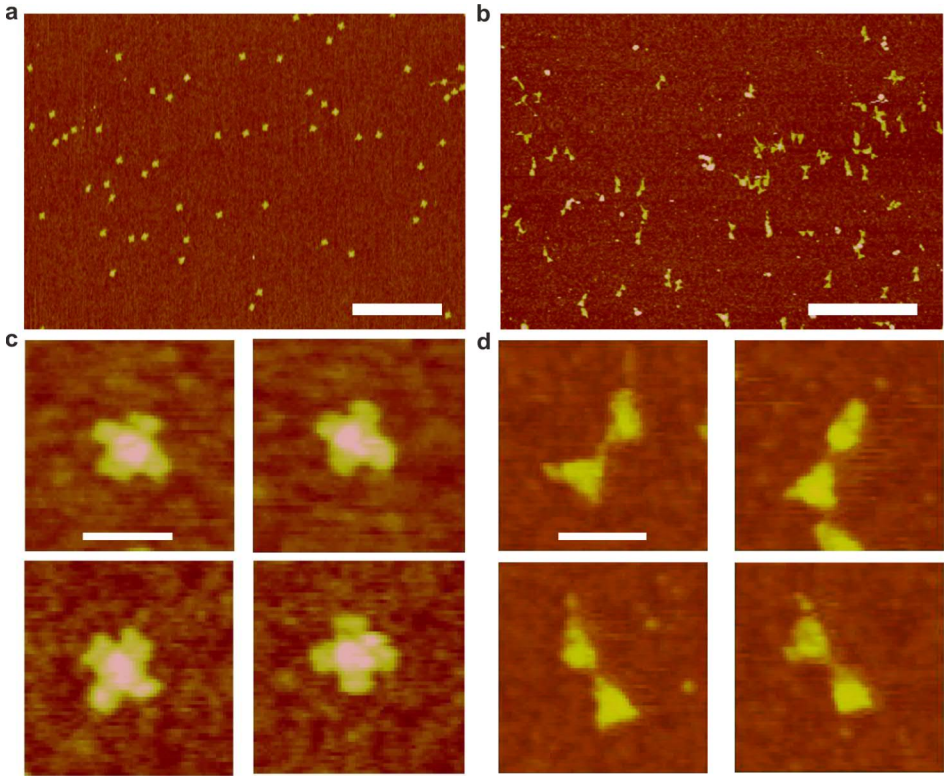

FIGURE 4.21 AFM micrograph of spray-coated ST and DT origami on silicon substrate. **a** and **c**, zoomed out and individual images of ST on Si. The scale bars are 1 μm. **b** and **d**, zoomed out and individual images of DT on Si. The scale bars are 100 nm.

The coating was carried out in a layer by layer fashion. After every deposition layer, the micro-droplets were let to evaporate in ambient conditions.

In the case of 2D DNA origami, 40 μl of the ST or DT with 1 nM concentration were sprayed on silicon substrates of size 10 mm $\times$ 10 mm. While the 3D origami, HT and HB, were used to test the patterning of origami through a macroscopic PDMS mask on glass substrates. A 160 μm thick PDMS mask with round openings was attached to a glass microscope slide, and 40 μl of HT or HB with 10 nM concentration were sprayed on the substrates with the same parameters as the 2D origami. Finally, the PDMS mask was removed from the glass slide.

A homogeneous coverage on untreated Si surfaces was obtained for both ST and DT origami by spray-coating, as shown in Fig. 4.21. In the zoomed out AFM images, both origami, especially STs, were well distributed across the shown area. The DT origami shows a certain degree of agglomeration, which has already happened after the folding process due to an unspecific blunt end stacking, which is typical for this particular design. From Fig. 4.21c,d, one can see that the shapes of both origami were well preserved even after replacing the buffer to pure water. However, due to its high flexibility the DT origami showed slightly bent conformation on surface.

On the other hand, fluorescence microscope images showed that patterning on a glass substrate with the large-scale PDMS mask by spray-coating was also suc-

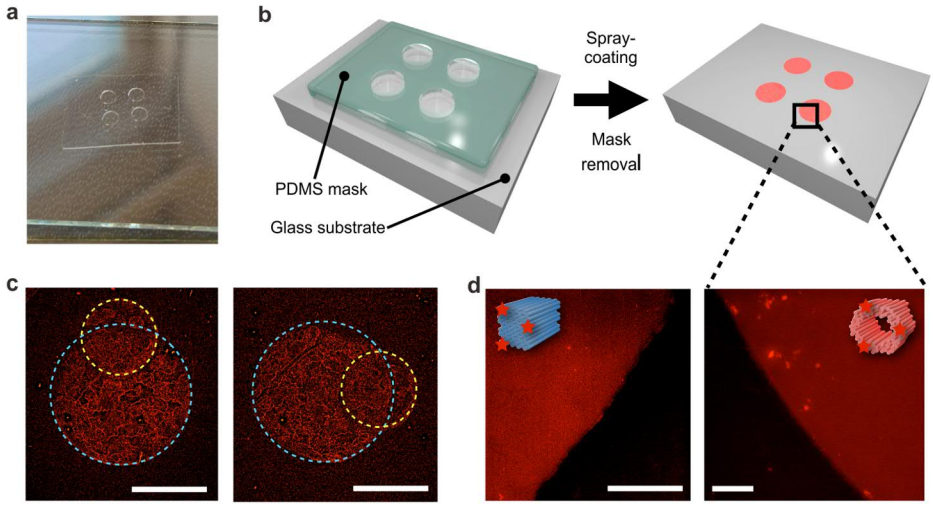

FIGURE 4.22 Patterning substrates with fluorescently labeled DNA origami. **a**, a photograph of a mechanical PDMS mask on top of a glass substrate. **b**, a schematic view of the patterning setup. **c**, Fluorescence micrographs of patterns created using spray-coating of Cy5-labeled HB origamis, two masks, one with large holes, the other with small holes were used sequentially. scale bars are 1 mm. **d**, fluorescence micrographs of the glass slides after they were coated with fluorescently labeled HBs (left) and HTs (right). The scale bars are 50 μm.

cessful, as can be seen from Fig. 4.22. The concentration of origami solution in this case was 10 nM to produce enough contrast for the fluorescence microscope. To note, both the HB and HT were purified before deposition, so the fluorescence signals were solely coming from the labeled DNA origami, not from the free dyes in solution. The micrograph in Fig. 4.22c demonstrates the feasibility of a sequential patterning technique with two different masks.

This spray-coating based method is very applicable for homogeneously deposition of DNA origami on different large-scale substrates without any pre-treatment. It is a straightforward and cost-effective method, since all the DNA origami deposited on the surface will be utilized and no washing is required after the deposition. A rough calculation results in a 1 euro per square meter cost with the current price of self-assembled DNA nano-constructs, which makes the material cost of DNA insignificant in such applications. The presented method can be easily scaled up and it enables fabrication of DNA origami-based samples on flexible substrates.

Chapter 5

Optical measurements of nanostructures made by DALI

Although in the previous chapter the plasmonic nanostructures fabricated by DALI method have been imaged with SEM showing outstanding accuracy and yield, their optical properties (and hence viability in various applications) can only be confirmed by proper optical characterization. In this chapter, three characterization methods are used, namely localized surface plasmon resonance (LSPR) spectroscopy, surface enhanced Raman spectroscopy (SERS) and circular dichroism (CD) spectroscopy. LSPR spectroscopy is the most basic and widely used method to study plasmonic nanoparticles, especially their resonance frequency dependence on material and geometry. SERS was used for testing the field enhancement effect of the bowtie antenna samples and explore their potential applications in molecular sensing. CD was used to verify the chiral optical behavior of the CDL samples. To compare the measured results with theory, theoretical spectra and electric field distributions were essential. However, due to the geometrical complexities of the fabricated nanoparticles, analytical solutions are difficult to calculate. In this case, the finite element method (FEM) simulation was used to solve approximate spectra and electric field distribution numerically.

5.1 LSPR spectroscopy

5.1.1 Measurement setup

LSPR spectroscopy can be realized in many different ways. We employed dark-field light-scattering measurement because it is a powerful method to measure an extremely small region or even individual particles. In this dark-field setup, either the forward or backward scattering can be measured depending on the transparency of the sample. However, the forward scattering is preferred due to the small scattering cross-section of the nanostructures fabricated by DALI. The particles or area of inter-

est is excited with high numerical aperture (NA) dark-field condenser and collected with a lower NA objective. A schematic illustration is shown in Fig. 5.1. In this way, only the scattered light following the LSPR spectrum is detected, providing a better signal-to-noise ratio. The signal was guided through an optical fiber with one end at the image plane of the microscope out port and the other end connected to a charge-coupled device (CCD) spectrometer. Thus the LSPR spectrum of the sample area covered by the end of the fiber in the image plane can be acquired.

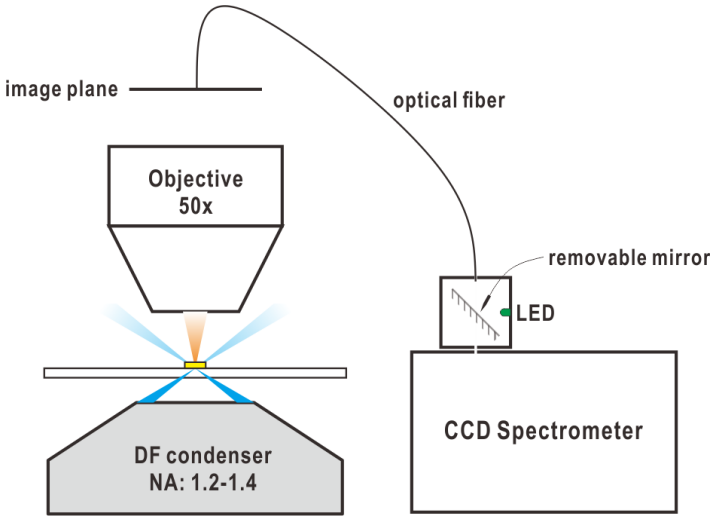

FIGURE 5.1 Dark-field light-scattering setup

To identify which portion of the image the optical fiber is covering, a green LED was used. The LED is placed near the spectrometer and can be reflected to the optical fiber end with a removable mirror. Because of the reversibility of light, the green light emitted from the spectrometer end of the fiber will go though the image plane of the microscope and can be seen with both the ocular and any camera attached to the microscope together with the dark field image of the sample. The diameter of the area where the optical fiber can cover ranges roughly from 10 µm to 50 µm depending on the fiber diameter. Before measurement, the location of the green spot can be recorded and then the LED is turned off and the mirror removed.

With the capability of measuring the spectrum of an area with a diameter of $\sim$ 10 µm, individual particle can be characterized when their density is low enough so that only one particle is presented in that 10 µm$\times$10 µm area. To achieve such a low density, the origami solution was diluted 1000 times before deposited on the substrate. Nevertheless, the correlation between the LSPR spectrum and the geometry of the particle has to be established to enable the simulation and comparison, which requires imaging the exactly same particle with both optical microscope and SEM. Due to their magnification mismatch, markers which can help to recognize sub-area are necessary. For this purpose, grids of 200 µm$\times$200 µm were exposed with UV lithography on the sample before metal deposition.

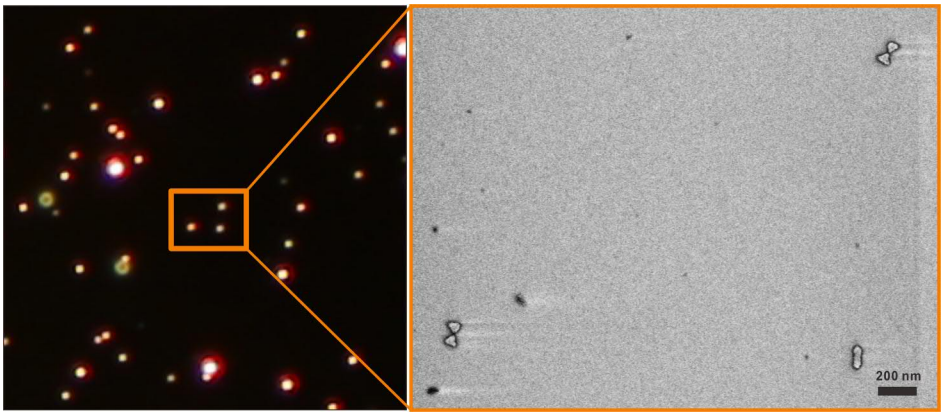

FIGURE 5.2 Dark-field microscope photo of nanostructures on a sapphire chip (left) and corresponding SEM image of a small pattern in the photo (right).

To further identify individual particles, their natural random patterns were used. After fabrication, the sample was first imaged with the optical microscope and photos of grids of interested was taken. Then, the same grids were found under SEM, and the patterns of a few particles can be slowly approached from the border of grid *via* a series of landmarks, like the pattern of three particles in Fig. 5.2. Finally the particles with ideal geometry were selected and their spectra were measured by the optical microscope.

Comparing with chemical synthesis, one advantage of the DALI method is the ability to fabricate complex asymmetric nanostructures. To fully understand the plasmonic properties of these nanostructures and prove they do possess the asymmetric behaviors as intended, spectra of the same particle excited with different electric field directions are needed. For example, the bowtie antenna structure should have very different spectra if the electric field is along the gap or perpendicular to its long axis.

In the field of optics, electric field direction is usually associated with polarization of light and can be manipulated with linearly polarizers. In the ideal case, the nanostructure should be excited with linear polarized light aligned with its geometry. But unfortunately, in the dark-field setup, even if the light come from a linearly polarized source, it will not preserve the polarization after being focused by the condenser.

This effect can be understood as depicted in Fig. 5.3. When unpolarized light passes though two linear polarizers, which are perpendicular to each other, no light will pass the second polarizer ideally, as in Fig. 5.3a. If a lens system is involved like in the case of a bright-field microscope, part of the light at the edge of the lenses will be able to pass the second polarizer. Because the light is bent most significantly at the edges, the direction and hence the polarization of the light is affected most. At the angles (multiplies of 45°) which are between the two polarizer directions, the light leaks most, as in Fig. 5.3b. In the last case with a dark-field condenser, the

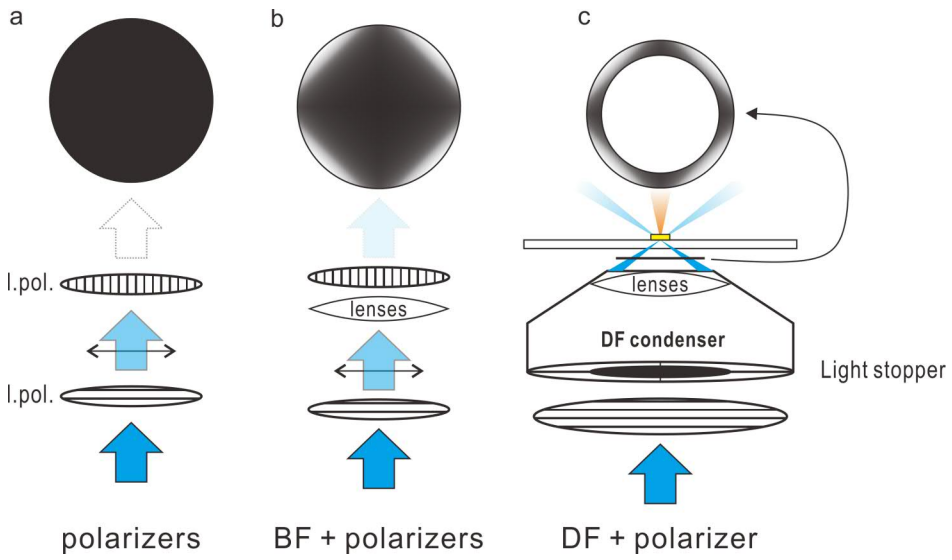

FIGURE 5.3 Schematic view of linear polarizer combined with dark-field condenser.

light-stopper will block the center of the source light beam, and only a ring of light at the perimeter can pass. If a linear polarizer is placed before the DF condenser, the excitation light, which can reach the sample, is hardly polarized since at the perimeter the polarization changes most.

Therefore, instead of exciting the nanostructures with linear polarized light and detecting the outcome, we chose to excite the nanostructures with unpolarized light, but then only measure the scattered light with a certain polarization which can be controlled by an analyzer (rotatable linear polarizer) after the objective. This should yield the same result as exciting with a linearly polarized light, if assuming that the plasmonic excitation does not alter the polarization. Since we are using low light intensities, which is well within a linear region, this is a valid assumption. The polarization angle with respect to the particle geometry can be calibrated before the measurement by aligning the analyzer to the grid with the help of a linear polarizer with a slit mask. The spectra were usually measured with a 15° interval which is limited by the precision of the scales on the analyzer roller.

The scattering spectrum can be calculated from the measurable signals as in Eq.5.1

$$I_{\text{scattering}} = \frac{I_{\text{signal}} - I_{\text{background}}}{I_{\text{lamp}} - I_{\text{darkcurrent}}}, \tag{5.1}$$

where $I_{\text{scattering}}$ is the scattering spectrum, I_{signal} is the measured signal from the plasmonic nanostructure of interest, $I_{\text{background}}$ is the background intensity near the nanostructure, I_{lamp} is the lamp spectrum, $I_{\text{darkcurrent}}$ is the dark current level of the spectrometer without any illumination. To eliminate the stray light scattered from nearby structures, the background was usually taken very near the nanostructure, so most of the irrelevant signal can be canceled after calculation. The lamp spectrum

was taken without sample in the bright field mode.

5.1.2 LSPR spectra and simulation

By using the aforementioned setup and method, numerous individual particles have been characterized. Among these nanostructures, gold bowtie (BO) structures with gaps were particularly emphasized, due to their theoretical divergence between two different axes. Several ST structures were also measured as control spectra since they are more symmetric than the BO structures. The spectra were taken in the wavelength range from 400 nm to ∼900 nm due to the grating and CCD detection limits of the spectrometer.

Bowtie

Most of the measured bowtie structures had two distinguishable modes: one is along the long axis, across the gap, which usually has a peak at longer wavelength (700 nm to 800 nm) and higher intensity; the other is roughly perpendicular to the long axis, with a resonance at shorter wavelengths (650 nm to 700 nm) and lower intensity. The measured LSPR spectra and FEM simulated (COMSOL Multiphysics) results of a typical bowtie are shown in Fig. 5.4. The intensity difference of the two modes is a proof of the existence of a gap mode. The electric field strength of the mode along the gap simulated with COMSOL has the highest field enhancement factor of 114 in the hotspot, *i.e.*, within the gap (Fig. 5.4b). It is 3.75 times higher than the enhancement factor of 24 of the perpendicular mode purely due to the sharp corners in Fig. 5.4c.

Since the resonance of the plasmonic nanoparticle is highly dependent on its size and shape, gold bowtie antenna with the highest gap-mode resonance wavelength in the visible range is very difficult to make by conventional lithography due to their resolution limit. In our case, the resonances of most bowtie antennas by DALI are within the visible region even they are on a sapphire substrate with a refractive index of over 1.7 which red-shifts the resonance. It thus demonstrates the strength of the fabrication method and potential applications in fluorescence enhancement (FE) for dyes in the red wavelengths.

Noticeably, the simulated spectra and the measured spectra are not exactly overlapping with each other, which is partly due to the unavoidable imperfect shape of the fabricated nanostructures. If the two triangles have a minor shape or size variance, their spectra may differ and contribute to a broadened or shifted peak. To reveal the effect of the heterogeneity of the fabricated BO structures on their optical properties, several FEM simulations were performed on gold BO structures with varying bending angles, thicknesses and gap sizes, which corresponded to the observed deformation. The simulated results indicated that the thickness and gap

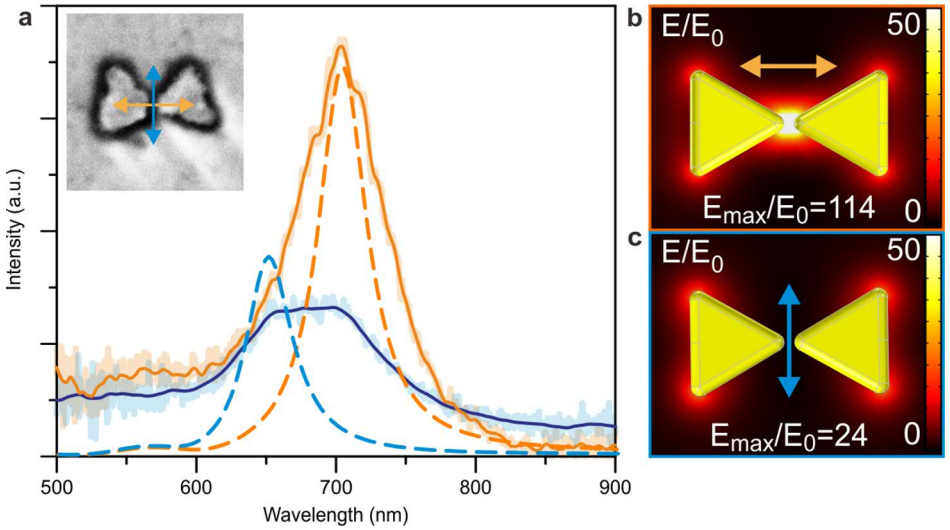

FIGURE 5.4 The measured and simulated LSPR spectra of an individual gold bowtie antenna. **a**, linear polarization LSPR spectra with color code corresponding to the arrows in the inset. Half-transparent areas are measured data points, while solid lines are smoothed data, and dashed lines are the FEM simulations. **b** and **c**, electric field enhancement factors simulated when the bowtie antenna structure is excited with corresponding polarization. The images are adapted and modified from article **A.IV**.

size have minor effects on both the LSPR gap mode and the maximum field enhancement, while the angle between two triangles yielded no noticeable effect (the simulated spectra can be seen in the supporting materials of article **A.IV**).

Cross

Unlike the BO and CDL structures which were designed targeting certain optical properties, ST was only used at the beginning of the DALI development as a test structure. Nonetheless, its symmetrical geometry can be used as a control sample in the LSPR measurement and simulation.

Surprisingly, some of the gold ST structures also showed two modes, though not as diverse as the two modes in the BO case. One of the measured ST particle and corresponding simulation results are shown in Fig. 5.5. The two modes of this particle were in the directions of the two arms perpendicular to each other. If the ST was perfectly symmetric, the two modes should degenerate, but apparently it is not the case. By simulating a cross-shaped particle with different vertical and horizontal arm lengths (the model in Fig. 5.5b and Fig. 5.5c), one can reproduce the two modes with corresponding resonance frequency (Fig. 5.5a dashed lines). However, the intensities of the modes were not exactly same as the measured spectra. It is possible that the divergence of the modes were caused not only by the arm length but also other geometrical attributes, *e.g.*, merging or tilting of the arms.

The LSPR spectroscopy of the particles made by DALI has verified that these metallic nanoparticles indeed exhibited the desired plasmonic properties including

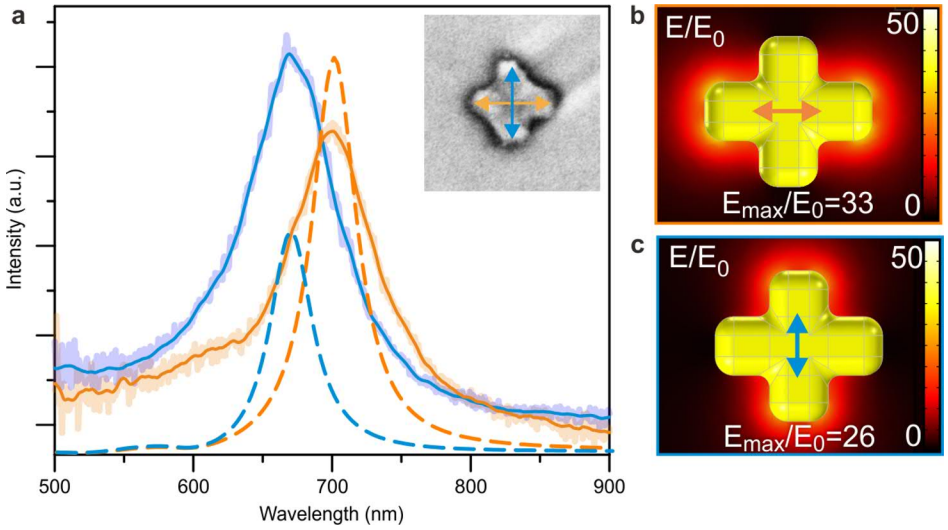

FIGURE 5.5 LSPR spectra and simulation results of an individual gold ST structure. **a**, linear polarization LSPR spectra with color code corresponding to the arrows in inset. Half-transparent area are measured data points, while solid lines are smoothed data, and dashed lines are the FEM simulations. **b** and **c**, electric field enhancement factors simulated when the ST structure is excited with corresponding polarization. The images are adapted and modified from article **A.IV**.

the resonance frequency and polarization dependency. Although the linear polarization measurement was carried out by detection of certain polarization rather than excitation, the results still represent the tendency of the polarization dependency. But on the other hand, the minor mismatches of the measured spectra and the simulation results demonstrate the complexity of these plasmonic nanostructures and how their optical properties are highly sensitive to fabrication defects.

5.2 Surface Enhanced Raman Scattering (SERS)

One of the most anticipated applications of plasmonic nanostructures is Surface Enhanced Raman Scattering or Surface Enhance Raman Spectroscopy (SERS). The SERS takes advantage of the fact that Raman scattering can be greatly enhanced when the scatterer is very near metallic surfaces or nanoparticles due to the electric field enhancement. Generally, the enhancement factor of SERS is proportional to the 4th order of electric field $|E|^4$ because both the excitation and scattering are simultaneously enhanced. In Section 5.1, the simulation of the bowtie antenna showed that the electric field enhancement in the hotspot can be as high as 114. With a 4th order relation, the Raman scattering can be enhanced $\sim 10^8$ times, which makes it very interesting to see whether the bowtie antenna fabricated with DALI can be efficiently used in SERS.

Sample preparation

Gold bowtie antennas were fabricated on a sapphire substrate by DALI, with parameters adjusted for producing a very small ($\sim$10 nm) gap. Approximately 10 µl of molecular marker solution of concentration of 1 µM in ethanol were directly dropped on the sample and naturally dried by evaporation. Two traditional SERS markers were used, namely Rhodamine 6G (R6G) and 2,2'-bipyridine (bipy).

Instrumentation

For the Raman measurement, a Bruker SENTERRA Raman Microscope was employed. It comprises a dispersive Raman spectrometer module and a confocal microscope module. In the Raman module, 785 nm wavelength laser with 100 mW power was used as an excitation, Raman scattering was detected by a spectrometer equipped with a Peltier cooled (-70°C) charge-coupled device (CCD) camera and a diffraction grating (1200 grooves/mm). A spectral resolution of 2 cm^{-1} was adjusted with a slit. The main part of the microscope module is a Olympus BX51 reflected light microscope equipped with a motorized sample stage of positioning accuracy of 0.1 µm. During the measurement, the laser power at the sample surface ranged from 1 to 10 mW and acquisition time ranged from 1 to 5 s. The area of the laser spot on the sample was about 1 µm in diameter.

SERS spectra

The SERS spectra of both R6G and bipy were measured with high resolution from the substrate with gold bowtie nanoantennas. The major signature peaks were clearly visible in the spectra as shown in Fig. 5.6a. Moreover, the fact that double or even triple peaks can be resolved, *e.g.*, around 1300 cm^{-1} for R6G and 1600 cm^{-1} for bipy has further demonstrated the spectral resolution. The spectral intensity from different measurement spots may vary, but the shape of the spectrum was very consistent. On the same sample, the SERS signal from the spots where nanostructure was absent was undetectable. The signal-to-noise ratio for this setup was not enough to measure the Raman scattering with the low concentration of molecules. Unfortunately, without a reliable non-enhanced Raman spectrum to compare with, the experimental enhancement factor which the bowtie antennas can provide is impossible to calculate.

According to the measurements on R6G and bipy, the bowtie nanoantenna fabricated with DALI is clearly highly SERS active. Although the enhancement factor has not been acquired yet, the spectral resolution so far appears to be promising. In addition, the results are quite reproducible. In future more sophisticated experimental design and instrument can be used to determine the actual enhancement factor. Furthermore, if the fabrication method without HF etching described in Section 4.4

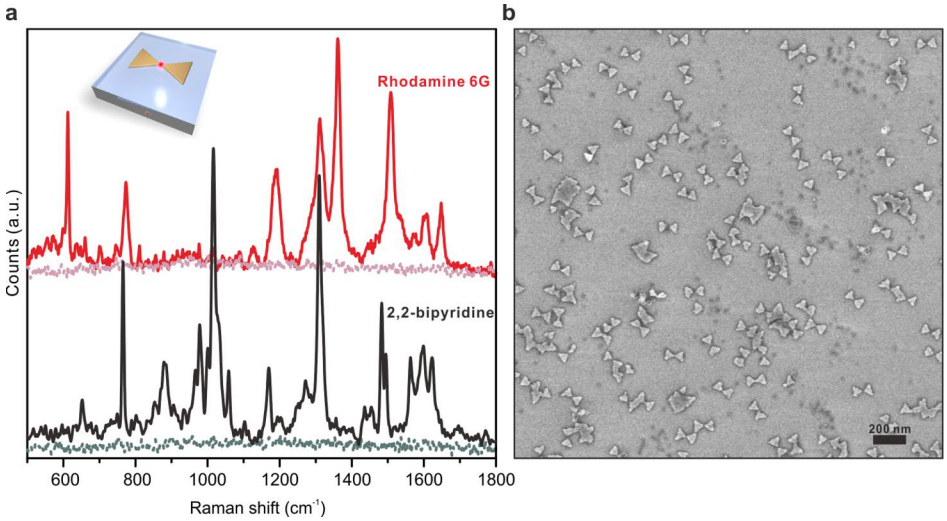

FIGURE 5.6 SERS spectra acquired from gold bowtie antenna substrates. **a**, SERS spectra of Rhodamine 6G (red curve) and 2,2′-bipyridine (black curve), flat lines are signal from the areas without bowtie nanostructures. **b**, a typical SEM image of gold bowtie antennas on sapphire substrate.

can be fully developed, changing the material of bowtie nanostructures from gold to silver can improve the enhancement even more.

5.3 Circular Dichroism (CD) spectroscopy

Circular Dichroism (CD) describes a phenomenon that a material or molecule absorbs left-handed circularly polarized light (L-CPL) and right-handed circularly polarized light (R-CPL) differently. It usually occurs when a molecule contains one or more chiral chromophores. CD spectroscopy is widely used in detecting organic molecules and biological macromolecules, *e.g.*, proteins and nucleic acid. Plasmonic nanostructures can also exhibit CD effect if their 3D geometry is chiral or if their geometry combined with asymmetric dielectric around the particles creates a chiral configuration. Because of their great field enhancement, chiral plasmonic nanostructures with CD effect can be used in improving the sensitivity of detecting chiral molecules. The gold CDL structures fabricated by DALI in Section 4.3.2 were aimed for this purpose. We have performed CD spectroscopy on both S-shaped CDL sample and a sample with roughly half-half S to Z ratio.

A Jasco J-715 CD spectrometer was used for characterizing the CDL samples. The spectrometer uses a 150 W xenon lamp as a source, and a photomultiplier tube (PMT, 400 nm to 1100 nm) as a detector. The source light is monochromatized and converted to linearly-polarized (LP) light by a double monochromator system. Then the LP light is modulated to L-CPL or R-CPL by a modulator which oscillate at 50 kHz frequency and directed to the sample chamber. Finally the absorbance is

detected by the PMT and CD is calculated by the subtraction of the absorbances of L-CPL and R-CPL.

The sapphire substrates with a monolayer of gold CDL nanostructures was placed in the sample chamber of the CD spectrometer perpendicularly to the incident CPL light. A rectangular aperture was closely situated at the backside of the sapphire chip to reduce the diffraction possibly caused by the chip edges.

For the S-CDL sample, in which 99% of the CDLs on the surface adapted an S conformation, characteristic CD spectrum was observed as shown in Fig. 5.7a (blue curve). A clear positive peak at 650 nm and a much wider negative peak around 950 nm can be identified. The widening of the negative peak is probably contributed by the distribution of different arm lengths of CDLs due to the slight folding of the DNA origami after deposition. The FEM simulations of individual CDL particles with different arm lengths (dashed line and dotted dashed line in Fig. 5.7a) supported the theory. While varying the arm length, the negative peak at 950 nm has shifted significantly, while the peak at 650 nm was affected much less.

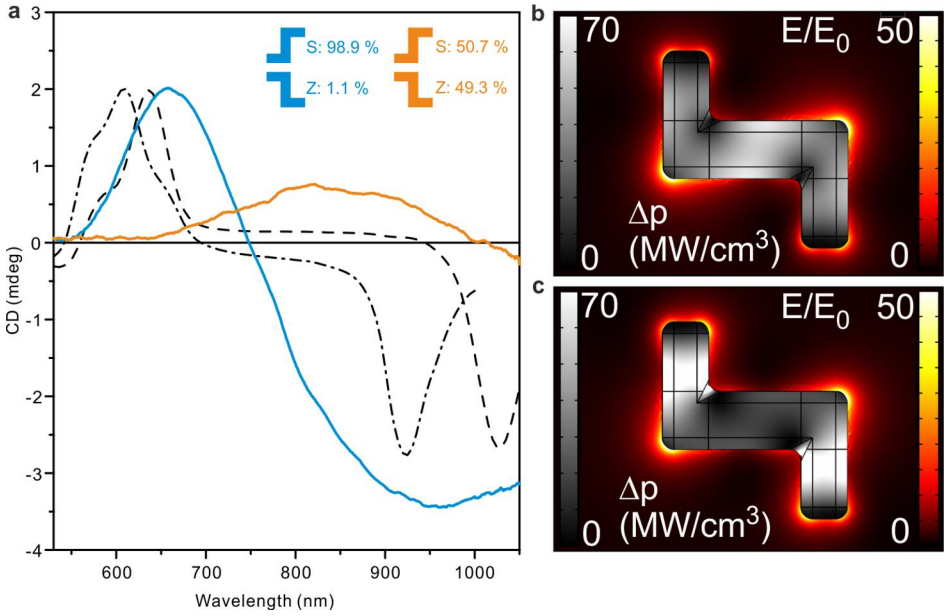

FIGURE 5.7 CD spectra and simulation of CDL samples. **a**, CD spectra of S-CDL sample (blue curve) and half-half CDL sample (orange curve), dashed line is COMSOL simulated CD of a symmetric CDL sample, and dotted dash line is simulated CDL particle with one arm shorter than the other. **b** and **c**, simulated electric field enhancement factor and powerloss of a single CDL particle excited with either L-CPL (**b**) or R-CPL (**c**). The images are adapted from article **A.IV** with modification.

The sample with roughly half S-CDLs and half Z-CDLs ideally should yield no contribution to the CD spectrum, and only a moderate feature around 850 nm was present in the spectrum (Fig. 5.7a orange curve). The origin of this feature could be contributed by the imperfection of the particle geometry or non-even S-to-Z ratio or even the shifting baseline caused by the instrument, which are nontrivial to exam.

However, the CD spectroscopy has clearly demonstrated that by altering the distribution of CDL sample with different handiness, the collective CD response of the sample can be manipulated.

Despite the clearly present CD effect, the intensity of the CD spectra was not very pronounced. However, taking into consideration the fact that the optical density (OD) of the sample was very low owing to only a monolayer of 20 nm thickness CDL structures in the path of the light, it was totally understandable. Not to mention that the CDLs on the surface were randomly organized in a amorphous lattice, the CD spectrum has not been enhanced by any periodicity. Naturally, the intensity of CD can be improved further by fabricating multiple layers of CDL on the same sample or let the DNA origami self-assemble into a lattice structure before performing DALI. In addition, the applicability of CDL structures for biomolecule detection is another important subject to be tested in the future.

Chapter 6

Summary and perspective

The DEP-related article explored the possibility to utilize DNA self-assembled structures in nanoelectronics applications. In **A.I**, four structurally different multilayered DNA origami were trapped between gold nanoelectrodes by DEP force. A yield of 40% to 63% for successful trapping was achieved. However, the trapped DNA origami showed different degrees of deformation, which was especially obvious for the structures in the honeycomb lattice. The deformation was possibly caused by the strong electric field applied and the interaction with the substrate. In addition, the electrical conductivity of the brick samples were characterized by both DC measurement and AC-IS at 90% RH, indicating an insulating behavior. Although some of the samples with multiple thiol-linkers at both ends were destroyed together with the SiO_2 substrate underneath them after DEP trapping, implying a high current flowing through, it is hard to conclude any mechanism for this phenomenon without further investigation. Nevertheless, the high current assumption agrees well with the reduced destruction observed after implementing series resistances.

In **A.II**, an SET-like device based on TX-tile with defined size and conjugated AuNPs were assembled in solution, trapped by DEP between gold electrodes and electrically measured at both the room temperature and low temperatures. Several chemical gold enhancement steps were needed to grow the AuNPs closer to each other in order to bring the device to a state showing Coulomb blockade up to the room temperature.

DEP is one of the very few techniques which can manipulate nanoscale DNA self-assemblies in solution, especially when it comes to connecting pre-assembled electronic devices to mesoscopic circuits. In the future, multilayered DNA origami can be tested as a better template for SET to bring AuNPs even closer, and thus to avoid the somewhat arbitrary chemical growth step. With the help of DEP, these structures can be trapped and measured electrically. However, a reliable yield for mass production will remain as a challenge.

The DALI fabrication method developed in articles **A.III** - **A.V** has shown the potential of DNA nanostructures to be integrated into industrial microfabrication processes. The discrete metallic nanostructures fabricated by evaporating metal

through SiO_2 masks with origami-shaped openings has a very high yield and precisely followed the shape of DNA origami. The parallelity (self-assembly) of DNA origami makes the DALI method easy to be transferred to large-scale fabrication process. For this, a demonstration to deposit DNA origami solution on any large surface without modification has been presented in **A.V**.

The metallic nanostructures fabricated by DALI are particularly useful in plasmonics. The method developed for flat optical grade sapphire substrate enabled various optical measurements, including LSPR, SERS and CD spectroscopy. The positive results of SERS and CD for bowtie antenna and CDL structures, respectively, have demonstrated that noble metal structures with special optical properties can be engineered by DNA nanotechnology.

There are still plenty of room to improve the DALI method, *e.g.*, dedicated reaction chamber for more homogeneous SiO_2 film quality, avoiding aggressive HF etching for wider choices of materials, *e.g.*, by addition of PMMA resist layer, and realization of periodically arranged structures for meta-materials. Even for the currently realized structures, further optical measurements are still to be performed, *e.g.*, fluorescence enhancement for the bowtie antenna, and chiral molecule sensing by the CDL structures.

In summary, although DNA is a biological molecule, the applications of DNA-based self-assemblies in the field of nanophysics, especially nanoelectronics and plasmonics are very unique and promising. The works in this thesis is only a tiny fraction of the efforts have been put into this direction, and therefore more exciting development is expected to appear in the imminent future.

Bibliography

[1] ROTHEMUND, P. W. K., *Folding DNA to create nanoscale shapes and patterns*. Nature **440** (2006) 297–302.

[2] DOUGLAS, S. M., DIETZ, H., LIEDL, T., HÖGBERG, B., GRAF, F., AND SHIH, W. M., *Self-assembly of DNA into nanoscale three-dimensional shapes*. Nature **459** (2009) 414.

[3] DIETZ, H., DOUGLAS, S. M., AND SHIH, W. M., *Folding DNA into twisted and curved nanoscale shapes*. Science **325** (2009) 725–730.

[4] HAN, D., PAL, S., NANGREAVE, J., DENG, Z., LIU, Y., AND YAN, H., *DNA origami with complex curvatures in three-dimensional space*. Science **332** (2011) 342–346.

[5] WATSON, J. D. AND CRICK, F. H. C., *Molecular structure of nucleic acids*. Nature **171** (1953) 737–738.

[6] NELSON, D. L., LEHNINGER, A. L., AND COX, M. M., *Lehninger principles of biochemistry* (Macmillan, 2008).

[7] LINKO, V. AND DIETZ, H., *The enabled state of DNA nanotechnology*. Curr. Opin. Biotechnol. **24** (2013) 555–561.

[8] NUMMELIN, S., KOMMERI, J., KOSTIAINEN, M. A., AND LINKO, V., *Evolution of Structural DNA Nanotechnology*. Adv. Mater. (2018).

[9] SEEMAN, N. C., *Nucleic acid junctions and lattices*. J. Theor. Biol. **99** (1982) 237–247.

[10] KALLENBACH, N. R., MA, R.-I., AND SEEMAN, N. C., *An immobile nucleic acid junction constructed from oligonucleotides*. Nature **305** (1983) 829–831.

[11] MAO, C., SUN, W., AND SEEMAN, N. C., *Designed two-dimensional DNA Holliday junction arrays visualized by atomic force microscopy*. J. Am. Chem. Soc. **121** (1999) 5437–5443.

[12] CHEN, J. AND SEEMAN, N. C., *Synthesis from DNA of a molecule with the connectivity of a cube*. Nature **350** (1991) 631–633.

[13] SEEMAN, N. C., *DNA in a material world*. Nature **421** (2003) 427–432.

[14] LABEAN, T. H., YAN, H., KOPATSCH, J., LIU, F., WINFREE, E., REIF, J. H., AND SEEMAN, N. C., *Construction, analysis, ligation, and self-assembly of DNA triple crossover complexes*. J. Am. Chem. Soc. **122** (2000) 1848–1860.

[15] LI, X., YANG, X., QI, J., AND SEEMAN, N. C., *Antiparallel DNA double crossover molecules as components for nanoconstruction*. J. Am. Chem. Soc. **118** (1996) 6131–6140.

[16] YAN, H., LABEAN, T. H., FENG, L., AND REIF, J. H., *Directed nucleation assembly of DNA tile complexes for barcode-patterned lattices*. Proc. Natl. Acad. Sci. U.S.A. **100** (2003) 8103–8108.

[17] LIU, D., WANG, M., DENG, Z., WALULU, R., AND MAO, C., *Tensegrity: construction of rigid DNA triangles with flexible four-arm DNA junctions*. J. Am. Chem. Soc. **126** (2004) 2324–2325.

[18] YAN, H., PARK, S. H., FINKELSTEIN, G., REIF, J. H., AND LABEAN, T. H., *DNA-templated self-assembly of protein arrays and highly conductive nanowires*. Science **301** (2003) 1882–1884.

[19] ROTHEMUND, P. W., EKANI-NKODO, A., PAPADAKIS, N., KUMAR, A., FYGENSON, D. K., AND WINFREE, E., *Design and characterization of programmable DNA nanotubes*. J. Am. Chem. Soc. **126** (2004) 16344–16352.

[20] LIU, D., PARK, S. H., REIF, J. H., AND LABEAN, T. H., *DNA nanotubes self-assembled from triple-crossover tiles as templates for conductive nanowires*. Proc. Natl. Acad. Sci. U.S.A. **101** (2004) 717–722.

[21] GOODMAN, R. P., BERRY, R. M., AND TURBERFIELD, A. J., *The single-step synthesis of a DNA tetrahedron*. Chem. Commun. (2004) 1372–1373.

[22] GOODMAN, R. P., SCHAAP, I. A., TARDIN, C. F., ERBEN, C. M., BERRY, R. M., SCHMIDT, C. F., AND TURBERFIELD, A. J., *Rapid chiral assembly of rigid DNA building blocks for molecular nanofabrication*. Science **310** (2005) 1661–1665.

[23] SHIH, W. M., QUISPE, J. D., AND JOYCE, G. F., *A 1.7-kilobase single-stranded DNA that folds into a nanoscale octahedron*. Nature **427** (2004) 618.

[24] WEI, B., DAI, M., AND YIN, P., *Complex shapes self–assembled from single–stranded DNA tiles*. Nature **485** (2012) 623.

[25] KE, Y., ONG, L. L., SHIH, W. M., AND YIN, P., *Three-dimensional structures self-assembled from DNA bricks*. Science **338** (2012) 1177–1183.

[26] ZHANG, F., JIANG, S., WU, S., LI, Y., MAO, C., LIU, Y., AND YAN, H., *Complex wireframe DNA origami nanostructures with multi-arm junction vertices*. Nat. Nanotechnol. **10** (2015) 779–784.

[27] VENEZIANO, R., RATANALERT, S., ZHANG, K., ZHANG, F., YAN, H., CHIU, W., AND BATHE, M., *Designer nanoscale DNA assemblies programmed from the top down*. Science **352** (2016) 1534–1534.

[28] BENSON, E., MOHAMMED, A., GARDELL, J., MASICH, S., CZEIZLER, E., ORPONEN, P., AND HÖGBERG, B., *DNA rendering of polyhedral meshes at the nanoscale*. Nature **523** (2015) 441–444.

[29] VOIGT, N. V., TØRRING, T., ROTARU, A., JACOBSEN, M. F., RAVNSBÆK, J. B., SUBRAMANI, R., MAMDOUH, W., KJEMS, J., MOKHIR, A., BESENBACHER, F., *et al.*, *Single-molecule chemical reactions on DNA origami*. Nat. Nanotechnol. **5** (2010) 200–203.

[30] LINKO, V., EERIKÄINEN, M., AND KOSTIAINEN, M. A., *A modular DNA origami-based enzyme cascade nanoreactor*. Chem. Commun. **51** (2015) 5351–5354.

[31] KUZYK, A., LAITINEN, K. T., AND TÖRMÄ, P., *DNA origami as a nanoscale template for protein assembly*. Nanotechnology **20** (2009) 235305.

[32] KUZYK, A., SCHREIBER, R., FAN, Z., PARDATSCHER, G., ROLLER, E.-M., HOGELE, A., SIMMEL, F. C., GOVOROV, A. O., AND LIEDL, T., *DNA-based self-assembly of chiral plasmonic nanostructures with tailored optical response*. Nature **483** (2012) 311–314.

[33] LAN, X., CHEN, Z., DAI, G., LU, X., NI, W., AND WANG, Q., *Bifacial DNA origami-directed discrete, three-dimensional, anisotropic plasmonic nanoarchitectures with tailored optical chirality*. J. Am. Chem. Soc. **135** (2013) 11441–11444.

[34] CHEN, Z., LAN, X., AND WANG, Q., *DNA Origami Directed Large-Scale Fabrication of Nanostructures Resembling Room Temperature Single-Electron Transistors*. Small **9** (2013) 3567–3571.

[35] MAUNE, H. T., HAN, S.-P., BARISH, R. D., BOCKRATH, M., GODDARD III, W. A., ROTHEMUND, P. W., AND WINFREE, E., *Self-assembly of carbon nanotubes into two-dimensional geometries using DNA origami templates*. Nat. Nanotechnol. **5** (2010) 61–66.

[36] ESKELINEN, A.-P., KUZYK, A., KALTIAISENAHO, T. K., TIMMERMANS, M. Y., NASIBULIN, A. G., KAUPPINEN, E. I., AND TÖRMÄ, P., *Assembly of Single-Walled Carbon Nanotubes on DNA-Origami Templates through Streptavidin–Biotin Interaction*. Small **7** (2011) 746–750.

[37] GOPINATH, A., MIYAZONO, E., FARAON, A., AND ROTHEMUND, P. W., *Engineering and mapping nanocavity emission via precision placement of DNA origami*. Nature **535** (2016) 401–405.

[38] KNUDSEN, J. B., LIU, L., BANK KODAL, A. L., MADSEN, M., LI, Q., SONG, J., WOEHRSTEIN, J. B., WICKHAM, S. F. J., STRAUSS, M. T., SCHUEDER, F., VINTHER, J., KRISSANAPRASIT, A., GUDNASON, D., SMITH, A. A. A., OGAKI, R., ZELIKIN, A. N., BESENBACHER, F., BIRKEDAL, V., YIN, P., SHIH, W. M., JUNGMANN, R., DONG, M., AND GOTHELF, K. V., *Routing of individual polymers in designed patterns*. Nat. Nanotechnol. **10** (2015) 892–898.

[39] SCHREIBER, R., DO, J., ROLLER, E.-M., ZHANG, T., SCHÜLLER, V. J., NICKELS, P. C., FELDMANN, J., AND LIEDL, T., *Hierarchical assembly of metal nanoparticles, quantum dots and organic dyes using DNA origami scaffolds*. Nat. Nanotechnol. **9** (2014) 74–78.

[40] KUZYK, A., SCHREIBER, R., ZHANG, H., GOVOROV, A. O., LIEDL, T., AND LIU, N., *Reconfigurable 3D plasmonic metamolecules*. Nat. Mater. **13** (2014) 862.

[41] LIU, N. AND LIEDL, T., *DNA-Assembled Advanced Plasmonic Architectures*. Chem. Rev. (2018).

[42] KUZYK, A., JUNGMANN, R., P. ACUNA, G., AND LIU, N., *DNA Origami Route for Nanophotonics*. ACS Photonics (2018).

[43] ACUNA, G., MÖLLER, F., HOLZMEISTER, P., BEATER, S., LALKENS, B., AND TINNEFELD, P., *Fluorescence enhancement at docking sites of DNA-directed self-assembled nanoantennas*. Science **338** (2012) 506–510.

[44] KÜHLER, P., ROLLER, E.-M., SCHREIBER, R., LIEDL, T., LOHMÜLLER, T., AND FELDMANN, J., *Plasmonic DNA-origami nanoantennas for surface-enhanced Raman spectroscopy*. Nano Lett. **14** (2014) 2914–2919.

[45] THACKER, V. V., HERRMANN, L. O., SIGLE, D. O., ZHANG, T., LIEDL, T., BAUMBERG, J. J., AND KEYSER, U. F., *DNA origami based assembly of gold nanoparticle dimers for surface-enhanced Raman scattering*. Nat. Commun. **5** (2014) 3448.

[46] PILO-PAIS, M., WATSON, A., DEMERS, S., LABEAN, T., AND FINKELSTEIN, G., *Surface-enhanced Raman scattering plasmonic enhancement using DNA origami-based complex metallic nanostructures*. Nano Lett. **14** (2014) 2099–2104.

[47] HUNG, A. M., MICHEEL, C. M., BOZANO, L. D., OSTERBUR, L. W., WALLRAFF, G. M., AND CHA, J. N., *Large-area spatially ordered arrays of gold nanoparticles directed by lithographically confined DNA origami*. Nat. Nanotechnol. **5** (2010) 121–6.

[48] ANDERSEN, E. S., DONG, M., NIELSEN, M. M., JAHN, K., SUBRAMANI, R., MAMDOUH, W., GOLAS, M. M., SANDER, B., STARK, H., OLIVEIRA, C. L., *et al.*, *Self-assembly of a nanoscale DNA box with a controllable lid*. Nature **459** (2009) 73.

[49] LO, P. K., KARAM, P., ALDAYE, F. A., MCLAUGHLIN, C. K., HAMBLIN, G. D., COSA, G., AND SLEIMAN, H. F., *Loading and selective release of cargo in DNA nanotubes with longitudinal variation*. Nat. Chem. **2** (2010) 319–328.

[50] ORA, A., JÄRVIHAAVISTO, E., ZHANG, H., AUVINEN, H., SANTOS, H. A., KOSTIAINEN, M. A., AND LINKO, V., *Cellular delivery of enzyme-loaded DNA origami*. Chem. Commun. **52** (2016) 14161–14164.

[51] FUNKE, J. J., KETTERER, P., LIELEG, C., SCHUNTER, S., KORBER, P., AND DIETZ, H., *Uncovering the forces between nucleosomes using DNA origami*. Sci. Adv. **2** (2016) e1600974.

[52] KETTERER, P., WILLNER, E. M., AND DIETZ, H., *Nanoscale rotary apparatus formed from tight-fitting 3D DNA components*. Sci. Adv. **2** (2016) e1501209.

[53] FLOOD, A. H., STODDART, J. F., STEUERMAN, D. W., AND HEATH, J. R., *Whence molecular electronics?* Science **306** (2004) 2055–2056.

[54] DEKKER, C. AND RATNER, M., *Electronic properties of DNA*. Phys. World **14** (2001) 29.

[55] ELEY, D. D. AND SPIVEY, D. I., *Semiconductivity of organic substances. Part 9. Nucleic acid in the dry state*. Trans. Faraday Soc. **58** (1962) 411–415.

[56] MURPHY, C. J., ARKIN, M. R., JENKINS, Y., GHATLIA, N. D., BOSSMANN, S. H., TURRO, N. J., AND BARTON, J. K., *Long-range photoinduced electron transfer through a DNA helix*. Science **262** (1993) 1025–1029.

[57] KELLEY, S. O., HOLMLIN, R. E., STEMP, E. D. A., AND BARTON, J. K., *Photoinduced electron transfer in ethidium-modified DNA duplexes: dependence on distance and base stacking*. J. Am. Chem. Soc. **119** (1997) 9861–9870.

[58] LEWIS, F. D., WU, T., ZHANG, Y., LETSINGER, R. L., GREENFIELD, S. R., AND WASIELEWSKI, M. R., *Distance-dependent electron transfer in DNA hairpins*. Science **277** (1997) 673–676.

[59] MEADE, T. J. AND KAYYEM, J. F., *Electron Transfer through DNA: Site-Specific Modification of Duplex DNA with Ruthenium Donors and Acceptors*. Angew. Chem. Int. Ed. **34** (1995) 352–354.

[60] NÚÑEZ, M. E., HALL, D. B., AND BARTON, J. K., *Long-range oxidative damage to DNA: effects of distance and sequence*. Chem Biol. **6** (1999) 85–97.

[61] LY, D., SANII, L., AND SCHUSTER, G. B., *Mechanism of charge transport in DNA: internally-linked anthraquinone conjugates support phonon-assisted polaron hopping*. J. Am. Chem. Soc. **121** (1999) 9400–9410.

[62] GIESE, B., AMAUDRUT, J., KOHLER, A.-K., SPORMANN, M., AND WESSELY, S., *Direct observation of hole transfer through DNA by hopping between adenine bases and by tunnelling*. Nature **412** (2001) 318.

[63] FINK, H.-W. AND SCHONENBERGER, C., *Electrical conduction through DNA molecules*. Nature **398** (1999) 407.

[64] BRAUN, E., EICHEN, Y., SIVAN, U., AND BEN-YOSEPH, G., *DNA-templated assembly and electrode attachment of a conducting silver wire*. Nature **391** (1998) 775.

[65] PORATH, D., BEZRYADIN, A., DE VRIES, S., AND DEKKER, C., *Direct measurement of electrical transport through DNA molecules*. Nature **403** (2000) 635.

[66] KASUMOV, A. Y., KOCIAK, M., GUERON, S., REULET, B., VOLKOV, V. T., KLINOV, D. V., AND BOUCHIAT, H., *Proximity-induced superconductivity in DNA*. Science **291** (2001) 280–282.

[67] ENDRES, R. G., COX, D. L., AND SINGH, R. R., *Colloquium: The quest for high-conductance DNA*. Rev. Mod. Phys. **76** (2004) 195.

[68] PORATH, D., LAPIDOT, N., AND GOMEZ-HERRERO, J., *Charge transport in DNA-based devices*, in *Introducing Molecular Electronics* (Springer, 2006), pp. 411–444.

[69] LINKO, V. AND TOPPARI, J. J., *Self-assembled DNA-based structures for nanoelectronics*. Journal of Self-Assembly and Molecular Electronics (SAME) **1** (2013) 101–124.

[70] HIPPS, K. W., *It's all about contacts*. Science **294** (2001) 536–537.

[71] TUUKKANEN, S., KUZYK, A., TOPPARI, J., HYTÖNEN, V., IHALAINEN, T., AND TÖRMÄ, P., *Dielectrophoresis of nanoscale double-stranded DNA and humidity effects on its electrical conductivity*. Appl. Phys. Lett. **87** (2005) 183102.

[72] VEDALA, H., ROY, S., DOUD, M., MATHEE, K., HWANG, S., JEON, M., AND CHOI, W., *The effect of environmental factors on the electrical conductivity of a single oligo-DNA molecule measured using single-walled carbon nanotube nanoelectrodes*. Nanotechnology **19** (2008) 265704.

[73] LINKO, V., PAASONEN, S.-T., KUZYK, A., TÖRMÄ, P., AND TOPPARI, J. J., *Characterization of the conductance mechanisms of DNA origami by AC impedance spectroscopy*. Small **5** (2009) 2382–2386.

[74] LINKO, V., LEPPINIEMI, J., PAASONEN, S.-T., HYTÖNEN, V. P., AND TOPPARI, J. J., *Defined-size DNA triple crossover construct for molecular electronics: modification, positioning and conductance properties*. Nanotechnology **22** (2011) 275610.

[75] TURKEVICH, J., STEVENSON, P. C., AND HILLIER, J., *The formation of colloidal gold*. J. Phys. Chem. **57** (1953) 670–673.

[76] MIRKIN, C. A., LETSINGER, R. L., MUCIC, R. C., AND STORHOFF, J. J., *A DNA-based method for rationally assembling nanoparticles into macroscopic materials*. Nature **382** (1996) 607–609.

[77] ALIVISATOS, A. P., JOHNSSON, K. P., PENG, X., WILSON, T. E., *et al.*, *Organization of 'nanocrystal molecules' using DNA*. Nature **382** (1996) 609.

[78] CHEN, S. AND CARROLL, D. L., *Synthesis and characterization of truncated triangular silver nanoplates*. Nano Lett. **2** (2002) 1003–1007.

[79] PÉREZ-JUSTE, J., PASTORIZA-SANTOS, I., LIZ-MARZÁN, L. M., AND MULVANEY, P., *Gold nanorods: synthesis, characterization and applications*. Coord. Chem. Rev. **249** (2005) 1870–1901.

[80] ZHAO, W.-B., ZHU, J.-J., AND CHEN, H.-Y., *Photochemical preparation of rectangular PbSe and CdSe nanoparticles*. J. Cryst. Growth **252** (2003) 587–592.

[81] KUMAR, P. S., PASTORIZA-SANTOS, I., RODRIGUEZ-GONZALEZ, B., DE ABAJO, F. J. G., AND LIZ-MARZAN, L. M., *High-yield synthesis and optical response of gold nanostars*. Nanotechnology **19** (2007) 015606.

[82] BRUST, M., WALKER, M., BETHELL, D., SCHIFFRIN, D. J., AND WHYMAN, R., *Synthesis of thiol-derivatised gold nanoparticles in a two-phase liquid–liquid system*. J. Chem. Soc., Chem. Commun. (1994) 801–802.

[83] LOVE, J. C., ESTROFF, L. A., KRIEBEL, J. K., NUZZO, R. G., AND WHITESIDES, G. M., *Self-assembled monolayers of thiolates on metals as a form of nanotechnology*. Chem. Rev. **105** (2005) 1103–1170.

[84] DUROCHER, S., REZAEE, A., HAMM, C., RANGAN, C., MITTLER, S., AND MUTUS, B., *Disulfide-linked, gold nanoparticle based reagent for detecting small molecular weight thiols*. J. Am. Chem. Soc. **131** (2009) 2475–2477.

[85] UVDAL, K., PERSSON, I., AND LIEDBERG, B., *Tricyclohexylphosphine adsorbed on gold*. Langmuir **11** (1995) 1252–1256.

[86] LEFF, D. V., BRANDT, L., AND HEATH, J. R., *Synthesis and characterization of hydrophobic, organically-soluble gold nanocrystals functionalized with primary amines*. Langmuir **12** (1996) 4723–4730.

[87] BRAUN, E., EICHEN, Y., SIVAN, U., AND BEN-YOSEPH, G., *DNA-templated assembly and electrode attachment of a conducting silver wire*. Nature **391** (1998) 775.

[88] WIRGES, C. T., TIMPER, J., FISCHLER, M., SOLOGUBENKO, A. S., MAYER, J., SIMON, U., AND CARELL, T., *Controlled nucleation of DNA metallization*. Angew. Chem. Int. Ed. **48** (2009) 219–223.

[89] PUCHKOVA, A., SOKOLOV, P., AND KASYANENKO, N., *Metallization of DNA on the surface*. J. Struct. Chem. **52** (2011) 1195–1201.

[90] RICHTER, J., SEIDEL, R., KIRSCH, R., MERTIG, M., POMPE, W., PLASCHKE, J., AND SCHACKERT, H. K., *Nanoscale palladium metallization of DNA*. Nanoscale **94** (2000) 8720.

[91] NGUYEN, K., MONTEVERDE, M., FILORAMO, A., GOUX-CAPES, L., LYONNAIS, S., JEGOU, P., VIEL, P., GOFFMAN, M., AND BOURGOIN, J.-P., *Synthesis of Thin and Highly Conductive DNA-Based Palladium Nanowires*. Adv. Mater. **20** (2008) 1099–1104.

[92] MERTIG, M., COLOMBI CIACCHI, L., SEIDEL, R., POMPE, W., AND DE VITA, A., *DNA as a selective metallization template*. Nano Lett. **2** (2002) 841–844.

[93] SEIDEL, R., COLOMBI CIACCHI, L., WEIGEL, M., POMPE, W., AND MERTIG, M., *Synthesis of platinum cluster chains on DNA templates: conditions for a template-controlled cluster growth*. J. Phys. Chem. B **108** (2004) 10801–10811.

[94] BECERRIL, H. A., LUDTKE, P., WILLARDSON, B. M., AND WOOLLEY, A. T., *DNA-templated nickel nanostructures and protein assemblies*. Langmuir **22** (2006) 10140–10144.

[95] SWAMI, A. S., BRUN, N., AND LANGEVIN, D., *Phase transfer of gold metallized DNA*. J. Cluster Sci. **20** (2009) 281–290.

[96] FISCHLER, M., SIMON, U., NIR, H., EICHEN, Y., BURLEY, G. A., GIERLICH, J., GRAMLICH, P. M., AND CARELL, T., *Formation of bimetallic Ag–Au nanowires by metallization of artificial DNA duplexes*. Small **3** (2007) 1049–1055.

[97] KEREN, K., KRUEGER, M., GILAD, R., BEN-YOSEPH, G., SIVAN, U., AND BRAUN, E., *Sequence-specific molecular lithography on single DNA molecules*. Science **297** (2002) 72–75.

[98] MONSON, C. F. AND WOOLLEY, A. T., *DNA-templated construction of copper nanowires*. Nano Lett. **3** (2003) 359–363.

[99] ZINCHENKO, A. A., YOSHIKAWA, K., AND BAIGL, D., *DNA-Templated Silver Nanorings*. Adv. Mater. **17** (2005) 2820–2823.

[100] CHEN, N., ZINCHENKO, A. A., AND YOSHIKAWA, K., *Probing biopolymer conformation by metallization with noble metals*. Nanotechnology **17** (2006) 5224.

[101] PU, S.-Y., ZINCHENKO, A., QIN, L.-L., YE, C.-W., XU, M., AND MURATA, S., *Photochemical metallization to fabricate DNA-templated gold nanorings*. Mater. Lett. **130** (2014) 168–171.

[102] BERTI, L., ALESSANDRINI, A., AND FACCI, P., *DNA-templated photoinduced silver deposition*. J. Am. Chem. Soc. **127** (2005) 11216–11217.

[103] YANG, L., SUN, B., MENG, F., ZHANG, M., CHEN, X., LI, M., AND LIU, J., *One-step synthesis of UV-induced Pt nanotrees on the surface of DNA network*. Mater. Res. Bull. **44** (2009) 1270–1274.

[104] ERLER, C., GÜNTHER, K., AND MERTIG, M., *Photo-induced synthesis of DNA-templated metallic nanowires and their integration into micro-fabricated contact arrays*. Appl. Surf. Sci. **255** (2009) 9647–9651.

[105] KEREN, K., BERMAN, R. S., BUCHSTAB, E., SIVAN, U., AND BRAUN, E., *DNA-templated carbon nanotube field-effect transistor*. Science **302** (2003) 1380–1382.

[106] LIU, J., GENG, Y., POUND, E., GYAWALI, S., ASHTON, J. R., HICKEY, J., WOOLLEY, A. T., AND HARB, J. N., *Metallization of branched DNA origami for nanoelectronic circuit fabrication*. ACS Nano **5** (2011) 2240–2247.

[107] PILO-PAIS, M., GOLDBERG, S., SAMANO, E., LABEAN, T., AND FINKELSTEIN, G., *Connecting the nanodots: programmable nanofabrication of fused metal shapes on DNA templates*. Nano Lett. **11** (2011) 3489–3492.

[108] SCHREIBER, R., KEMPTER, S., HOLLER, S., SCHÜLLER, V., SCHIFFELS, D., SIMMEL, S. S., NICKELS, P. C., AND LIEDL, T., *DNA origami-templated growth of arbitrarily shaped metal nanoparticles*. Small **7** (2011) 1795–1799.

[109] LIU, H., CHEN, Y., HE, Y., RIBBE, A. E., AND MAO, C., *Approaching the limit: can one DNA oligonucleotide assemble into large nanostructures?* Angew. Chem. Int. Ed. **45** (2006) 1942–1945.

[110] GENG, Y., LIU, J., POUND, E., GYAWALI, S., HARB, J. N., AND WOOLLEY, A. T., *Rapid metallization of lambda DNA and DNA origami using a Pd seeding method*. J. Mater. Chem. **21** (2011) 12126–12131.

[111] GENG, Y., PEARSON, A. C., GATES, E. P., UPRETY, B., DAVIS, R. C., HARB, J. N., AND WOOLLEY, A. T., *Electrically conductive gold-and copper-metallized DNA origami nanostructures*. Langmuir **29** (2013) 3482–3490.

[112] PEARSON, A. C., LIU, J., POUND, E., UPRETY, B., WOOLLEY, A. T., DAVIS, R. C., AND HARB, J. N., *DNA origami metallized site specifically to form electrically conductive nanowires*. J. Phys. Chem. B **116** (2012) 10551–10560.

[113] UPRETY, B., GATES, E. P., GENG, Y., WOOLLEY, A. T., AND HARB, J. N., *Site-specific metallization of multiple metals on a single DNA Origami template*. Langmuir **30** (2014) 1134–1141.

[114] SUN, W., BOULAIS, E., HAKOBYAN, Y., WANG, W. L., GUAN, A., BATHE, M., AND YIN, P., *Casting inorganic structures with DNA molds*. Science **346** (2014) 1258361.

[115] HELMI, S., ZIEGLER, C., KAUERT, D. J., AND SEIDEL, R., *Shape-controlled synthesis of gold nanostructures using DNA origami molds*. Nano Lett. **14** (2014) 6693–6698.

[116] DENG, Z. AND MAO, C., *Molecular lithography with DNA nanostructures*. Angew. Chem. Int. Ed. **43** (2004) 4068–4070.

[117] BECERRIL, H. A. AND WOOLLEY, A. T., *DNA shadow nanolithography*. Small **3** (2007) 1534–1538.

[118] JIN, Z., SUN, W., KE, Y., SHIH, C.-J., PAULUS, G. L., WANG, Q. H., MU, B., YIN, P., AND STRANO, M. S., *Metallized DNA nanolithography for encoding and transferring spatial information for graphene patterning*. Nat. Commun. **4** (2013) 1663.

[119] SURWADE, S. P., ZHOU, F., WEI, B., SUN, W., POWELL, A., O'DONNELL, C., YIN, P., AND LIU, H., *Nanoscale Growth and Patterning of Inorganic Oxides Using DNA Nanostructure Templates*. J. Am. Chem. Soc. **135** (2013) 6778–6781.

[120] SURWADE, S. P., ZHAO, S., AND LIU, H., *Molecular lithography through DNA-mediated etching and masking of SiO2*. J. Am. Chem. Soc. **133** (2011) 11868–11871.

[121] ZHOU, F., MICHAEL, B., SURWADE, S. P., RICARDO, K. B., ZHAO, S., AND LIU, H., *Mechanistic Study of the Nanoscale Negative-Tone Pattern Transfer from DNA Nanostructures to SiO2*. Chem. Mater. **27** (2015) 1692–1698.

[122] POHL, H. A., *Some effects of nonuniform fields on dielectrics*. J. Appl. Phys. **29** (1958) 1182–1188.

[123] JONES, T., *Electromechanics of Particles* (Cambridge University Press, 1995).

[124] ZHENG, L., BRODY, J. P., AND BURKE, P. J., *Electronic manipulation of DNA, proteins, and nanoparticles for potential circuit assembly*. Biosens. Bioelectron. **20** (2004) 606–619.

[125] POHL, H. A., *Dielectrophoresis the behavior of neutral matter in nonuniform electric fields.* (Cambridge University Press, 1978).

[126] CASTELLANOS, A., RAMOS, A., GONZALEZ, A., GREEN, N. G., AND MORGAN, H., *Electrohydrodynamics and dielectrophoresis in microsystems: scaling laws*. J. Phys. D: Appl. Phys. **36** (2003) 2584.

[127] MASUDA, S., WASHIZU, M., AND KAWABATA, I., *Movement of blood cells in liquid by nonuniform traveling field*. IEEE Trans. Ind. Appl. **24** (1988) 217–222.

[128] MARKX, G. H. AND PETHIG, R., *Dielectrophoretic separation of cells: continuous separation*. Biotechnol. Bioeng. **45** (1995) 337–343.

[129] MORGAN, H., HUGHES, M. P., AND GREEN, N. G., *Separation of submicron bioparticles by dielectrophoresis*. Biophys. J. **77** (1999) 516–525.

[130] HÖLZEL, R. AND BIER, F. F., *Dielectrophoretic manipulation of DNA*. IEE Proc.: Nanobiotechnol. **150** (2003) 47–53(6).

[131] CICORIA, R. AND SUN, Y., *Dielectrophoretically trapping semiconductive carbon nanotube networks*. Nanotechnology **19** (2008) 485303.

[132] VIJAYARAGHAVAN, A., BLATT, S., WEISSENBERGER, D., ORON-CARL, M., HENNRICH, F., GERTHSEN, D., HAHN, H., AND KRUPKE, R., *Ultra-large-scale directed assembly of single-walled carbon nanotube devices*. Nano Lett. **7** (2007) 1556–1560.

[133] HAKALA, T. K., LINKO, V., ESKELINEN, A.-P., TOPPARI, J. J., KUZYK, A., AND TÖRMÄ, P., *Field-Induced Nanolithography for High-Throughput Pattern Transfer*. Small **5** (2009) 2683–2686.

[134] TUUKKANEN, S., KUZYK, A., TOPPARI, J. J., HÄKKINEN, H., HYTÖNEN, V. P., NISKANEN, E., RINKIÖ, M., AND TÖRMÄ, P., *Trapping of 27 bp–8 kbp*

DNA and immobilization of thiol-modified DNA using dielectrophoresis. Nanotechnology **18** (2007) 295204.

[135] JACKSON, J. D., *Classical electrodynamics* (John Wiley & Sons, 1999).

[136] BOHREN, C. F. AND HUFFMAN, D. R., *Absorption and scattering of light by small particles* (John Wiley & Sons, 2008).

[137] GRABERT, H. AND DEVORET, M. H., *Single charge tunneling, Coulomb blockade phenomena in nanostructures* (Springer US, 1992).

[138] SCHOELKOPF, R. J., WAHLGREN, P., KOZHEVNIKOV, A. A., DELSING, P., AND PROBER, D. E., *The radio-frequency single-electron transistor (RF-SET): A fast and ultrasensitive electrometer*. Science **280** (1998) 1238–1242.

[139] ROSSI, A., TANTTU, T., HUDSON, F. E., SUN, Y., MÖTTÖNEN, M., AND DZURAK, A. S., *Silicon Metal-oxide-semiconductor Quantum Dots for Single-electron Pumping*. J. Vis. Exp. (2015).

[140] KAUPPINEN, J. P., LOBERG, K. T., MANNINEN, A. J., PEKOLA, J. P., AND VOUTILAINEN, R. A., *Coulomb blockade thermometer: Tests and instrumentation*. Rev. Sci. Instrum. **69** (1998) 4166–4175.

[141] LIU, W., ZHONG, H., WANG, R., AND SEEMAN, N. C., *Crystalline Two-Dimensional DNA-Origami Arrays*. Angew. Chem. Int. Ed. **50** (2011) 264–267.

[142] RUBIN, J. J. AND VAN UITERT, L. G., *Growth of sapphire and ruby by the Czochralski technique*. Mater. Res. Bull. **1** (1966) 211–214.

[143] ARTEAGA, O., SANCHO-PARRAMON, J., NICHOLS, S., MAOZ, B. M., CANILLAS, A., BOSCH, S., MARKOVICH, G., AND KAHR, B., *Relation between 2D/3D chirality and the appearance of chiroptical effects in real nanostructures*. Opt. Express **24** (2016) 2242–2252.

[144] CASTRO, C. E., KILCHHERR, F., KIM, D.-N., SHIAO, E. L., WAUER, T., WORTMANN, P., BATHE, M., AND DIETZ, H., *A primer to scaffolded DNA origami*. Nat. Methods **8** (2011) 221–229.

[145] KIM, D.-N., KILCHHERR, F., DIETZ, H., AND BATHE, M., *Quantitative prediction of 3D solution shape and flexibility of nucleic acid nanostructures*. Nucleic Acids Res. **40** (2012) 2862–2868.

[146] BAI, X.-C., MARTIN, T. G., SCHERES, S. H. W., AND DIETZ, H., *Cryo-EM structure of a 3D DNA-origami object*. Proc. Natl. Acad. Sci. U.S.A. **109** (2012) 20012–20017.

[147] ARIAS, A. C., MACKENZIE, J. D., MCCULLOCH, I., RIVNAY, J., AND SALLEO, A., *Materials and Applications for Large Area Electronics: Solution-Based Approaches*. Chem. Rev. **110** (2010) 3–24.

A.I

Boxuan Shen[1]*
Veikko Linko[2,3,4]*
Hendrik Dietz[2]
J. Jussi Toppari[1]

[1]Department of Physics, Nanoscience Center, University of Jyväskylä, Jyväskylä, Finland
[2]Physik Department, Walter Schottky Institute, Technische Universität München, Garching, Germany
[3]Biohybrid Materials, Department of Biotechnology and Chemical Technology, Aalto University, Aalto, Espoo, Finland
[4]Molecular Materials, Department of Applied Physics, Aalto University, Aalto, Espoo, Finland

Received July 4, 2014
Revised August 14, 2014
Accepted August 25, 2014

Research Article

Dielectrophoretic trapping of multilayer DNA origami nanostructures and DNA origami-induced local destruction of silicon dioxide

DNA origami is a widely used method for fabrication of custom-shaped nanostructures. However, to utilize such structures, one needs to controllably position them on nanoscale. Here we demonstrate how different types of 3D scaffolded multilayer origamis can be accurately anchored to lithographically fabricated nanoelectrodes on a silicon dioxide substrate by DEP. Straight brick-like origami structures, constructed both in square (SQL) and honeycomb lattices, as well as curved "C"-shaped and angular "L"-shaped origamis were trapped with nanoscale precision and single-structure accuracy. We show that the positioning and immobilization of all these structures can be realized with or without thiol-linkers. In general, structural deformations of the origami during the DEP trapping are highly dependent on the shape and the construction of the structure. The SQL brick turned out to be the most robust structure under the high DEP forces, and accordingly, its single-structure trapping yield was also highest. In addition, the electrical conductivity of single immobilized plain brick-like structures was characterized. The electrical measurements revealed that the conductivity is negligible (insulating behavior). However, we observed that the trapping process of the SQL brick equipped with thiol-linkers tended to induce an etched "nanocanyon" in the silicon dioxide substrate. The nanocanyon was formed exactly between the electrodes, that is, at the location of the DEP-trapped origami. The results show that the demonstrated DEP-trapping technique can be readily exploited in assembling and arranging complex multilayered origami geometries. In addition, DNA origamis could be utilized in DEP-assisted deformation of the substrates onto which they are attached.

Keywords:
Dielectrophoresis / DNA nanostructures / Electrical properties / Nanofabrication / Nanomanipulation
DOI 10.1002/elps.201400323

Additional supporting information may be found in the online version of this article at the publisher's web-site

1 Introduction

During the last three decades, DNA has become an extensively utilized material in nanoscale fabrication aiming toward bionanotechnological applications [1]. Today, one of the most applied techniques in structural DNA nanotechnology is a DNA origami [2], which is based on folding a long single-stranded DNA into a desired shape with the help of a set of short oligonucleotides. DNA origami enables fabrication of various 2D [2] and 3D [3] shapes with designed curvatures, twists, and bends [4, 5]. Recently, also scaffold-free origamis [6, 7] and origamis based on 3D meshing have been produced [8]. Functionalization of these custom-built structures and patterning on them can be realized with nanometer precision, which opens up numerous attractive opportunities in designing tailored devices such as drug-delivery vehicles

Correspondence: Dr. J. Jussi Toppari, Department of Physics, Nanoscience Center, University of Jyväskylä, P.O. Box 35, FI-40014 Jyväskylä, Finland
E-mail: j.jussi.toppari@jyu.fi

Abbreviations: **AC-IS**, AC impedance spectroscopy; **AFM**, atomic force microscope; **HCL**, honeycomb lattice; **RH**, relative humidity; **SiO_2**, silicon dioxide; **SQL**, square lattice; **TEM**, transmission electron microscope

*These authors contributed equally to this work.

Colour Online: See the article online to view Figs. 1–4 in colour.

[9, 10], artificial ion channels [11], and molecular-level electronic circuits [12]. The rapid growth of the field—including current trends and the recent intriguing applications—has been extensively reviewed in references [13, 14].

To characterize the properties of DNA nanostructures and especially to make use of them in diverse applications, these structures have to be incorporated into larger systems/networks. That requires controllable anchoring of the structures to specific areas on a chosen substrate. There exist several ways to immobilize DNA objects to the desired locations on a chip, such as chemical (thiol-based) attachment combined with standard lithographic methods [15, 16], attachment to structure-specific lithographically fabricated confined spaces [17], and guiding/anchoring them to electrodes or solid-state nanopores using electric fields [18–20]. The exact positioning of DNA origamis further enables a nanoscale platform, for example, for examining single-molecule level reactions [21] or translocations of molecules [19,20]. In addition, studying mechanical [22] and electrical [22, 23] properties of single DNA origamis becomes possible when the structures are precisely integrated into the measurement setup.

In this article, we present a dynamic dielectrophoresis (DEP) [24] based trapping and immobilization method of four structurally distinct 3D multilayer DNA origami objects. The trapping and subsequent immobilization of the origami structures were achieved by applying an AC voltage to lithographically fabricated nanoelectrodes on a silicon dioxide (SiO_2) substrate. The presented method enables trapping with single-structure precision, thus providing a platform for various applications in nanotechnology. Although there exist reports on trapping of DNA molecules [25–31] and other DNA structures [31, 32] by electric fields, so far only 2D DNA origamis have been precisely trapped by DEP [18]. Therefore, this is the first demonstration of successful DEP-based trapping and immobilization of the 3D multilayer DNA origami structures.

The origami objects used in the experiments are shown in Fig. 1. We used two straight brick-like shapes stacked either in square (SQL) [33] or honeycomb lattice (HCL) [3] of DNA helices, and two other structures having either a curved "C" shape or an angular "L" shape in HCL. Previous work has revealed that 2D and 3D origamis can be substantially deformed under high electric fields [18, 22]. For this reason, we examined the influence of the trapping force (electric field gradient) on the structural deformation of the origamis and tuned the trapping parameters accordingly. Further, we explored the effect of the origami geometry to the single-structure trapping yield and the influence of thiol-linker modifications (incorporated into the origami structures) on the immobilization characteristics.

Furthermore, the electrical conductivity of a single plain brick-like structure was characterized revealing highly resistive behavior. However, when the thiol-linkers were incorporated into the ends of the origami structure for potentially more appropriate immobilization and covalent contacts, we observed an abrupt formation of a well-defined etched area in the SiO_2 substrate strictly between the fingertip-type electrode pair. The definite mechanism of this origami-induced "nanocanyon" formation during the DEP trapping is not completely clear, but according to our results the thiol modifications considerably enhance the observed phenomenon. The canyon formation was most efficient by a thiol-modified brick packed in SQL.

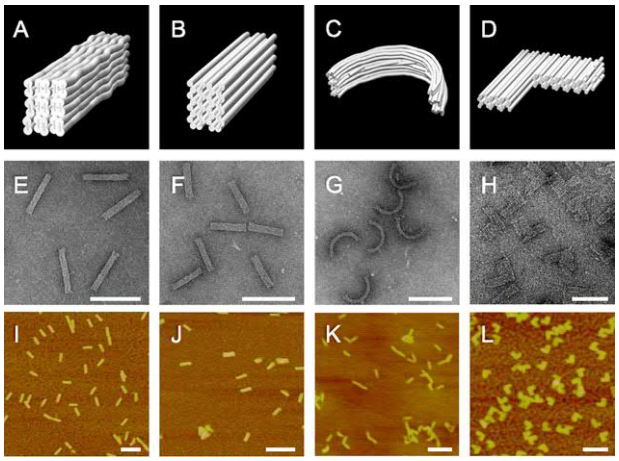

Figure 1. CanDo-simulated [36] solution shapes of the multilayer DNA origamis (A–D) used in the trapping experiments, as well as TEM (E–H) and AFM images (I–L) of the same structures: (A), (E), and (I) 30-helix bundle "brick" in square lattice (SQL); (B), (F), and (J) 32-helix bundle "brick" in honeycomb lattice (HCL); (C), (G), and (K) curved "C" shape; (D), (H), and (L) angular "L" shape. The "C" and "L" are constructed in HCL. The scale bars are 100 nm in TEM images and 200 nm in AFM images.

The reported results shine light onto the mechanical and electrical properties of multilayer origami structures under high electric fields. The proposed trapping method could readily find applications in organizing complex origami shapes into larger assemblies. Moreover, the origami-induced physical deformation of SiO_2 could be employed in DNA-based nanofabrication similarly as the previously reported chemical patterning of oxide layers by means of origami templates [34, 35].

2 Materials and methods

2.1 DNA origami fabrication and purification

DNA origami structures were designed using caDNAno software v0.2 [37]. All the structures were designed in a HCL except a 30-helix brick, which was constructed in a SQL. DNA oligonucleotide strands, that is, so-called staples, were produced by solid-phase chemical synthesis (Eurofins MWG) with high-purity salt-free purification grade (Eurofins MWG). The folding buffer of origamis contained 5 mM Tris-base, 1 mM EDTA, 20 mM $MgCl_2$, and 5 mM NaCl (pH 8). For the scaffold strand, 7249 (C-shape), 7560 (30-helix and 32-helix bricks), or 7704 (L-shape) base long M13mp18-phage-derived genomic DNA was used at 20 nM concentration. Staple strands (including optional thiol modifications) were

added with 10× excess (200 nM) to the scaffold strand. For folding the structures the temperature was ramped from 65°C to 60°C at 15 min/°C and from 59°C to 40°C at 3 h/°C [38]. Finally, the ready structures were stored at 4°C. The quality of the folding was verified by 2% agarose gel electrophoresis (running buffer 0.5× TBE with 11 mM $MgCl_2$) showing that all structures were folded with an acceptable yield (the quality was also verified by transmission electron microscope (TEM) and atomic force microscope (AFM) imaging, as shown in Fig. 1). The excess staple strands were removed by spin filtering (Amicon Ultra filters with MWCO 100 kDa) and through the filtering the buffer was exchanged to a lower conductivity Hepes/NaOH-based buffer (see Section 2.3) in order to improve the DEP efficiency. When thiolated strands were incorporated into the ends of the origamis, DTT was added to the final solution as a reducing agent in order to break disulfide bonds.

2.2 Electrode fabrication

Two different electrode geometries were used: (i) straight electrodes—used for trapping of unmodified plain structures and characterizing their electrical properties—and (ii) electrodes containing titanium resistors near the gap—used for trapping of thiolated structures (see Sections 3.2 and 3.3 for their specific use). In both cases electrodes were fabricated on a slightly boron-doped (100)-silicon substrate with 300-nm-thick thermally grown SiO_2 on the top. PMMA (Microchem A2 PMMA) resist was spin coated at 2000 rpm and baked for 5 min on a hot plate (160°C). After patterning by an electron beam lithography system (Raith eLine), the resist was developed by immersing the sample in a mixed (1:3) solution of methyl-iso-butylketon and isopropyl alcohol for about 30 s at room temperature (22°C). After that the sample was rinsed in isopropyl alcohol. Undeveloped residues from the mask openings were removed using a short flash of oxygen plasma in a reactive ion etcher (Oxford Plasmalab 80 Plus). Subsequent evaporation of metal took place in an ultrahigh vacuum chamber (pressure 10^{-8} mbar during the evaporation). After evaporation, the PMMA mask was removed by liftoff in hot acetone. Before trapping, possible PMMA residues were removed from the substrate by oxygen plasma, which also made the surface hydrophilic.

For straight electrodes the evaporation of metal was carried out at 0° angle. The thickness of the evaporated gold layer was 20 nm, under which 2–3 nm of titanium was deposited as an adhesion layer. The fabrication process was same as, for example, in Ref. 18. The incorporation of the Ti resistors into the electrodes was realized by utilizing a meander line geometry and an angle evaporation. Evaporation of 10 nm of titanium was done again at 0° angle. However, the subsequent gold evaporation was done at ~70° angle in the direction of the gap, so that on the parts perpendicular to the gap, gold was not deposited on the substrate but on the walls of the resist instead. After the liftoff procedure only a thin Ti layer having high resistance, ~70 kΩ, was left on these parts. Ten-nanometer-thick gold layer was evaporated from both directions (±70°) to ensure a correct width of the gap. An AFM image of typical electrodes with embedded Ti-resistors is shown in Fig. 2A.

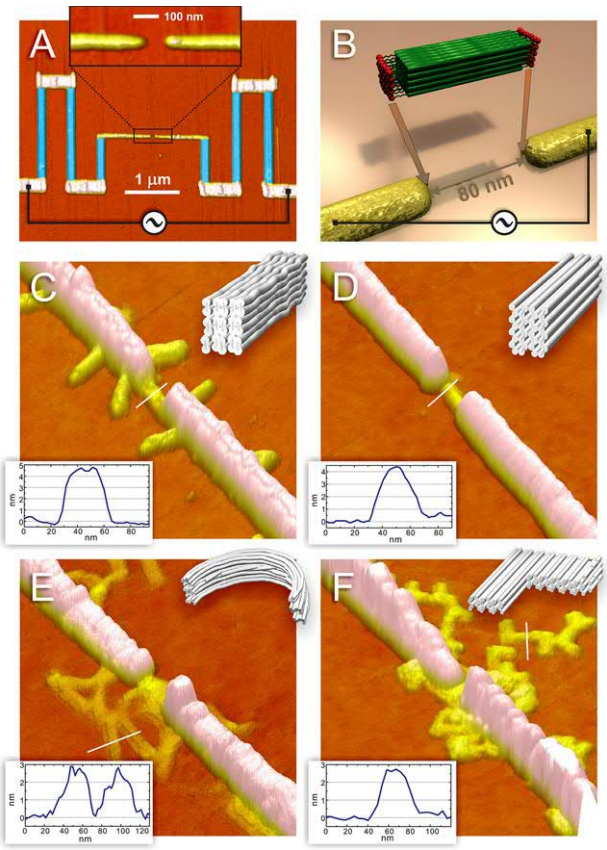

Figure 2. (A) AFM image of gold nanoelectrodes with embedded Ti-resistors (marked as blue false color). This setup was used for DEP trapping of thiol-modified origami structures. Width of the electrodes near the gap is ~30 nm and the gap size is about 80 nm. The inset shows a zoomed-in image of the gap region. (B) Schematic view of trapping a brick-like DNA origami (with thiol-linkers) by DEP. (C)–(F) AFM images of distinct 3D multilayer origami structures trapped between the gold nanoelectrodes: (C) 30-helix brick in SQL; (D) 32-helix brick in HCL; (E) "C" shape in HCL; (F) "L" shape in HCL. The lower left insets show a cross-section along the white line on the AFM images. The upper right inset is the CanDo-simulated [36] image of the origami structure.

2.3 DEP trapping of DNA origami

DEP experiments were performed by incubating a 5 µL droplet of spin-filtered low conductivity origami solution (buffer: 6 mM HEPES, 2 mM NaOH, and 3 mM magnesium acetate, conductivity 275 μScm^{-1}) on the surface of a chip with the nanoelectrodes for 1–5 min while simultaneously applying a sinusoidal AC voltage to the electrodes. When exploring the optimal trapping parameters, the DEP frequency was varied from 8 to 13 MHz, and the voltage from 0.6 to 1.5 V_{pp} (peak-to-peak value). After trapping, the sample was gently washed with deionized water and dried by a flow

of dry nitrogen. With careful tuning of the DEP parameters (see Section 3.1 for the detailed parameters), it is possible to trap and precisely immobilize a single origami structure between the nanoelectrodes. Schematic view of the trapping procedure is shown in Fig. 2B.

2.4 TEM and AFM imaging

For the TEM imaging, the folded (either purified or unpurified) origami structures were deposited onto glow-discharged formvar-supported carbon-coated Cu400 TEM grids and negatively stained using a 2% aqueous uranyl formate solution containing 25 mM NaOH. Imaging was carried out using a transmission electron microscope (Philips CM100) at 100 kV acceleration voltage. Images were acquired using an advanced microscopy techniques 4 × 4 megapixel CCD camera.

For the AFM imaging, the spin-filtered origami structures were deposited onto a mica surface, incubated for 2 min, and dried with a nitrogen flow. All samples (including samples after the DEP trapping) were imaged using a tapping mode AFM (Veeco Dimension 3100).

2.5 Electrical measurements

DC conductivity of single SQL and HCL bricks immobilized between the nanoelectrodes was measured at distinct relative humidity (RH) levels and compared to similar measurements made for control samples (see Section 3.2). The bias voltage was applied from a homemade low-noise battery powered voltage source. While sweeping the voltage through the range of ± 0.3 V, the current was measured via highly sensitive current preamplifier (DL-instruments 1211) capable of measuring pA currents. Finally, both the voltage and the measured current were recorded by a PC running a LabView program (National Instruments).

Moreover, the electrical properties of trapped bricks were characterized by AC impedance spectroscopy (AC-IS) [23, 32] within the frequency range from 97 mHz to 100 kHz. The amplitude of the applied AC bias voltage was 50 mV. For the AC-IS measurements, two Stanford Research 830 lock-in amplifiers equipped with a general-purpose interface bus were connected to a computer running a specific LabVIEW program. All the measurements were done in electromagnetically shielded room, and using the straight electrode geometry.

3 Results and discussion

3.1 DEP trapping of origamis and immobilization to gold nanoelectrodes

All the four types of 3D DNA origami structures shown in Fig. 1 were successfully trapped and immobilized by DEP. Single brick-like structures, constructed either in SQL (30-helix brick) or HCL (32-helix brick) could be trapped and immobilized exactly between the opposing fingertip-type electrodes by careful tuning of the trapping parameters. After trapping, the SQL brick maintained its shape appropriately, but the bricks constructed in HCL were usually slightly deformed and flattened on a substrate, as seen in Fig. 2C and D. Furthermore, the precise immobilization enabled us to measure the electrical conductance of single brick bridging the gap (see Section 3.2).

Moreover, we demonstrated that single "C"- and "L"-shaped origamis (in HCL) could be equally trapped and immobilized. However, it was rather challenging to achieve high yields and clearly recognizable shapes of the structures bridging the electrodes. As one can see from the AFM images (Fig. 2E and F), a bunch of "C" and "L" structures could be gathered to the vicinity of the gap, but it is difficult to distinguish the actual shape of the object in the gap (more images of the trapped origamis can be found in Supporting Information). Plausibly, different origami shapes can have slightly distinct polarizability properties; "L" shape is flat, whereas the other origamis have rod-like shapes (see Fig. 1). This can induce the differences on the trapping. The "C" shape, for one, turned out to be especially sensitive to the high electric field gradients. Deformations were clearly observed after trapping as seen in Fig. 2E. This can be attributed to the structural properties of the object. The curvature was created by adding local base skips and loops into the design that further induce a global bending of the object via internal stresses [4]. As seen in Fig. 1K, some structures might have straightened already when they were deposited and immobilized onto an AFM substrate. However, TEM images (Fig. 1G) show that under those particular conditions origamis can maintain their shape decently.

The optimal results in trapping of single structures or small bundles were obtained when the DEP frequency was tuned to 12.5 MHz and voltage (peak-to-peak) to 0.8–1.5 V_{pp}. Trapping time was varied from 3 to 5 min and the sample concentration was 1/50–1/20 of a filtered sample concentration (estimated concentration after filtration was ~10 nM). The optimal parameters for each DNA origami object are listed in Table 1. The modest variations in the parameters are due to the slightly different geometries of the electrodes, the size and the shape of the origami (distinct polarization properties of the structures), and the concentration of origamis in the trapping solution (the exact concentration after spin filtering is demanding to control exactly). It was observed that all types of origami structures were efficiently immobilized to the gold nanoelectrodes with or without the thiol-linkers indicating the covalent sulfur–gold bonds are not necessarily needed for the appropriate immobilization [18, 23].

The trapping yields (number of samples showing positive trapping results divided by a number of total samples used) are shown in Table 1. Three of four types of origamis have total trapping yields higher than 50%, which demonstrates the feasibility of the method. It should be noted, that the total trapping yield could easily reach 100%, if the trapping

Table 1. Optimized DEP parameters for "single-structure trapping" and the trapping yields of DNA origami objects achieved by using these parameters.

	30-Helix brick (SQL)	32-Helix brick (HCL)	Curved "C" shape (HCL)	Angular "L" shape (HCL)
Voltage (V_{pp})	0.9	0.9	0.8	1.5
AC frequency (MHz)	12.5	12.5	12.5	12.5
Dilution ratio	1/50	1/50	1/20	1/50
Trapping time (min)	5	5	5	3
Total trapping yield (%)	52	60	63	40
- Single structure (%)	31	20	10	13
- Small bundles (%)	21	40	53	27
Empty sample (%)	48	40	37	60

In total, 121 samples were used in the experiments.

voltage was raised and/or the concentration of DNA origamis in a DEP solution was increased. However, in this case the probability to trap only a single structure between the electrodes (single-structure trapping) becomes minimal. Thus, the yields shown in Table 1 are achieved with the carefully tuned parameters that maximize the chances to trap just a single object. The single-structure trapping yields were 20% or more for both brick-like origamis. In general, it seems that multilayer 3D origamis perform reasonably well under DEP, since the single-structure trapping yields exceed 10% yield reported for 2D origamis [18].

3.2 Electrical conductivity of single unmodified DNA origami structures

Characterization of the DC electrical resistance of a single unmodified (without thiol-linkers) brick-like origami (both 30-helix and 32-helix) immobilized exactly between the nanoelectrodes (straight electrode geometry) was carried out at room temperature both in dry conditions and at 90% RH. The results were compared to similar measurements made for control samples; samples treated similarly as the origami samples except the trapping solution did not contain any origami structures (or any other DNA) (the same method was used in [23, 32]). The obtained resistance values at 90% RH varied from 30 GΩ to over 200 GΩ, which indicates an insulating behavior of a plain multilayer DNA origami. In dry conditions the resistances were even much higher as reported earlier [23, 32]. Examples of current–voltage (*I*–*V*) curves measured from three samples and a control are shown in Fig. 3A.

In addition, the electrical properties were characterized in more detail by AC-IS (see Section 2.5). Measured frequency-dependent impedance for one of the trapped SQL brick is presented as a Cole–Cole plot in Fig. 3B. Within the whole frequency range, both the imaginary and the real part of the impedance of 3D DNA origami were considerably higher than the values measured previously for 2D origami or (2D) TX-tile structures [23, 32]. The impedance data measured from the origami samples resembled the controls. This clearly indicates an insulating behavior. AC-IS measurement were carried out at the high humidity (RH = 90%).

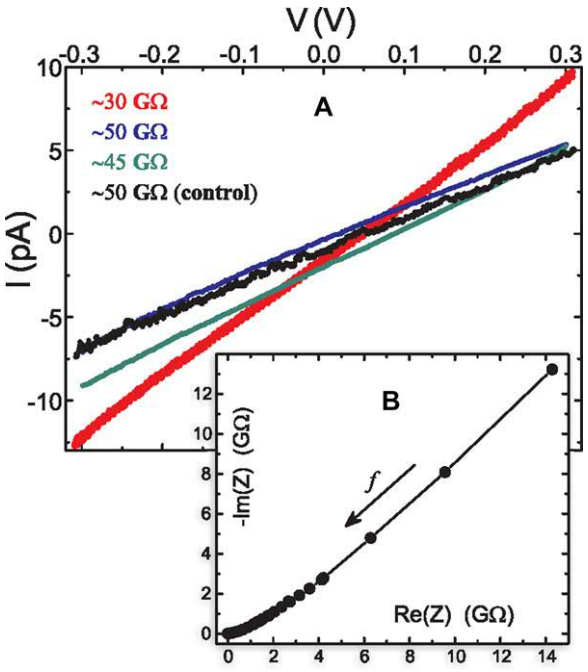

Figure 3. (A) *I*–*V* curves measured from trapped and immobilized single unmodified 30-helix brick origamis in SQL in high relative humidity conditions (RH ~90%) (color data). Black data points were measured from a control sample. (B) Results of the AC-IS measurements presented as a Cole–Cole plot for one of the samples shown in (A). Arrow points the direction of increasing frequency, that is, from 97 mHz to 100 kHz.

3.3 Nanocanyon formation by thiolated DNA origami structures

Since the observed fully insulating behavior of the plain origami structures is controversial among the results reported earlier [23, 32, 39, 40], thiol-linkers were incorporated into the ends of the SQL brick origamis (18 thiols per each side) in order to see if a potential enhancement of the conductance would take place. Surprisingly, the trapping of the thiol-modified SQL bricks resulted in a complete destruction of the straight electrodes (electrodes utilized in electrical measurements). DEP trapping and immobilization of thiol-modified

origamis without electrode explosion was observed only in a few cases, and the electrical conductivity of these samples was subsequently characterized. Nevertheless, the resistances of such samples were in the same order of magnitude as the unmodified origamis.

Yet, it is likely that in the intact (not destructed) samples the thiol-modified SQL bricks did not form proper covalent contacts (sulfur–gold bonds) with the electrodes, which would equally explain the low electrical conductivity observed. On the other hand, in the samples containing destructed electrodes the thiol-modified origamis might have formed a covalent bond with the electrodes. The appropriate linking of the origamis to the electrodes might have induced high local conductivity and subsequent explosion of the straight electrodes due to short circuiting. To confirm this reasoning, titanium resistors were integrated into the electrodes (see Fig. 2A and Section 2.2). Consequently, additional Ti-resistors should prevent the complete destruction of the electrodes. We observed that the added resistors indeed averted the electrode destruction but instead induced a formation of a "nanocanyon" locally in the SiO_2 substrate. The canyon was formed exactly between the nanoelectrodes, that is, at the position where the origami should have been trapped, as shown in Fig. 4A and B. DEP trapping of a thiol-modified 30-helix brick in the SQL formed well-defined nanocanyons with typical lateral dimensions similar to the width and the length of the origami. Depth of the canyon was varying from 10 to 40 nm. See Supporting Information for more images of nanocanyons.

In order to further study the nanocanyon formation, we carried out several control experiments. We incubated an electrode chip either in pure water, the trapping buffer, or the buffer with high Mg^{++} content, while applying the DEP voltage to the electrodes. These control experiments did not yield any canyons and even higher trapping voltages (~5 V_{pp}) were not enough to deform the electrodes or the SiO_2 substrate. We furthermore studied the canyon formation by DEP trapping 42 nucleotides long thiolated DNA oligonucleotides [41]. By trapping the thiolated oligonucleotides the canyons were not formed until the trapping voltage was raised to as high as 5 V_{pp}. Even then, the significantly higher force (5 V_{pp} vs. 1 V_{pp}) was only enough to produce faint canyons, as seen in Fig. 4C. The depth of the canyon created by extremely high DEP force and the thiolated oligonucleotides was only ~1–2 nm, which is much less than the depth of a canyon (10–40 nm) formed by the thiolated SQL brick. In addition, the shape of the canyon was not as precise, as the tips of the electrodes were destroyed within a 100–200 nm range from the gap (Fig. 4C). Similar shallow and imprecise canyons were infrequently observed when unmodified origamis were trapped with remarkably high voltages. Hence, one could argue that (i) thiols enable the efficient charge transfer from the electrodes into the solution, and (ii) the origami structure is needed to guide the charges to induce a local high current between the electrodes.

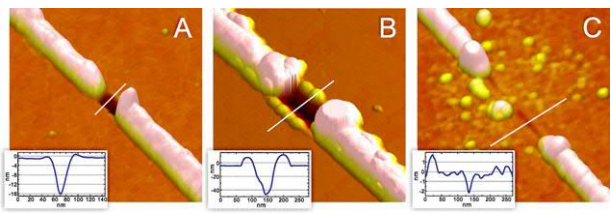

Figure 4. (A) and (B) AFM images of deep "nanocanyons" formed after trapping of thiol-modified 30-helix bricks in SQL with 1 V_{pp}. (C) A faint "canyon" and a minor electrode destruction created by trapping of thiolated 42 nucleotides long oligonucleotides with 5 V_{pp} as a control. In (A) and (B) the electrodes are intact, while in (C) they have been ruined within 100–200 nm distance from the gap.

Taken into account that without the integrated Ti-resistors the trapping of the thiol-modified origami structures resulted in an entire destruction of the nanoelectrodes near the gap, the observations indicate that the canyon formation is related to origami-induced high currents. This could be achieved, for example, by a localized counterion cloud of a DNA origami (disruptive discharge) or by direct electrical conductivity via the origami at high AC frequencies [39]. Alternatively the canyon formation could be based on the thiol-chemistry at the electrode interface(s) [42]. The yield of the canyon formation by the straight thiolated SQL brick structures was high, but in contrast, the yields were negligible when thiolated curved or angular origami shapes were trapped with the electrodes with Ti-resistors. The differences in canyon formation between the distinct origami shapes could be attributed to their structural properties. The helices (and therefore also the thiols) are more closely packed in the SQL brick than in other structures. Closely packed thiols and helices could plausibly cause high local currents/charge transfer at the electrode interface(s). If the DNA helices can efficiently support the charge migration, it should be noted that the bricks (both in SQL and HCL) favorably have parallel DNA helices extending from one electrode to another, whereas the helices in one arm of the L shape are perpendicular to the electrodes. The C shape, for one, is significantly curved. The orientation of helices could explain distinct conductivities through the gap (and thus differences in yields of canyon formation), since the conductance of helices in transverse direction (across the diameter of a helix) is negligible [43]. However, in order to thoroughly explain the observed phenomena, more comprehensive experiments are needed.

4 Concluding remarks

We have successfully demonstrated the efficient AC-DEP-based trapping and immobilization of distinct 3D multilayer DNA origami structures between gold nanoelectrodes on an SiO_2 substrate. The immobilization could be realized with or without additional thiol-linkers. The trapping yields—even single-structure trapping yields—for all four types of 3D structures used were similar or higher than previously reported yields for 2D origamis [18]. The brick-like origami in SQL seemed to be the most robust structure for DEP trapping—it is equally the sturdiest object according to the CanDo simulations. DNA origamis having HCL were often

deformed to some extent under high and localized electric fields (high DEP-trapping forces).

The delicate electrical measurements of unmodified immobilized bricks showed insulating behavior with the lowest resistance of a DNA origami being $\sim$30 GΩ at RH = 90%. However, when thiol-modified SQL bricks were trapped using the electrodes containing the additional resistors, a localized and rather unexpected destruction of the SiO_2 substrate between the electrodes was observed. The trapping experiments indicate that both thiol-linkers and straight origami nanostructures are needed for formation of a well-defined nanocanyon. One reasonable explanation would be that the thiols (or other type of linkers) are required for rapid charge transfer at the electrode interface (charge transfer between the electrodes, DEP buffer, and DNA), while the electrical conductivity through the gap could simultaneously be enhanced by the closely packed DNA helices or the counterions surrounding the DNA object. This interpretation is supported by the fact that the canyon formation yield is strongly dependent on the origami shape.

These findings are interesting in the field of molecular electronics (molecular level charge transfer and circuitry) and equally in structural DNA nanotechnology (mechanical robustness of multilayer DNA origami objects and their electrical/dielectrophoretic properties). The proposed trapping and positioning method combines the benefits of top-down and bottom-up techniques; it could readily find applications in a large-scale assembly of origami templates having high spatial patterning resolution [17]. DEP trapping is in principle a nondestructive method for assembling unmodified 3D origamis. Although the objects might be deformed under DEP, it should be noted that they are not destructed. If one uses DNA origami merely as a simple template, DEP would be a decent method to connect origami nanostructures to the macroscopic setup. Furthermore, it could be equally possible to transfer these DEP-organized geometries to the chosen electrodeless substrates [44]. In summary, there are plenty of applications where this method could be efficiently utilized. Nevertheless, our study shows that the trapping parameters and conditions should be carefully tuned and adjusted for the optimal results. For any nanotechnological implementation where the conformation of an origami object is immensely important, for example, if the origami template is equipped with distance-dependent functionalizations, the shape and the structural properties of the DNA origami should be deliberately chosen.

We thank Fabian Kilchherr for TEM images of 32-helix brick and Jonas Funke and Christian Wachauf for discussions. V.L. thanks the support through the Emil Aaltonen Foundation. This work was financed by Academy of Finland (Projects No. 218182, 263262, 263526, and 135193) and an European Research Council Starting Grant 256270 (to H.D.).

The authors have declared no conflict of interest.

5 References

[1] Seeman, N. C., *Annu. Rev. Biochem.* 2010, *79*, 65–87.

[2] Rothemund, P. W. K., *Nature* 2006, *440*, 297–302.

[3] Douglas, S. M., Dietz, H., Liedl, T., Högberg, B., Graf, F., Shih, W. M., *Nature* 2009, *459*, 414–418.

[4] Dietz, H., Douglas, S. M., Shih, W. M., *Science* 2009, *325*, 725–730.

[5] Han, D., Pal, S., Nangreave, J., Deng, Z., Liu, Y., Yan, H., *Science* 2011, *332*, 342–346.

[6] Wei, B., Dai, M., Yin, P., *Nature* 2012, *485*, 623–626.

[7] Ke, Y., Ong, L. L., Shih, W. M., Yin, P., *Science* 2012, *338*, 1177–1183.

[8] Han, D., Pal, S., Yang, Y., Jiang, S., Nangreave, J., Liu, Y., Yan, H., *Science* 2013, *339*, 1412–1415.

[9] Douglas, S. M., Bachelet, I., Church, G. M., *Science* 2012, *335*, 831–834.

[10] Mikkilä, J., Eskelinen, A.-P., Niemelä, E. H., Linko, V., Frilander, M. J., Törmä, P., Kostiainen, M. A., *Nano Lett.* 2014, *14*, 2196–2200.

[11] Langecker, M., Arnaut, V., Martin, T. G., List, J., Renner, S., Mayer, M., Dietz, H., Simmel, F. C., *Science* 2012, *338*, 932–936.

[12] Maune, H. T., Han, S. P., Barish, R. D., Bockrath, M., Goddard, W. A. III, Rothemund, P. W. K., Winfree, E., *Nat. Nanotechnol.* 2010, *5*, 61–66.

[13] Pinheiro, A. V., Han, D., Shih, W. M., Yan, H., *Nat. Nanotechnol.* 2011, *6*, 763–772.

[14] Linko, V., Dietz, H., *Curr. Opin. Biotechnol.* 2013, *24*, 555–561.

[15] Gerdon, A. E., Oh, S. S., Hsieh, K., Ke, Y., Yan, H., Soh, H. T., *Small* 2009, *5*, 1942–1946.

[16] Ding, B., Wu, H., Xu, W., Zhao, Z., Liu, Y., Yu, H., Yan, H., *Nano Lett.* 2010, *10*, 5065–5069.

[17] Kershner, R. J., Bozano, L. D., Micheel, C. M., Hung, A. M., Fornof, A. R., Cha, J. N., Rettner, C. T., Bersani, M., Frommer, J., Rothemund, P. W. K., Wallraff, G. M., *Nat. Nanotechnol.* 2009, *4*, 557–561.

[18] Kuzyk, A., Yurke, B., Toppari, J. J., Linko, V., Törmä, P., *Small* 2008, *4*, 447–450.

[19] Bell, N. A. W., Engst, C. R., Ablay, M., Divitini, G., Ducati, C., Liedl, T., Keyser, U. F., *Nano Lett.* 2012, *12*, 512–517.

[20] Wei, R., Martin, T. G., Rant, U., Dietz, H., *Angew. Chem. Int. Ed.* 2012, *51*, 4864–4867.

[21] Scheible, M. B., Pardatscher, G., Kuzyk, A., Simmel, F. C., *Nano Lett.* 2014, *14*, 1627–1633.

[22] Plesa, C., Ananth, A. N., Linko, V., Gülcher, C., Katan, A. J., Dietz, H., Dekker, C., *ACS Nano* 2014, *8*, 35–43.

[23] Linko, V., Paasonen, S.-T., Kuzyk, A., Törmä, P., Toppari, J. J., *Small* 2009, *5*, 2382–2386.

[24] Pohl, H. A., *Dielectrophoresis: The Behaviour of Neutral Matter in Nonuniform Electric Field*. Cambridge University Press, Cambridge, UK 1978.

[25] Washizu, M., Kurosawa, O., *IEEE Trans. Ind. Appl.* 1990, *26*, 1165–1172.

[26] Hughes, M. P., *Nanotechnology* 2000, *11*, 124–132.

[27] Burke, P. J., *Encycl. Nanosci. Nanotechnol.* 2004, *6*, 623–641.

[28] Tuukkanen, S., Kuzyk, A., Toppari, J. J., Häkkinen, H., Hytönen, V. P., Niskanen, E., Rinkiö, M., Törmä, P., *Nanotechnology* 2007, *18*, 295204.

[29] Hölzel, R., *IET Nanobiotechnol.* 2009, *3*, 28–45.

[30] Kuzyk, A., *Electrophoresis* 2011, *32*, 2307–2313.

[31] Linko, V., Toppari, J. J., *J. Self-Assembly Mol. Electron.* 2013, *1*, 101–124.

[32] Linko, V., Leppiniemi, J., Paasonen, S.-T., Hytönen, V. P., Toppari, J. J., *Nanotechnology* 2011, *22*, 275610.

[33] Ke, Y., Douglas, S. M., Liu, M., Sharma, J., Cheng, A., Leung, A., Liu, Y., Shih, W. M., Yan, H., *J. Am. Chem. Soc.* 2009, *131*, 15903–15908.

[34] Surwade, S. P., Zhao, S., Liu, H., *J. Am. Chem. Soc.* 2011, *133*, 11868–11871.

[35] Surwade, S. P., Zhou, F., Wei, B., Sun, W., Powell, A., O'Donnell, C., Yin, P., Liu, H., *J. Am. Chem. Soc.* 2013, *135*, 6778–6781.

[36] Castro, C. E., Kilchherr, F., Kim, D.-N., Shiao, E. L., Wauer, T., Wortmann, P., Bathe, M., Dietz, H., *Nat. Methods* 2011, *8*, 221–229.

[37] Douglas, S. M., Marblestone, A. H., Teerapittayanon, S., Vazquez, A., Church, G. M., Shih, W. M., *Nucleic Acids Res.* 2009, *37*, 5001–5006.

[38] Sobczak, J.-P. J., Martin, T. G., Gerling, T., Dietz, H., *Science* 2012, *338*, 1458.

[39] Bobadilla, A. D., Bellido, E. P., Rangel, N. L., Zhong, H., Norton, M. L., Sinitskii, A., Seminario, J. M., *J. Chem. Phys.* 2009, *130*, 171101.

[40] Bellido, E. P., Bobadilla, A. D., Rangel, N. L., Zhong, H., Norton, M. L., Sinitskii, A., Seminario, J. M., *Nanotechnology* 2009, *20*, 175102.

[41] Linko, V., Leppiniemi, J., Shen, B., Niskanen, E., Hytönen, V. P., Toppari, J. J., *Nanoscale* 2011, *3*, 3788–3792.

[42] Bindoli, A., Fukuto, J. M., Forman, H. J., *Antioxid. Redox Signal.* 2008, *10*, 1549–1564.

[43] Katsouras, I., Piliego, C., Blom, P. W. M., de Leeuw, D. M., *Nanoscale* 2013, *5*, 9882–9887.

[44] Hakala, T. K., Linko, V., Eskelinen, A.-P., Toppari, J. J., Kuzyk, A., Törmä, P., *Small* 2009, *5*, 2683–2686.

A.II

NANO LETTERS

Letter

pubs.acs.org/NanoLett

Toward Single Electron Nanoelectronics Using Self-Assembled DNA Structure

Kosti Tapio,[*,†] Jenni Leppiniemi,[‡,⊥] Boxuan Shen,[†] Vesa P. Hytönen,[‡,⊥] Wolfgang Fritzsche,[§] and J. Jussi Toppari[*,†]

[†]University of Jyvaskyla, Department of Physics, Nanoscience Center, P.O. Box 35, FI-40014 University of Jyväskylä, Finland

[‡]BioMediTech, University of Tampere, Lääkärinkatu 1, FI-33520 Tampere, Finland

[⊥]Fimlab Laboratories, Biokatu 4, FI-33520 Tampere, Finland

[§]Leibniz Institute of Photonic Technology (IPHT), Albert-Einstein-Strasse 9, Jena 07745, Germany

Supporting Information

ABSTRACT: DNA based structures offer an adaptable and robust way to develop customized nanostructures for various purposes in bionanotechnology. One main aim in this field is to develop a DNA nanobreadboard for a controllable attachment of nanoparticles or biomolecules to form specific nanoelectronic devices. Here we conjugate three gold nanoparticles on a defined size TX-tile assembly into a linear pattern to form nanometer scale isolated islands that could be utilized in a room temperature single electron transistor. To demonstrate this, conjugated structures were trapped using dielectrophoresis for current−voltage characterization. After trapping only high resistance behavior was observed. However, after extending the islands by chemical growth of gold, several structures exhibited Coulomb blockade behavior from 4.2 K up to room temperature, which gives a good indication that self-assembled DNA structures could be used for nanoelectronic patterning and single electron devices.

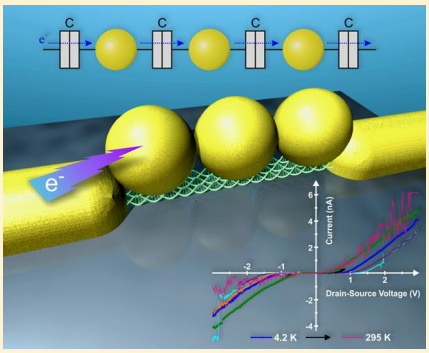

KEYWORDS: *DNA, gold nanoparticles, conjugation, dielectrophoresis, DNA metallization, single electron transistor*

Modern research has concentrated on reducing the physical size of electronic devices. Even though the diffraction limit has been pushed to 7 nm resolution,[1] the traditional top-down semiconductor fabrication process used in industry is approaching its limits. Meanwhile modern nanoscale procedures based on bottom-up fabrication and molecules start to offer even commercially viable alternative solutions, which also provide promises of mass production via fully parallel fabrication.[2−4] DNA-based self-assembled structures offer stable and flexible nanostructure miniaturization with millions of copies produced simultaneously within a one-pot experiment.[5,6] First-generation DNA-based artificial structures were 2D single-layer structures such as double (DX)[7] and triple (TX) crossover-tiles,[8] and later DNA origamis,[6] but over the time the methods have been extended to grids,[9,10] double-layer tiles,[10] curved ring-structures,[11] multilayer 3D origamis,[12] and even hollow and functional 3D objects.[13] Also, with the development of all-encompassing designing and simulation tools for DNA structures,[14] DNA nanotechnology has bloomed into a wide range of applications, e.g., as nanobreadboard,[15] nanoreactors,[16] artificial ion channels,[17] nanorobots,[18] and drug delivery vehicles.[19,20]

Recently, DNA structures have proved to be a versatile template for controllable assembly of metal nanoparticles, allowing the creation of well-defined nanostructures consisting of, e.g., a linear chain of nanoparticles,[21,22] helical patterned structures,[23] and cross patterns.[24] These kinds of structures can offer different tunable electrical or optical properties, e.g., surface enhanced Raman spectroscopy,[25] or can be employed in drug delivery.[26]

In this work we used a TX-tile based DNA-structure as a scaffold for linear patterning of gold nanoparticles. Different conjugation conditions like temperature and buffer content were investigated. To further demonstrate the effectiveness and usefulness of this method, we evaluated the use of the conjugated structure as a linear chain of metallic islands for a single electron transistor (SET),[27] which is one of the most studied and highly desired nanodevices and can be employed, e.g., as an extremely sensitive electrometer,[28] single electron pump for a quantum current standard,[29] or Coulomb blockade thermometer.[30] A severe downside of most SET devices is their requirement for cryogenic temperatures to work, which is due to their limited charging energy E_C. In order to function properly up to room temperature, the physical dimensions of SET islands need to be about ten nanometers or smaller, which is hardly possible by conventional e-beam lithography or other top-down methods. So far, this has been achieved only by using highly sophisticated special methods such as phase-shift mask

Received: June 10, 2016
Revised: September 16, 2016
Published: October 4, 2016

DOI: 10.1021/acs.nanolett.6b02378
Nano Lett. 2016, 16, 6780−6786

UV lithography,[31] manipulation of carbon nanotubes by tip of a scanning probe microscope,[32] or molecular deposition at cryogenic temperatures.[33] Meanwhile, the fabrication of gold nanoparticles (AuNP) down to few nanometers[34,35] and DNA structures under 100 nm are well-established methods and offer a less complex, much cheaper, robust, and more rapid way to produce nanoscale building blocks[36] for, e.g., SET. Therefore, DNA origamis have already been used to assembly metallic nanostructures to form SET-like structures, however, without successful electrical characterization.[37] Although there have also been reports about metal nanoparticles electrostatically attached along a double-stranded DNA positioned into electrode gap, the electrical characterization of these particle chains yielded a quite high resistance, which was explained by the heterogeneous arrangement including gaps of more than tunneling distances.[38,39]

In this report we overcome these challenges by using the highly defined TX-tile structure and precise particle attachment, accompanied by dielectrophoretic (DEP) trapping of single DNA-based structures between prefabricated gold nanoelectrodes. Yet, even we managed to arrange the particles homogeneously between the electrodes and very close together, we still had to include an extra chemical gold growth step to provide short enough tunneling gaps.[40] The TX-tile structure utilized in this work has been proven to be a poor electric conductor[38] but an excellent scaffold for particle attachment,[22] which makes it an ideal building block for nanoelectronics. The obtained results show that AuNP conjugated TX-tile structure with subsequent chemical gold expansion, can exhibit Coulomb blockade, which is the prerequisite for a working SET, from 4.2 K all the way up to room temperature. To our knowledge this is the first demonstration of precisely and controllably constructed, positioned and electrically characterized DNA-based assembly showing potential for single electron nanoelectronics.

We utilize a DNA scaffold structure formed by two different TX-tiles (A and B) that are both composed of three double-stranded DNA helices connected by crossovers. Both ends of the tile A attach to one end of the tile B, thus forming a complex of tileB−tileA−tileB (BAB complex or BAB), as illustrated in Figure 1a together with the AuNP attachment scheme. The symmetricity in the design of the components ensures only one possible configuration to take place. An atomic force microscope (AFM) image of BAB complexes on mica is shown in Figure 1b. The average length of fabricated BAB complex is 50−60 nm, which corresponds well to the theoretical length of the BAB of 55 nm.[41] Both tiles, A and B, contain a unique sticky end, i.e., free single stranded DNA (ssDNA) extension, in the middle of the tile, which we use to anchor an AuNP functionalized with complementary DNA strands ($AuNP_A$ for A-tile and $AuNP_B$ for B-tile). The distance between the sticky ends is 14 nm. This scheme was selected, since functionalized AuNPs and DNA structures can be conjugated precisely, rapidly and with adjustable spacing via sticky end locations. We carried out the conjugation process by mixing $AuNP_A$ and $AuNP_B$ to solution containing BAB complexes roughly in stoichiometric ratio $AuNP_A$:$AuNP_B$:BAB = 1:2:1, and annealing the solution slowly from 45 to 21 °C with a ramping rate of 0.0025 °C/s (see Supporting Information). The localized surface plasmon resonance (LSPR) peak of the $AuNP_A$ and $AuNP_B$ is around 520 nm (see Supporting Information, Figure S1), which corresponds to the average diameter of 10−15 nm.[42] The functionalized

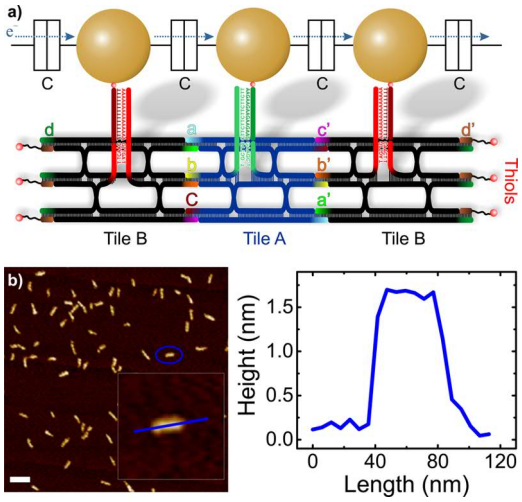

Figure 1. (a) Schematic illustration of BAB complex with two different sticky ends pointing up (bright red and green). The spacing between the sticky ends is 14 nm. Gold nanoparticles conjugated with complementary DNA strand (dark red and dark green) are attached to these sticky ends and serve as a chain of isolated islands for SET. *C* is the capacitance of the tunnel junctions formed between the AuNPs or AuNP and electrode by a tiny gap filled with single strand DNA and air. The figure is not in scale. (b) AFM image of BAB complexes deposited on a mica surface. The inset shows the circled single BAB complex, where the height cross-section on the right is taken along the blue line. The height of the structure is 1−2 nm, and the average length is 50−60 nm, which is in good agreement with the predicted length of the BAB complex. The scale bar is 100 nm.

AuNPs and the BAB structures were fabricated according to the published procedures.[41,43−45]

Figure 2 presents AFM images of conjugated BAB-AuNP assemblies deposited on a freshly cleaved mica surface. The annealing process has a reasonable yield (19−45%) of BAB-AuNP assemblies containing three nanoparticles (trimers). The average distance between the outer particles is 50−100 nm, which corresponds quite well to the theoretical size of BAB-AuNP complex with three AuNPs. A fraction of the assemblies are linear, but mostly they are curved or bent, which can be due to electrostatic repulsion between functionalized, negatively charged AuNPs, or due to interfacial forces during adsorption to the surface and drying. There are also other products such as individual nanoparticles or assemblies containing only two nanoparticles.

To further highlight the importance of the proper annealing step, we annealed AuNPs and BAB structures using faster ramping rate (0.01 °C/s) or incubated them only at room temperature. After such treatments, there are only a few linear chains found, and most of the particles and DNA structures are found to be located separated from each other (see Supporting Information, Figures S2−S4). This difference can be understood via thermodynamics of the DNA hybridization and considering that AuNPs conjugated with ssDNA experience repulsion from each other, when tried to confine in a lattice like configuration,[46] mostly due to the Coulombic repulsion between two negatively charged particles. In elevated starting temperature, the poorly formed BAB-AuNP assemblies (only partial DNA hybridization) dissociate, and while lowering the temperature, the bonds with highest dissociation energy, i.e., optimal DNA hybridization, will form first. However, this process is time-consuming, since the DNA hybridization

DOI: 10.1021/acs.nanolett.6b02378
Nano Lett. 2016, 16, 6780−6786

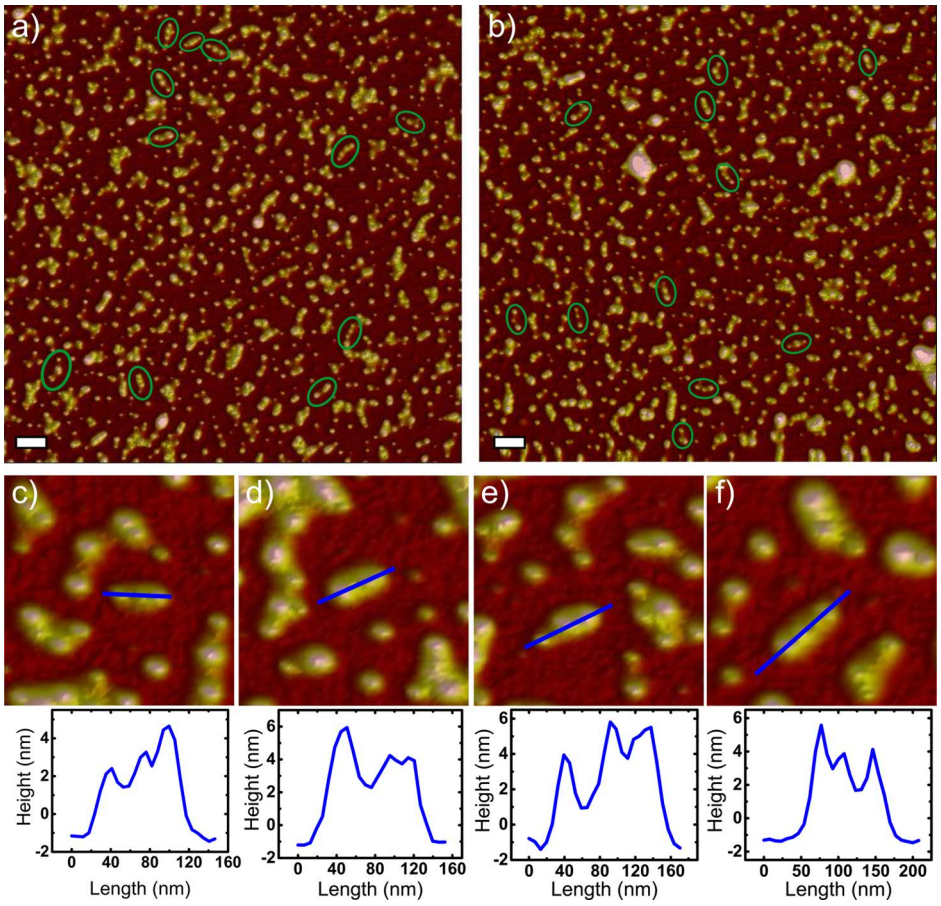

Figure 2. (a–b) AFM images of BAB-AuNP assemblies on a mica surface. Green circles highlight some of the structures containing three gold nanoparticles. The scale bars are 200 nm. (c–f) Close-up images with cross sections of some of the trimer structures. The size of the AuNPs varies between 4 and 7 nm, and typical distances between the outer particles are 50–100 nm.

strength (hydrogen bonds) is weaker in the elevated temperature, and the ionic repulsion between AuNPs will hinder the binding of closely packed AuNPs on the BAB structure. Increasing the annealing time will increase the probability that the AuNPs will fully hybridize with the sticky ends of the BAB structure. On the other hand, if the initial temperature is too low, partially hybridized DNA will not dissociate leading to loosely bound AuNPs that come off more easily over time. Therefore, increasing both temperature and the annealing time could help to assemble the particles closer to each other on the BAB scaffold in the single sticky end binding scheme used here. Furthermore, the binding of nanoparticle to a scaffold can be very sensitive to binding mechanism between the AuNP and the scaffold.[47] It is possible that the binding interaction of the $AuNP_A$ and the middle tile A is lower compared to repulsion between nanoparticles or to Brownian motion and thus lower binding efficiency is observed to the tile A. The efficiency of binding all three particles to a BAB complex could be improved by adding more sticky ends to the binding sites in both of the tiles. This approach could also enable attachment of the nanoparticles closer together, as already demonstrated down to 3 nm distances,[48,49] which could further make the additional step of chemical Au deposition unnecessary.

The BAB-AuNP assembly has physical dimensions at the nanometer scale, which makes it ideal to serve as isolated islands for SET. Here we consider a system illustrated above in Figure 1a, that consist of three islands, two connecting electrodes (source and drain) attached to the thiols on the ends of the BAB complex, and capacitive tunnel junctions (electronics symbols), i.e., gaps between the islands/AuNPs filled with ssDNA attached to the AuNPs and air. In dry state, the thickness of the ssDNA layer on top of the AuNP should be less than one nanometer, which should not hinder particle-to-particle and electrode-to-particle tunneling.

In the context of this work, the islands have two possible configurations: (i) the outer AuNPs on the sides are both directly connected to the electrodes, thereby effectively only the AuNP in the middle forms the island, or (ii) all AuNPs are isolated yielding three separate islands. In order to promote an electron to the islands, one needs to overcome the threshold bias voltage V_{th}, which depends on the island configuration.[50] The SiO_2 layer under the islands is several hundreds of nanometers thick, so one can neglect the capacitive coupling to the substrate, i.e., the back gate capacitance. When neglecting also background charges the threshold voltage becomes in the case of (i) $V_{th} = e/2C$, while in the case (ii) $V_{th} = 3e/2C$. Here e is the electron charge and C the tunneling capacitance (see Figure 1).

Assuming that the electrodes have similar dimension as the AuNPs and surface facing to AuNPs is approximately spherical, one can predict the capacitances of the system (see Supporting Information). Here we take AuNPs to be 10 nm in diameter,

DOI: 10.1021/acs.nanolett.6b02378
Nano Lett. 2016, 16, 6780–6786

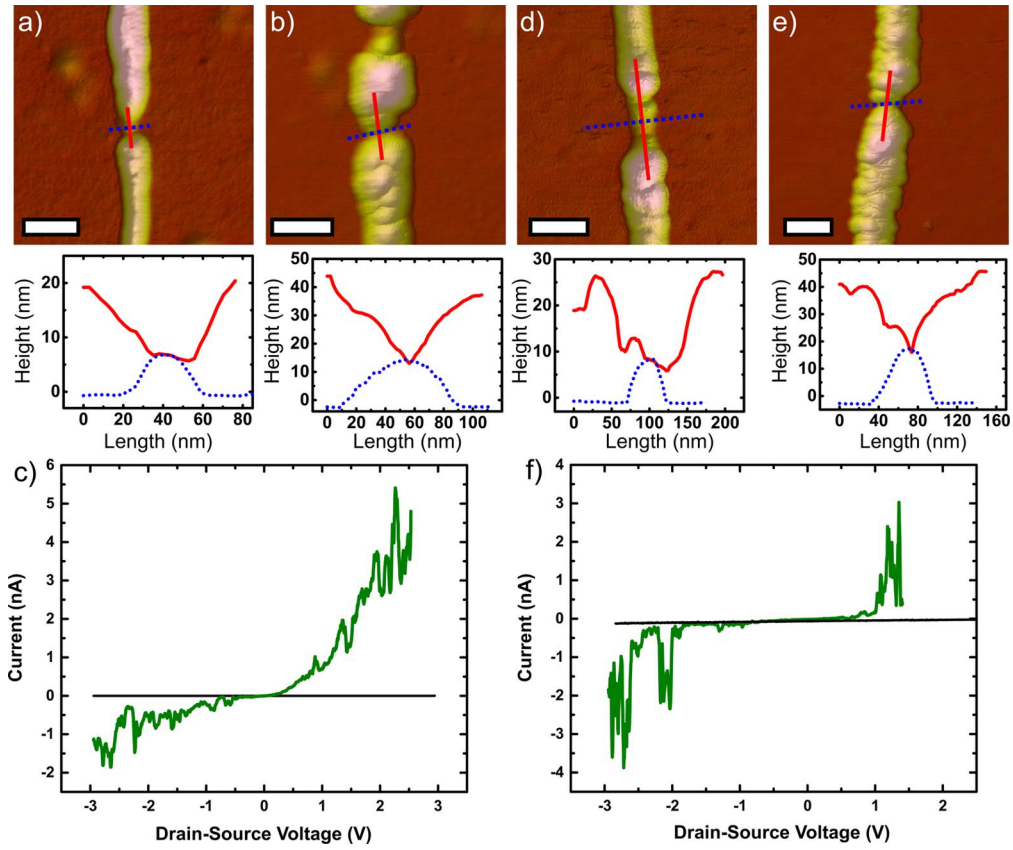

Figure 3. (a) AFM image with cross sections of the sample 1 with a trapped DNA-AuNP trimer assembly between the gold nanoelectrodes and (b) the same sample after five steps of the gold growth process. (c) The $I-V$ characteristics of the sample 1 initially (black) and after the gold growth processes (green) at room temperature. The Coulomb blockade shows linear nonconducting region near 0 V and in respect to voltage nonsymmetric conduction behavior at voltages higher than the threshold voltage. (d) AFM image with cross sections of a sample 2 and (e) the same sample after three steps of gold growth process. (f) The $I-V$ characteristics of the sample 2 initially (black) and after the gold growth processes (green) at room temperature. The scale bars are 100 nm.

along the trapped sample 2 shown in Figure 3d, and also according to the average size given by the LSPR measurements. In general, we managed to trap mainly conjugates with particles close to 10 nm, which is probably due to the tendency of DEP trapping to favor bigger objects. Then the shortest distance between the particles should be 4 nm and the relative dielectric constant between them approximately one, i.e., air. This yields for the particle-to-particle and particle-to-electrode capacitance C = 0.45 aF, in which case the charging energy exceeds the thermal energy at $T \approx 300$ K, which means that the Coulomb blockade starts to be observable close to room temperature.[27] The threshold voltage for the Coulomb blockade V_{th} is then 0.18 V for the configuration (i) and 0.54 V for the configuration (ii).

We finally trapped the BAB-AuNP assemblies between fingertip-type gold electrodes fabricated by electron beam lithography on a silicon chip covered with silicon dioxide (see Supporting Information S5), using dielectrophoresis (DEP). The silicon chip under the device can in principle act as a back gate for the transistor operation. However, in our case the high resistance of the low-doped silicon at low temperatures prevented the back gate operation. In DEP, an object is polarized by inhomogeneous external electric field and the cumulated charges at the object moves it either to the maximum or to the minimum of the electric field. In solution, the DEP force competes with Brownian motion and AC-electro-osmotic flows.[51,52] If osmotic flows are small, the DEP trapping favors larger structures, since the Brownian motion scales inversely with the dimension $\propto V^{-1/3}$. Therefore, for the BAB-AuNP assemblies the DEP favors complexes containing three gold nanoparticles to be trapped over those containing one or two, as well as bigger particles over smaller ones, as mentioned above. We used AC voltage (12.5 MHz, 1 V_{pp}, see Supporting Information) between the electrodes for the DEP trapping to avoid electrophoretic effects due to the negative charge of DNA.

Two examples, sample 1 and 2, of trapped BAB-AuNP trimers are shown in Figure 3a and d, respectively. It seems that the average size of the AuNPs in these figures are larger than in Figure 2, which is reasonable to expect since DEP favors larger structures. After trapping, the electrodes were connected to a DC-source and $I-V$-characteristics, i.e., current, I, versus drain−source bias voltage, V, were measured at room temperature (for more details see Supporting Information), which showed linear, TΩ-range, nonconducting behavior as shown in Figure 3c and f (black line). This is most probably due to too large gaps between AuNPs within the trimer, since nanoparticles had diameters about 10 nm and theoretical distance between the particles was 14 nm, which corresponds to gap size of at least 4 nm. Since the tunneling probability

DOI: 10.1021/acs.nanolett.6b02378
Nano Lett. 2016, 16, 6780−6786

decays exponentially as a function of distance, optimal tunnel junctions are below 2 nm in thickness.[53−56] To minimize the gaps and to improve the tunneling probability, the structures in Figure 3a and d were grown larger by a stepwise chemical gold growth process (see Supporting Information). In each step, gold ions were reduced on the structure thereby growing it larger, and *I*−*V*-characteristics were measured after each step, until the Coulomb blockade was observed. Figure 3b and e show the same samples 1 and 2 after the Au growth. This process mostly resulted in a grainy structure, and the overall yield of Au-grown structures to display the Coulomb blockade was about 12%.

The Coulomb blockade was typically observed after 3−5 growing steps as illustrated in Figure 3c and f (green line). The *I*−*V* characteristics indicate threshold voltages of −0.5 V and +0.25 V for the sample 1 and −1.9 V and +1 V for the sample 2, respectively, which for the sample 1 seems to fit into the case (ii) where there are three isolated islands forming the SET. On the other hand, sample 2 has higher threshold voltages than the theoretically estimated values. In both samples the current shows strong fluctuations and sudden jumps. To eliminate the thermal effects such as thermal hopping, the sample 1 was cooled down to liquid helium temperature 4.2 K and measured in various temperatures between that and the room temperature (see Figure 4). As the sample is cooled down, the thermal

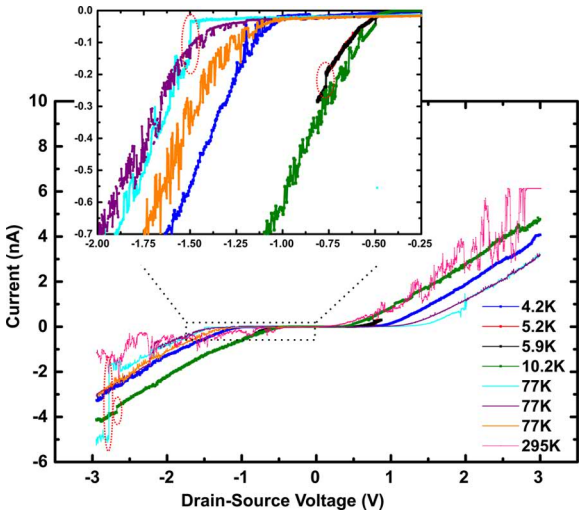

Figure 4. *I*−*V* characteristics of the sample 1 measured from 4.2 K to room temperature. The inset shows details of the current curves at 77 K and below. The random current fluctuations, i.e., thermal noise, quench as the temperature goes down, but rapid switching and jumps between different *I*−*V* curves (red circulated places) due to sudden changes in background charges are still observed.

fluctuations in current clearly decrease, but one can still observe sudden jumps, but now more like switching between specific states (see red circulated places in Figure 4). Also, at 77 K (orange and violet curves in inset), the current rapidly switches mostly between only two different *I*−*V* characteristics resembling random telegraph noise. Most likely both the jumps and the telegraph-like noise are due to random fluctuations in the backgrounds charge, which essentially have a similar effect as quick manipulations of the gate voltage of the SET.[53−56] This is also implicated by changing of the threshold voltage even at the same temperature with no clear pattern (see orange, violet, and cyan curves in Figure 4).

One explanation for the larger measured threshold voltage in sample 2 is that the grainy structures might result in not just three but several individual isolated islands, which all contribute to the capacitance of the SET. These islands can form a long chain of serially connected capacitors, which means lower capacitance and higher threshold voltages as well as charging energy.

To estimate the overall composition of sample 2, we use the measured threshold voltage of +1 V to calculate the overall capacitance *C* and then use that information to estimate the size and number of the isolated islands involved (see Supporting Information): If one would still assume that there is only three separated AuNPs, then the nanoparticle size and separation should be roughly 1.25 nm, which is clearly not the case as show in the Figure 3. By making the assumption that the tunneling distance or the gap between two islands is roughly 1 nm and the size of the conjugated BAB-AuNP structure is 50−100 nm, one would need roughly 6−8 nanoparticles that have the diameter of 8−11 nm to achieve the threshold voltage of +1 V. This estimated diameter is also close to the observed gold growth of the conjugated structures (10−20 nm) in Figure 3, making this a plausible explanation.

This also means that the observed Coulomb blockade might not originate from the nanoparticles of the trimer structure alone, but rather from the granular outcome of the gold growth process. To verify this, we trapped also plain nonconjugated BAB complexes between the fingertip electrodes and applied the same gold growth process to them (see Supporting Information, Figures S6−S8).

For most of the cases the Au-growth process of a trapped plain BAB complex eventually resulted in electrodes growing together with varying contact resistances (kΩ to TΩ, see Supporting Information, Figures S6 and S7). However, with one sample we could observe the Coulomb blockade also in this case (see Supporting Information, Figure S8). The key advantage of the use of DNA-guided nanoparticles, i.e., trimers, as a basement for the growth is that the trimer structure offers a ready-made template for the growing process, which offers higher probability to form isolated construction, where the Coulomb blockade is observable even at room temperature.

In summary, we have demonstrated that functionalized AuNPs can be attached in a controllable manner to the BAB TX-tile complex and that the longer annealing process enhances the yield of the conjugation. The most probable obstacle for the conjugation is the steric and Coulombic repulsions between AuNPs, since most of the observed trimer structures had bent shape. Also, the second most frequent structures present in the AFM images were AuNP-BAB assemblies with two nanoparticles, where the AuNPs were observed only at the sides. Both of these observations are probably due to the fact that we used only single ssDNA attachment site for each AuNP. Thus, the attached AuNPs have a lot of freedom to move as the formed single dsDNA may not be enough to keep the particles very close to each other. Shortening the annealing time resulted in more complexes containing only 1−2 AuNPs and individual BAB complexes, which may indicate that particles need longer heating to bind and assemble together to the DNA structures. One possible way to improve the formation of assemblies containing three particles would be to modify both tiles of our TX-tile structure to incorporate several binding sites for each nanoparticle, so

DOI: 10.1021/acs.nanolett.6b02378
Nano Lett. 2016, 16, 6780−6786

that the total binding energy would better overcome the electrostatic repulsion of AuNPs. This could also allow a closer spacing of the nanoparticles and thus chemical Au deposition could be even avoided. However, any modification can have negative effects on the robustness and formation of the TX-tile structure, so one might also consider using, e.g., DNA origami structures.[24,25,37]

In contrast to more commonly applied methods based on random deposition, we successfully demonstrated controllable trapping of single conjugated trimers between the gold nanoelectrodes by dielectrophoresis, thus enabling direct electrical measurements. Unfortunately, the trapped trimers did not directly function as SETs. However, we were able to process them to a state, where the Coulomb blockade could be observed from 4.2 K up to room temperature, by rather straightforward gold enhancement step (chemical gold growth). In some rare cases we could obtain the same result by enhancing just trapped plain BAB complexes, which indicates that the conjugated nanoparticles are not necessary the genuine source of the Coulomb blockade, but the gold grains/particles formed during the gold growth process can form separate extra islands and thus enhance the blockade also. However, without the BAB-AuNP assembly, the process is rather random and less probable to take place. Therefore, the AuNP-DNA conjugated structures offer a powerful novel method for the fabrication of nanoelectronics components, and further research on new protocols to better exploit the method is needed.

■ ASSOCIATED CONTENT

Supporting Information

The Supporting Information is available free of charge on the ACS Publications website at DOI: 10.1021/acs.nanolett.6b02378.

A more detailed experimental section, atomic force microscopy images (height mode) of AuNP-BAB structures conjugated by incubating at room temperature and using lower ramp, the theoretical formulation of the charging energy and the capacitance of two isolated metal spheres, estimation of the composition of the sample 2 based on the threshold voltage, the schematics of the used fingertip electrode structure, the DNA sequences of the BAB structure, and the control samples of trapped plain BAB structures (PDF)

■ AUTHOR INFORMATION

Corresponding Authors

*E-mail: kosti.t.o.tapio@jyu.fi.
*E-mail: j.jussi.toppari@jyu.fi.

Funding

The work has been financially supported by Academy of Finland (Projects 130900, 218182, 263262, 263526, 258309, 263540, 290506) and the project PPP Finland (FKZ 54776298 and 50020468) by DAAD.

Notes

The authors declare no competing financial interest.

■ ACKNOWLEDGMENTS

The authors thank Alla Nykytenko for the valuable help in the AuNP functionalization with ssDNA and Professor Janne Ihalainen and his group for overall support on the work. The authors would also like to acknowledge the input of Juhani Julin and thank Professor Ilari Maasilta for enlightening discussions. The Academy of Finland (projects 130900, 218182, 263262, 263526, 258309, 263540, 290506) and the project PPP Finland (FKZ 54776298 and 50020468) supported by DAAD are gratefully acknowledged for the financial support enabling this work.

■ ABBREVIATIONS

2D, two-dimensional; 3D, three-dimensional; DNA, deoxyribonucleic acid; BAB, a linear DNA nanostructure comprising of TX-tiles connected as Tile B−Tile A−Tile B; trimer, the BAB complex conjugated with three gold nanoparticles; AC, alternating current; DC, direct current; V_{pp}, peak-to-peak voltage

■ REFERENCES

(1) Mojarad, N.; Gobrecht, J.; Ekinci, Y. *Microelectron. Eng.* **2015**, *143*, 55−63.
(2) Woo, S.; Rothemund, P. W. K. *Nat. Commun.* **2014**, *5*, 4889.
(3) Rafat, A. A.; Pirzer, T.; Scheible, M. B.; Kostina, A.; Simmel, F. C. *Angew. Chem., Int. Ed.* **2014**, *53*, 7665−7668.
(4) Linko, V.; Shen, B.; Tapio, K.; Toppari, J. J.; Kostiainen, M. A.; Tuukkanen, S. *Sci. Rep.* **2015**, *5*, 15634.
(5) Seeman, N. C. *Nature* **2003**, *421*, 427−431.
(6) Rothemund, P. W. K. *Nature* **2006**, *440*, 297−302.
(7) Winfree, E.; Liu, F.; Wenzler, L. A.; Seeman, N. C. *Nature* **1998**, *394*, 539−544.
(8) Wei, B.; Mi, Y. *Biomacromolecules* **2005**, *6*, 2528−2532.
(9) Han, D.; Pal, S.; Yang, Y.; Jiang, S.; Nangreave, J.; Liu, Y.; Yan, H. *Science* **2013**, *339*, 1412−1415.
(10) Liu, W.; Zhong, H.; Wang, R.; Seeman, N. C. *Angew. Chem., Int. Ed.* **2011**, *50*, 264−267.
(11) Han, D.; Pal, S.; Nangreave, J.; Deng, Z.; Liu, Y.; Yan, H. *Science* **2011**, *332*, 342−346.
(12) Douglas, S. M.; Dietz, H.; Liedl, T.; Högberg, B.; Graf, F.; Shih, W. M. *Nature* **2009**, *459*, 414−418.
(13) Andersen, E. S.; Dong, M.; Nielsen, M. M.; Jahn, K.; Subramani, R.; Mamdouh, W.; Golas, M. M.; Sander, B.; Stark, H.; Oliveira, C. L. P.; Pedersen, J. S.; Birkedal, V.; Besenbacher, F.; Gothelf, K. V.; Kjems, J. *Nature* **2009**, *459*, 73−76.
(14) Douglas, S. M.; Marblestone, A. H.; Teerapittayanon, S.; Vazquez, A.; Church, G. M.; Shih, W. M. *Nucleic Acids Res.* **2009**, *37*, 5001−5006.
(15) Eskelinen, A.-P.; Kuzyk, A.; Kaltiaisenaho, T. K.; Timmermans, M. Y.; Nasibulin, A. G.; Kauppinen, E. I.; Törmä, P. *Small* **2011**, *7*, 746−750.
(16) Linko, V.; Eerikäinen, M.; Kostiainen, M. A. *Chem. Commun.* **2015**, *51*, 5351−5354.
(17) Langecker, M.; Arnaut, V.; Martin, T. G.; List, J.; Renner, S.; Mayer, M.; Dietz, H.; Simmel, F. C. *Science* **2012**, *338*, 932−936.
(18) Douglas, S. M.; Bachelet, I.; Church, G. M. *Science* **2012**, *335*, 831−834.
(19) Mikkilä, J.; Eskelinen, A.-P.; Niemelä, E. H.; Linko, V.; Frilander, M. J.; Törmä, P.; Kostiainen, M. A. *Nano Lett.* **2014**, *14*, 2196−2200.
(20) Perrault, S. D.; Shih, W. M. *ACS Nano* **2014**, *8*, 5132−5140.
(21) Ding, B.; Deng, Z.; Yan, H.; Cabrini, S.; Zuckermann, R. N.; Bokor, J. *J. Am. Chem. Soc.* **2010**, *132*, 3248−3249.
(22) Li, H.; Park, S. H.; Reif, J. H.; LaBean, T. H.; Yan, H. *J. Am. Chem. Soc.* **2004**, *126*, 418−419.
(23) Liu, H.; Shen, X.; Wang, Z.-G.; Kuzyk, A.; Ding, B. *Nanoscale* **2014**, *6*, 9331−9338.
(24) Kuzyk, A.; Schreiber, R.; Zhang, H.; Govorov, A. O.; Liedl, T.; Liu, N. *Nat. Mater.* **2014**, *13*, 862−866.
(25) Graham, D.; Thompson, D. G.; Smith, W. E.; Faulds, K. *Nat. Nanotechnol.* **2008**, *3*, 548−551.
(26) Linko, V.; Ora, A.; Kostiainen, M. A. *Trends Biotechnol.* **2015**, *33*, 586−594.

DOI: 10.1021/acs.nanolett.6b02378
Nano Lett. 2016, 16, 6780−6786

(27) Grabert, H.; Devoret, M. H. *Single Charge Tunneling, Coulomb Blockade Phenomena in Nanostuctures*, NATO ASI Ser. B, Vol. *294*; Plenum Press, 1992.
(28) Schoelkopf, R. J.; Wahlgren, P.; Kozhevnikov, A. A.; Delsing, P.; Prober, D. E. *Science* **1998**, *280*, 1238−1242.
(29) Rossi, A.; Tanttu, T.; Hudson, F. E.; Sun, Y.; Möttönen, M.; Dzurak, A. S. *J. Visualized Exp.* **2015**, *100*, 52852.
(30) Kauppinen, J. P.; Loberg, K. T.; Manninen, A. J.; Pekola, J. P.; Voutilainen, R. A. *Rev. Sci. Instrum.* **1998**, *69*, 4166−4175.
(31) Sun, Y.; Rusli; Singh, N. *IEEE Trans. Nanotechnol.* **2011**, *10*, 96−98.
(32) Postma, H. W.; Teepen, T.; Yao, Z.; Grifoni, M.; Dekker, C. *Science* **2001**, *293*, 76−79.
(33) Kubatkin, S.; Danilov, A.; Hjort, M.; Cornil, J.; Brédas, J.-L.; Stuhr-Hansen, N.; Hedegård, P.; Bjørnholm, T. *Nature* **2003**, *425*, 698−701.
(34) Turkevich, J.; Stevenson, P. C.; Hillier, J. *Discuss. Faraday Soc.* **1951**, *11*, 55−75.
(35) Zeng, S.; Yong, K.-T.; Roy, I.; Dinh, X.-Q.; Yu, X.; Luan, F. *Plasmonics* **2011**, *6*, 491−506.
(36) Gates, E. P.; Dearden, A. M.; Woolley, A. T. *Crit. Rev. Anal. Chem.* **2014**, *44*, 354−370.
(37) Chen, Z.; Lan, X.; Wang, Q. *Small* **2013**, *9*, 3567−3571.
(38) Maubach, G.; Fritzsche, W. *Nano Lett.* **2004**, *4*, 607−611.
(39) Maubach, G.; Born, D.; Csaki, A.; Fritzsche, W. *Small* **2005**, *1*, 619−624.
(40) Pearson, A. C.; Liu, J.; Pound, E.; Uprety, B.; Woolley, A. T.; Davis, R. C.; Harb, J. N. *J. Phys. Chem. B* **2012**, *116*, 10551−10560.
(41) Linko, V.; Leppiniemi, J.; Paasonen, S.-T.; Hytönen, V. P.; Toppari, J. J. *Nanotechnology* **2011**, *22*, 275610.
(42) Haiss, W.; Thanh, N. T. K.; Aveyard, J.; Fernig, D. G. *Anal. Chem.* **2007**, *79*, 4215−4221.
(43) Zhang, X.; Servos, M. R.; Liu, J. *Langmuir* **2012**, *28*, 3896−3902.
(44) Csaki, A.; Kaplanek, P.; Möller, R.; Fritzsche, W. *Nanotechnology* **2003**, *14*, 1262−1268.
(45) Storhoff, J. J.; Elghanian, R.; Mucic, R. C.; Mirkin, C. A.; Letsinger, R. L. *J. Am. Chem. Soc.* **1998**, *120*, 1959−1964.
(46) Zhang, J.; Liu, Y.; Ke, Y.; Yan, H. *Nano Lett.* **2006**, *6*, 248−251.
(47) Mudalige, T. K.; Gang, O.; Sherman, W. B. *Nanoscale* **2012**, *4*, 2855−2858.
(48) Thacker, V. V.; Herrmann, L. O.; Sigle, D. O.; Zhang, T.; Liedl, T.; Baumberg, J. J.; Keyser, U. F. *Nat. Commun.* **2014**, *5*, 3448.
(49) Roller, E.-M.; Khorashad, L. K.; Fedoruk, M.; Schreiber, R.; Govorov, A. O.; Liedl, T. *Nano Lett.* **2015**, *15*, 1368−1373.
(50) Hanke, U.; Müller, H.-O.; Chao, K.-A. *Phys. Rev. B: Condens. Matter Mater. Phys.* **1997**, *55*, 16.
(51) Pohl, H. A. *J. Appl. Phys.* **1951**, *22*, 869−871.
(52) Kuzyk, A.; Yurke, B.; Toppari, J. J.; Linko, V.; Törmä, P. *Small* **2008**, *4*, 447−450.
(53) Likharev, K. K. *Proc. IEEE* **1999**, *87*, 606−632.
(54) Yadavalli, K. K.; Orlov, A. O.; Snider, G. L.; Korotkov, A. N. *J. Vac. Sci. Technol., B: Microelectron. Process. Phenom.* **2003**, *21* (6), 2860−2864.
(55) Altshuler, B. L.; Lee, P. A.; Webb, R. A. *Mesoscopic Phenomena in Solids*; Elsevier, 1991; pp 173−271.
(56) Korotkov, A. N. *Int. J. Electron.* **1999**, *86*, 511−547.

DOI: 10.1021/acs.nanolett.6b02378
Nano Lett. 2016, 16, 6780−6786

A.III

Nanoscale

COMMUNICATION

View Article Online
View Journal

Cite this: DOI: 10.1039/c5nr02300a

Received 10th April 2015,
Accepted 28th May 2015

DOI: 10.1039/c5nr02300a

www.rsc.org/nanoscale

Custom-shaped metal nanostructures based on DNA origami silhouettes†

Boxuan Shen,‡[a] Veikko Linko,‡[b] Kosti Tapio,[a] Mauri A. Kostiainen*[b] and J. Jussi Toppari*[a]

The DNA origami technique provides an intriguing possibility to develop customized nanostructures for various bionanotechnological purposes. One target is to create tailored bottom-up-based plasmonic devices and metamaterials based on DNA metallization or controlled attachment of nanoparticles to the DNA designs. In this article, we demonstrate an alternative approach: DNA origami nanoshapes can be utilized in creating accurate, uniform and entirely metallic (*e.g.* gold, silver and copper) nanostructures on silicon substrates. The technique is based on developing silhouettes of the origamis in the grown silicon dioxide layer, and subsequently using this layer as a mask for further patterning. The proposed method has a high spatial resolution, and the fabrication yields can approach 90%. The approach allows a cost-effective, parallel, large-scale patterning on a chip with fully tailored metallic nanostructures; the DNA origami shape and the applied metal can be specifically chosen for each conceivable implementation.

During the past three decades a great variety of different nanoscale objects have been constructed using DNA as a programmable building material.[1,2] One of the most promising and robust methods for bottom-up fabrication with DNA is the so-called origami technique,[3] which is based on folding a long single-stranded DNA scaffold into a desired shape with the help of a set of synthetic "staple" strands. It was originally designed for flat 2D single-layer structures, but since then the method has been generalized for partially double-layered tiles,[4] hollow 3D objects,[5] multilayer 3D origamis,[6] and structures containing customized curvatures and twists.[7,8] Lately, methods allowing 3D meshing of DNA structures[9] and scaffold-free origamis[10,11] have been demonstrated. The techniques include powerful software for designing[12] and simulating[13–15] the shapes of the user-defined structures. These methods together form a versatile tool-kit for the designers. Recent progress in the field of structural DNA nanotechnology[16,17] has yielded a plethora of intriguing bionanotechnological applications, such as artificial ion channels,[18] nanoreactors,[19] gatekeepers for nanopores[20–22] and drug delivery vehicles.[23–25]

In addition to the aforementioned applications, the superior spatial addressability of the self-assembled DNA structures can be utilized in nanoscale patterning. Reliable nanoparticle patterning on the DNA architectures is a key feature for miniaturizing electronics[26,27] and developing photonic metamaterials,[28] as well as for novel plasmonic nanostructures and devices.[29–31] The reported assemblies include various types of DNA scaffolds decorated with complex or chiral nanoparticle geometries[32–35] and DNA-templated growth of metallic nanoshapes.[36–38] Lately, hollow origamis have been used as "molds" for casting metal nanoparticles, *i.e.*, for guiding the growth of the encapsulated metallic "seed" particles into the desired nanoshapes.[39,40] Furthermore, single DNA molecules or structures can be directed and anchored to the selected areas of lithographically fabricated substrates in order to form desired patterns,[41–49] or alternatively, the DNA objects can be directly tiled together into well-ordered large-scale assemblies.[4,50–52]

In this communication, we expand the toolbox of bottom-up-based methods by presenting a novel technique for creating uniform custom-shaped metallic nano-objects directly on the silicon chip by exploiting the high spatial accuracy of DNA origami nanoarchitectures (see Fig. 1). We believe that the method can readily open up new opportunities in nanolithographic sample fabrication aiming towards metamaterials and nanoplasmonics. Through further optimization, the technique could be generalized for other substrates, as well as for larger and more complex DNA-based assemblies.

[a]*University of Jyvaskyla, Department of Physics, Nanoscience Center, P.O. Box 35, FI-40014 University of Jyväskylä, Finland. E-mail: j.jussi.toppari@jyu.fi*
[b]*Biohybrid Materials, Department of Biotechnology and Chemical Technology, Aalto University, P.O. Box 16100, FI-00076 Aalto, Espoo, Finland. E-mail: mauri.kostiainen@aalto.fi*

†Electronic supplementary information (ESI) available: CanDo-simulated solution shape of a rectangular origami. Fabrication and purification of DNA origamis. Experimental details, instrumentation and fabrication procedures for metallic nanostructures. Statistics of the dimensions of the gold nanostructures. Additional SEM images of the gold nanostructures. See DOI: 10.1039/c5nr02300a

‡Equal contribution.

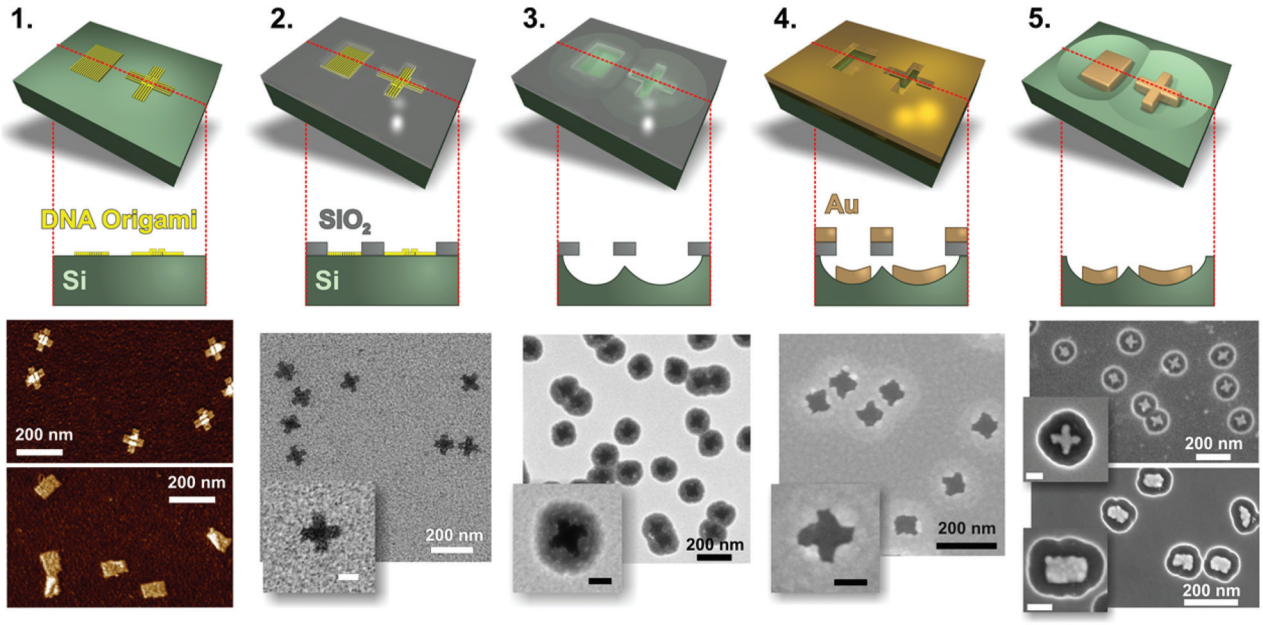

Fig. 1 Fabrication of gold nanostructures. *Step 1*: DNA origami structures ("Seeman tiles"[4] (ST) and "Rothemund rectangles"[3] (RR)) are deposited onto the silicon (Si) substrate. Note that due to the highly twisted shape of RR, some rectangles might appear slightly squeezed or rolled-up on the substrate. *Step 2*: Silicon dioxide (SiO_2) layer is grown in a chemical vapor deposition (CVD) process on the Si chip. The oxide layer grows selectively, and thus "DNA origami silhouettes" are created. *Step 3*: The "silhouettes" are used as the openings in etching of the silicon underneath the SiO_2 layer. The reactive ion etched (RIE) wells in the silicon are clearly visible beneath the silhouettes. *Step 4*: Gold is deposited onto the chip using an ultra-high vacuum (UHV) electron beam evaporator. *Step 5*: The SiO_2 layer (with the metal on top) is removed in a HF : HCl-based lift-off procedure. This leaves the DNA origami-shaped gold nanostructures on the silicon chip. The scale bars in the insets are 50 nm.

Briefly, our method relies on the selective growth of a thin silicon dioxide layer[53] on top of the silicon substrate (with the native oxide) that supports the deposited DNA origami shapes (Fig. 1: steps 1 and 2). The SiO_2 primarily grows on top of the silicon, and thus the process leaves the "DNA origami silhouettes" as openings in the formed SiO_2 layer (step 2). The aforementioned layer can be used as a mask for plasma etching (RIE) the silicon beneath the opening (step 3). The procedure allows forming smooth and rounded wells in the silicon, which have the SiO_2 window with the origami-shaped opening on the top (step 3). The origami silhouette can be subsequently used as a mask for depositing metal by evaporation onto the chip (step 4). Finally, the SiO_2 layer can be removed by hydrofluoric acid (HF) and hydrochloride (HCl)-based wet etching, leaving just the origami-shaped metallic nanostructures on the silicon chip (step 5).

We have demonstrated the fabrication of the metal nanoshapes using three different metals (gold, copper and silver) and two structurally different DNA objects: single-layer "Rothemund rectangle"[3] (RR) (92 nm × 72 nm) and partially double-layered cross-shaped "Seeman tile"[4] (ST) (two 95 nm × 30 nm layers crossing each other) (step 1, Fig. 1). The origami designs were fabricated in 1× TAE (40 mM Tris, 19 mM acetic acid, 1 mM EDTA) buffer with 12.5 mM Mg^{++} using 5–20 nM scaffold strand concentration and 10× excess of staple strands (IDT). The side strands for both structures were left out in order to avoid blunt-end stacking of the objects. The annealing ramps for the folding of the structures are the same as reported previously.[3,4] The quality of the folding was verified with agarose gel electrophoresis and AFM imaging (tapping mode, Veeco Dimension 3100). The structures can be optionally purified (excess amount of staple strands removed/buffer exchanged) by spin-filtering (see ESI†). However, we observed that the purification step is not necessarily needed in the successful fabrication procedure.

For the substrate, we used a slightly boron-doped p-type silicon chip (6 × 6 mm), which was cleaned with hot acetone and isopropanol followed by a brief sonication (2 min) and a RIE-based (Oxford Plasmalab 80 Plus) oxygen plasma treatment (oxygen flow 50 sccm, plasma power 200 W, temperature 30 °C and time 20 min). The plasma treatment was carried out in order to induce hydroxyl (–OH) group formation on the silicon surface (negatively charged and hydrophilic substrate), and therefore to help immobilize DNA origami *via* Mg^{++} ions. 5 μl of DNA origami solution in 1× TAE buffer with 100 mM Mg^{++} was pipetted onto the silicon chip right after the plasma treatment. The sample was incubated in a closed chamber for 5 min, washed 3 times with 50 μl of double-distilled (dd) H_2O and finally gently dried under a N_2 gas flow (step 1, Fig. 1).

The Si chip with the immobilized DNA origami structures was placed in a 1.5-liter glass desiccator for 16 hours together with two small glass vials containing tetraethyl orthosilicate (TEOS, ≥99.0%, Sigma-Aldrich) and ammonium hydroxide (NH_4OH, 25% NH_3 in H_2O, Baker Analyzed). In addition,

80 grams of silica gel, which was conditioned overnight in a humidity chamber (Weiss Climatic test chamber, 80% relative humidity, room temperature), were positioned at the bottom of the desiccator in order to improve the quality of the grown silicon dioxide layer. The aforementioned chemical vapor deposition (CVD) treatment reliably created precise origami silhouettes in the 5–10 nm thick silicon dioxide layer (step 2, Fig. 1), since the oxide predominantly grows on the bare areas of the chip.[53]

The sample with the formed silhouettes was etched using RIE (step 3, Fig. 1). First, in order to expose the Si surface beneath the grown silicon dioxide layer (including the formed native oxide layer), 2–4 nm of SiO_2 was etched away (CHF_3 flow 25 sccm, Ar flow 25 sccm, plasma power 100 W, temperature 25 °C and time 12–24 s). Subsequently, 57 nm of Si was etched (SF_6 flow 100 sccm, O_2 flow 8 sccm, plasma power 50 W, temperature 30 °C and time 30 s) resulting in the rounded silicon wells beneath the SiO_2 windows.

The following metal deposition (gold, copper or silver) was carried out using an electron beam evaporator (step 4, Fig. 1) in an ultra-high vacuum chamber (UHV). 20 nm of metal was perpendicularly evaporated onto the sample surface at a rate of 0.04 nm s^{-1} (for copper) or 0.06 nm s^{-1} (for gold and silver). After the metal deposition, the SiO_2 mask together with the metal film on top of it was removed in a lift-off procedure using HF (38%)/HCl (38%) (12 : 1) solution for gold or 4% HF in H_2O for copper and silver. Finally, the sample was washed with ddH_2O and dried under N_2 flow (step 5 with gold structures is presented in Fig. 2 and 3).

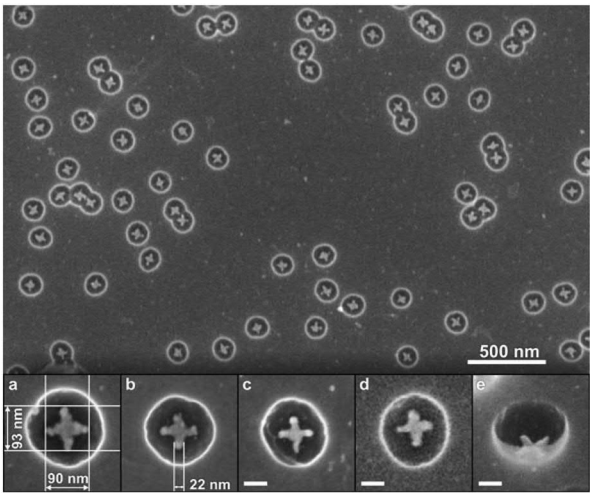

Fig. 2 *Step 5 for ST origami.* SEM image shows the high yield of patterning; 86 ± 3% of all the observed particles are correctly formed metallic cross-like structures. Subfigures (a)–(d) show the close-up images of the typical well-formed gold nanostructures on the silicon chip. Subfigure (e) is a tilted SEM image of the metallic cross in the silicon well. The scale bars in (c)–(e) are 50 nm. The dimensions of the gold nanostructures are slightly (7–25%) smaller than the dimensions in the original DNA origami design.

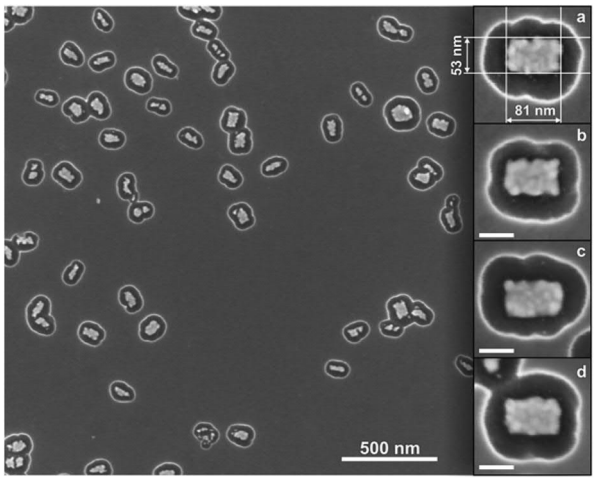

Fig. 3 *Step 5 for RR origami.* SEM image of the gold rectangular shapes on the Si substrate. The particle size distribution is much wider than in the ST case, which can be attributed to the highly twisted conformation of the RR structures in the Si chip. However, by taking this into account, the yield for the fabrication is acceptable: 65 ± 2%. Subfigures (a)–(d) show the close-up images of the desired shapes. The scale bars are 50 nm.

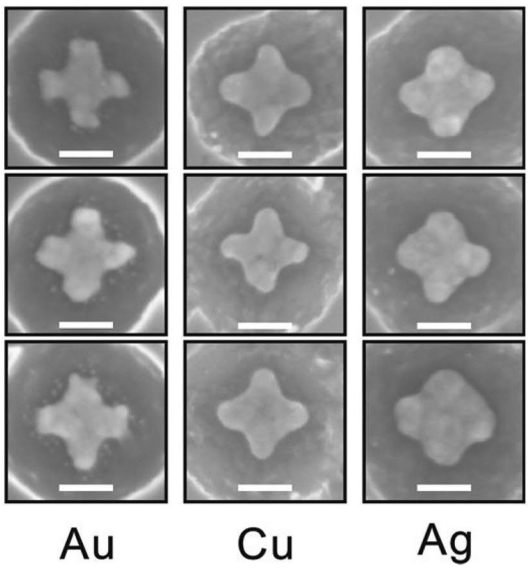

Fig. 4 SEM images of the ST shapes made out of gold (Au), copper (Cu) and silver (Ag). The scale bars are 50 nm.

Fig. 4 shows the feasibility of the proposed fabrication method: it illustrates ST patterns made out of different metals, *i.e.* gold, copper and silver. It is noteworthy to mention that the shape of the metallic ST structure becomes slightly rounded in the case of silver and copper deposition due to the native oxidation of these metals. The ready samples were imaged with AFM (Veeco Dimension 3100) or SEM (Raith eLine).

For ST-patterning (Fig. 2), 86 ± 3% of all the observed particles were correctly formed metallic (gold) crosses, and the yield for the RR-based objects (Fig. 3) was 65 ± 2% (see the ESI† for the details). The adopted solution shapes for both origamis are twisted to some extent (especially RR, see the ESI†), but the twisted origamis can be straightened when they land onto the substrate. However, some structures do not adopt the desired orientation on the silicon substrate after their deposition, and thus the yield accordingly decreased. By choosing twist-corrected and more rigid origami structures for patterning one could presumably increase the success rate.

In addition, it was observed that RR-based gold nanostructures had an average width of 37 ± 10 nm and an average length of 80 ± 6 nm (see the ESI† for the statistics of the dimensions). For the gold ST-patterns the average length in both directions was 89 ± 6 nm and the average width of the arm was 23 ± 7 nm. The length of ST-patterned metallic structures is close to the length of the origami (on average only ~7% smaller), but the width is about 25% smaller compared to the original origami design. In the case of the RR-based metallic structures, the length corresponds to that of the origami structure (~15% smaller), but the width is on average about 48% smaller than designed, mainly because the twisted RR origami tends to roll up around its longer axis on the silicon substrate. Moreover, there are two plausible explanations for the slightly reduced dimensions of the gold nanoshapes. One is that although the silicon dioxide layer mainly grows perpendicular to the Si substrate, it can also grow on the walls of the silhouettes, thus resulting in a decreased size of the opening. The other is that the evaporated gold may adhere or cluster onto the edges of the mask, which moderately reduces the size of the silhouettes. Nevertheless, the obtained yields indicate that the proposed technique is highly reproducible (additional SEM images of the gold nanostructures in the ESI†).

Conclusions

As a conclusion, we report a novel high-throughput technique for fabricating uniform and tailored metallic nanostructures on a silicon chip. The fabrication method exploits the high spatial addressability of the tailored DNA nanostructures. We have demonstrated the feasibility and modularity of the technique by utilizing two structurally different scaffolded DNA origamis for creating the origami silhouettes, and three different metals for deposition (gold, copper and silver, Fig. 4). The advantage of the method is that, in principle, one can use any kind of origami shape (dimers, multimers and even larger arrays are equally accessible) and any metal that survives HF or HF/HCl etching. However, the fabrication of large and complex structures might require more anisotropic etch profiles of silicon, which can be achieved by utilizing advanced lithographic techniques such as a deep reactive ion etching (DRIE).[54]

In general, one has to pay extra attention to the actual solution shape of the DNA origami in order to avoid non-uniform size distribution of the fabricated metal nanostructures. One intriguing possibility to increase the impact of the method would be to use scaffold-free origamis[10,11] for fabricating any desired patterns in a cost-effective manner, *i.e.* by utilizing just one set of staple strands. We believe that our method could be equally extended to other substrates – such as sandwiched Si-based multilayered substrates – by completely removing the silicon layer once the metal pattern has been formed. The aforementioned approach could readily facilitate the fabrication on the transparent surfaces and thus the characterization of plasmonic properties of the created nanoshapes.

In contrast to previously reported DNA-templated metallic shapes,[36–38] our method is easy, cost-effective and it allows uniform, regular and accurate structures. Compared to the recently reported innovative DNA mold approach,[39,40] our method allows the use of a variety of metals and still it provides a similar patterning resolution. In addition, it might allow an easier route to fabricate specific nanoshapes or even larger origami-based arrays. However, our technique is substrate-based and thus, creating nanoparticles in a solution-phase is not accessible. Despite that, well-ordered large-scale parallel patterning could be realized *e.g.* by exploiting electric fields for directing the origami shapes on the chip,[49] and subsequently transferring the created array to the target substrate.[55]

To date, DNA- and substrate-based molecular lithography approaches have not fully contemplated the possibilities of fabricating metallic nanoshapes. Rather, previous studies cover either a positive- or negative-tone decoration of silicon and silicon oxide,[53,56,57] or DNA-assisted graphene patterning.[58] However, our straightforward method offers a novel and attractive way to combine bottom-up-based molecular self-assembly with standard top-down lithographic techniques. As a result, the proposed method facilitates the user-defined fabrication of metallic nanoshapes for a great variety of applications.

Acknowledgements

This work was supported by the Academy of Finland (grants 218182, 263526, 258309, 263504, 267497, 273645). In addition, V. L. and M. A. K. acknowledge financial support from Biocentrum Helsinki, Emil Aaltonen Foundation and EU EMRP (SIB61). This work was carried out under the Academy of Finland's Centres of Excellence Programme (2014–2019).

Notes and references

1 N. C. Seeman, *J. Theor. Biol.*, 1982, **99**, 237–247.
2 N. C. Seeman, *Nano Lett.*, 2010, **10**, 1971–1978.
3 P. W. K. Rothemund, *Nature*, 2006, **440**, 297–302.

4 W. Liu, H. Zhong, R. Wang and N. C. Seeman, *Angew. Chem., Int. Ed.*, 2011, **50**, 264–267.
5 E. S. Andersen, M. Dong, M. M. Nielsen, K. Jahn, R. Subramani, W. Mamdouh, M. M. Golas, B. Sander, H. Stark, C. L. P. Oliveira, J. S. Pedersen, V. Birkedal, F. Besenbacher, K. V. Gothelf and J. Kjems, *Nature*, 2009, **459**, 73–76.
6 S. M. Douglas, H. Dietz, T. Liedl, B. Högberg, F. Graf and W. M. Shih, *Nature*, 2009, **459**, 414–418.
7 H. Dietz, S. M. Douglas and W. M. Shih, *Science*, 2009, **325**, 725–730.
8 D. Han, S. Pal, J. Nangreave, Z. Deng, Y. Liu and H. Yan, *Science*, 2011, **332**, 342–346.
9 D. Han, S. Pal, Y. Yang, S. Jiang, J. Nangreave, Y. Liu and H. Yan, *Science*, 2013, **339**, 1412–1415.
10 B. Wei, M. Dai and P. Yin, *Nature*, 2012, **485**, 623–626.
11 Y. Ke, L. L. Ong, W. M. Shih and P. Yin, *Science*, 2012, **338**, 1177–1183.
12 S. M. Douglas, A. H. Marblestone, S. Teerapittayanon, A. Vazquez, G. M. Church and W. M. Shih, *Nucleic Acids Res.*, 2009, **37**, 5001–5006.
13 C. E. Castro, F. Kilchherr, D.-N. Kim, E. L. Shiao, T. Wauer, P. Wortmann, M. Bathe and H. Dietz, *Nat. Methods*, 2011, **8**, 221–229.
14 D.-N. Kim, F. Kilchherr, H. Dietz and M. Bathe, *Nucleic Acids Res.*, 2012, **40**, 2862–2868.
15 K. Pan, D.-N. Kim, F. Zhang, M. R. Adendorff, H. Yan and M. Bathe, *Nat. Commun.*, 2014, **5**, 5578.
16 V. Linko and H. Dietz, *Curr. Opin. Biotechnol.*, 2013, **24**, 555–561.
17 F. Zhang, J. Nangreave, Y. Liu and H. Yan, *J. Am. Chem. Soc.*, 2014, **136**, 11198–11211.
18 M. Langecker, V. Arnaut, T. G. Martin, J. List, S. Renner, M. Mayer, H. Dietz and F. C. Simmel, *Science*, 2012, **338**, 932–936.
19 V. Linko, M. Eerikäinen and M. A. Kostiainen, *Chem. Commun.*, 2015, **51**, 5351–5354.
20 N. A. W. Bell, C. R. Engst, M. Ablay, G. Divitini, C. Ducati, T. Liedl and U. F. Keyser, *Nano Lett.*, 2012, **12**, 512–517.
21 R. Wei, T. G. Martin, U. Rant and H. Dietz, *Angew. Chem., Int. Ed.*, 2012, **51**, 4864–4867.
22 C. Plesa, A. N. Ananth, V. Linko, C. Gülcher, A. J. Katan, H. Dietz and C. Dekker, *ACS Nano*, 2014, **8**, 35–43.
23 S. M. Douglas, I. Bachelet and G. M. Church, *Science*, 2012, **335**, 831–834.
24 J. Mikkilä, A.-P. Eskelinen, E. H. Niemelä, V. Linko, M. J. Frilander, P. Törmä and M. A. Kostiainen, *Nano Lett.*, 2014, **14**, 2196–2200.
25 S. D. Perrault and W. M. Shih, *ACS Nano*, 2014, **8**, 5132–5140.
26 H. T. Maune, S.-P. Han, R. D. Barish, M. Bockrath, W. A. Goddard III, P. W. K. Rothemund and E. Winfree, *Nat. Nanotechnol.*, 2010, **5**, 61–66.
27 V. Linko and J. J. Toppari, *J. Self-Assem. Mol. Electron.*, 2013, **1**, 101–124.
28 C. M. Soukoulis and M. Wegener, *Nat. Photonics*, 2011, **5**, 523–530.
29 M. R. Jones, K. D. Osberg, R. J. Macfarlane, M. R. Langille and C. A. Mirkin, *Chem. Rev.*, 2011, **111**, 3736–3827.
30 S. J. Tan, M. J. Campolongo, D. Luo and W. Cheng, *Nat. Nanotechnol.*, 2011, **6**, 268–276.
31 J. Chao, Y. Lin, H. Liu, L. Wang and C. Fan, *Mater. Today*, 2015, DOI: 10.1016/j.mattod.2015.01.018.
32 J. Sharma, R. Chhabra, C. S. Andersen, K. V. Gothelf, H. Yan and Y. Liu, *J. Am. Chem. Soc.*, 2008, **130**, 7820–7821.
33 A. J. Mastroianni, S. A. Claridge and A. P. Alivisatos, *J. Am. Chem. Soc.*, 2009, **131**, 8455–8459.
34 A. Kuzyk, R. Schreiber, Z. Fan, G. Pardatscher, E.-M. Roller, A. Högele, F. C. Simmel, A. O. Govorov and T. Liedl, *Nature*, 2012, **483**, 311–314.
35 E.-M. Roller, L. K. Khorashad, M. Fedoruk, R. Schreiber, A. O. Govorov and T. Liedl, *Nano Lett.*, 2015, **15**, 1368–1373.
36 M. Pilo-Pais, S. Goldberg, E. Samano, T. H. LaBean and G. Finkelstein, *Nano Lett.*, 2011, **11**, 3489–3492.
37 R. Schreiber, S. Kempter, S. Höller, V. Schüller, D. Schiffels, S. S. Simmel, P. C. Nickels and T. Liedl, *Small*, 2011, **7**, 1795–1799.
38 J. Liu, Y. Geng, E. Pound, S. Gyawali, J. R. Ashton, J. Hickey, A. T. Woolley and J. N. Harb, *ACS Nano*, 2011, **5**, 2240–2247.
39 S. Helmi, C. Ziegler, D. J. Kauert and R. Seidel, *Nano Lett.*, 2014, **14**, 6693–6698.
40 W. Sun, E. Boulais, Y. Hakobyan, W. L. Wang, A. Guan, M. Bathe and P. Yin, *Science*, 2014, **346**, 1258361.
41 A. Kuzyk, B. Yurke, J. J. Toppari, V. Linko and P. Törmä, *Small*, 2008, **4**, 447–450.
42 A. E. Gerdon, S. S. Oh, K. Hsieh, Y. Ke, H. Yan and H. T. Soh, *Small*, 2009, **5**, 1942–1946.
43 R. J. Kershner, L. D. Bozano, C. M. Micheel, A. M. Hung, A. R. Fornof, J. N. Cha, C. T. Rettner, M. Bersani, J. Frommer, P. W. K. Rothemund and G. M. Wallraff, *Nat. Nanotechnol.*, 2009, **4**, 557–561.
44 V. Linko, S.-T. Paasonen, A. Kuzyk, P. Törmä and J. J. Toppari, *Small*, 2009, **5**, 2382–2386.
45 A. M. Hung, C. M. Micheel, L. D. Bozano, L. W. Osterbur, G. M. Wallraff and J. N. Cha, *Nat. Nanotechnol.*, 2010, **5**, 121–126.
46 V. Linko, J. Leppiniemi, B. Shen, E. Niskanen, V. P. Hytönen and J. J. Toppari, *Nanoscale*, 2011, **3**, 3788–3792.
47 V. Linko, J. Leppiniemi, S.-T. Paasonen, V. P. Hytönen and J. J. Toppari, *Nanotechnology*, 2011, **22**, 275610.
48 A. Gopinath and P. W. K. Rothemund, *ACS Nano*, 2014, **8**, 12030–12040.
49 B. Shen, V. Linko, H. Dietz and J. J. Toppari, *Electrophoresis*, 2015, **36**, 255–262.
50 A. A. Rafat, T. Pirzer, M. B. Scheible, A. Kostina and F. C. Simmel, *Angew. Chem., Int. Ed.*, 2014, **53**, 7665–7668.
51 S. Woo and P. W. K. Rothemund, *Nat. Commun.*, 2014, **5**, 4889.
52 Y. Ke, L. L. Ong, W. Sun, J. Song, M. Dong, W. M. Shih and P. Yin, *Nat. Chem.*, 2014, **6**, 994–1002.

53 S. P. Surwade, F. Zhou, B. Wei, W. Sun, A. Powell, C. O'Donnell, P. Yin and H. Liu, *J. Am. Chem. Soc.*, 2013, **135**, 6778–6781.
54 F. Marty, L. Rousseau, B. Saadany, B. Mercier, O. Français, Y. Mita and T. Bourouina, *Microelectron. J.*, 2005, **36**, 673–677.
55 T. K. Hakala, V. Linko, A.-P. Eskelinen, J. J. Toppari, A. Kuzyk and P. Törmä, *Small*, 2009, **5**, 2683–2686.
56 S. P. Surwade, S. Zhao and H. Liu, *J. Am. Chem. Soc.*, 2011, **133**, 11868–11871.
57 F. Zhou, B. Michael, S. P. Surwade, K. B. Ricardo, S. Zhao and H. Liu, *Chem. Mater.*, 2015, **27**, 1692–1698.
58 Z. Jin, W. Sun, Y. Ke, C. J. Shih, G. L. C. Paulus, Q. H. Wang, B. Mu, P. Yin and M. S. Strano, *Nat. Commun.*, 2013, **4**, 1663.

A.IV

APPLIED SCIENCES AND ENGINEERING

Plasmonic nanostructures through DNA-assisted lithography

Boxuan Shen,[1,2]* Veikko Linko,[2,3]* Kosti Tapio,[1] Siim Pikker,[1] Tibebe Lemma,[1]† Ashwin Gopinath,[4] Kurt V. Gothelf,[5,6] Mauri A. Kostiainen,[2,3]‡ J. Jussi Toppari[1]‡

Programmable self-assembly of nucleic acids enables the fabrication of custom, precise objects with nanoscale dimensions. These structures can be further harnessed as templates to build novel materials such as metallic nanostructures, which are widely used and explored because of their unique optical properties and their potency to serve as components of novel metamaterials. However, approaches to transfer the spatial information of DNA constructions to metal nanostructures remain a challenge. We report a DNA-assisted lithography (DALI) method that combines the structural versatility of DNA origami with conventional lithography techniques to create discrete, well-defined, and entirely metallic nanostructures with designed plasmonic properties. DALI is a parallel, high-throughput fabrication method compatible with transparent substrates, thus providing an additional advantage for optical measurements, and yields structures with a feature size of ~10 nm. We demonstrate its feasibility by producing metal nanostructures with a chiral plasmonic response and bowtie-shaped nanoantennas for surface-enhanced Raman spectroscopy. We envisage that DALI can be generalized to large substrates, which would subsequently enable scale-up production of diverse metallic nanostructures with tailored plasmonic features.

INTRODUCTION

Metallic nanostructures are widely used and explored because of their unique optical properties, such as selective field enhancement via plasmonic resonances, and their potency to serve as components of novel metamaterials (*1*, *2*). However, the currently available fabrication techniques are not feasible for creating complex and sufficiently small metallic shapes for metamaterials functioning at the visible wavelength range. The common wet chemical methods merely yield geometrically limited structures, whereas the standard lithography that allows arbitrary shapes does not provide the required spatial accuracy. Meanwhile, programmable self-assembly of nucleic acids enables the fabrication of custom, precise objects with nanoscale dimensions (*3*, *4*). These structures can be further harnessed as templates for building novel materials and nanodevices with diverse functionalities (*5*–*10*). However, approaches to transfer their spatial information to metal nanostructures have been limited to direct patterning with nanoparticles (*7*, *8*, *11*–*13*) or chemical growth of attached seed particles (*14*–*18*).

Here, we present a parallel, high-throughput DNA-assisted lithography (DALI) method that genuinely combines the high resolution and structural versatility of DNA origami (*19*–*24*) with the robustness of the conventional lithography to create discrete, well-defined, and entirely metallic nanostructures with designed plasmonic properties. DALI is a parallel, high-throughput fabrication method compatible with transparent substrates. The technique facilitates the production of large plasmonic metasurfaces with small (~10 nm) feature sizes, and at present, it is the only viable method for this purpose because of its freedom from costly optical or electron-beam patterning. We demonstrate its feasibility by producing metal nanostructures with chiral plasmonic response and bowtie-shaped nanoantennas for surface-enhanced Raman spectroscopy (SERS). Overall, DALI provides a straightforward approach to overcome the abovementioned prominent obstacles and opens up completely new avenues in nanofabrication.

RESULTS

We prepared four different DNA origami designs: the so-called Seeman tile (ST) (*25*), a bowtie origami (BO), and two versions of a chiral double-L (CDL), that is, CDL with and without protruding staple strand extensions to control its landing orientation on a silicon substrate (Fig. 1A, top). The origami structures were folded in a thermal annealing process with high yield, and the structural integrity of each design was verified by atomic force microscopy (AFM) (Fig. 1A, middle) and agarose gel electrophoresis (see fig. S1). To demonstrate the versatility of DALI (Fig. 1B), we converted the abovementioned DNA designs to discrete one-to-one metallic shapes (Fig. 1A, bottom) and characterized their plasmonic properties in detail.

The folded origami structures were deposited without any purification onto an oxygen plasma–cleaned substrate consisting of a transparent bottom layer [sapphire (Al_2O_3) or silicon nitride (Si_3N_4)] and a top layer of amorphous silicon, grown by plasma-enhanced chemical vapor deposition (PECVD) (Fig. 1B, steps 1 to 3). After the deposition, a silicon dioxide (SiO_2) layer was formed on top of the silicon in a selective CVD process (Fig. 1B, step 4) (*26*, *27*). The oxide primarily grows on the bare areas of the silicon and only slightly on top of the deposited DNA origami. The thin oxide layer on top of the origami can be easily removed by short reactive ion etching (RIE). Therefore, the formed oxide layer can be further used as a stencil for the following process steps.

The rest of the procedure starts with isotropic RIE etching of the silicon underneath the oxide film through the origami-shaped holes (Fig. 1B, step 5). This step is followed by a physical vapor deposition (PVD) of a gold film under ultrahigh vacuum conditions (Fig. 1B,

[1]Department of Physics, Nanoscience Center, P.O. Box 35, 40014 University of Jyväskylä, Finland. [2]Biohybrid Materials, Department of Bioproducts and Biosystems, Aalto University, 00076 Aalto, Finland. [3]HYBER Centre of Excellence, Department of Applied Physics, Aalto University, 00076 Aalto, Finland. [4]Department of Bioengineering, California Institute of Technology, Pasadena, CA 91125, USA. [5]Centre for DNA Nanotechnology, Interdisciplinary Nanoscience Center, iNANO, Aarhus University, Gustav Wieds Vej 14, 8000 Aarhus C, Denmark. [6]Department of Chemistry, Aarhus University, Langelandsgade 140, 8000 Aarhus C, Denmark.
*These authors contributed equally to this work.
†Present address: Departamento de Física, Faculdade de Ciências e Tecnologia, Universidade Estadual Paulista, Presidente Prudente, SP 19060-900, Brazil.
‡Corresponding author. Email: mauri.kostiainen@aalto.fi (M.A.K.); j.jussi.toppari@jyu.fi (J.J.T.)

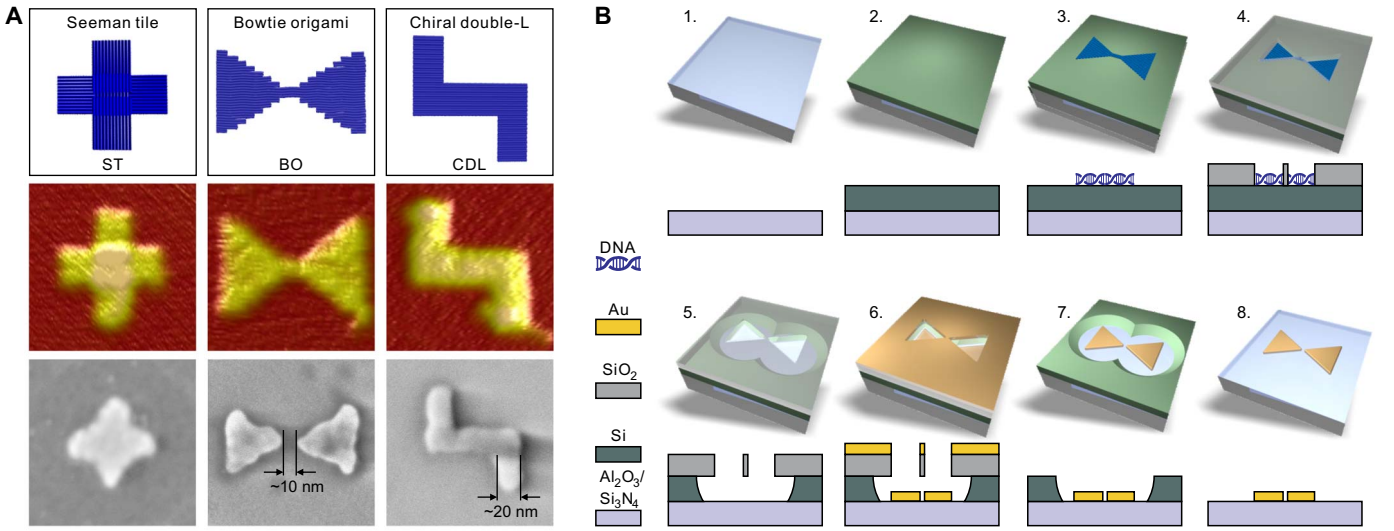

Fig. 1. DNA origami designs, a step-by-step fabrication procedure of the DALI method. (**A**) Top: Designed DNA origami shapes (from left to right): ST, BO, and CDL. Middle: AFM images of the folded structures on a mica substrate. Bottom: Scanning electron microscopy (SEM) images of gold nanostructures created by the fabrication method described in detail in (B). The AFM and SEM images are 150 nm × 150 nm in size. (**B**) Steps of the fabrication procedure. Step 1: A transparent sapphire (Al_2O_3)/silicon nitride (Si_3N_4) chip is freshly cleaned by acetone and isopropanol. Step 2: An amorphous silicon layer is grown on top of the substrate by PECVD. Step 3: The substrate is treated by oxygen plasma, after which the DNA origami nanostructures (BO shown here as an example) are drop-casted on the chip. Step 4: The silicon dioxide (SiO_2) layer is selectively grown on the bare silicon by CVD, leaving DNA origami–shaped silhouettes in the layer. Step 5: Using the grown SiO_2 layer as a mask, the silicon underneath is etched away by RIE. Step 6: The metal is deposited onto the chip using PVD in ultrahigh vacuum. Step 7: The SiO_2 layer is removed in a liftoff process using hydrogen fluoride–based wet etching. Step 8: The remaining silicon is removed by RIE, thus leaving the DNA origami–shaped metal nanostructure on the substrate.

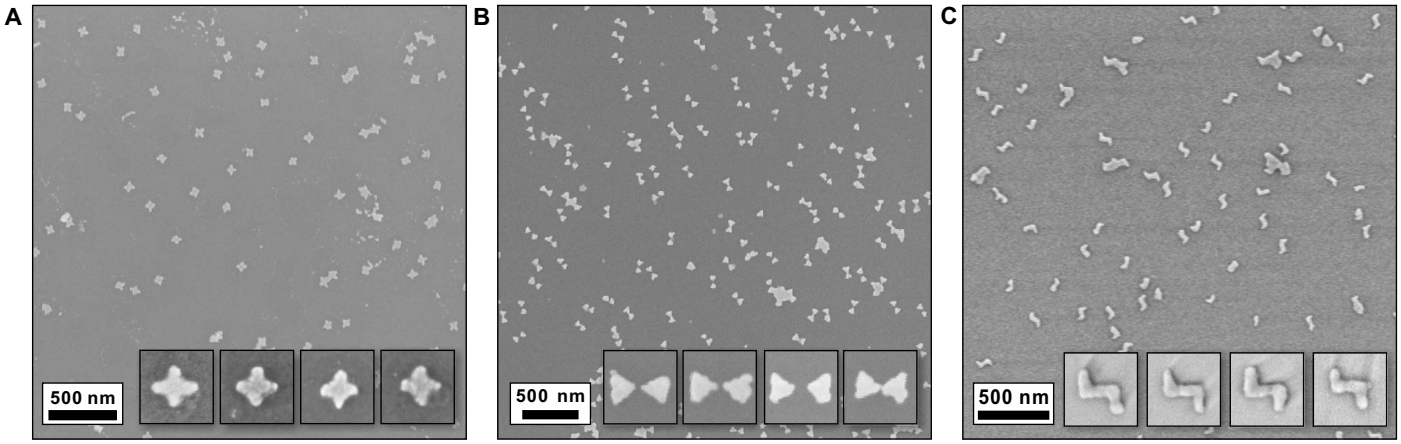

Fig. 2. Large-area SEM images of the structures created with DALI. (**A**) AuPd ST structures on Si_3N_4. (**B**) Au BO structures on Si_3N_4. (**C**) Au CDL structures on sapphire. All the inset images are 150 nm × 150 nm in size.

step 6). Finally, the silicon dioxide stencil and the remaining silicon are etched away (Fig. 1B, steps 7 and 8), which results in discrete origami-shaped metal nanostructures on the transparent substrate (Fig. 2). The produced metal structures are uniform in size and shape, and the density of the structures can be easily tuned by varying the parameters of the deposition step (step 3). Most of all, the parallel fabrication provides high throughput and resolution with a feature size of ~10 nm; the width of the arms for STs and CDLs is ~20 nm, and the gap size for the BOs can be less than 10 nm (Figs. 1A and 2B). The detailed fabrication procedure is presented in note S1.

Besides its capability of fabricating nanostructures with specific shapes (as ST and CDL) and with relatively high yields (see the "Fabrication yield analysis" section in the Appendix of the Supplementary Materials), DALI can also be used to produce particle pairs that are separated by adjustable nanoscale gaps. An example of this structure is a bowtie-shaped optical antenna, the shape that has been widely harnessed in different optical applications. This is due to its characteristic highly confined plasmonic mode within the gap that provides an extreme field enhancement. For applications such as surface-enhanced sensing (*28*) and fluorescence enhancement (*29*), it is essential to tune the wavelength of the maximum enhancement, which substantially depends on the selected material, size, and exact shape of the structure, in particular on the sharpness of the tips and the size of the gap. To obtain the maximum enhancement within the visible wavelength range, the size

of the gap between the antennas needs to be below 10 nm on a glass substrate (*29*, *30*). To date, this resolution has only been achieved by focused beam lithography (electron or ion beam). This is an expensive scanning technique, which makes it unsuitable for large-scale production.

To demonstrate that our DALI method provides the necessary accuracy to produce efficient optical bowtie antennas, we used the designed BO shape (Fig. 1A) as a template. The gap between the two triangles can be formed because the thin silicon oxide layer grown on top of the origami (fabrication step 4) appears to be thicker at the narrow part of the BO than at the triangles. The reason is that the silicon oxide grows slowly on top of the BO starting from the edges of the already formed oxide layer, and these edges can merge at the thin bridge between the two triangles, resulting in a nonuniform thickness profile of the oxide. Using careful etching techniques in step 5, we obtain a stencil mask with two individual triangles separated by a nanometer-scale gap. By merely controlling the processing times in fabrication steps 4 and 5, the gap size and therefore the resulting plasmonic resonance can be tuned (see note S2). This feature enabled us to fabricate the smallest, entirely metallic bowtie antenna that has ever been reported (~125 nm in the long axis including two sub–60-nm triangles and a gap ranging from 5 to 20 nm), verified by detailed characterization of the optical/plasmonic properties of the produced structures (see below). In addition, to show the uniformity of DALI-fabricated structures, we analyzed numerous bowtie antennas from one fabrication batch and determined the average gap size, thickness, and bending angle, that is, angle between the triangles. We obtained 12 ± 5 nm (SD) for the gap size, 21.6 ± 0.2 nm (SD) with ~2-nm mean roughness for the thickness, and 179 ± 12° (SD) for the bending angle (note S1).

For plasmonic characterization, we measured the scattering spectra at different polarization angles from single metallic nanoantennas (note S3) using a dark-field microscope coupled to a spectrometer via an optical fiber (details in note S4). This allowed us to separately determine the localized surface plasmon resonances (LSPRs) of the structure both along and perpendicular to the gap. As a control and as a comparison, we also characterized the metallic ST shapes.

For the BO shapes, we observed the highest LSPR peaks at the polarizations along the gap (λ_{max} at 704 nm) and perpendicular to the gap (λ_{max} at 650 to 700 nm), as shown in Fig. 3A (additional spectra from different samples shown in note S5). The LSPR peak associated with the gap mode has higher intensity and longer wavelength than the perpendicular mode, which is in good agreement with the earlier reports (*28*–*30*) and with the finite element method (FEM) simulated data shown in Fig. 3A. The simulated spatial distributions of the field enhancement for these two main modes are plotted in the insets of Fig. 3A. Because our structure is smaller than the previously reported bowties, the observed LSPR peaks accordingly appear at shorter wavelengths (despite the fact that the sapphire substrate has a higher refractive index than indium tin oxide/glass substrates used in the earlier studies) (*29*, *30*).

To estimate the LSPR variations within a single fabrication batch, we simulated the structures with geometries differing from the optimal shape by the amount of the observed SD (see above). The bending angle change within the SD had no noticeable effect on the LSPR peak position or the field enhancement. However, an increase in the thickness (by mean roughness) or in the gap size (by SD) yielded 8.5- or 12.5-nm blue shifts in the gap mode resonance, respectively. Moreover, these changes induced 12 and 30% decreases in the field enhancement. Only the thickness variation had an effect on the perpendicular mode, inducing a 6.5-nm blue shift with a negligible decrease in the field enhancement. In summary, the changes in plasmonic properties due to the observed variations in the fabrication process were insignificant, thus revealing the homogeneity of the DALI process (for more details, see fig. S15).

In the case of metallic ST shapes, we typically observed the highest LSPR peaks at polarizations along the arms of the cross (Fig. 3B). For a fully symmetric ST, these peaks should overlap, but due to an unavoidable slight asymmetry between the two arms, the peaks usually appeared at slightly different wavelengths. This is in qualitative agreement with the simulated data shown in Fig. 3B. The LSPR resonances for the BO and ST structures lay within the same wavelength region, but the key difference is the obtained maximum field enhancement. As can be seen from

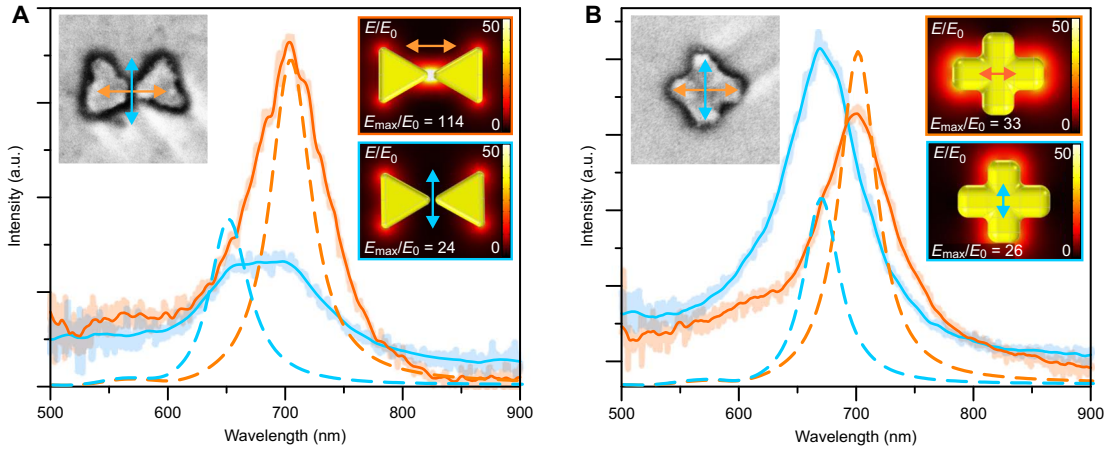

Fig. 3. Experimental and simulated linear polarization scattering spectra for single BO- and ST-shaped gold nanostructures. (**A** and **B**) Dark-field scattering spectra of the BO and ST shapes (SEM images shown in the left insets, 200 nm × 200 nm in size) measured at two different polarization angles (indicated by correspondingly colored arrows in the insets). Lines show the smoothed spectra, whereas the original data are shown faded in the background. Dashed lines show simulated scattering spectra for the BO and ST shapes in (A) and (B), respectively. The right-side insets show a field enhancement, that is, the local electric field (E) divided by the incoming electric field (E_0) at the chosen polarization angles (shown by colored arrows) at the middle height of the structure, that is, 10 nm above the surface. The main LSPR modes are at 650 and 705 nm for the BO and at 670 and 700 nm for the slightly asymmetric ST. The maximum local field enhancement, E_{max}/E_0, for each sample is also stated in each inset. a.u., arbitrary units.

the simulation results in the insets of Fig. 3 (A and B), the excitation of the BO gap mode should yield a maximum field enhancement almost four times as high as that of the other modes, which all have very similar responses.

The abovementioned LSPR measurement can be used to verify the desired plasmonic activity of the fabricated nanostructures. Yet, for more application-oriented purposes and to verify the effective plasmonic hotspots, we demonstrated the feasibility of the BO antennas for SERS by using two typical SERS markers with opposite charges (namely, rhodamine 6G and 2,2-bipyridine). The samples were fabricated by pipetting a droplet of the chosen 1 μM marker solution onto a sapphire chip so that the droplet covered both the prefabricated metallic BOs and the clean sapphire surface (clean surface was used as a reference). After drying the droplet, we characterized the chip using Raman microscopy. The characteristic Raman spectra of both markers were detected with significantly high resolution (Fig. 4A) on the areas covered by the BO antennas (Fig. 4A, inset), whereas no Raman signal was observed from the empty areas of the chip (Fig. 4A, dotted lines).

As a final demonstration of the versatility of the DALI method, we fabricated planar chiral structures, which are of fundamental importance in metamaterials and in biosensing applications, especially in enhancing the detection of different molecular enantiomers. In particular, the miniaturization of these structures to the sub–100-nm scale is essential to fabricate metamaterials that function in the visible spectrum. To produce a controlled chiral optical response within this wavelength range, we designed a CDL-shaped origami with suitable dimensions. However, to produce a sample with the desired response, most of the CDL origamis should have a specified orientation after the deposition, that is, CDLs should land on the O_2 plasma–treated Si substrate in either S- or Z-shaped orientation. We observed that when 37.5 mM Mg^{2+} was used in the deposition buffer, ~80% of the plain CDL origamis tend to adsorb onto the Si surface with the S-shaped orientation. However, at 70 mM or higher Mg^{2+} concentration, the deposition yielded equal amounts of S- and Z-shaped orientations. Besides merely adjusting the Mg^{2+} concentration, it is possible to efficiently alter the distribution of S- and Z-shaped orientations by incorporating dozens of protruding staple strand extensions into the design. The reason is that if these single-stranded DNA (ssDNA) protrusions are attached only to the one side of the origami, then the strands act as an entropic brush, and therefore, the structures prefer to land with the staple strand extension side up. Here, by introducing a total of 114 poly-T_{20} overhangs into the design, the bias toward the S-shaped orientation could be increased up to 99% (see the "Fabrication yield analysis" section in the Appendix of the Supplementary Materials).

By converting the CDL origami into metallic nanostructures, we could produce planar chiral samples with diverse CD responses (Fig. 4D) depending on the deposition process. A sample with randomly oriented CDLs (equal amount of S- and Z-shaped orientations, unmodified CDL) (Fig. 4B) and a sample with S-shaped orientation–biased CDLs ("swimmer strand"–equipped CDL) (Fig. 4C) exhibited very different broadband CD effects in the wavelength range of 500 to 1050 nm. The sapphire chip with only S-shaped gold nanostructures showed a well-defined peak at 650 nm and a wide negative peak at 950 nm, which qualitatively agrees with the FEM simulations (black lines in Fig. 4D). The simulated power loss inside the metal shows a clear difference between the two opposite circularly polarized excitations (Fig. 4D, insets), whereas the effect in the local field enhancement is small, which is also clear from the matching absorption spectra between the S- and Z-shaped orientations (note S6). This confirms that the observed CD response is due to the chiral shape of the metal structures.

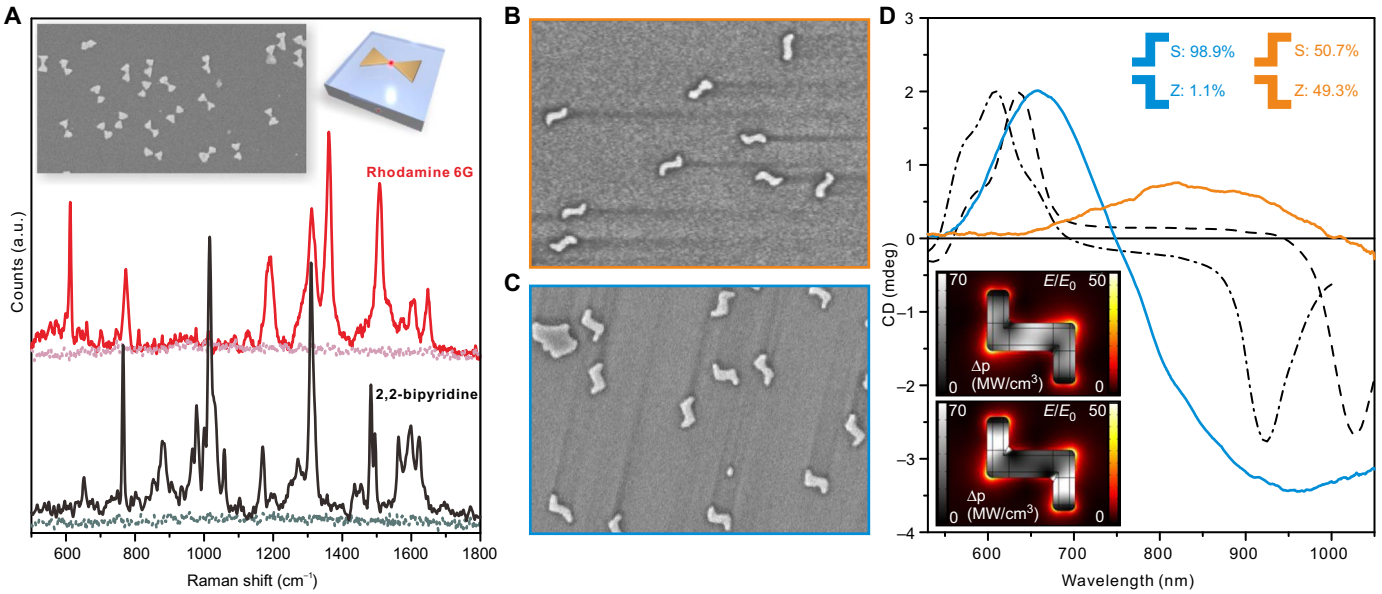

Fig. 4. Metallic BO shapes for SERS and CDL shapes for creating chiral plasmonic response. (**A**) Raman spectra (baseline-corrected) measured from a sample containing nanosized gold BOs coated with either the rhodamine 6G (red) or 2,2-bipyridine molecules (black). Lighter dotted lines show the response of the same concentration of the molecules on a pure substrate without the BOs. (**B**) SEM of a sample containing 50:50 distribution of S- and Z-shaped metallic CDLs on a sapphire substrate. (**C**) SEM of a sample with ~99% of the CDLs in the S-configuration on a sapphire substrate. The SEM images (B and C) are 1.4 μm × 1 μm in size. (**D**) Orange and blue curves: Averaged and baseline-corrected CD spectra measured from the samples shown in (B) and (C). Black lines: Simulated CD response for a symmetric (dashed) and slightly asymmetric (dash-dotted) S-shaped CDL. Insets show the field enhancement (color scale) and power loss inside the metal (grayscale) for the symmetric CDL and for the right-handed (upper) and left-handed (lower) circularly polarized 640-nm excitation light.

The broadness of the negative peak at 950 nm compared to the simulations can be attributed to a variation of the length in the end pieces of the fabricated metallic CDLs, which is also visible in Fig. 4 (B and C). The two simulations show a CD response of a fully symmetric CDL structure along the origami dimensions (dashed line) and a similar asymmetric structure with the end pieces asymmetrically shortened (dash-dotted line). This shows that the peak at 640 nm is almost unaffected, whereas the negative peak shifts considerably, thus providing a wide feature when averaged over the distribution of symmetric and asymmetric CDLs. The CD spectrum of the randomly oriented sample showed only insignificant broad spectral features, which demonstrate the lack of preferred surface orientation. It is noteworthy that despite a very small optical density of the setup (perpendicular incident light passing through a monolayer of 20-nm-thick CDLs), the CD effect was clearly observed. This strongly implies that the sensitivity could be further improved, thus opening up potential applications in chiral molecule sensing.

DISCUSSION

The DALI method enables highly parallel fabrication of arbitrary-shaped plasmonic nanostructures with well-defined shapes using self-assembled DNA origami templates. Because DNA origami designs are straightforward to produce in high yields and, in DALI, do not require any additional treatment or purification steps, the method is robust and provides high throughput. We demonstrated this by fabricating three different metallic nanoshapes on transparent substrates, including bowtie nanoantennas with controllable plasmonic resonances at the visible range (the minimum bowtie gap that was characterized was 8 nm) and planar CDL structures that provide a clear CD response. As a final note, we believe that the cheap wafer-scale production of plasmonic metasurfaces can be achieved using the DALI method because it does not rely on costly patterning methods and is compatible with various deposition techniques (*10*, *31*, *32*) for large lattice structures spatially ordered in both position and orientation. Furthermore, we are positive that this novel method can find intriguing applications in biosensing and in the fabrication of bioinspired surfaces and dielectric metamaterials (*33*).

MATERIALS AND METHODS

Design of DNA structures

The BO and CDL were designed using caDNAno (*34*) and CanDo (*35*, *36*) software. ST was fabricated as explained by Liu *et al.* (*25*). All the structures are based on the 7249-nucleotide-long M13mp18 plasmid scaffold strand. The BO structure is twist-corrected, that is, the twist resulting from the square lattice packing (*35*–*37*) is relaxed by additional base skips in the design (*35*, *36*, *38*) according to a CanDo simulation. Side strands in the BO and CDL designs contain TTTTTTTT (poly-T_8) overhangs to prevent the blunt-end stacking of the origami structures. In the case of ST, the side strands were omitted (*25*). Two different versions of the CDL were fabricated: a plain unmodified version and a version with the staple strand extensions at one side. These extensions were used to bias the landing orientation of the CDL structure (Fig. 4, B and C). The folding and characterization procedures for all the origami shapes are described below. The caDNAno designs for the BO and CDL and the complete list of staple strands are presented in the Appendix of the Supplementary Materials. The staple extensions (114 strands) of the CDL replace one to one the strands from the set of "core strands pool #1" (green color in the caDNAno design, see the Appendix in the Supplementary Materials). These strands hybridize to the scaffold via the same sequence as core strands pool #1, but the extended strands contain poly-T_{20} overhangs at the 5′-end. The protrusions are designed in such a way that the CDL will adopt an S-shaped orientation when deposited onto the substrate, that is, all the poly-T extensions are pointing out from the substrate and the unmodified side of the CDL is attached to the substrate.

DNA origami fabrication

The DNA origami structures were prepared as 100-μl quantities by mixing the following components: (i) 40 μl of 2.5× TAE buffer with Mg^{2+} [100 mM tris, 47.5 mM acetic acid, 2.5 mM EDTA, 31.25 mM $MgCl_2$ (pH ~8.3)]; (ii) 40 μl of staple strand mix (each staple at ~500 nM concentration) [The staple strand mix was prepared by pipetting equal amounts of each staple strand (Integrated DNA Technologies, initial concentration of 100 μM in water, ~200 strands per design) and mixing them together. This resulted in about 500 nM concentration for each strand in the staple strand mix. If the origami contains less than 200 strands (as in ST: 177 strands), then 500 nM concentration was achieved by dilution with water]; and (iii) 20 μl of the scaffold strand M13mp18 (100 nM in water) (Tilibit Nanosystems).

The final concentration of the scaffold strand in a total reaction volume of 100 μl was 20 nM, and the concentration of magnesium was 12.5 mM. The staple strands were used in 10× excess compared to the M13mp18 scaffold strand (each staple at 200 nM concentration). The following thermal annealing ramp was used for folding: From 90° to 70°C with increments of 0.2°C/8 s, from 70° to 60°C with increments of 0.1°C/8 s, and from 60° to 27°C with increments of 0.1°C/2 min. Finally, the solution was stored at 12°C. After folding, the theoretical maximum concentration of DNA origami is 20 nM.

Gel electrophoresis for DNA origami

Gel electrophoresis was used to verify the quality of the DNA origami folding (see fig. S1). Agarose gels (2%) were prepared by dissolving 2 g of agarose (Bioline, Molecular Grade) into 100 ml of 1× TAE buffer with 11 mM Mg^{2+} (40 mM tris, 19 mM acetic acid, 1 mM EDTA, 11 mM $MgCl_2$). The gel was stained using 100 μl of ethidium bromide solution (0.625 mg/ml). Ten microliters of DNA origami solution were mixed with 2 μl of 6× loading dye (New England Biolabs). M13mp18 ssDNA (at 100 nM) was used as a reference at 40 nM concentration by diluting it with the folding buffer (1× TAE buffer with 12.5 mM Mg^{2+}). The gel wells were loaded with 10 μl of the sample. The gels were run with a constant voltage of 90 V for 45 to 60 min and imaged under ultraviolet (UV) light (Bio-Rad equipment, Image Lab Software).

Atomic force microscopy

The AFM (Veeco, Dimension 3100) was used to characterize the sample after the DNA origami deposition and to verify the successful formation of the origami-shaped opening in the SiO_2. The AFM imaging of these openings was usually carried out in tapping mode with a scan size varying from 1 to 10 μm. The tip velocity ranged from 2 to 15 μm/s. For the analysis of the uniformity of the DALI-fabricated metallic nanostructure, numerous bowtie antennas from a single batch were characterized using the peak force tapping mode in air (Bruker, Icon), where the scan size was from 1 to 5 μm and the tip velocity was from 1.5 to 10 μm/s.

Scanning electron microscopy

Sapphire is an insulator, and thus, imaging with a scanning electron microscope (Raith eLine scanning electron microscopy system) induces

charging of the substrate. To reduce the distortion caused by the charging effect, low acceleration voltages (5 to 10 kV) were used. In addition, the scanning times were minimized to reduce the current exposed to a small area. The images were taken with a 30-μm aperture in a continuous averaging mode. Brightness and contrast levels were adjusted to compensate for the charging effect.

DNA-assisted lithography

See note S1 for details about general lithography materials and methods. Details about sample preparation for single-particle LSPR measurement can be found in note S3.

Single-particle linear polarization LSPR measurement

To measure the single-particle spectra, an Olympus BX51TRF microscope with Olympus MPLANFL N objectives (5×/20×/50×) was used for imaging. The excitation light was generated using a halogen lamp (Olympus 100 W) inside a lamp housing (Olympus U-LH100IR-1-7). Dark-field imaging was carried out using a dark-field condenser (Olympus U-DCW). An analyzer (Olympus U-AN360-3) was used to select the polarization of the measured light, and a linear polarizer (Thorlabs LPVISE200-A 2") was used to align the analyzer. A custom-made slit mask was used to align the polarizer and the marker grid of the sample. The light was extracted by placing a fiber (Thorlabs UM22-300-custom; core size, 300 μm) onto the output port of the microscope and by focusing the tip of the fiber to the image plane of the port. The other end of the fiber was connected to a collimator (Thorlabs) that was, in turn, connected to a custom-made switch box (Thorlabs). The measured light was focused to the slit of the spectrograph [Princeton Instruments SP2150 (Acton)] equipped with a charge-coupled device (CCD) camera (Andor iVac DR-324B-FI) to record the spectra. The dark-field images were recorded using a Canon EO5 6D camera connected to the other microscope port. The whole setup was located inside an electromagnetically shielded room, and the spectrograph and the CCD camera were connected to a computer using a Black Box IC404A fiber extender. A Thorlabs M530L3-mounted light-emitting diode connected to the switch box was used to visualize the position of the fiber spot on the sample, whereas a *XYZ*-micrometer translational stage was used to move the fiber in the microscope view and to focus the fiber spot (fig. S10A). Andor Solis (version 4.18) was used to measure the spectra, and Canon EOS utility was used to take the dark-field images remotely. The single-particle spectroscopy (SPS) microscope setup is schematically illustrated in fig. S10C (see note S4 for details).

CD measurement of CDL samples

The CD measurements of the CDLs on a sapphire substrate were carried out using a Jasco J-715 CD spectrometer. The sample surface was placed perpendicularly to the incident beam. For all the samples measured, the illumination direction was from the back side (sapphire side) to the particle side. A measurement with a reverse direction would yield the same result due to the symmetry. In addition, a square aperture of 4 mm × 4 mm was used in direct contact to the back side of the sample to reduce the diffraction of the sample edges.

Surface-enhanced Raman spectroscopy

The SERS measurements were carried out using a Senterra dispersive Raman microscope (BRUKER). Confocal Raman spectroscopy was used to acquire SERS of the molecule-BO samples. Raman scattering was detected using a Peltier-cooled (−70°C) CCD camera (255 × 1024 pixels), focusing only within the fingerprint regions (500 to 1800 cm^{-1}). Detection was carried out using 180° geometry and a near-infrared diode laser (785 nm) for the excitation. The spectrometer was equipped with a diffraction grating (1200 grooves/mm), and the slit provided a spectral resolution of 2 cm^{-1}. The laser power at the sample ranged from 1 to 10 mW, and the acquisition time ranged from 1 to 5 s. The area of the laser spot on the samples was approximately 1 μm in diameter. The molecular markers with 1 μM concentration in ethanol were drop-casted on the BO sample surface before the measurement. The setup was calibrated using built-in templates and internal Raman standards.

SUPPLEMENTARY MATERIALS

Supplementary material for this article is available at http://advances.sciencemag.org/cgi/content/full/4/2/eaap8978/DC1

note S1. DALI.
note S2. Gap formation in a BO structure.
note S3. Single-particle LSPR sample fabrication.
note S4. Single-particle linear polarization LSPR measurement.
note S5. Additional single-particle linear polarization LSPR spectra.
note S6. UV-Vis measurement of CDL samples.
note S7. Numerical simulations.
fig. S1. Agarose gel electrophoresis of DNA origamis.
fig. S2. DNA origami deposition on the Si surface.
fig. S3. Schematic view of the reaction chamber setup for the SiO_2 growth.
fig. S4. Fabrication of trenches/silhouettes with different DNA origami shapes.
fig. S5. Isotropic RIE etching of silicon.
fig. S6. PVD of gold.
fig. S7. HF liftoff (removal of the SiO_2 mask).
fig. S8. AFM images with the corresponding thickness profiles and a SEM image of Au bowtie antennas on a sapphire substrate.
fig. S9. Schematic illustration of the oxide growth in the vicinity of the BO on a Si substrate.
fig. S10. Schematics of the SPS setup.
fig. S11. Single-structure spectra of different metallized origami shapes.
fig. S12. Normalized UV-Vis spectra of CDL samples with S-configuration and random orientation.
fig. S13. Simulation geometry for a CDL particle (S-shaped orientation) with a clockwise polarized incident light and used mesh.
fig. S14. Geometries of the different types of particles for the Comsol simulations.
fig. S15. Simulated LSPR spectra and field enhancements (E/E_0 at resonance frequency) for the optimal bowtie structure and for the structures with geometries altered by the amount of the observed SDs.
table S1. Parameters for a-Si CVD.
table S2. Parameters for O_2 plasma RIE.
table S3. Parameters for RIE SiO_2 etching.
table S4. Parameters for RIE Si etching.
Appendix
Design and sequences of BO
Design and sequences of CDL
Additional SEM data set
Fabrication yield analysis
References (*39*–*41*)

REFERENCES AND NOTES

1. V. M. Shalaev, Optical negative-index metamaterials. *Nat. Photonics* **1**, 41–48 (2007).
2. Z. Wang, F. Cheng, T. Winsor, Y. Liu, Optical chiral metamaterials: A review of the fundamentals, fabrication methods and applications. *Nanotechnology* **27**, 412001 (2016).
3. M. R. Jones, N. C. Seeman, C. A. Mirkin, Programmable materials and the nature of the DNA bond. *Science* **347**, 1260901 (2015).
4. V. Linko, H. Dietz, The enabled state of DNA nanotechnology. *Curr. Opin. Biotechnol.* **24**, 555–561 (2013).
5. N. V. Voigt, T. Tørring, A. Rotaru, M. F. Jacobsen, J. B. Ravnsbæk, R. Subramani, W. Mamdouh, J. Kjems, A. Mokhir, F. Besenbacher, K. V. Gothelf, Single-molecule chemical reactions on DNA origami. *Nat. Nanotechnol.* **5**, 200–203 (2010).
6. H. T. Maune, S.-p. Han, R. D. Barish, M. Bockrath, W. A. Goddard III, P. W. K. Rothemund, E. Winfree, Self-assembly of carbon nanotubes into two-dimensional geometries using DNA origami templates. *Nat. Nanotechnol.* **5**, 61–66 (2010).

7. A. Kuzyk, R. Schreiber, Z. Fan, G. Pardatscher, E.-M. Roller, A. Högele, F. C. Simmel, A. O. Govorov, T. Liedl, DNA-based self-assembly of chiral plasmonic nanostructures with tailored optical response. *Nature* **483**, 311–314 (2012).
8. G. P. Acuna, F. M. Möller, P. Holzmeister, S. Beater, B. Lalkens, P. Tinnefeld, Fluorescence enhancement at docking sites of DNA-directed self-assembled nanoantennas. *Science* **338**, 506–510 (2012).
9. J. B. Knudsen, L. Liu, A. L. Bank Kodal, M. Madsen, Q. Li, J. Song, J. B. Woehrstein, S. F. J. Wickham, M. T. Strauss, F. Schueder, J. Vinther, A. Krissanaprasit, D. Gudnason, A. A. A. Smith, R. Ogaki, A. N. Zelikin, F. Besenbacher, V. Birkedal, P. Yin, W. M. Shih, R. Jungmann, M. Dong, K. V. Gothelf, Routing of individual polymers in designed patterns. *Nat. Nanotechnol.* **10**, 892–898 (2015).
10. A. Gopinath, E. Miyazono, A. Faraon, P. W. K. Rothemund, Engineering and mapping nanocavity emission via precision placement of DNA origami. *Nature* **535**, 401–405 (2016).
11. B. Ding, Z. Deng, H. Yan, S. Cabrini, R. N. Zuckermann, J. Bokor, Gold nanoparticle self-similar chain structure organized by DNA origami. *J. Am. Chem. Soc.* **132**, 3248–3249 (2010).
12. R. Schreiber, J. Do, E.-M. Roller, T. Zhang, V. J. Schüller, P. C. Nickels, J. Feldmann, T. Liedl, Hierarchical assembly of metal nanoparticles, quantum dots and organic dyes using DNA origami scaffolds. *Nat. Nanotechnol.* **9**, 74–78 (2014).
13. S. J. Tan, M. J. Campolongo, D. Luo, W. Cheng, Building plasmonic nanostructures with DNA. *Nat. Nanotechnol.* **6**, 268–276 (2011).
14. R. Schreiber, S. Kempter, S. Holler, V. Schüller, D. Schiffels, S. S. Simmel, P. C. Nickels, T. Liedl, DNA origami-templated growth of arbitrarily shaped metal nanoparticles. *Small* **7**, 1795–1799 (2011).
15. M. Pilo-Pais, S. Goldberg, E. Samano, T. H. LaBean, G. Finkelstein, Connecting the nanodots: Programmable nanofabrication of fused metal shapes on DNA templates. *Nano Lett.* **11**, 3489–3492 (2011).
16. S. Helmi, C. Ziegler, D. J. Kauert, R. Seidel, Shape-controlled synthesis of gold nanostructures using DNA origami molds. *Nano Lett.* **14**, 6693–6698 (2014).
17. W. Sun, E. Boulais, Y. Hakobyan, W. L. Wang, A. Guan, M. Bathe, P. Yin, Casting inorganic structures with DNA molds. *Science* **346**, 1258361 (2014).
18. Z. Jin, W. Sun, Y. Ke, C.-J. Shih, G. L. C. Paulus, Q. H. Wang, B. Mu, P. Yin, M. S. Strano, Metallized DNA nanolithography for encoding and transferring spatial information for graphene patterning. *Nat. Commun.* **4**, 1663 (2013).
19. P. W. K. Rothemund, Folding DNA to create nanoscale shapes and patterns. *Nature* **440**, 297–302 (2006).
20. E. S. Andersen, M. Dong, M. M. Nielsen, K. Jahn, R. Subramani, W. Mamdouh, M. M. Golas, B. Sander, H. Stark, C. L. P. Oliveira, J. S. Pedersen,V. Birkedal, F. Besenbacher, K. V. Gothelf, J. Kjems, Self-assembly of a nanoscale DNA box with a controllable lid. *Nature* **459**, 73–76 (2009).
21. S. M. Douglas, H. Dietz, T. Liedl, B. Högberg, F. Graf, W. M. Shih, Self-assembly of DNA into nanoscale three-dimensional shapes. *Nature* **459**, 414–418 (2009).
22. D. Han, S. Pal, J. Nangreave, Z. Deng, Y. Liu, H. Yan, DNA origami with complex curvatures in three-dimensional space. *Science* **332**, 342–346 (2011).
23. E. Benson, A. Mohammed, J. Gardell, S. Masich, E. Czeigler, P. Orponen, B. Högberg, DNA rendering of polyhedral meshes at the nanoscale. *Nature* **523**, 441–418 (2015).
24. R. Veneziano, S. Ratanalert, K. Zhang, F. Zhang, H. Yan, W. Chiu, M. Bathe, Designer nanoscale DNA assemblies programmed from the top down. *Science* **352**, 1534 (2016).
25. W. Liu, H. Zhong, R. Wang, N. C. Seeman, Crystalline two-dimensional DNA-origami arrays. *Angew. Chem. Int. Ed.* **50**, 264–267 (2011).
26. S. P. Surwade, F. Zhou, B. Wei, W. Sun, A. Powell, C. O'Donnell, P. Yin, H. Liu, Nanoscale growth and patterning of inorganic oxides using DNA nanostructure templates. *J. Am. Chem. Soc.* **135**, 6778–6781 (2013).
27. B. Shen, V. Linko, K. Tapio, M. A. Kostiainen, J. J. Toppari, Custom-shaped metal nanostructures based on DNA origami silhouettes. *Nanoscale* **7**, 11267–11272 (2015).
28. N. Liu, M. L. Tang, M. Hentschel, H. Giessen, A. P. Alivisatos, Nanoantenna-enhanced gas sensing in a single tailored nanofocus. *Nat. Mater.* **10**, 631–636 (2011).
29. A. Kinkhabwala, Z. Yu, S. Fan, Y. Avlasevich, K. Müllen, W. E. Moerner, Large single-molecule fluorescence enhancements produced by a bowtie nanoantenna. *Nat. Photonics* **3**, 654–657 (2009).
30. M. Kaniber, K. Schraml, A. Regler, J. Bartl, G. Glashagen, F. Flassig, J. Wierzbowski, J. J. Finley, Surface plasmon resonance spectroscopy of single bowtie nano-antennas using a differential reflectivity method. *Sci. Rep.* **6**, 23203 (2016).
31. V. Linko, B. Shen, K. Tapio, J. J. Toppari, M. A. Kostiainen, S. Tuukkanen, One-step large-scale deposition of salt-free DNA origami nanostructures. *Sci. Rep.* **5**, 15634 (2015).
32. A. Gopinath, P. W. K. Rothemund, Optimized assembly and covalent coupling of single-molecule DNA origami nanoarrays. *ACS Nano* **8**, 12030–12040 (2014).
33. A. Arbabi, Y. Horie, M. Bagheri, A. Faraon, Dielectric metasurfaces for complete control of phase and polarization with subwavelength spatial resolution and high transmission. *Nat. Nanotechnol.* **10**, 937–943 (2015).
34. S. M. Douglas, A. H. Marblestone, S. Teerapittayanon, A. Vazquez, G. M. Church, W. M. Shih, Rapid prototyping of 3D DNA-origami shapes with caDNAno. *Nucleic Acids Res.* **37**, 5001–5006 (2009).
35. C. E. Castro, F. Kilchherr, D.-N. Kim, E. L. Shiao, T. Wauer, P. Wortmann, M. Bathe, H. Dietz, A primer to scaffolded DNA origami. *Nat. Methods* **8**, 221–229 (2011).
36. D.-N. Kim, F. Kilchherr, H. Dietz, M. Bathe, Quantitative prediction of 3D solution shape and flexibility of nucleic acid nanostructures. *Nucleic Acids Res.* **40**, 2862–2868 (2011).
37. Y. Ke, S. M. Douglas, M. Liu, J. Sharma, A. Cheng, A. Leung, Y. Liu, W. M. Shih, H. Yan, Multilayer DNA origami packed on a square lattice. *J. Am. Chem. Soc.* **131**, 15903–15908 (2009).
38. H. Dietz, S. M. Douglas, W. M. Shih, Folding DNA into twisted and curved nanoscale shapes. *Science* **325**, 725–730 (2009).
39. M.-H. Chien, L.-W. Nien, B.-K. Chao, J.-H. Li, C.-H. Hsueh, Effects of the rotation angle on surface plasmon coupling of nanoprism. *Nanoscale* **8**, 3660–3670 (2016).
40. D. P. Fromm, A. Sundaramurthy, P. J. Schuck, G. Kino, W. E. Moerner, Gap-dependent optical coupling of single "bowtie" nanoantennas resonant in the visible. *Nano Lett.* **4**, 957–961 (2004).
41. R. L. Olmon, B. Slovick, T. W. Johnson, D. Shelton, S.-H. Oh, G. D. Boreman, M. B. Raschke, Optical dielectric function of gold. *Phys. Rev. B* **86**, 235147 (2012).

Acknowledgments: We thank E. Hulkko, H. Häkkänen, J. A. Ihalainen, M. Pettersson, T. A. Puurtinen, J. Simonen (University of Jyväskylä), and S. Tuukkanen (Tampere University of Technology) for discussions and valuable comments. **Funding:** This work was supported by the Academy of Finland (projects 130900, 135193, 218182, 263526, 286845, and 289947), the Jane and Aatos Erkko Foundation, the Finnish Cultural Foundation, the Finnish Academy of Science and Letters (Vilho, Yrjö and Kalle Väisälä Foundation), the Emil Aaltonen Foundation, and the U.S. Office of Naval Research (award no. N000141410702). The work was carried out under the Academy of Finland Centres of Excellence Programme (2014–2019).
Author contributions: B.S., V.L., and J.J.T. conceived the study and, together with K.T., S.P., T.L., A.G., K.V.G., and M.A.K., designed the experiments. B.S. performed the lithography of the samples. B.S. and K.T. performed AFM and SEM imaging and optical measurements. V.L. conceived, designed, fabricated, and characterized the DNA origami nanostructures and contributed to the development of the lithography method. A.G. and K.V.G. contributed to the design of the chiral DNA origami and to the optimization of its deposition procedure. S.P. carried out simulations related to optical measurements. T.L. performed the SERS measurements. B.S., V.L., K.T., M.A.K., and J.J.T. prepared the main manuscript. All authors discussed the results, analyzed the data, and commented on the manuscript.
Competing interests: The authors declare that they have no competing interests.
Data and materials availability: All data needed to evaluate the conclusions in the paper are present in the paper and/or the Supplementary Materials. Additional data related to this paper may be requested from the authors.

Submitted 7 September 2017
Accepted 8 January 2018
Published 2 February 2018
10.1126/sciadv.aap8978

Citation: B. Shen, V. Linko, K. Tapio, S. Pikker, T. Lemma, A. Gopinath, K. V. Gothelf, M. A. Kostiainen, J. J. Toppari, Plasmonic nanostructures through DNA-assisted lithography. *Sci. Adv.* **4**, eaap8978 (2018).

A.V

SCIENTIFIC REPORTS

OPEN

One-step large-scale deposition of salt-free DNA origami nanostructures

Received: 19 June 2015
Accepted: 28 September 2015
Published: 23 October 2015

Veikko Linko[1], Boxuan Shen[2], Kosti Tapio[2], J. Jussi Toppari[2], Mauri A. Kostiainen[1] & Sampo Tuukkanen[3]

DNA origami nanostructures have tremendous potential to serve as versatile platforms in self-assembly -based nanofabrication and in highly parallel nanoscale patterning. However, uniform deposition and reliable anchoring of DNA nanostructures often requires specific conditions, such as pre-treatment of the chosen substrate or a fine-tuned salt concentration for the deposition buffer. In addition, currently available deposition techniques are suitable merely for small scales. In this article, we exploit a spray-coating technique in order to resolve the aforementioned issues in the deposition of different 2D and 3D DNA origami nanostructures. We show that purified DNA origamis can be controllably deposited on silicon and glass substrates by the proposed method. The results are verified using either atomic force microscopy or fluorescence microscopy depending on the shape of the DNA origami. DNA origamis are successfully deposited onto untreated substrates with surface coverage of about 4 objects/mm^2. Further, the DNA nanostructures maintain their shape even if the salt residues are removed from the DNA origami fabrication buffer after the folding procedure. We believe that the presented one-step spray-coating method will find use in various fields of material sciences, especially in the development of DNA biochips and in the fabrication of metamaterials and plasmonic devices through DNA metallisation.

DNA has astonishing potential as programmable nanoscale construction material for the bottom-up-based nanofabrication[1] and for a great variety of bionanotechnological applications[2]. To date, a plethora of design strategies for assembling DNA molecules into customized structures and templates have been introduced[2]. Arguably, one of the most elegant one is a scaffolded DNA origami technique, which enables a straightforward fabrication of arbitrary two- (2D)[3] and three-dimensional (3D)[4,5] nanoshapes, meshed structures[6] as well as large assemblies with high spatial addressability[7].

Recently, DNA nanoarchitectures have been utilized in various innovative applications that truly underline the feasibility of the structural DNA nanotechnology. DNA origamis can serve as molecular scale circuit boards in nanoelectronics[8], scaffolds for plasmonic structures[9,10] and gatekeepers for solid-state nanopores[11,12]. Biotechnological examples include smart molecular devices[13,14] such as nanorobots[15], cellular delivery vehicles[16,17], and synthetic ion channels[18].

Despite the fact that DNA origami itself has limited properties in optics and in electronics[19–22], its use in templating is extremely promising. There exist plenty of placement and deposition methods for DNA origamis that are useful for patterning on different substrates. One straightforward way is to utilize chemically modified surfaces, which enable selective anchoring of the origamis[23–25], whereas some substrates can be used to assist large-scale lattice formation of DNA origamis[26–28]. In addition, hierarchically

[1]Aalto University, Department of Biotechnology and Chemical Technology, Biohybrid Materials, Espoo, P.O. Box 16100, FI-00076 Aalto, Finland. [2]University of Jyvaskyla, Department of Physics, Nanoscience Center, Jyväskylä, P.O. Box 35, FI-40014 University of Jyväskylä, Finland. [3]Tampere University of Technology, Department of Automation Science and Engineering, Tampere, P.O. Box 692, FI-33101, Finland. Correspondence and requests for materials should be addressed to M.A.K. (email: mauri.kostiainen@aalto.fi) or S.T. (email: sampo.tuukkanen@tut.fi)

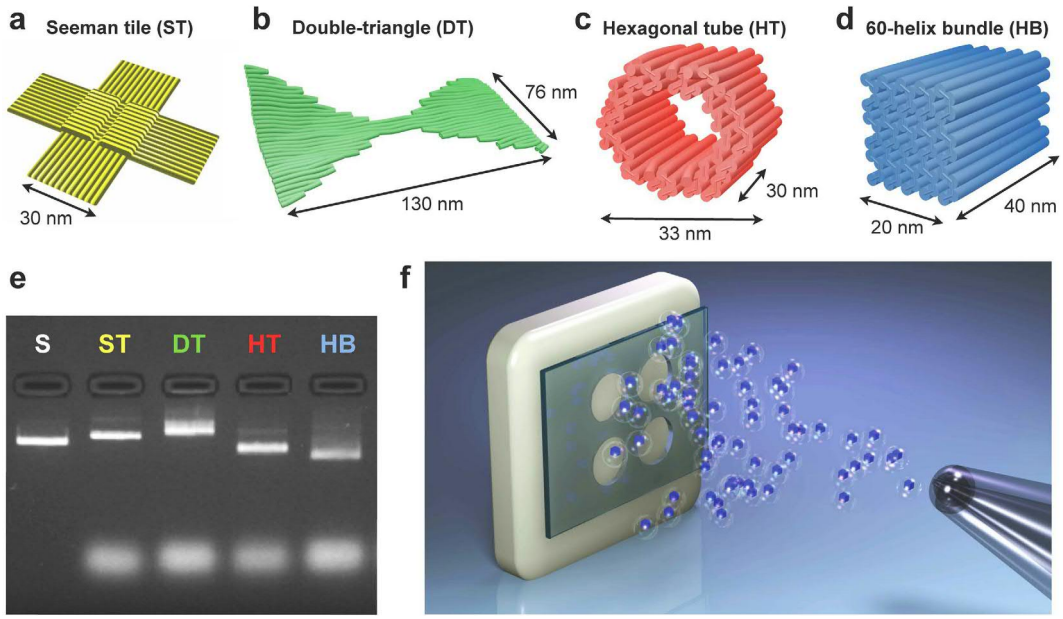

Figure 1. DNA origami nanostructures for patterning. (**a**) Seeman tile (ST)[7], (**b**) double-triangle (DT), (**c**) hexagonal tube (HT)[52] and (**d**) 60-helix bundle (HB). (**b**–**d**) are CanDo-simulated[57] deformed solution shapes, resolved using caDNAno design files[58] as inputs. (**e**) Agarose gel electrophoresis of the well-folded DNA structures described in (**a**–**d**). S = scaffold strand (M13mp18), which is used as a reference sample. (**f**) A schematic view of patterning a substrate (white colour) through an optionally used mechanical mask (green colour, openings 1–2 mm in diameter). DNA origami nanostructures (blue 60-helix bundles) are sprayed onto the substrate using an airbrush device. Figure (**f**) is not in scale.

ordered nanosystems can be obtained by combining DNA structures with patterned substrates, such as lithographically fabricated confined wells[29,30] and other surface patterns, which are specifically designed for the alignment of DNA structures[31,32]. Moreover, single DNA molecules[33–35] and complex DNA nanoarchitectures[36–38] can be selectively guided and anchored onto substrates by means of electric fields. Nevertheless, in order to utilize such approaches one has to pay extra attention to the deposition conditions (salt concentration, pH, surface chemistry etc.). In many occasions, the required treatments and prevalent conditions set strict limitations to the conceivable applications.

In general, print-coating technologies provide high-throughput and low-cost patterning methods for solution processable materials[39]. Although aqueous dispersion of DNA is solution processable, these techniques have not been so far adapted in the field of structural DNA nanotechnology. However, in this article we show that the high spatial addressability of the structurally different DNA origamis can be genuinely combined with the large-scale print-coating methods. The authors have previously demonstrated the feasibility of the solution processing techniques in various other applications, such as stretchable electrodes[40], piezoelectric sensors[41,42], transparent touch panels[43], supercapacitors[44,45] and energy harvesters[46,47]. The same methods are now expanded to the field of DNA nanotechnology.

In this study a spray-coating technique is used to achieve a straightforward, fast and cost-effective way to pattern substrates with custom-shaped DNA structures on large scale (Fig. 1). The deposition areas demonstrated here are ~10 cm^2, but the method can be easily scaled-up to wafer-scales and even larger surfaces. The proposed method does not require special substrate conditions or washing procedures, and moreover, salt residues from the DNA origami buffer can be eliminated by removing salt ions right before the coating procedure. With this method, the fabricated DNA origami dispersions can be utilised fully without any loss of material, which makes the relative cost of DNA reagents negligible. Thus, this highly robust technique could find use in many applications. Homogeneous large-scale DNA patterns could be exploited e.g. in creating DNA origami microarrays[48], whereas DNA origami-based metallic assemblies[49] can yield intriguing opportunities for developing nanoplasmonics[10,50] and metamaterials[51].

Results

DNA origami nanostructures. In this work, four different DNA origami structures were prepared by folding the M13mp18 scaffold strand with the help of specific sets of staple strands. 2D single-layer DNA architectures, a Seeman tile (ST)[7] and a double-triangle (DT) were fabricated for studying the coating with scanning probe microscopy. Furthermore, two 3D multilayer and fluorescently labelled DNA architectures, a hexagonal tube (HT)[52] and a 60-helix bundle (HB) were utilised when the coating was characterised using optical microscopy. The DNA origami shapes and their dimensions are presented

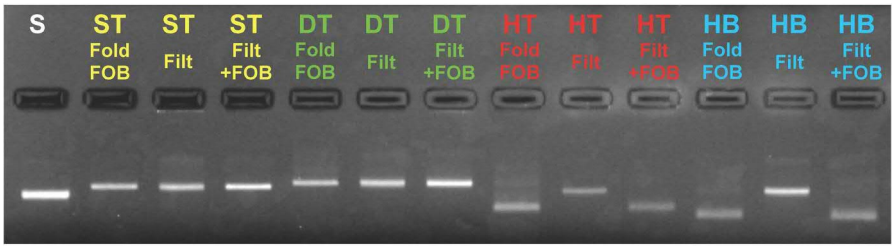

Figure 2. Agarose gel electrophoresis for all four types of DNA origami structures. Fold = DNA structures after folding in the folding buffer (FOB) (for ST and DT FOB is 1× TAE + 12.5 mM Mg^{2+} and for HT and HB 1× TAE + 20 mM Mg^{2+}). Filt = DNA structures filtered with pure water. Filt+FOB = Filtered DNA structures stored in water for 1 day, after which the buffer conditions have been adjusted to the same as for folding. S is a scaffold strand (M13mp18), which is used as a reference sample.

in Fig. 1a–d. The correct folding of all four DNA objects was verified using agarose gel elecrophoresis (Fig. 1e) by comparing the running speed of the leading bands to the reference sample (M13mp18 scaffold). In addition, correct HT and HB folding was confirmed using transmission electron microscopy (Supplementary Fig. S1 and Supplementary Note 2).

The excess DNA staple strands (bright areas at the bottom of the gel lanes (Fig. 1e)) were removed in a nondestructive spin-filtering process. In general, spin-filtering technique is a straightforward way for exchanging the buffer and for efficiently removing salt from the starting solution[36]. For filtering of the samples, pure water was used, which practically removes all the Mg^{2+} ions and other salt residues from the DNA origami annealing solution (see Methods section for the details). Mg^{2+} concentration changes from 12.5–20 mM to as low as 1–4 μM. Importantly, agarose gel electrophoresis analysis (Fig. 2) proves that the DNA structures stay intact in the purification process. Although HT and HB bands shift in the gel after water-filtering (due to the different buffer conditions), the bands appear again at the exactly same positions once the salt and buffer have been added, i.e. the folding conditions have been restored.

The agarose gel analysis was repeated 14 weeks later for the spin-filtered samples in water (Supplementary Fig. S2). It showed that the DNA origamis are stable in water over long time. However, it is probable that slight agglomeration of the objects starts to occur over time if the storage solution has a high origami concentration. Hence, all the spray-coating experiments reported in this article were performed immediately after the purification step.

Spray-coating and patterning with DNA nanostructures. The purified and salt-free DNA origamis (in water) were deposited using a spray-coating method (Fig. 1f). The spray-coating was performed using a manual airbrush which was kept at 5–10 cm distance from the substrate. The coating was carried out in a layer-like fashion by spraying a small layer at a time. The droplets were let to dry between the successively deposited layers. In this work, two different approaches were applied; first, we aimed at homogeneous coverage of 2D ST and DT origamis on silicon substrates (without masking), and second, formation of large-area patterns of fluorescently labelled 3D HT and HB origamis (with masking).

Homogeneous substrate coverage using DNA origamis. The two single-layer DNA origamis (ST and DT) were deposited on untreated silicon substrates by spray-coating the dilute DNA origami solutions (1 nM). The homogeneous coverage was obtained for both ST and DT origamis as can be seen from the atomic force microscope (AFM) images (Fig. 3a–d) and the histograms showing the nearest-neighbour distances (Fig. 3e,f) obtained with the coating parameters optimised for the homogeneous coverage (see the Methods section for the details). In addition, spray-coating with the optimised parameters resulted in the surface coverage values of 4.6 ± 0.8 objects/μm^2 (standard deviation, s.d.) and 3.9 ± 0.4 objects/μm^2 (s.d.) for ST and DT, respectively. The statistics of the particle coverage distribution and the nearest-neighbour distances were determined from several different AFM images.

Further, since the structures used in these experiments were flat, the structural details of the DNA objects could be fully resolved by AFM. For both structures the correct DNA origami shapes are well preserved as seen in Fig. 3c,d. This is a significant observation, taking into account that the salt has been removed from the deposition solution. The DT structure is highly flexible (the most flexible among these four structures, see Supplementary Fig. S3), and thus some objects tend to adopt slightly bent conformations on the substrate. In addition, some DT bundles were observed, but these small aggregates are formed already in the folding process via unspecific base stacking interactions between the objects (this can be seen as a faint multimer-tail in the DT lane in Fig. 1e).

Large-area patterning with DNA origamis. The patterns of two fluorescently labelled (Cy5) 3D multilayer DNA origamis (HT and HB) were deposited onto glass slides through a mechanical polydimethylsiloxane (PDMS) mask (Fig. 4a,b). HT and HB structures were deposited at 10 nM concentration

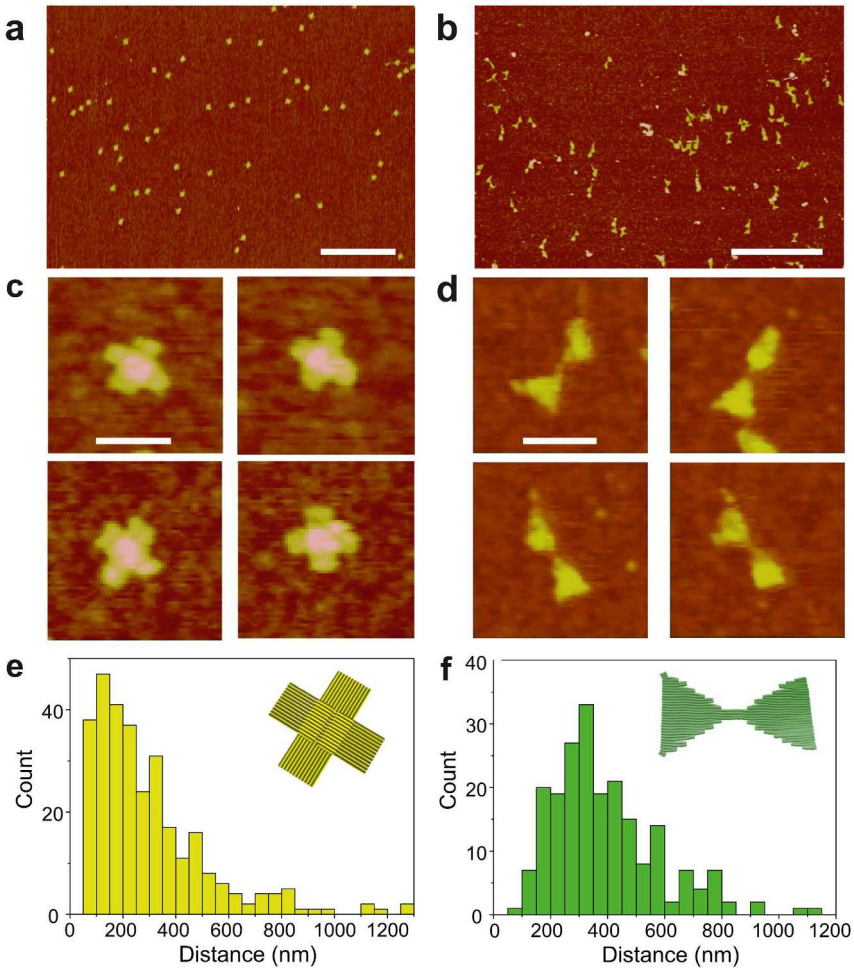

Figure 3. Purified and salt-free 2D DNA origami nanostructures deposited onto the untreated silicon substrates using a spray-coating technique. AFM images of (**a**) Seeman tile (ST) and (**b**) double-triangle (DT) coated substrates. The scale bars are 1 μm. (**c**,**d**) Zoomed-in images of single objects. The scale bars are 100 nm. (**e**,**f**) Histograms of the nearest-neighbour distances for deposited ST and DT origami shapes. The deposition was carried out using optimised parameters for homogeneous coating.

(10× more concentrated than the solutions used in coating of silicon substrates) in order to get enough contrast in fluorescence imaging. After coating and mask removal, the formation of HT and HB patterns on transparent glass substrates were verified using optical fluorescence microscopy. The characterisation shows that the PDMS mask edges are very sharp and the fluorescence is fairly distributed in the patterned area (Fig. 4c,d). In Fig. 4c 60-helix bundles with different concentrations (first 10 nM and second 5 nM) are deposited sequentially onto the glass substrate through two different masks (first through a mask with larger holes and then through a mask with smaller holes). Optical microscopy was used here instead of AFM in order to demonstrate the feasibility of the method also on sub-millimeter and millimeter scale. Moreover, the structural details of 3D DNA origamis are hardly visible in AFM.

The PDMS mask attaches well to flat substrates, such as silicon, glass or plastic, preventing the spray-coated drops from penetrating between the mask and the substrate[45]. In addition, the removal of the mask does not harm the obtained DNA origami pattern, and the same mask can be used several times for coating. The pattern design can be arbitrarily chosen, and the silicon mold for the mask can be prepared with high accuracy by exploiting conventional microfabrication methods. In addition, as shown in Fig. 4c, the patterning can be realised in a sequential fashion, enabling the controllable formation of complex patterns. These results show that the proposed method is highly applicable for a large-scale substrate patterning with DNA origami nanostructures.

Conclusions

As a conclusion, we have shown that structurally distinct DNA origami nanostructures can be uniformly deposited on different substrates. The proposed deposition method is versatile and has outstandingly high yield, since all the material placed in the spray-coating device will be homogeneously deposited onto

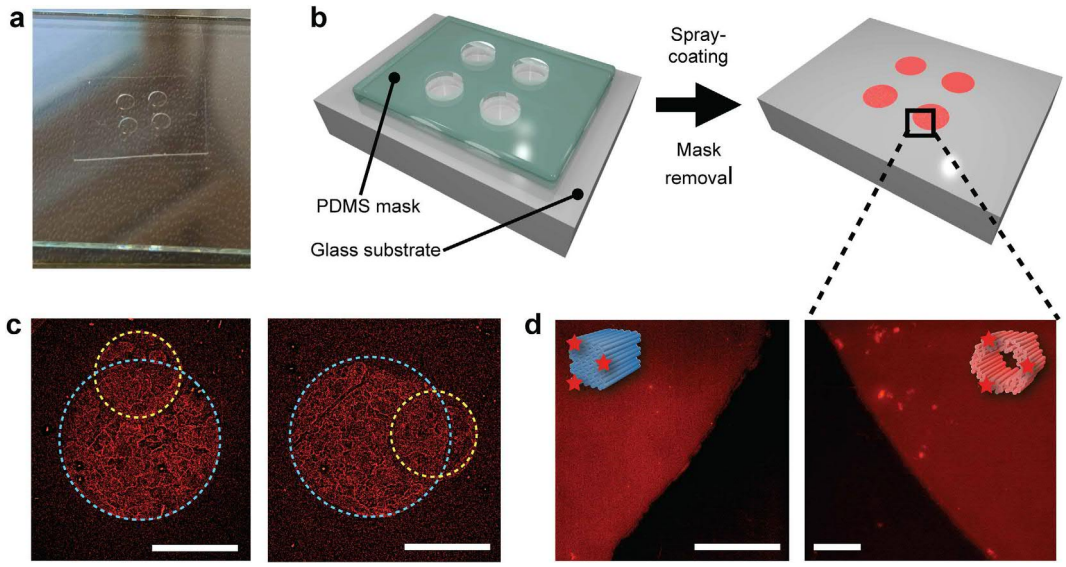

Figure 4. Patterning substrates with fluorescently labelled DNA origamis. (**a**) A photograph of a mechanical polydimethylsiloxane (PDMS) mask (with round 1.8 mm diameter openings) on top of the glass substrate. (**b**) A schematic view of the patterning setup. Spray-coating of labelled DNA origamis is carried out through the PDMS mask. (**c**) Fluorescence micrographs of patterns created using sequential spray-coating of Cy5-labelled and purified 60-helix bundles (HB) onto a glass substrate. HBs were deposited first through a mask with large holes (1.8 mm in diameter, blue dashed circle) and after that through a mask having slightly smaller holes (1 mm in diameter, yellow dashed circle). The scale bars are 1 mm. (**d**) Fluorescence micrographs of the glass substrates after coating with Cy5-labelled and purified HBs (left) and hexagonal tubes (right). Micrographs in (**d**) were taken after the mask removal at the edges of the formed round patterns (diameter 1.8 mm) as indicated by the black square and the dashed lines. The scale bars are 50 μm.

the selected substrates, opposite to the common drop casting techniques. This is also a straightforward coating method, since it does not require additional washing steps or optional pre-treatments of the substrates. Furthermore, the method enables wafer-scale deposition and patterning of DNA origamis within minutes making the method highly cost-effective. This is an important detail in the field of structural DNA nanotechnology, since large-scale fabrication of complex DNA nanostructures is still relatively expensive[53]. Thus, the efficient large-scale deposition methods are urgently needed for conceivable applications. An estimated cost of large-scale DNA origami coating with the surface coverage obtained in this work (about 4 objects/μm^2) would be of the order of 1 euro per square meter, which is rather inexpensive compared to typical substrate costs.

The presented method can be easily scaled up, and interestingly, it also enables the utilisation of flexible substrates, such as plastics, making the technique truly versatile. This feature could be exploited in a roll-to-roll production line, where large surfaces can be coated with homogeneous films. The method has potential implementations for example in creating large-scale DNA chips and self-assembly -based biosensors on specific substrates[54]. Further, metallisation of DNA nanoshapes[49,55] might enable fabrication of large films with attractive plasmonic or electrical properties.

Methods

DNA origami preparation. DNA origami nanostructures (Fig. 1a–d) were fabricated, analysed and purified as described below.

DNA origami folding. A double-triangle structure (Supplementary Fig. S3 and S4) was folded in 100 μl quantities using 20 nM M13mp18 scaffold strand (New England Biolabs or Tilibit Nanosystems) and a set of 163 staple strands (Supplementary Table S3) (IDT, standard desalting) at 10× excess (200 nM). The design contains skipped scaffold bases to compensate the undesired global twisting of the object (the twist is caused by the square packaging of helices[56]) (Supplementary Fig. S4). The folding took place in a buffer containing 1× TAE (40 mM tris(hydroxymethyl)aminomethane (Tris), 1 mM ethylenediaminetetraacetic acid (EDTA), and acetic acid for adjusting pH to 8.3), 5 mM NaCl and 12.5 mM $MgCl_2$. The thermal folding ramp (for G-Storm G1 thermal cycler) is shown below:

- From 90 °C to 70 °C: 0.2 °C decrease/8 seconds.
- From 70 °C to 60 °C: 0.1 °C decrease/8 seconds.

- From 60 °C to 27 °C: 0.1 °C decrease/2 minutes.
- Store at 12 °C.

For a 60-helix bundle (Supplementary Fig. S5), 141 staple strands (Supplementary Table S4) and additional 6 linker strands (Supplementary Table S2 and Supplementary Note 4) for anchoring Cy5-labelled strands (Supplementary Note 4) were used (IDT, standard desalting). The reagents and quantities are the same as above, except that the folding buffer contained 20 mM $MgCl_2$. The folding steps are listed below:

- From 65 °C to 59 °C: 1.0 °C decrease in 15 minutes.
- From 59 °C to 40 °C: 0.25 °C decrease in 45 minutes.
- Store at 12 °C.

A Seeman tile[7] and a hexagonal tube[52] were folded similarly as reported in the original articles. Sidestrands for both structures were omitted in order to avoid blunt-end stacking of the objects. For HT, 5 linker strands (Supplementary Table S1 and Supplementary Note 4) were used for anchoring the Cy5-labelled strands (Supplementary Note 4).

Agarose gel electrophoresis. Agarose gel electrophoresis (Fig. 1e) was used for verifying the quality of the folding. 2 grams of agarose (Sigma-Aldrich) was mixed with 100 ml of 1× TAE buffer containing 11 mM $MgCl_2$, and the gel was stained with 80 μl of ethidium bromide (EthBr) solution (0.625 mg/l). The samples were prepared by mixing 10–20 μl of concentration-adjusted DNA origami solution with 2–4 μl of 6× Blue Loading Dye (New England Biolabs). 10 μl of each sample was loaded into a gel pocket. M13mp18 scaffold strand was used as a reference. 1× TAE including 11 mM $MgCl_2$ was used as a running buffer and the gel was run with a constant voltage of 90–95 V for 45–70 minutes.

DNA origami purification. After verifying the quality of folding, the excess amount of staple strands and unbound Cy5-labeled strands as well as salt residues were removed from the DNA origami solution in a non-destructive spin-filtering process. For filtering, we used 0.5 ml filter columns with 100 kDa molecular weight cut-off (Millipore Amicon Ultra YM-100). Filtration steps (3 filtering rounds) are described below.

- 50 μl of DNA solution was diluted to 500 μl in a filter column placed in a 2 ml tube using Milli-Q water, and the diluted solution was spun with 14,000 rcf for 3 minutes.
- A flowthrough was discarded and 450 μl of water was added to the filter.
- Sample was spun another time repeating the steps described above. For the third similar filtering round the centrifugation time was adjusted to 5 minutes.
- Finally, the filter was turned upside down in a fresh 2 ml tube and was spun 2 minutes at 1,000 rcf in order to collect the solution from the filter membrane.

After each filtration round the volume of the solution was brought down to 15–20 μl. Therefore, it can be estimated that by 3 filtering rounds the Mg^{2+} concentration can be reduced from 12.5–20 mM to 1–4 μM. The concentration of the final DNA origami solution was estimated to be around 20 nM. The spray-coating was performed immediately after the purification step in order to prevent possible aggregation of the DNA objects (Supplementary Fig. S2 and Supplementary Note 3)

Spray-coating of DNA origamis. DNA origami nanostructures were spray-coated on silicon and glass substrates using two different approaches as described below.

Films of single-layer DNA origamis. Spray-coating of the DNA origami solutions on silicon substrate (chips of size 10 mm × 10 mm, total spraying area roughly 30 mm × 30 mm) was carried out with a manual airbrush (nozzle size 300 μm) using compressed air (pressure ~3 bar) as a carrier gas. The coating was performed sequentially by depositing a layer of droplets (barely visible to eye) at the time. After every deposition layer, droplets were let to evaporate in ambient conditions. Typically the substrates were fully patterned within several minutes. The films of Seeman tile (ST) and double-triangle (DT) were deposited on silicon substrates (without masking) using 40 μl of 1 nM DNA origami solution.

Patterns of multilayer DNA origamis. The patterns of fluorescently labelled hexagonal tubes (HT) and 60-helix bundles (HB) were formed on glass substrates (microscope slides of size 75 mm by 25 mm). Same spray-coating conditions were used here as explained above. For each glass slide 40 μl of 10 nM DNA origami solution was used. The pattern was defined by spray-coating through a 160 μm thick polydimethylsiloxane (PDMS) film with round openings.

The PDMS film (Fig. 4a) was prepared from a silicone elastomer kit (Sylgard 184) using base/curing agent mix ratio 10:1. The mixture was spin-coated at 700 rpm for 1 min on a glass plate and cured 4 h at 60 °C in the oven. Round openings of 1.0 and 1.8 mm diameter were then patterned to the PDMS film using mechanical cutting tools.

Sample characterisation. The substrates with homogeneously covered single-layer DNA origami structures (ST and DT) were characterised using atomic force microscopy (AFM). For multilayer DNA structures (HT and HB), fluorescence microscopy was utilized. The structural characterisation of multilayer origamis was carried out using transmission electron microscopy (TEM) (Supplementary Fig. S1 and Supplementary Note 2).

AFM imaging. Silicon and glass substrates with immobilized DNA origamis (ST and DT) were imaged using AFM (Veeco Dimension 3100 or 5000) in tapping mode with a scan rate of 1.0–1.5 Hz.

Fluorescence microscopy. Glass slides patterned with fluorescently labelled DNA origamis (HT and HB) were imaged using a Nikon Eclipse Ti microscope equipped with a 4× magnification object or a BioTek Cytation 3 microscope with a 20× magnification object. Cy5 was excited using either 638 nm laser (Nikon setup) or 590 nm LED cube (BioTek setup).

References

1. Seeman, N. C. DNA in a material world. *Nature* **421,** 427–431 (2003).
2. Linko, V. & Dietz, H. The enabled state of DNA nanotechnology. *Curr. Opin. Biotechnol.* **24,** 555–561 (2013).
3. Rothemund, P. W. K. Folding DNA to create nanoscale shapes and patterns. *Nature* **440,** 297–302 (2006).
4. Douglas, S. M. *et al.* Self-assembly of DNA into nanoscale three-dimensional shapes. *Nature* **459,** 414–418 (2009).
5. Dietz, H., Douglas, S. M. & Shih, W. M. Folding DNA into twisted and curved nanoscale shapes. *Science* **325,** 725–730 (2009).
6. Benson, E. *et al.* DNA rendering of polyhedral meshes at the nanoscale. *Nature* **523,** 441–444 (2015).
7. Liu, W., Zhong, H., Wang, R. & Seeman, N. C. Crystalline two-dimensional DNA-origami arrays. *Angew. Chem. Int. Ed.* **50,** 264–267 (2011).
8. Maune, H. T. *et al.* Self-assembly of carbon nanotubes into two-dimensional geometries using DNA origami templates. *Nature Nanotech.* **5,** 61–66 (2010).
9. Kuzyk, A. *et al.* DNA-based self-assembly of chiral plasmonic nanostructures with tailored optical response. *Nature* **483,** 311–314 (2012).
10. Chao, J., Lin, Y., Liu, H., Wang, L. & Fan, C. DNA-based plasmonic nanostructures. *Mater. Today* **18,** 326–335 (2015).
11. Wei, R., Martin, T. G., Rant, U. & Dietz, H. DNA origami gatekeepers for solid-state nanopores. *Angew. Chem. Int. Ed.* **51,** 4948–4951 (2012).
12. Plesa, C. *et al.* Ionic permeability and mechanical properties of DNA origami nanoplates on solid-state nanopores. *ACS Nano* **8,** 35–43 (2014).
13. Li, J., Fan, C., Pei, H., Shi, J. & Huang, Q. Smart drug delivery nanocarriers with self-assembled DNA nanostructures. *Adv. Mater.* **25,** 4386–4396 (2013).
14. Linko, V., Ora, A. & Kostiainen, M. A. DNA nanostructures as smart drug-delivery vehicles and molecular devices. *Trends Biotechnol.* **33**, 586-594 (2015).
15. Douglas, S. M., Bachelet, I. & Church, G. M. A logic-gated nanorobot for targeted transport of molecular payloads. *Science* **335,** 831–834 (2012).
16. Mikkilä, J. *et al.* Virus-encapsulated DNA origami nanostructures for cellular delivery. *Nano Lett.* **14,** 2196–2200 (2014).
17. Perrault, S. D. & Shih, W. M. Virus-inspired membrane encapsulation of DNA nanostructures to achieve *in vivo* stability. *ACS Nano* **8,** 5132–5140 (2014).
18. Langecker, M. *et al.* Synthetic lipid membrane channels formed by designed DNA nanostructures. *Science* **338,** 932–936 (2012).
19. Bobadilla, A. D. *et al.* DNA origami impedance measurement at room temperature. *J. Chem. Phys.* **130,** 171101 (2009).
20. Linko, V., Paasonen, S.-T., Kuzyk, A., Törmä, P. & Toppari, J. J. Characterization of the conductance mechanisms of DNA origami by AC impedance spectroscopy. *Small* **5,** 2382–2386 (2009).
21. Bellido, E. P. *et al.* Current-voltage-temperature characteristics of DNA origami. *Nanotechnology* **20,** 175102 (2009).
22. Linko, V. & Toppari, J. J. Self-assembled DNA-based structures for nanoelectronics. *J. Self-Assembly Mol. Electron.* **1,** 101–124 (2013).
23. Gerdon, A. E. *et al.* Controlled delivery of DNA origami on patterned surfaces. *Small* **5,** 1942–1946 (2009).
24. Penzo, E., Wang, R., Palma, M. & Wind, S. J. Selective placement of DNA origami on substrates patterned by nanoimprint lithography. *J. Vac. Sci. Technol. B* **29,** 06F205 (2011).
25. Shah, F. A., Kim, K. N., Lieberman, M. & Bernstein, G. H. Roughness optimization of electron-beam exposed hydrogen silsesquioxane for immobilization of DNA origami. *J. Vac. Sci. Technol. B* **30,** 011806 (2012).
26. Noh, H., Hung, A. M. & Cha, J. N. Surface-driven DNA assembly of binary cubic 3d nanocrystal superlattices. *Small* **7,** 3021–3025 (2011).
27. Woo, S. & Rothemund, P. W. K. Self-assembly of two-dimensional DNA origami lattices using cation-controlled surface diffusion. *Nat. Commun.* **5,** 4889 (2014).
28. Rafat, A. A., Pirzer, T., Scheible, M. B., Kostina, A. & Simmel, F. C. Surface-assisted large-scale ordering of DNA origami tiles. *Angew. Chem. Int. Ed.* **53,** 7665–7668 (2014).
29. Kershner, R. J. *et al.* Placement and orientation of individual DNA shapes on lithographically patterned surfaces. *Nature Nanotech.* **4,** 557–561 (2009).
30. Gopinath, A. & Rothemund, P. W. K. Optimized assembly and covalent coupling of single-molecule DNA origami nanoarrays. *ACS Nano* **8,** 12030–12040 (2014).
31. Pearson, A. C. *et al.* Chemical alignment of DNA origami to block copolymer patterned arrays of 5 nm gold nanoparticles. *Nano Lett.* **11,** 1981–1987 (2011).
32. Ding, B. *et al.* Interconnecting gold islands with DNA origami nanotubes. *Nano Lett.* **10,** 5065–5069 (2010).
33. Chou, C.-F. *et al.* Electrodeless dielectrophoresis of single- and double-stranded DNA. *Biophys. J.* **83,** 2170–2179 (2002).
34. Tuukkanen, S. *et al.* Trapping of 27 bp-8 kbp DNA and immobilization of thiol-modified DNA using dielectrophoresis. *Nanotechnology* **18,** 295204 (2007).
35. Linko, V. *et al.* Growth of immobilized DNA by polymerase: bridging nanoelectrodes with individual dsDNA molecules. *Nanoscale* **3,** 3788–3792 (2011).
36. Kuzyk, A., Yurke, B., Toppari, J. J., Linko, V. & Törmä, P. Dielectrophoretic trapping of DNA origami. *Small* **4,** 447–450 (2008).
37. Linko, V., Leppiniemi, J., Paasonen, S.-T., Hytönen, V. P. & Toppari, J. J. Defined-size DNA triple crossover construct for molecular electronics: modification, positioning and conductance properties. *Nanotechnology* **22,** 275610 (2011).
38. Shen, B., Linko, V., Dietz, H. & Toppari, J. J. Dielectrophoretic trapping of multilayer DNA origami nanostructures and DNA origami-induced local destruction of silicon dioxide. *Electrophoresis* **36,** 255–262 (2015).

39. Arias, A. C., MacKenzie, J. D., McCulloch, I., Rivnay, J. & Salleo, A. Materials and applications for large area electronics: solution-based approaches. *Chem. Rev.* **110,** 3–24 (2010).
40. Tuukkanen, S. *et al.* Stretching of solution processed carbon nanotube and graphene nanocomposite films on rubber substrates. *Synt. Met*. **191,** 28–35 (2014).
41. Tuukkanen, S. *et al.* Solution-processible electrode materials for a heat-sensitive piezoelectric thin-film sensor. *Synt. Met*. **162,** 1987–1995 (2012).
42. Rajala, S., Tuukkanen, S. & Halttunen, J. Characteristics of piezoelectric polymer film sensors with solution-processable graphene-based electrode materials. *IEEE Sens. J.* **15,** 3102–3109 (2015).
43. Vuorinen, T. *et al.* Printable, transparent, and flexible touch panels working in sunlight and moist environments. *Adv. Funct. Mater.* **24,** 6340–6347 (2014).
44. Lehtimäki, S. *et al.* Low-cost, solution processable carbon nanotube supercapacitors and their characterization. *Appl. Phys. A* **117,** 1329–1334 (2014).
45. Tuukkanen, S. *et al.* Printable and disposable supercapacitor from nanocellulose and carbon nanotubes. In *Electronics System-Integration Technology Conference (ESTC), 2014,* 1–6 (IEEE, 2014).
46. Porhonen, J., Rajala, S., Lehtimäki, S. & Tuukkanen, S. Flexible piezoelectric energy harvesting circuit with printable supercapacitor and diodes. *IEEE Trans. Electron Devices* **61,** 3303–3308 (2014).
47. Lehtimäki, S. *et al.* Performance of printable supercapacitors in an RF energy harvesting circuit. *Int. J. Elec. Power* **58,** 42–46 (2014).
48. Scheible, M. B., Pardatscher, G., Kuzyk, A. & Simmel, F. C. Single molecule characterization of DNA binding and strand displacement reactions on lithographic DNA origami microarrays. *Nano Lett.* **14,** 1627–1633 (2014).
49. Shen, B., Linko, V., Tapio, K., Kostiainen, M. A. & Toppari, J. J. Custom-shaped metal nanostructures based on DNA origami silhouettes. *Nanoscale* **7,** 11267–11272 (2015).
50. Jones, M. R., Osberg, K. D., Macfarlane, R. J., Langille, M. R. & Mirkin, C. A. Templated techniques for the synthesis and assembly of plasmonic nanostructures. *Chem. Rev.* **111,** 3736–3827 (2011).
51. Soukoulis, C. M. & Wegener, M. Past achievements and future challenges in the development of three-dimensional photonic metamaterials. *Nat. Photon*. **5,** 523–530 (2011).
52. Linko, V., Eerikäinen, M. & Kostiainen, M. A. A modular DNA origami-based enzyme cascade nanoreactor. *Chem. Commun.* **51,** 5351–5354 (2015).
53. Pinheiro, A. V., Han, D., Shih, W. M. & Yan, H. Challenges and opportunities for structural DNA nanotechnology. *Nature Nanotech*. **6,** 763–772 (2011).
54. Zhang, X., Rahman, M., Neff, D. & Norton, M. L. DNA origami deposition on native and passivated molybdenum disulfide substrates. *Beilstein J. Nanotechnol.* **5,** 501–506 (2014).
55. Schreiber, R. *et al.* DNA origami-templated growth of arbitrarily shaped metal nanoparticles. *Small* **7,** 1795–1799 (2011).
56. Ke, Y. *et al.* Multilayer DNA origami packed on a square lattice. *J. Am. Chem. Soc.* **131,** 15903–15908 (2009).
57. Castro, C. E. *et al.* A primer to scaffolded DNA origami. *Nat. Methods* **8,** 221–229 (2011).
58. Douglas, S. M. *et al.* Rapid prototyping of 3D DNA-origami shapes with caDNAno. *Nucleic Acids Res.* **37,** 5001–5006 (2009).

Acknowledgements

This work was supported by the Academy of Finland (grants 218182, 263526, 258309, 263504, 267497, 273645). In addition, V.L. and M.A.K. acknowledge financial support from Biocentrum Helsinki, Emil Aaltonen Foundation and EU EMRP (SIB61). This work was carried out under the Academy of Finland's Centres of Excellence Programme (2014–2019) and made use of Aalto University Microscopy Center (Aalto-NMC) facilities. We thank Jenny Kiviaho and Marika Eerikäinen for TEM analysis of 3D DNA origamis, Erika Järvihaavisto for technical assistance and Visa Ruokolainen for assisting in fluorescence microscopy imaging.

Author Contributions

V.L. and S.T. designed research and conceived the experiments; V.L., B.S. and S.T. performed the experiments; V.L. and S.T. prepared the main manuscript; V.L., B.S., K.T., J.J.T., M.A.K. and S.T. analysed the results and edited/reviewed the manuscript.

Additional Information

Supplementary information accompanies this paper at http://www.nature.com/srep

Competing financial interests: The authors declare no competing financial interests.

How to cite this article: Linko, V. *et al.* One-step large-scale deposition of salt-free DNA origami nanostructures. *Sci. Rep.* **5**, 15634; doi: 10.1038/srep15634 (2015).